

**Modified hexamethyldisilazane (HMDS) – assisted
synthesis of surfactant free metal chalcogenide
nanoparticles and their applications as catalysts
and photoresponsive materials**

**A thesis submitted for the degree of
DOCTOR OF PHILOSOPHY
in
CHEMISTRY
By**

SRINIVAS BILLAKANTI



**SCHOOL OF CHEMISTRY
UNIVERSITY OF HYDERABAD
HYDERABAD - 500046
INDIA
July 2017**

Dedicated
to



My Father & Mother

CONTENTS

STATEMENT	(i)
DECLARATION	(ii)
CERTIFICATE	(iii)
TABLE OF CONTENTS	(iv)
ACKNOWLEDGEMENTS	(x)
LIST OF SCHEMES	(xiv)
LIST OF FIGURES	(xv)
LIST OF TABLES	(xix)
ACRONYMS	(xx)
SYNOPSIS	(xxii)

Chapter 1

Introduction

1.1. Nanoscale materials and their properties	2
1.1.1. Surface area	3
1.1.2. Quantum confinement	4
1.1.3. Optical properties	5
1.2. Application of nanoparticles	7
1.2.1. Nanoparticles as catalysts	8
1.2.2. Nanoparticles as photocatalysts	10
1.2.3. Nanoparticles in photovoltaic cells	11
1.3. Synthesis of metal chalcogenide nanoparticles	14
1.3.1. Stoichiometric varieties in metal chalcogenides and general synthetic approach	14
1.3.2. Synthesis of copper chalcogenides	15

1.3.3. Synthesis of cadmium chalcogenides	17
1.3.4. Synthesis of bismuth chalcogenides	18
1.3.5. Synthesis of nickel chalcogenides	19
1.3.6. Synthesis of ternary systems	21
1.4. Role of capping agents and the stability of the nanoparticles	23
1.4.1. Architecture of capping agent	23
1.4.2. Modes of stabilization	24
1.5. Definition of the problem	25
1.6. Scope of the thesis	27
1.7. References	29

Chapter 2

Recyclable Ni₃S₄ nanocatalyst for hydrogenation of nitroarenes

2.1. Introduction	46
2.2. Experimental section	47
2.2.1. Materials	47
2.2.2. Synthesis of nickel sulphide nanoparticles	47
2.2.3. Hydrogenation of the nitroarenes	48
2.2.4. Instruments and sample preparation	48
2.3. Results and discussion	49
2.3.1. Synthesis of Ni ₃ S ₄ nanocatalyst	49
2.3.2. Characterization of Ni ₃ S ₄ nanomaterial	51
2.3.3. Microscopic investigation of Ni ₃ S ₄ nanoparticles	53
2.3.4. Ni ₃ S ₄ nanoparticles as the catalyst	56
2.3.5. Recyclability	61
2.4. Summary	63

2.5. References	63
------------------------	-----------

Chapter 3

Stabilizer free copper sulphide nanostructures for rapid photocatalytic decomposition of rhodamine B

3.1. Introduction	68
3.2. Experimental section	70
3.2.1. Materials	70
3.2.2. Synthesis of CuS microflowers	70
3.2.3. Synthesis of Cu ₂ S nanoparticles	71
3.2.4. Photocatalysis	71
3.3. Results and Discussion	72
3.3.1. Modified HMDS-assisted synthetic method	72
3.3.2. Characterization of CuS nanomaterial	74
3.3.3. Dimensions and flower morphology of CuS particles	76
3.3.4 Anisotropic growth of (1 0 3) _{CuS} planes: self-assembly of nanoscale flakes	77
3.3.5. Stoichiometric modification-Cu ₂ S nanoparticles formation	79
3.3.6. Optical properties	83
3.3.7. CuS flowers as photocatalyst	84
3.3.8. Effect of amount of catalyst and intensity of photons	89
3.3.9. Recyclability	91
3.3.10. Clean surfaces and enhancement of photocatalytic activity	94
3.4. Summary	95
3.5. References	96

Chapter 4

Effect of surfactant or support material free CdS nanoparticles on Cr(VI) removal

4.1. Introduction	100
4.2. Experimental section	102
4.2.1. Materials	102
4.2.2. Synthesis of surfactant free CdS nanoparticles	102
4.2.3. Photocatalytic activity test	102
4.2.4. Electrochemical activity test	103
4.4.5. Recycling test	103
4.3. Results and discussion	104
4.3.1. Surfactant free CdS nanoparticles	104
4.3.2. Photocatalytic performance	110
4.3.3. Significance of surface clean CdS nanoparticles	112
4.3.4. Stability of photocatalyst and recyclability	115
4.4. Summary	118
4.5. References	119

Chapter 5

Photo-responsive Bi₂S₃ nanoflakes: Synthesis and device fabrication at ambient conditions

5.1. Introduction	124
5.2. Experimental section	125
5.2.1 Materials	125
5.2.2 Synthesis of Bi ₂ S ₃ nanoflakes	125
5.2.3. Electronic measurements	126

5.3. Results and discussion	127
5.3.1. Synthesis of Bi ₂ S ₃ nanomaterials	127
5.3.2. Structure and composition of Bi ₂ S ₃ nanoflakes	128
5.3.3. Optical properties	133
5.4. Electronic properties	134
5.4.1. Device construction	134
5.4.2. I-V Studies	136
5.4.3. Intensity dependent studies	137
5.4.4. Transient studies	138
5.4.5. Impedance analysis	141
5.5. Summary	142
5.6. References	142

Chapter 6

Synthesis of ternary metal chalcogenide nanoparticles for solar cell device fabrication

6.1. Introduction	148
6.2. Experimental section	150
6.2.1. Materials	150
6.2.2. Common synthetic procedure for In ₂ S ₃ , CuInS ₂ , Cu ₂ SnS ₃ and Cu ₃ SnS ₄ nanoparticles	150
6.2.3. Fabrication of device	151
6.3. Results and discussion	152
6.3.1. Synthesis and characterization	152
6.4. Fabrication of CIS/CTS based solar cell and device performance	162
6.4.1. Future plan for the fabrication of device	166

6.4. Summary	166
6.5. References	167

Chapter 7

Summary and conclusions

7.1. Summary and conclusions	171
Supplementary material	175
Publications	185
Presentations and posters	187



STATEMENT

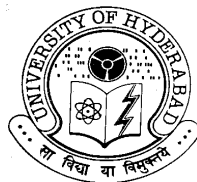
I hereby declare that the matter embodied in the thesis is the result of investigation carried out by me in the School of Chemistry, University of Hyderabad, Hyderabad, India, under the supervision of **Prof. K. Muralidharan**.

In keeping with the general practice of reporting scientific observations, due acknowledgements have been made wherever the work described is based on the findings of other investigators. Any omission, which might have occurred by oversight or error is regretted.

Billakanti Srinivas

University of Hyderabad

July, 2017



DECLARATION

I **Srinivas Billakanti** hereby declare that this thesis entitled “*Modified hexamethyldisilazane (HMDS) – assisted synthesis of surfactant free metal chalcogenide nanoparticles and their applications as catalysts and photoresponsive materials*” submitted by me under the supervision and guidance of **Prof. K. Muralidharan**, School of Chemistry, University of Hyderabad is a bonafide research work which is also free from plagiarism. I also declare that it has not been submitted previously in part or full to this University or any other University or Institution for the award of any degree or diploma. I hereby agree that my thesis can be deposited in shodhgana/INFLIBNET.

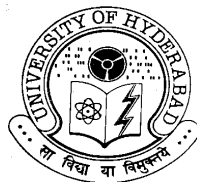
Date: 17th July 2017

Billakanti Srinivas

Reg. No.: 12CHPH10

Signature of the supervisor:

Prof. K. Muralidharan



CERTIFICATE

This is to certify that the thesis entitled “**Modified hexamethyldisilazane (HMDS) – assisted synthesis of surfactant free metal chalcogenide nanoparticles and their applications as catalysts and photoresponsive materials**” submitted by **Billakanti Srinivas** bearing registration number **12CHPH10** in partial fulfillment of the requirements for award of Doctor of Philosophy in the School of Chemistry is a bonafide work carried out by him under my supervision and guidance. This thesis is free from plagiarism and has not been submitted previously in part or in full to this or any other University or Institution for award of any degree or diploma. Further the student has six publications before submission of the thesis for adjudication and has produced evidences for the same in the form of reprints.

Parts of this thesis have been published in the following publications:

1. **Billakanti Srinivas**, Baskaran Ganesh Kumar and Krishnamurthi Muralidharan, *ChemistrySelect*, 2017, **2**, 4753 – 4758. (**Chapter 2**)
2. **Billakanti Srinivas**, Baskaran Ganesh Kumar and Krishnamurthi Muralidharan, *Journal of Molecular Catalysis A: Chemical*, 2015, **410**, 8–18. (**Chapter 3**)
3. Baskaran Ganesh Kumar, **Billakanti Srinivas** and Krishnamurthi Muralidharan, *Materials Research Bulletin*, 2017, **89**, 108–115. (**Chapter 5**)

He has also made presented in the following Conferences:

1. **Billakanti Srinivas**, Bhaskaran Ganesh Kumar and Krishnamurthi Muralidharan, presented a **poster** at Modern Trends in Inorganic Chemistry (**MTIC- XV**) held at department of chemistry, **IIT- Roorkee**, India on **13-16 Dec. 2013**.
2. **Billakanti Srinivas** Presented **Oral Presentation** “Stabilizer free copper sulphide nanostructures for rapid photocatalytic decomposition of rhodamine B” presented at **Chemfest-2016**, 13th Annual In-House Symposium on **Feb. 2016** in School of Chemistry, University of Hyderabad, Hyderabad, India.
3. **Billakanti Srinivas** and Krishnamurthi Muralidharan, presented a **poster** at **CRSI NSC-21** conducted at the CSIR-Indian Institute of Chemical Technology (**IICT**), Hyderabad. During the period **13-16 July, 2017**.

Further the student has passed the following courses towards fulfillment of course work requirement for Ph.D:

Course	Title	Credits	Pass/Fail
1. CY-801	Research Proposal	3	Pass
2. CY-802	Chemistry Pedagogy	3	Pass
3. CY-806	Instrumental Methods B	3	Pass
4. CY-850	Chemistry of Materials	3	Pass

Prof. K. Muralidharan
(Thesis Supervisor)

Dean
School of Chemistry

ACKNOWLEDGEMENTS

I wish to express my deep sense of gratitude and profound thanks to my supervisor **Prof. K. Muralidharan**, for his invaluable guidance, constant encouragement, inspiring and thought provoking discussions throughout my Ph. D. program. I have been able to learn a great deal from him and consider my association as a rewarding experience for me. I am also thankful to my madam Bhuvaneswari garu.

I would like to thank the present and former Deans, School of Chemistry, for their support and help on various occasions. I am extremely thankful individually to all the faculty members of the school for their kind help and cooperation at various stages of my stay in the campus. Especially my doctoral committee members **Prof. V. Baskar** and **Prof. T. Jana** for their constant support throughout my research career. Financial assistance from UGC, New Delhi in the form of junior and senior research fellowship are sincerely acknowledged.

The acknowledgements part would not complete without mentioning my teachers right from school days to post graduation. The teachers who encouraged me in a right way from school days onwards are Devacharry sir, Srinu sir, Y. Saidulu sir, B. Saidulu sir, V. Anjaiah sir, Janaiah sir, Sathyam sir, Krishnamurthi sir and Ravinder sir. My intermediate teachers like **M. Venkata reddy** sir, **Mahinder reddy** sir my inspiration for chemistry subject, Dharma reddy sir and my B. Sc., teachers like **Srinivas charry** sir, **Giri** sir, Raju sir, Narender sir, **Bramha charry** sir and **Srinivas charry** sir for their inspirational teaching. My professors from the OU chemistry department, **Prof. M.Vithal**, **Prof. G. Veerabhadram**, **Prof. Moorthi**, **Prof. Jagannadam**, **Prof. Srinivas** and **Prof. Veerasomaiah** for their encouragement and inspirational teaching.

I am really grateful to have all my seniors like Dr. Sekher Reddy, Dr. Hanumanth rao, Dr. Vignesh Babu, Dr. Ganesh Kumar, Dr. Praveen, Dr. Sanyasi Naidu, Dr. Srinivas, Dr. Anuj (ACRHEM), Dr. Vikas (NIT Kurukshethra). I am only the junior for above all and they treated me as their own brother. My special thanks to **Dr. Sekher Reddy**, he helped me a lot in my initial days in Ph. D. carrier. My special thanks to **Dr. Vignesh Babu**, **Dr. Ganesh Kumar** and **Dr. K. Praven Kumar Naik** they only thought me so many research techniques and handling of

sensitive reactions. And I am really glad to have association with **Dr. Sanyasi Naidu** for valuable discussion and encouragement. I am thank full to **Dr. R. Manigandhan** And also my special thanks to my lovable juniors like **Venky, Hanumandlu, Manzoore, anjana** and **Bhavana** for their timely help in all the times and friendly environment in the lab. And my special thanks to my project students like Venkateswarlu, Sanjay, Venu, **Siva Ganga**, Dayalan, Laxman, **Nithin, Vishnavi, Akshana**, Aswini, **Shreyas, Hemanarayan** and UGC visiting students like Kamalesh, Mohan raj and Ramar for their friendly environment in the lab.

I am privilege to have a brother like **Dr. Sivarama Krishna** and Parvathi vadina, and my special thanks to **Dr. Kesava Rao**, for listening my doubts and valuable discussions, the days we spent with them in the fast four years was unforgettable. My special thanks to **Lankesh** anna for spending cheerful time with me. And my special friends with whom i spend all the time is **Ramakrishna (RK), Narender (Babu), Haresh and Konda reddy**. And my special thanks to friends and neighbours like Shiva reddy, Anand, Dr. Nagaprasad, Gopi and Dr. Ramu.

I am also thankful to my batch mates (2012) like Uday, Ramusagar, Sathi, Mohan, Anand, Sudheer, Krishna rao, Venkata Ramudu, Krishna Naik, Suresh, Krishna reddy, Koushik, Navendu, Surjana, Lasya, Divya, Ranjani and Tulasi. My special thanks to **Thamilarasan** and **Naveen** for NMR doubts clarifications and being with me all times. And also special thanks to my friends like Narasimha, Dr. Malakappa, Dr. KSN Raju, Dr. Kondareddy, Dr. Ramesh (TJ lab), Shakthivel (RB Lab), Prabhkar (AKS Lab), Ugandhar, Battu Sathish (NCL Pune), P. Sandeep (IISER Pune), Bolla Srinivas, Sandheep and Vamshi (IICT). My juniors like Allu Siva, Anil, Tanmy, Surender reddy, Ramesh, Senthil, Rangu Prasad, Nagamaiah, Prabaker and all others.

My special thanks to Dr. Ashok for initial days help. I am also thank full to my senior friends like Dr. Pawan, Dr. Thirupati, Dr. Sudheer, Dr. Chandu, Sunil, Dr. Ramuyadav, Linganna (Lee), Dr. Nagarjuna (VB Lab), Dr. Allu Srinu, Vikranth, Obaiah, Dr. Ramana, Dr. Karunaker, Dr. Guptha, Dr. Hari, Dr. Nagarjuna (AKS lab), Dr. Yasin, Sashi, and all other seniors in school of chemistry. Special thanks to my seniors like **Dr. Narayan** (RC Lab), **Dr. Sathish** (SPal Lab) and **Dr. Srinivas** (SPal Lab) for their help in various situations.

My hearty full thanks to **Muvva Durga Prasad (DP), Pankaj, Sunil and Durgesh singh** for their timely help for TEM, FESEM and NMR facility in all the times.

I thank all the non-teaching staff members for their support on my research. It's my privilege to acknowledge Mr. Varaprasad (glass blower), Mr. Satyanarayana, Mr. Turab, Mrs. Vijayalaxmi, Mr. Venkateswar rao (NMR), Mr. Ramana (SXR), Gomathi (FT-IR), Kumar (PXRD), Anand (cylinders), Shetty (bills) and Sambasivarao (LN₂). I would also like to express my sincere gratitude to Mr. Pavan of Central Instruments Laboratory (CIL), UoH for their help with SEM experiments. I also sincerely thank centre for Nanotechnology, UoH for allowing me to use the TEM facility.

My hearty full thanks to **Ramakrishna mama** and **Ramesh mama** and their family members and **Linganna** (BC state leader) for their help in all the times.

Especially, I would like to thank my M.Sc classmates from Osmania University like **Prem, Vasantha Sheker, Karunaker, Venky, Kiran, Gopal, Dayaker** and **Madhu**. I never forget the days which we spent in OU campus, Arts College, movies, **Telangana movement** and B-hostel. And also thank full to **Swapna, Shivallela**, Madhavi, Pravallika, Srinivas, Rajender, Sai, Vital, Ravikiran, Chennareddy, Ramakrishna, Rakhi and also my seniors like **Karthik anna, Mohan anna, Naveen anna**, Venkatakrishna, Kanakaraju, Suresh, Suman and others.

I am also thankful to my B. Sc., friends like **Ravi kumar, Jani, Giri**, Janaki ramulu, Prabaker, Ravinder Reddy, Sravan, Madhu, Ramesh, Ravi, Raju, Mahender, Shanker, Shankara chary, Hymavathi, Renuka, Jyothi, Banagaramma, Poolamma, Anitha and others too for their help in all the ways. I am also thankful to my Intermediate friends like Ravi kumar, Jagadesh (Jagan), Vijay, Sudaker, Sujitha, Swathi.

I am also thankful to my school friends like Nagarjuna, Nagaiah, Venkanna, Chennai, Srinu, Shanker, Jagadesh, Sravan, Saidulu, Renuka, Jyothi, Masthan, Nagamma, Krishnaveni and all for their unconditional love and true friendship.

I, also thanks to my family members Nagaiah babai, Pinny, Narasaiah pedananna, Peddamma, Saidamma pinny, Narayana babai and Chandrakala pinny and Kanakaiah babai, Mangamma pinny and Anjaiah babai, Anjaiah mama and

family, Krishnaveni, Ramana, Kalyani, Chandana and family, Anjaiah mama and Pedda akka, Chinnaka and family, Nelakka and family, Raju and family, mamaiah, atthamma, Lakshmi vadina and family (HYD), L. Srinu mama and akka, L. anjaiah mama(Teacher) and akka, A. Thirupathi babai and family, Panga Narayanamma for her blessings, Ch. Bixam mama and family, P. Anji babai, L. Sathis, Sanjeev bava, Nagaiah bava and family, Narsaiah bava, Sathi bava, Anji babu and family, N. Sathi and Venky mama. My special thanks to all my cousin brothers and sisters like Chinna srinu, Krishnaveni, Ramana, Kalyani, Shivakrishna, Aadi Narayan, Chandan, Uma, Gouthani, Raju, Uday, Vamshi and Papanna for their love and affection on me.

My heart goes to my beloved parents **Amma, Nanna, Akka, Mama (Sheker), Anna** and **Vadina** are my inspiration and they all back bone of my life and I thank them sciencierly. Their patience, prayers and faith in the almighty, waited all these long years to see me reaching this stage. Their blessings and care always gave me new zeal and enthusiasm to do something more with perfection. At this juncture today I dedicate my thesis to my family members my mother **Smt. B. Seethamma** and to my father **Mr. B. Somaiah**. My sincere thanks goes to my sister Smt. L. Radha and my Uncle Mr. Shekar, my brother Mr. B. Venkanna and vadina Smt. B. Shailaja for ther support and encouragement in all the ways. My special thanks to my chota hero's like **Nikhil raj, Joshitha** and **Shrihan** who have been a source of relief while I am away from the work. My special thanks to my Spouse **Smt. B. Sravani** for her sacrifices and understanding me in all the ways.

I express my sincere regards to all my friends and well-wishers for their moral support, motivation and encouragement.

Srinivas

List of Schemes

1.1	Synthetic methodology for modified HMDS - assisted synthesis	27
2.1	Representation of sequence of the reaction for Ni_3S_4 NPs synthesis	49
2.2	Reduction of the nitroarenes using the Ni_3S_4 nanoparticles as catalyst	56
3.1	Schematic illustration of synthesis of CuS and Cu_2S nanoparticles	73
4.1	Schematic illustration of synthesis of surfactant free CdS NPs	104
5.1	The modified HMDS-assisted synthesis of Bi_2S_3 nanoflakes	127
6.1	Generalised reaction of synthesis of ternary metal chalcogenides	150
6.2	Synthesis of In_2S_3 nanoparticles	153

List of Figures

1.1	Classification of nanomaterials	2
1.2	Pictorial representation explaining increase in surface area	3
1.3	Band gap diagram of atomic level to bulk matter	4
1.4	Surface plasmon resonance oscillation for a sphere	6
1.5	Fluorescence emission of CdSe and absorption spectra of gold NPs	6
1.6	Applications of nano catalysts in different fields	9
1.7	Schematic representation of working of photovoltaic cell	12
1.8	Schematic representation of CuInGaS₂/Se₂based quantum dot solar cell	13
1.9	Systematic representation of the architecture of the capping agent	24
1.10	Schematic description of stages involved in colloidal synthesis	25
1.11	Representation of different applications of synthesized NPs.	28
2.1	²⁹Si NMR studies of the reaction mixture at different time intervals	49
2.2	PXRD pattern of as synthesized Ni₃S₄ NPs	50
2.3	Time dependent PXRD patterns of Ni₃S₄ NPs	50
2.4	EDAX spectrum of as synthesized Ni₃S₄ NPs	51
2.5	TEM micrographs of as synthesized Ni₃S₄ NPs	52
2.6	Particles distribution diagram from the TEM micrographs	52
2.7	HRTEM micrograph of the Ni₃S₄ NPs	53
2.8	FTIR spectra of the Ni₃S₄ NPs	53
2.9	Controlled reaction to prove catalytic activity of Ni₃S₄ NPs	55
2.10	BET isotherm of as synthesized Ni₃S₄ NPs	58
2.11	Recyclability analysis of the nickel sulphide	59
2.12	Thermal stability of the catalyst	60
2.13	TEM micrograph of the reused Ni₃S₄ NPs	60

3.1	Pictorial representation of the water pollution	66
3.2	Pictorial representation of the photocatlytic degradation of waste water	67
3.3	Powder X-ray diffraction pattern of copper sulphide nanostructures	72
3.4	EDAX spectrum of CuS nanostructures	73
3.5	FTIR spectrum of copper sulphide nanostructures	73
3.6	TEM micrograph of copper sulphide nanostructures	75
3.7	TEM and HRTEM image of a CuS nanoflakes	77
3.8	PXRD patterns of stoichiometric variation	78
3.9	Powder X-ray diffraction pattern of Cu₂S NPs	78
3.10	EDAX spectrum of Cu₂S NPs	79
3.11	FTIR spectrum of Cu₂S NPs	79
3.12	TEM images of Cu₂S NPs with different magnifications	80
3.13	HRTEM micrograph of a Cu₂S NPs	81
3.14	UV–visible reflectance spectrum of CuS and Cu₂S nanostructures	82
3.15	Photocatalytic activity of the CuS Flowers.	84
3.16	Structure of Rhodamine B dye	85
3.17	Absorption kinetics of photolysis, catalysis and photocatalysis	85
3.18	Influence of photons (a) and catalyst (b) in the photocatalysis	88
3.19	Recyclability of CuS photocatalyst	90
3.20	Rate constant measurements during recycling process	91
4.1	Pictorial representation of the water pollution by the Cr(VI)	99
4.2	PXRD spectrum of as synthesized surfactant free CdS NPs	103
4.3	EDAX spectrum of CdS NPs	103
4.4	Morphological study of surfactant free CdS nanocatalyst	104
4.5	TEM micrographs of as synthesized CdS NPs	104

4.6	Particles distribution diagram from the FESEM micrographs	105
4.7	HRTEM micrograph of as synthesized CdS NPs	106
4.8	HRTEM micrograph of the CdS NPs	106
4.9	FTIR spectra of the CdS NPs	107
4.10	UV-vis diffuse reflectance spectra (DRS) of CdS NPs	107
4.11	BET surface area analysis of CdS NPs	108
4.12	Photocatalytic activity of the CdS NPs	109
4.13	Controlled reactions of Cr(VI) reductions	110
4.14	Transient photocurrent responses of CdS NPs	112
4.15	Recyclability studies of the CdS NPs	114
4.16	XRD pattern of as synthesized and recycled CdS NPs	115
4.17	EDAX spectrum of reused CdS Catalyst	115
4.18	FESEM micrographs of the reused CdS NPs	116
5.1	PXRD pattern of the Bi ₂ S ₃ nanoflakes	126
5.2	FTIR spectrum of the Bi ₂ S ₃ nanoflakes	127
5.3	FESEM micrographs of the Bi ₂ S ₃ nanoflakes	128
5.4	EDAX spectrum of the Bi ₂ S ₃ nanoflakes	128
5.5	Large area TEM image of the Bi ₂ S ₃ nanoflakes	129
5.6	TEM micrographs of the Bi ₂ S ₃ NPs	130
5.7	HRTEM micrograph of the Bi ₂ S ₃ NPs	131
5.8	Solid state UV analysis of the Bi ₂ S ₃ flakes	131
5.9	Device making from the dry casting	132
5.10	Cross sectional view of the device with circuits.	133
5.11	Energy level diagram of the device components.	134
5.12	Two probe I-V measurements (532 nm, 122 W.m ⁻²).	135

5.13	Intensity-dependent measurement of the device	136
5.14	Transient measurements of the device	137
5.15	A magnified cycle of the transient studies	138
5.16	Nyquist plot of Bi₂S₃ nanoflakes	139
6.1	PXRD and EDAX of In₂S₃ NPs	151
6.2	FESEM images of In₂S₃ NPs	152
6.3	PXRD and EDAX of CuInS₂ NPs	153
6.4	PXRD and EDAX of Cu₂SnS₃ NPs	153
6.5	PXRD and EDAX of Cu₃SnS₄ NPs	154
6.6	FESEM images of CuInS₂ NPs	154
6.7	FESEM images of Cu₂SnS₃ NPs	155
6.8	FESEM images of Cu₃SnS₄ NPs	155
6.9	FT-IR spectrum of CuInS₂.	157
6.10	FT-IR spectrum of Cu₂SnS₃.	157
6.11	FT-IR spectrum of Cu₃SnS₄.	158
6.12	UV–Vis spectrum of as prepared CuInS₂. Inset: bandgap (1.40 eV).	158
6.13	UV–Vis spectrum of as prepared Cu₂SnS₃. Inset: band gap (1.40 eV).	159
6.14	UV–Vis spectrum of as prepared Cu₃SnS₄. Inset: band gap (1.15 eV).	159
6.15	Schematic illustration of a typical CIS/CIGS/CTS photovoltaic device	160
6.16	Photographs of solar cells fabricated in different sizes	161
6.17	Pictorial representation of structure of the solar cell device	161
6.18	Cross sectional view and elemental mapping of the device (solar cell)	162
6.19	I-V curve determined after measurement of a CuInS₂ fabricated device	163
6.20	I-V curve determined after measurement of CTS fabricated device	163

List of Tables

1.1	Representative application of nanomaterials	7
1.2	Variable stoichiometries of copper chalcogenides	15
1.3	General synthetic methods for copper chalcogenide nanoparticles	16
1.4	General synthetic methods for CdS nanoparticles	18
1.5	General synthetic methods for Bi₂S₃ nanoparticles	19
1.6	Variable stoichiometries of nickel chalcogenides	20
1.7	General synthetic methods for nickel sulphide nanoparticles	21
1.8	General synthetic methods for CI(S/Se)₂ and CTS nanoparticles	22
2.1	Controlled reactions for Ni₃S₄ nanoparticles synthesis	50
2.2	Results of nickel sulphide catalyzed reduction of nitrobenzenes	58
2.3	Comparison table of numerous catalysts with various nitroaromatics	59
4.1	Comparisons between CdS NPs on reduction of Cr(VI)	113
5.1	Transient studies of Bi₂S₃ photodetector	140
6.1	Reported efficiencies for the CTS based solar cells	149
6.2	Experimental details for the synthesis of metal chalcogenides	151
6.3	The absorption maxima and band gap values of ternary systems	158
6.4	I-V characteristics of fabricated devices	166

List of Acronyms

NPs	Nanoparticles
NCs	Nanocrystals
QDs	Quantum dots
QDSCs	Quantum dot solar cells
CIGS	Copper Indium Gallium Sulfide
CTS	Copper Tin Sulfide
ITO	Indium Tin Oxide
CVD	Chemical vapor deposition
CAFS	Chemical aerosol flow synthesis
SMAD	Solvated metal atom dispersion method
TOPO	Trioctylphosphine oxide
HAD	Hexadecylamine
DDT	Dodecanethio
CTAB	Cetyltrimethylammonium bromide
HMDS	1,1,1,3,3,3-Hexamethyldisilazane
OLA	Oleylamine
PVP	Polyvinylpyrrolidone
PXRD	Powder X-ray Diffraction
EDAX or EDS	Energy dispersive spectroscopy
SEM	Scanning Electron Microscopy
FESEM	Field Emission Scanning Electron Microscopy
TEM	Transmission Electron Microscopy
HRTEM	High-resolution Transmission Electron

	Microscopy
FFT	Fast Fourier Transmission
SAED	Selected Area Electron Diffraction
NMR	Nuclear Magnetic Resonance Spectroscopy
TG-DTG	Thermo Gravimetric and Differential Thermo Gravimetric Analysis
FT-IR	Fourier Transform Infra-Red Spectroscopy
JCPDS	Joint Committee on Powder Diffraction Standards
UV-Vis-NIR	Ultraviolet Visible near Infra-Red spectroscopy

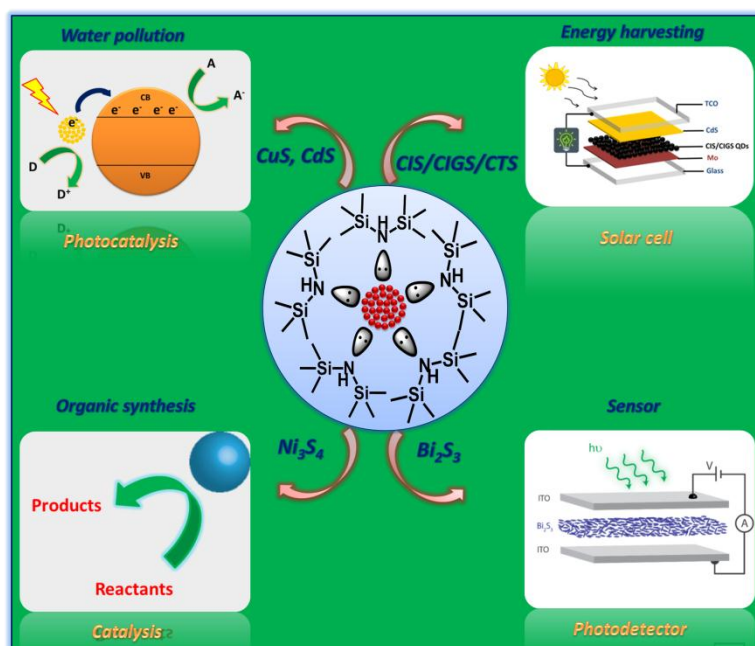
SYNOPSIS

Thesis Title: Modified hexamethyldisilazane (HMDS) – assisted synthesis of surfactant free metal chalcogenide nanoparticles and their applications as catalysts and photoresponsive materials

The thesis comprises six chapters including an introduction chapter.

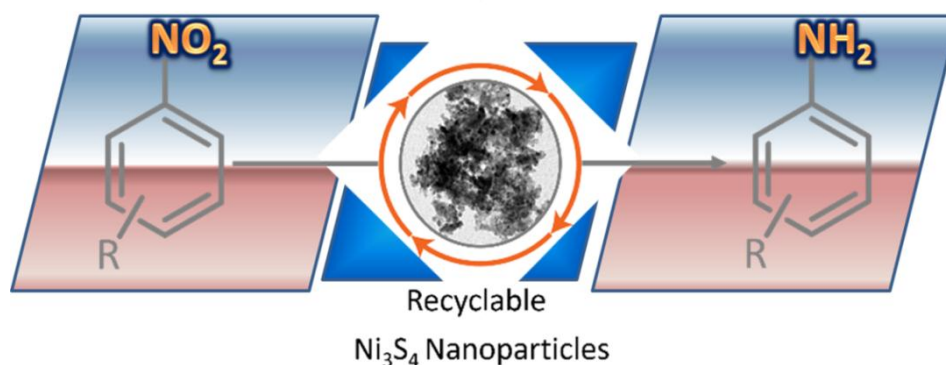
Chapter 1: Introduction

The **chapter 1** discusses a few selective applications of nanoparticles in catalysis, photocatalysis and photoresponsive studies. Furthermore, a brief survey of the various reported strategies used for the synthesis of metal sulphides nanoparticles (NPs) has been illustrated. The need of surfactant or stabilizer molecules in the synthesis of NPs have been explained. The adverse effect of the presence of the organic molecules on the surface of NPs pertaining to their use as catalyst and as material to construct the solar cells is identified, which defines the problem for the present work. Comparison on different generations of solar cells and a description on device structure of quantum dot solar cell are also included in this chapter. The chapter 1 also highlights the available methods and present synthetic approach used in this thesis work to achieve the NPs without any organic capping stabilizing agents.



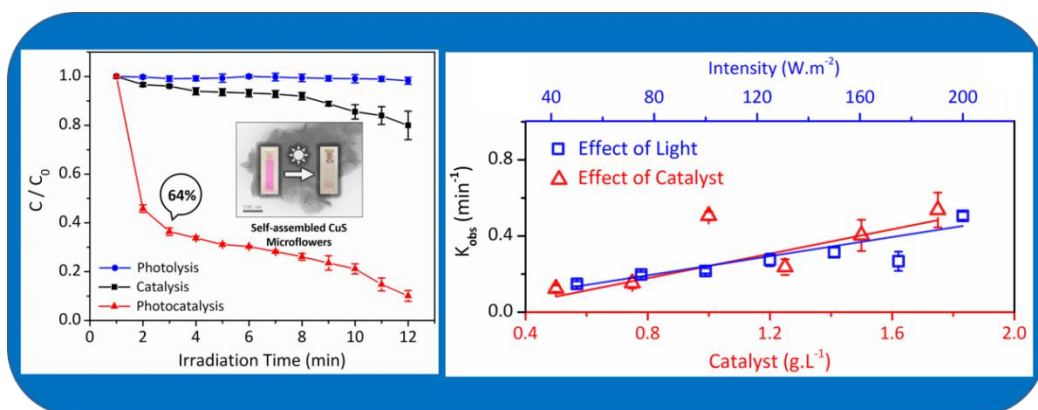
Chapter 2: Recyclable Ni₃S₄ nanocatalyst for hydrogenation of nitroarenes

In this chapter, the synthesis of surface clean nanoparticles of Ni₃S₄, which is rare phase of nickel sulphides, is described and catalytic activity of the synthesized nanoparticles were discussed. Nanoparticles were synthesized in a single step via hexamethyldisilazane (HMDS)-assisted method using NiCl₂ and thiourea as starting materials. This synthetic method yielded phase pure, spherical Ni₃S₄ nanoparticles of mean size 17 (\pm 4) nm having clean surfaces. The nanoparticles were characterized thoroughly by PXRD, FTIR, EDAX, and TEM analyses. Since newly produced Ni₃S₄ nanoparticles in our reaction had exposed surfaces, the catalytic behaviour of these particles was assessed by using it as a catalyst in the reduction reaction of aromatic nitro groups. We have demonstrated Ni₃S₄ nanoparticle as a versatile catalyst for the nitro hydrogenation of both activated and deactivated nitrobenzenes using hydrazine as a hydrogen source to yield corresponding amines in high yield (~90 %). The heterogeneous catalyst, Ni₃S₄ nanoparticles was recycled more than ten times without any change its activity. We have ascribed the enhanced catalytic activity of these Ni₃S₄ nanoparticles to their clean surfaces without any surfactant molecules around them.



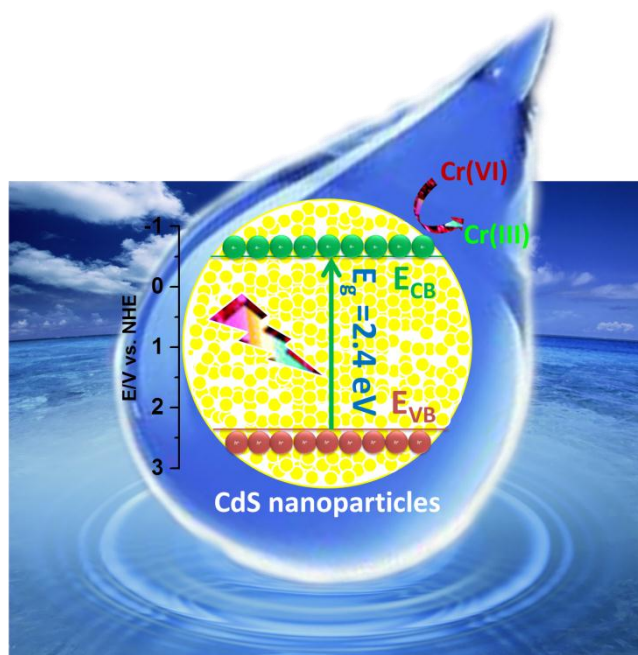
Chapter 3: Stabilizer free copper sulphide nanostructures for rapid photocatalytic decomposition of rhodamine B

In this chapter hexamethyldisilazane assisted synthesis of CuS, Cu₂S nanostructures and photocatalytic activity of the synthesized nanostructures were discussed. Hexamethyldisilazane assisted method yielded hexagonal CuS nanoparticles with average size of 22 ± 6 nm and cubic Cu₂S nanoparticles with average size of 52 ± 10 nm. The capping agents present on the surfaces of nanoparticles unfavourably modify the properties of the nanostructures. Particularly in the catalysis, most of the potential catalytic centres are screened by the capping agents. Therefore, we have developed a novel method of synthesizing stabilizer-free CuS and Cu₂S nanostructures for photocatalytic applications. These nanostructures were synthesized by modified HMDS assisted synthetic method at 130 °C. The CuS microflowers were constructed by self-assembly of nanoflakes which was grown through anisotropic growth of (1 0 3) planes. We have demonstrated an efficient photocatalytic activity of CuS nanostructures through photocatalytic decomposition of Rhodamine B dye. The CuS flowers rapidly decomposed Rhodamine B in solution (12 min). The efficient catalytic activity is explained by invoking clean surfaces of nanoparticles. We have also demonstrated the influence of illumination intensity on the efficiency of catalyst and the recyclability.



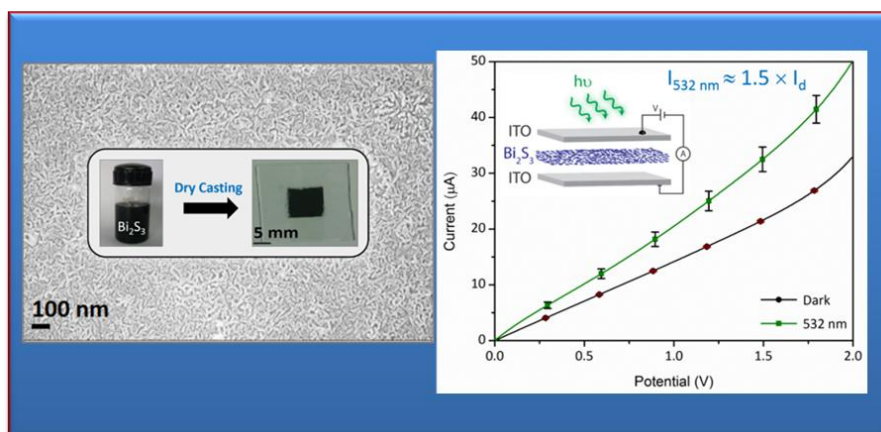
Chapter 4: Effect of surfactant or support material free CdS nanoparticles on Cr(VI) removal

This chapter describes the production of organic surfactant molecules or support material free CdS nanoparticles and its efficient photocatalytic activity for the reduction of toxic Cr(VI) to the less toxic and much less mobile form of Cr(III). We have synthesized the template free CdS nanoparticles by adopting the solution phase hexamethyldisilazane (HMDS)-assisted chemical synthetic method using CdCl_2 and thiourea as the precursors. The nanoparticles were characterized by PXRD, FESEM, and TEM. We have demonstrated an excellent photocatalytic performance of as-prepared CdS nanoparticles under visible light illumination for the reduction of Cr(VI) to Cr(III) at acidic pH. The enhanced catalytic activity of CdS nanoparticles was explained by the availability of clean surfaces in the absence of insulating organic molecules as a surfactant or stabilizing agent. This situation encouraged the efficient separation of photoexcited electron-hole pairs, which was confirmed from the observed fast and uniform transient photocurrent response during transient studies and less resistance on to the separation of interfacial charges in the electrochemical impedance spectra (EIS). The catalyst also showed good photocatalytic stability and reusability, which makes it as an excellent candidate for waste water treatment.



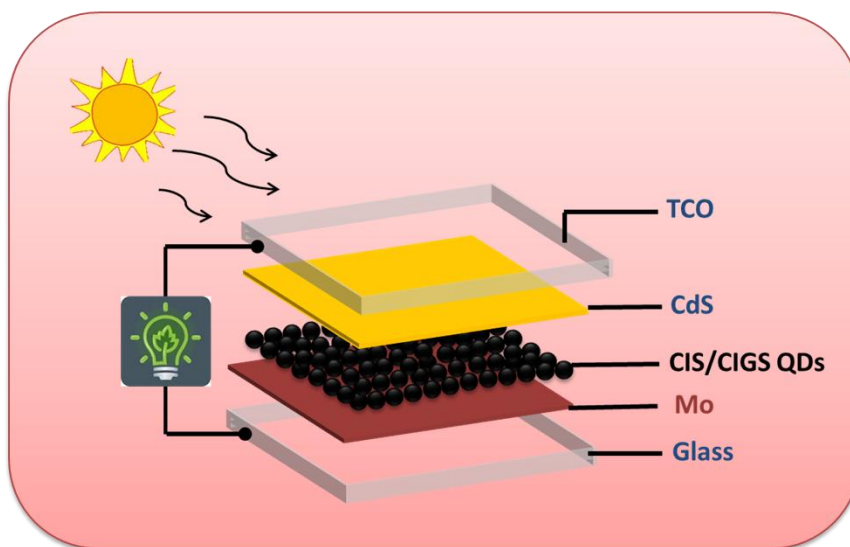
Chapter 5: Photo-responsive Bi_2S_3 nanoflakes: Synthesis and device fabrication at ambient conditions

This chapter describes hexamethyldisilazane (HMDS) assisted syntheses of Bi_2S_3 nanoflakes and its photo-responsive properties. Since the optoelectronic devices consist multicomponent interfaces, the synthesis of nanoparticles and fabrication of devices play a significant role in quality, cost, and fast fabrication of devices. The wet chemical synthesis holds the great promise of controlling of these factors. Herein, we have developed a wet chemical method for the synthesis of one-dimensional Bi_2S_3 nanoflakes and demonstrated its photo-responsivity by fabricating prototype device by dry-casting of Bi_2S_3 suspensions on the electrodes. A key advantage of the present approach is the synthesis and fabrications were carried out in the ambient conditions.



Chapter 6: Synthesis of ternary metal chalcogenide nanoparticles for solar cell device fabrication

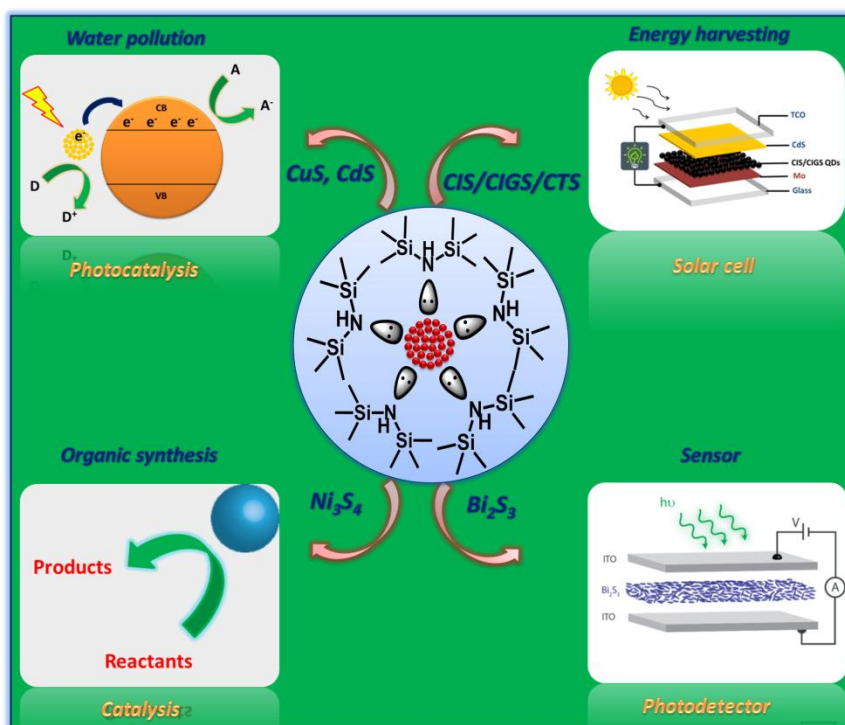
Ternary metal sulphide nanoparticles, CuInS_2 , Cu_2SnS_3 and Cu_3SnS_4 were synthesized using the modified hexamethyldisilazane (HMDS) - assisted synthetic method. The structure, the shape and the composition of these nanomaterials were investigated using powder X-ray diffraction (XRD), field emission electron microscopy (FESEM) and energy dispersive X-ray analysis (EDX). PXRD pattern of CuInS_2 showed tetragonal structure. FESEM images of CuInS_2 NPs revealed a bead like morphology of size 10-20 nm. PXRD pattern of both Cu_2SnS_3 and Cu_3SnS_4 were showed tetragonal and orthorhombic structures respectively. FESEM images of both Cu_2SnS_3 and Cu_3SnS_4 showed 30-50 nm aggregation of spherical NPs. The EDAX analysis of CuInS_2 , Cu_2SnS_3 and Cu_3SnS_4 displayed no signal for any organic moieties confirming the purity of the materials. The solar cells were fabricated by a simple drop-costing method and their efficiency was measured. Based on the preliminary analysis, the fabricated devices had only a little response as solar cell, but the procedure needs to be standardized to achieve higher efficiency.



Chapter 1

Abstract

The introductory chapter gives a brief review of the synthesis and applications of binary and ternary metal chalcogenides. Some of the applications covered in this chapter are catalysis, photocatalysis and photoresponsive materials. An account of the various strategies available in the literature for the synthesis of NPs is also included. The presence of organic surfactant molecules as the capping agent covering the surface of NPs and their influence on the property and applications are discussed in detail. The last part of this chapter sets an idea about how to overcome the issues related the presence of organic surfactant molecules as the synthetic strategy adopted in the present work.



Introduction

1.1. Nanoscale materials and their properties

The study of properties of materials at the nanoscale is termed as nanoscience. Nanoparticles (NPs) are ultrafine particles having a size in the range of 1-100 nm. They have interesting optical, magnetic and electrical properties, which are not found in their bulk counterparts. In modern terminology, NPs are described as quantum dots (QDs), artificial atoms (three-dimensionally ordered NPs), and nanoclusters (a group of NPs). NPs exist in the form of semiconductors (e.g. Si, Ge, TiO_2 , Fe_2O_3 , ZnO) [1, 2], metals (e.g. Al, Ag, Au, Cu) [3], carbon materials (e.g. graphene, fullerenes) [4], polymers (e.g. Polystyrene) [5], metal complexes and biological systems (e.g. DNA, Liposomes). They also exist in different geometrical forms like spheres, flowers, rods, wells, wires, flakes and wafers [6].

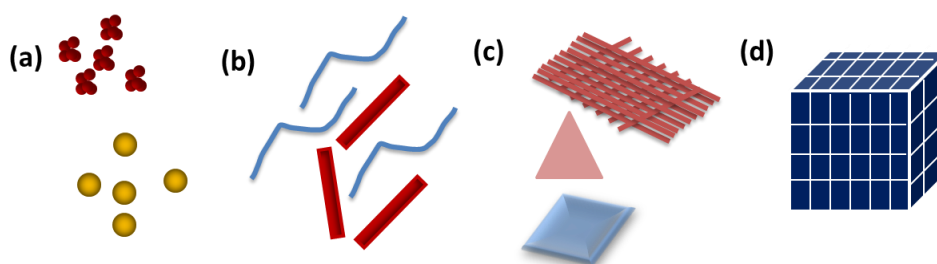


Figure 1.1. Classification of nanomaterials (a) 0-D spheres and clusters, (b) 1-D nanofibers, wires, and rods, (c) 2-D films, plates, and networks, (d) 3-D nanomaterials

Pokropivny and Skorokhod [7] classified the nanostructured materials into 0-D, 1-D, 2-D and 3-D nanoscale materials, which is illustrated in Figure 1.1. In 0-D system (quantum dot), the electrons are confined in their motion in all three directions. Examples: spheres and nanoclusters. In 1-D system (quantum wire), the electrons are free to travel in one direction and confined in the other two directions. Examples: Nanofibers, nanowires, and nanorods. In 2-D system (quantum well), the electrons can easily move in two directions but confined in one direction. Examples: Nanofilms, nanoplates and branched structures. In 3-D system (bulk), the electrons are free to move in all three directions, and there are

Introduction

no confinement and limitations. Example: powders, multilayer, fibrous and polycrystalline materials wherein nanostructural elements of 0-D, 1-D and 2-D are closely related with each other and form interfaces.

1.1.1. Surface area

Surface area is the portion of exposed area of an object. Figure 1.2 explains how the surface to volume ratio increase by the reduction of the particle size. Thus, the NPs have a relatively larger surface area compared to the same volume of the bulk material. The increased surface to volume ratio [8] leads to a characteristic change in physicochemical properties of the material such as the decrease in the melting point, increase in the band gap [9] and significant special capabilities like catalytic and bacterial action. The surface area of particles has a significant influence on reaction rate since chemical reactions take place at the surface level. A larger surface area provides more space for reactions to occur. Thus, a material having particles in nanoscale showed better catalytic activity compared to the same material in bulk.

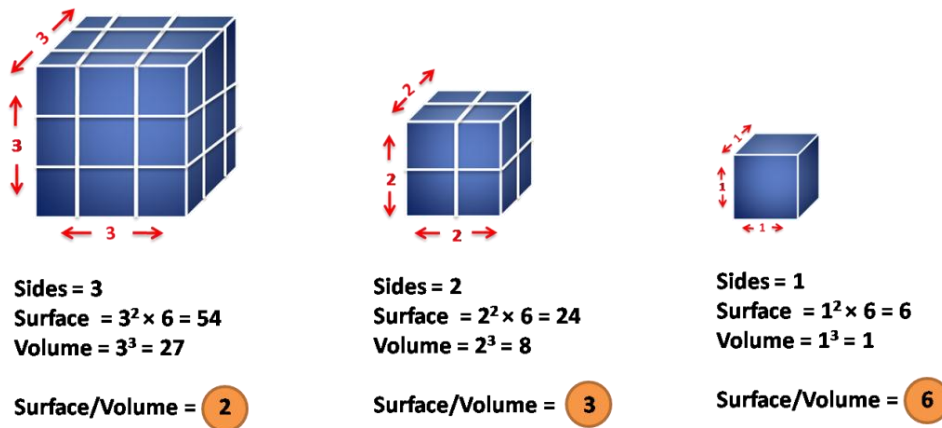


Figure 1.2. Pictorial representation explaining increase in surface area with the reduction in particle size.

1.1.2. Quantum confinement

An interesting change in the properties of the material in the nanoscale is the quantum confinement. When the particle-making materials are at tiny sizes, the electrons are confined in all direction leading to a change in electronic energy levels from continuum to discrete and finally appear similar like atoms. Hence, the energy gap between VB and CB increases (Figure 1.3) [10]. This observation also explains the formation of these bands as matter grows from atoms or molecules to NPs to bulk matter. In bulk matter, the bands are formed by the merger of a bunch of contiguous energy levels of many atoms or molecules. As the particle size gets smaller and reaches the nanoscale, where every particle is made up of an only finite number of atoms, the number of overlapping orbitals or energy levels decreases and the width of the band becomes narrow. As an extreme case, a single atom or molecule will have very discrete energy levels that are represented by single lines. These phenomena are explained schematically in Figure 1.3.

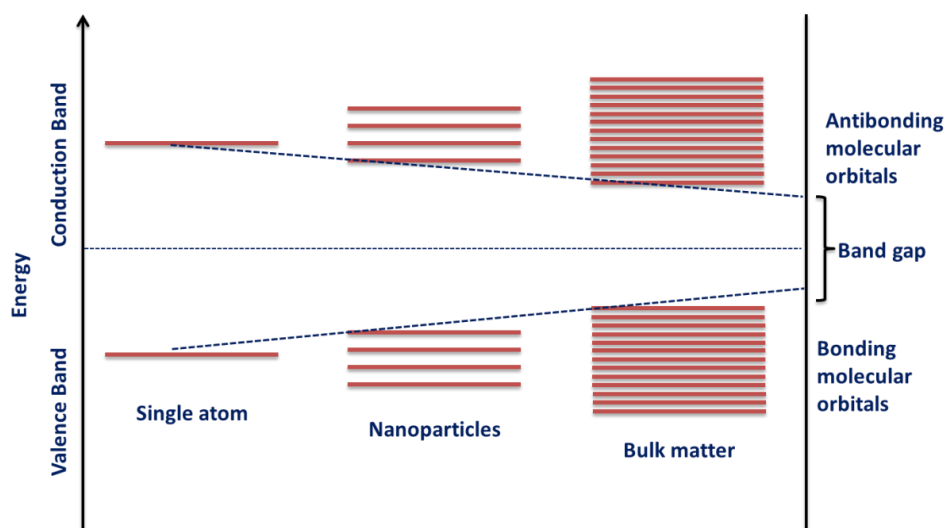


Figure 1.3. Description of sequential change in band gap from atomic level to bulk matter.

Introduction

The change in the electronic energy levels from continuum to discrete explains the reason why the NPs have wider band gap than the corresponding bulk matter. With the increase in the band gap, the forbidden region becomes larger, and hence, the NPs exhibit lower electrical conductivity. This quantum confinement effect can easily be detected by the shift in absorption spectrum towards the lower wavelength blue region [11]. Thus, the actual energy level of VB and CB, as well as the band gap of the semiconductor materials, are deciding factor to choose a material for a particular application.

1.1.3. Optical properties

Due to their quantum confinement, quantum dots (QDs) show some unique and fascinating optical properties and high photostability. The properties of NPs are tunable by varying the size and stoichiometry of the materials. As illustrated in Figure 1.4, the optical properties of NPs arise because of the interaction of light with the localized surface plasmon bound to them. Localized surface plasmons are charge density oscillations arising in NPs when their size is much smaller than the wavelength of light [12]. The color due to the collective oscillation of electrons in the conduction band is known as the surface plasmon oscillation.

A simple change in size or shape of NPs alters their optical properties. Figure 1.5 depicts a change in optical properties of CdSe and Au NPs with the change in size and shape respectively. It is apparent from the figure that there is a shift in absorption maxima of CdSe NPs with different size. The largest particles emitted in the region of red while blue emission was observed for the smallest clusters. Similarly, the optical property of the Au NPs changes dramatically when anisotropy is added to them especially in the growth of nanorods [13].

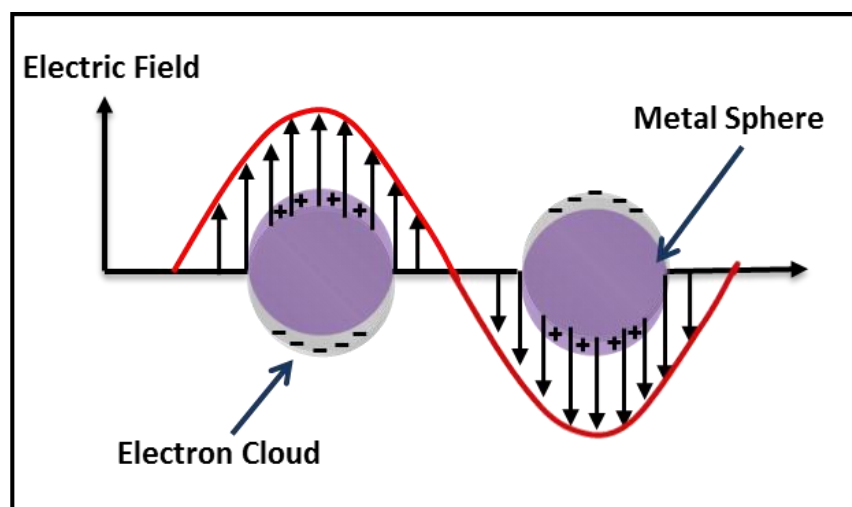


Figure 1.4. Surface plasmon resonance oscillation for a sphere showing the displacement of the conduction electron charge cloud relative to the nuclei [12].

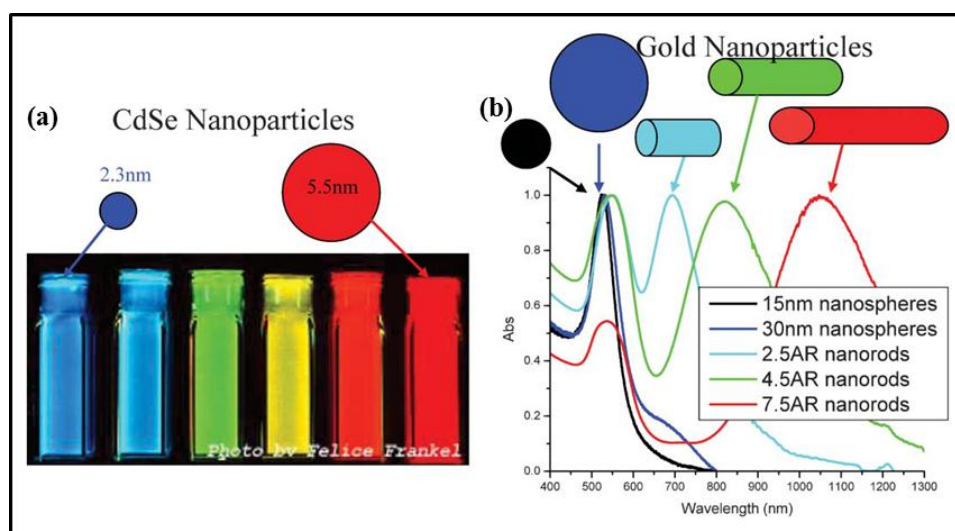


Figure 1.5. (a) Fluorescence emission of CdSe quantum dots of various sizes. (b) Absorption spectra of gold nanoparticles of various sizes and shapes [13].

Introduction

1.2. Application of nanoparticles

The nanomaterials have various applications in the whole spectrum of science stretching from agricultural science to space technology. The size and stoichiometric dependent properties of NPs provided options for their use in various research fields (Table 1.1). Since the applications are vast, we have focused our attention towards the catalytic, photocatalytic and photovoltaic applications only.

Table 1.1. Representative applications of nanomaterials.

Application	Materials	Ref.
Solar cell	CdSe, Cu ₂ S, CuInS ₂ /Se ₂ NPs	[14]
LED	CdSe, CdZnSe alloy, CdSe-ZnS core shell NPs	[15]
Photodetectors	CdSe, PbSe, PbS NPs	[16]
Catalyst	Pd, Cu, MoO ₂ , Ru ₅ Pt NPs	[17]
Fluorescent biological labels	CdSe-CdS core-shell NPs	[18]
High energy materials	Al NPs	[19]
Sensors	Si nanowires SnO ₂ nanowires, SnO ₂ Ni _x nanowires, TiO ₂ , In ₂ O ₃ , TiO ₂ -SiO ₂ composite	[20]
Explosives		
Chemosensor (gases and metals)		
DNA	CdSe-ZnS core shell	
Plasmon ruler	Ag and Au NPs	[21]
Lasers	CdSe-ZnS NPs	[22]
Magnetic storage media	CoCrTa, CoCrPt, SmCo NPs	[23]
Carbon monoxide dissociation(for artificial fuels)	Co NPs	[24]
High performance color paints	ZnO dispersions	[25]
Photocatalyst	Hetero junction NPs: CdSe-CdS-Pt	[26]
Finger print visualization	Au NPs	[27]
Nanomedicine	Au NPs	[28]
Electrode materials	Nano metal oxides, SnSb alloy NPs	[29]
Water purification	Polyurethane coated silver NPs	[30]
Water splitting	TiO ₂ NPs	[31]

1.2.1. Nanoparticles as catalysts

A catalyst plays a significant role in the production of fine chemicals, fertilizers and plastics as well as the remediation of environmental pollutants. Even though, homogeneous catalysts are highly efficient there is an inherent problem of catalyst separation for recycling reducing their utilization. Heterogeneous catalysis offers a more convenient option for catalyst recovery. However, the catalytic activity is limited as the surface atoms only are involved in catalyzing the reaction.

The field of nanocatalysis in which the NPs are used to catalyze reactions has undergone an exponential growth during the past decade. Because the NPs have a large surface-to-volume ratio compared to bulk materials (Section 1.1.1), they are attractive materials to use as catalysts. Therefore, many metal and semiconductor NPs are employed in a variety of homogeneous and heterogeneous catalytic and photocatalytic reactions (Figure 1.6) [32]. In 1996, the possibility of synthesizing transition metal NPs having different shapes and the potential of using different shapes to catalyze various reactions [33]. Narayanan and El-Sayed have shown that shapes with more corners and edge atoms have a higher reactivity than similar NPs with fewer corner and edge atoms in homogeneous catalysis. Thus, the shape and crystal structure differences can lead to different catalytic rates [34].

Introduction



Figure 1.6. Applications of nanocatalysts in different fields.

Transition metals supported by various substrates are used as catalysts in many reactions involving heterogeneous catalysis [35, 36]. Three methods are employed to prepare nanocatalysts for heterogeneous catalysts, *viz.*, adsorption of NPs onto supports, grafting of NPs onto supports and fabrication of nanostructures onto supports by lithographic techniques. Some common supports used in the preparation of supported metal NPs catalysts are; carbon [37], silica [38], alumina [39], TiO_2 [40] and polymers [41]. Many of the fuel cell reactions have been conducted by using transition metal NPs which are supported on various forms of carbon [42]. Pd and Ni NPs supported on the oxidized diamond were used as catalysts for the methane decomposition reaction to produce the carbon nano whiskers [37g].

Most of the semiconducting nanomaterials have shown higher catalytic activity in heterogeneous catalysis. CuS quantum dots (QDs) were used as catalysts in Biginelli reactions, and they exhibited good catalytic activity for the synthesis of dihydropyrimidinones [43]. Flower-like Ni_7S_6 NPs showed much

higher activity and selectivity in the hydrogenations of nitrobenzene and chloronitrobenzenes with different chlorine substituent site [44]. Single-phase nickel sulphides such as NiS, NiS₂, Ni₃S₄ and Ni₇S₆ were prepared by using a temperature controlled precursor injection method and were applied in the study of the catalytic reduction of 4-nitrophenol [45]. Recently, it was revealed that the activities of platinum NPs of various shapes were indeed different for the same electron-transfer reaction in colloidal solution [46]. This potential shape dependent catalysis adds the advantage of selective utilization of NPs as catalysts. Of course, being small with corners and edges made their surface atoms unstable during the chemical reaction they catalyze, leading to the change in their shape [47].

1.2.2. Nanoparticles as photocatalysts

Semiconductor nanomaterials are the prime candidates for photocatalytic applications since they show a strong absorption of light in the visible regime. The semiconductor nanostructure facilitates the separation of charge carriers generated by light absorption; these electrons and holes induce reductive and oxidative reactions leading to photocatalysis. Nanostructured semiconductors have faster electron migration and charge generation rate due to their higher surface area-to-volume ratio than the bulk [48]. Titanium dioxide is an excellent photocatalyst because of its low cost, high stability, and environmental friendliness. However, it showed photoactivity only under ultraviolet light irradiation, due to its large band gap energy of 3.2 eV. Therefore, the development of new visible-light active photocatalysts is one of the most significant subjects in photocatalysis research.

Many metal sulphide visible light sensitive semiconductor photocatalysts, such as CdS, CuS, ZnS, Bi₂S₃ and Sb₂S₃ have been developed [49]. CdS nanostructures were used as a photocatalyst for the reduction of aromatic nitro compounds under the irradiation of blue LED (3W) [50]. The well-defined one-dimensional (1D) CdS@MoS₂ (CM) core-shell nanowires were prepared by

Introduction

hydrothermal synthesis and used as photocatalyst for photocatalytic hydrogen evolution under illumination of visible light [51]. CdS nanowires–RGO nanocomposites were synthesized and used for selective reduction of nitro organics under visible light irradiation [52]. The uniform CdS nanospheres/graphene hybrid nanocomposites were used as photocatalysts for selective reduction of nitro-organics in water under visible-light irradiation [53]. The highly dispersed phase of SnO₂ on TiO₂ and Fe₂O₃ on Au nanopillars were used as photocatalysts for the enhanced hydrogen generation by photocatalysis [54].

Template free flower-like CdS NPs were synthesized by a facile hydrothermal approach and as-prepared CdS NPs were used as photocatalyst for the photodegradation of various organic dyes [55]. CuS NPs synthesized by chemical dealloying method exhibited excellent photocatalytic activity towards the degradation of rhodamine B, methylene blue and methyl orange [56]. Monodisperse CuS/ZnS nanocomposite has been synthesized successfully by an ion-exchange method, and their photocatalytic activity was evaluated through the photocatalytic decomposition of rhodamine B in aqueous solution under visible-light irradiation [57]. The photocatalytic activity of nanoporous ZnS NPs was evaluated by conducting the photodegradation of eosin B dye at ambient temperature [58]. Many metal oxide visible-light sensitive semiconductors such as TiO₂, ZrO₂, SnO₂, CeO₂, Fe₂O₃, Al₂O₃, and In₂O₃, have been studied as photocatalysts [59]. Porous crystalline ZnO NPs were prepared by hydrothermal treatment, and their photocatalytic activity was studied by photocatalytic degradation of Rhodamine B in water at ambient temperature [60]. A range of environmental clean-up technologies has been developed for wastewater treatment, which uses iron oxide nanomaterials as nanosorbents and photocatalysts [61].

1.2.3. Nanoparticles in photovoltaic cells

Photovoltaic cells, working based on the principle of photovoltaic effect, convert sunlight directly into electric current (Figure. 1.7). The efficiency of the

conversion process ranges from a few percent up to nearly 37 percent [62] depending on the type of photovoltaic cell. In photovoltaic cells, energy conversion happens in three steps; (i) Generation of the exciton (hole-electron pair) by absorption of light (ii) Separation of excitons (iii) Collection of charges. The layer of materials which absorb sunlight is called as the active layer, and it is normally sandwiched between p and n layer materials for charge separation. The silicon-based solar cell has been extensively studied and has been in practical use. The high cost of manufacturing and long energy payback time hinder the large spread silicon solar cells for PV power generation. Therefore, it is desired to obtain relatively high conversion efficiency from inexpensive materials with low production cost and low-energy consumption.

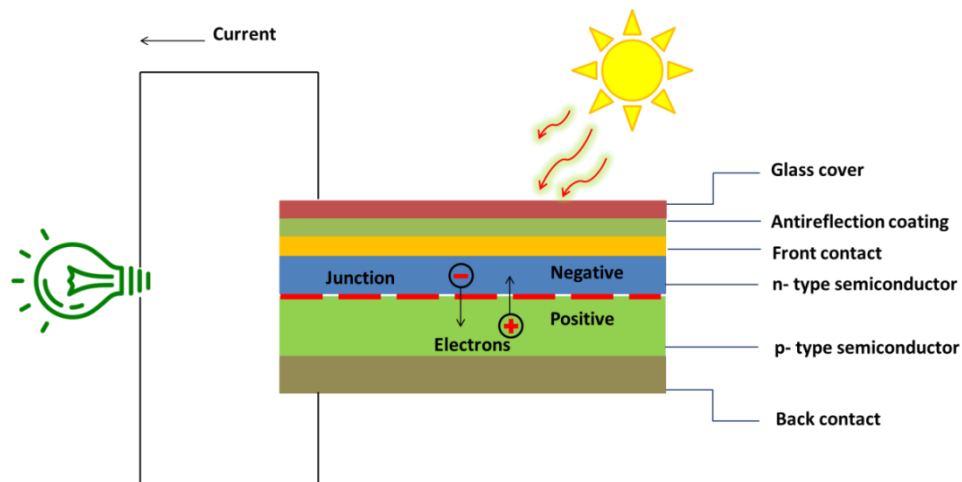


Figure 1.7. Schematic representation of working of photovoltaic cell.

The thermodynamic limit or Shockley- Queisser limit established the ideal band gap of active materials as 1.1 eV [63]. Therefore, many materials having band gap close to this limit have been used to fabricate the solar cells. Among the numerous materials utilized for the fabrication of solar cells, the quantum dots (QDs) are attractive because of their suitable band gaps, efficient optical adsorption, nonlinear optical properties, and less toxicity. Comprehensive research is going on to increase the efficiency of QDSCs by making materials using simple synthetic procedures and by adopting easy fabrication techniques.

Introduction

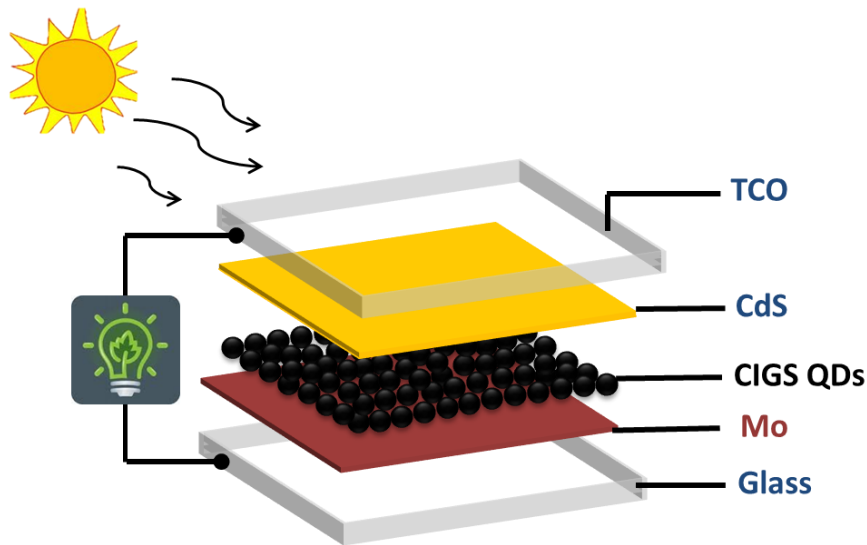


Figure 1.8. Schematic representation of $\text{CuInGaS}_2/\text{Se}_2$ based quantum dot solar cell.

Ternary metal chalcogenides such as CuInS_2 NCs [64] and $\text{CuInGa}(\text{S}/\text{Se})_2$ (CIGS) [65] have direct band gap with energies well matching to the solar spectrum, high radiation stability, high absorption coefficients and low toxicity, which make them as suitable material for PV solar cells. Solar cells showing high efficiency of ~20% at laboratory conditions have been achieved using CIGS. Schematic representation of $\text{CuInGaS}_2/\text{Se}_2$ based quantum dot solar cell is shown in Figure 1.8. In the fabrication of CIGS type solar cells, CIGS is a p-type active layer, which absorbs sunlight and generates an exciton, CdS was used as the buffer layer and ITO/FTO as electrodes. A transparent conductive oxide is used as front contact layer while molybdenum coated by the sputtering process is used as a back contact layer. This fabrication approach eliminated the need for processing steps such as chemical bath deposition of the CdS layer, high-temperature post deposition sulfurization treatment, and a cyanide bath etch step to correct phase purity and grain size. However, the efficiency of solar cells made using NPs depends on the purity of the materials obtained by chemical synthesis.

1.3. Synthesis of metal chalcogenide nanoparticles

1.3.1. Stoichiometric varieties in metal chalcogenides and general synthetic approach

The synthesis of NPs with good monodispersity, crystallinity, and purity for targeted applications is a challenge. Various strategies of syntheses of semiconductor nanocrystals have been developed by utilizing different metal sources so that the composition, size, shape and surface protection can be regulated. Two types of general approaches are used to produce NPs; one is top-down approach, and another one is the bottom-up approach. In the top-down method, the bulk material is brought into a smaller dimension by applying various tools (external force), such as etching, various lithographic techniques, ball milling and sol-gel technique. This method is very useful for the large-scale industrial production of nanomaterials.

The bottom-up method refers to making of NPs from atoms based on the atomic transformation or molecular condensations. The bottom-up approach can be divided into physical and chemical methods. Physical methods are not cheap and not easily adaptable for manufacturing. Chemical methods are favorable due to their potential for scalability, better control in sizes, shapes, less expensive and simple instrumentation. These chemical methods include sol-gel, co-precipitation, colloidal method, chemical vapor deposition (CVD), and thermal decomposition.

Properties and applications of NPs are specific to stoichiometries of the material. From the inorganic materials point of view, chalcogenides, especially copper sulphide (Cu_xS), cadmium sulphide (CdS), bismuth sulphide (Bi_2S_3) and nickel sulphide (Ni_xS_y) have received considerable attention in recent years owing to their wide stoichiometric compositions. The shape, size, stoichiometric composition and crystal structure control the optical and electrical properties of these sulphides. Specifically, for the past few years, various efforts have been developed to control the architecture and spatial patterning of metal chalcogenide semiconductor particles [66].

Introduction

The main focus of this thesis is the synthesis of metal sulphide NPs and hence solution-based colloidal preparation of nanomaterials is highlighted in this chapter. Some of the representative synthetic procedures for copper sulphide (Cu_xS), cadmium sulphide (CdS), bismuth sulphide (Bi_2S_3), nickel sulphide (Ni_xS_y), copper indium sulphide (CIS) and copper tin sulphide (CTS) are explained in the following sections.

1.3.2. Synthesis of copper chalcogenides

In the metal chalcogenides family, copper chalcogenides (CuS , Cu_2S , and Cu_{2-x}Se) are relatively cheap, less hazardous and valuable materials for device fabrication. Copper sulphides are important p-type compounds, and they gained much importance because of their variable stoichiometric compositions (Table 1.2), valence states, nanocrystal morphologies and the differences in the crystal structures.

Table 1.2. Variable stoichiometries of copper chalcogenides

Name	Composition	Band gap (eV)	Reference
covellite	CuS	2.2	[66-69]
chalcocite	Cu_2S	1.2	[70]
anilite	Cu_7S_4	2.11	[71]
	$\text{Cu}_{1.75}\text{S}$		
digenite	$\text{Cu}_{1.8}\text{S}$	1.75	[72]
	Cu_9S_5		
djurleite	$\text{Cu}_{31}\text{S}_{16}$	2.19	[73]
	$\text{Cu}_{1.94}\text{S}$		

Among the eight Cu_xS compositions, the most stable structures are copper rich Cu_2S (chalcocite) and copper deficient stoichiometric phases, i.e. CuS (covellite), $\text{Cu}_{1.75}\text{S}$ (anilite), $\text{Cu}_{1.8}\text{S}$ or Cu_9S_5 (digenite) and $\text{Cu}_{1.96}\text{S}$ (djurleite). Despite their stability, a selective synthesis of a single structure of Cu_xS NPs is a challenge. Control in the synthesis to obtain a specific composition can be achieved by altering the Cu/S ratio, temperature, changing the precursor materials and stabilizing ligands. These copper sulphides behaved as semiconductors with

either direct or indirect band gaps depending on the stoichiometric ratio of Cu to S. The percentage of copper is known to control the band gap of Cu_xS . The band gap of Cu_xS increases with a decrease in the x (Stoichiometry) value. For example, band gap is 1.2 eV for Cu_2S , 1.75 eV for $\text{Cu}_{1.8}\text{S}$ and 2.2 eV for CuS . Concerning these band gap values, CuS can absorb maximum solar energy among the Cu_xS .

Covellite (CuS) phase has been used in solar hydrogen production, while chalcocite (Cu_2S) is widely used as a likely replacement of high-cost Pt counter electrodes in quantum dot-sensitized solar cells (QDSSCs) [66, 68, 74]. Furthermore, CuS nanocrystals have been found as one of the possible materials for the use in catalysis, biosensor, tissue imaging, drug delivery, Li-ion battery and memory cell [75]. Therefore, it is imminent to synthesize CuS that is suitable for possible applications in the solar cells and other optoelectronic devices. The methods used to synthesize copper chalcogenides in variable stoichiometries are listed in Table 1.3.

Table 1.3. General synthetic methods for copper chalcogenide nanoparticles

Author Name	Scheme		
X. Huang et al., (76)	$\text{Cu}(\text{NO}_3)_2 \cdot 3\text{H}_2\text{O} + (\text{NH}_2)_2\text{CS}$	$\xrightarrow[24 \text{ h}]{150 \text{ }^\circ\text{C}}$	CuS NPs (Covellite)
J. Yin et al., (77)	$\text{Cu}(\text{Oac})_2 \cdot \text{H}_2\text{O} + \text{CS}_2 + \text{HDA}$	$\xrightarrow[24 \text{ h}]{120 \text{ }^\circ\text{C}}$	CuS NPs (Covellite)
Y. Qian et al., (78)	$\text{CuCl}_2 \cdot 2\text{H}_2\text{O} + \text{C}_{12}\text{H}_{25}\text{SH}$	$\xrightarrow[12 \text{ h}, 160 \text{ }^\circ\text{C}]{\text{NaS}_2\text{CNEt}_2, \text{C}_{17}\text{H}_{33}\text{COOH}}$	$\text{Cu}_2\text{S NPs}$ (Chalcocite)

Introduction

B. A. Korgel et al., (79)	$\text{CuCl}_2 + \text{C}_6\text{H}_{14}\text{S}_2 + \text{C}_{12}\text{H}_{25}\text{SH}$ 1,6-hexane dithiol dodecane thiol	Ethanol 185 °C, 1.5 h	Cu_2S NPs (Chalcocite)
A. P. Alivisatos et al., (80)	$\text{Cu}(\text{NO}_3)_2 + \text{C}_{12}\text{H}_{25}\text{SH} + \text{C}_7\text{H}_{15}\text{COONa}$	CHCl_3 148 °C, 2.5 h	Cu_2S NPs (Chalcocite)
W. Zheng et al., (81)	$\text{CuSO}_4 \cdot 5\text{H}_2\text{O} + [\text{BMIm}][\text{SeO}_2(\text{OCH}_3)]$	$\text{N}_2\text{H}_4 \cdot \text{H}_2\text{O}$ H_2O , 150 °C autoclave and 12 h	Cu_{2-x}Se NPs (Berzelianite)
L. Zhu et al., (82)	$\text{CuI} + \text{Na}_2\text{SeO}_3 + \text{CTAB}$	$\text{H}_2\text{O}/\text{Hexanol}$ Ultrasonication, 4 h	Cu_{2-x}Se NPs
B.G. Kumar et al., (83)	$\text{CuCl}_2 + \text{HMDS} + \text{S}$	reflux 6 h	CuS NPs

1.3.3. Synthesis of cadmium chalcogenides

CdS is an important IV-VI semiconductor having large effective Bohr radius ($\text{CdS}=2.4 \text{ \AA}$) and have the band gap as 2.41 eV. Because of its suitable band gap CdS is used as photocatalyst and buffer layer in CIGS based solar cells. Various methods are reported for the synthesis of CdS NPs, some of them are listed in Table 1.4 below.

Table 1.4. General synthetic methods for CdS nanoparticles

Author Name	Scheme
K. H. Whitmire et al., (84)	$[\text{Cd}(\text{pydc})(\text{tu})_2] + \text{Oleylamine/CTAB} \xrightarrow[16 \text{ h}]{120 \text{ }^\circ\text{C} - 170 \text{ }^\circ\text{C}} \text{CdS NPs}$
Y. Qian et al., (85)	$\text{Cd}(\text{OAc})_2 \cdot 2\text{H}_2\text{O} + \text{NaS}_2\text{CNET}_2 \cdot 3\text{H}_2\text{O} \xrightarrow[180 \text{ }^\circ\text{C}, 48 \text{ h}]{\text{ethylenediamine and dodecanethiol}} \text{CdS NPs}$
Y. Li et.al., (86)	$\text{Cd}(\text{NO}_3)_2 \cdot 4\text{H}_2\text{O} + \text{thioacetamide} \xrightarrow[120 \text{ }^\circ\text{C}, 30 \text{ min}]{\text{ethyleneglycol and PEI}} \text{CdS NPs}$
S. Oh Cho et al., (87)	$\text{CdCl}_2 + \text{N,N-dimethylformamide} \xrightarrow[200 \text{ }^\circ\text{C}, 10 \text{ h}]{\text{thiourea}} \text{CdS NPs}$

1.3.4. Synthesis of bismuth chalcogenides

Another important class of metal chalcogenides is bismuth chalcogenides, which earned much importance especially due to its optoelectronic properties. The family of bismuth sulphides can exist in three types of stoichiometric variable forms such as BiS, BiS₂ and Bi₂S₃ NPs. Among these phases, the Bi₂S₃ form is only well studied because of the stability factors. The high availability of sulphur and bismuth in the earth crust is also an important factor for the use of Bi₂S₃ for optoelectronic applications. Orthorhombic bismuth sulphide (Bi₂S₃) is an important semiconductor with the direct band gap of 1.3 to 1.7 eV and a large absorbance coefficient [88]. It is used as thermoelectric, electronic, and photoresponsive materials. Thin-films of Bi₂S₃ is good light-harvesting substrates with absorption in the visible and near-IR part of the solar spectrum, which allows their applications in photodiode arrays and photovoltaic converters [89]. While a

Introduction

significant work on the Bi_2S_3 based photodetector is known [90], there is still need for the search of best synthetic methods and simplicity in processing methods [91]. Various methods are available for the synthesis of Bi_2S_3 NPs, some of them are shown in Table 1.5.

Table 1.5. General synthetic methods for Bi_2S_3 nanoparticles

Author Name	Scheme
S. Ge et al., (92)	$\text{Bi}(\text{NO}_3)_3 \cdot 5\text{H}_2\text{O} + \text{ethylene glycol(EG)} \xrightarrow[6 \text{ h}]{220^\circ\text{C}} \text{Bi NPs} \xrightarrow[400^\circ\text{C, 10 min}]{\text{S, hot furnace}} \text{Bi}_2\text{S}_3 \text{ NPs}$
S. Thirumaran et al., (93)	$\text{Tris(N,N-difurfuryldithiocarbamate-S,S') bismuth(III)} \xrightarrow[60^\circ\text{C, 20 min}]{\text{chloroform-diethylenetriamine}} \text{Bi}_2\text{S}_3 \text{ NPs}$
C. Hu et.al., (94)	$\text{Bi}(\text{NO}_3)_3 \cdot 5\text{H}_2\text{O} + \text{LiNO}_3/\text{KNO}_3 \xrightarrow[8-72 \text{ h}]{140^\circ\text{C}-200^\circ\text{C}} \text{Bi}_2\text{S}_3 \text{ NPs}$ <p style="text-align: center;">1:2</p>
Y. Qian et al., (95)	$\text{BiCl}_3 + \text{thiourea} + \text{C}_{17}\text{H}_{33}\text{COOK (potassium oleate)} \xrightarrow[90^\circ\text{C, 5 h}]{\text{ethylene glycol}} \text{Bi}_2\text{S}_3 \text{ NPs}$

1.3.5. Synthesis of nickel chalcogenides

The family of nickel sulphides has different complex phases of nickel sulphides such as NiS ($\alpha\text{-NiS}$ and $\beta\text{-NiS}$), Ni_3S_2 , NiS_2 , Ni_3S_4 , Ni_9S_8 , and Ni_7S_6 (Table 1.6). The presence of various phases makes the synthesis of single-phase nickel sulphide complicated. Nickel sulphide NPs exist in morphologies such as layer-rolled, hexagonal, cuboids, nanobelts, three-dimensional flower-like rhombohedral and dodecahedral [45]. Nickel sulphides with a controlled

morphology are of great interest due to their potential applications as hydrogenation catalysts and electrode materials.

Table 1.6. Variable stoichiometries of nickel chalcogenides

Name	Composition	Reference
millerite	NiS	[96]
pyrite	NiS ₂	[97]
heazelwoodite	Ni ₃ S ₂	[98]
polydymite	Ni ₃ S ₄	[99-104]
godlevskite	Ni ₆ S ₅	[105]
godlevskite	Ni ₇ S ₆	[106]
godlevskite	Ni ₉ S ₈	[107]

Among the various stoichiometries of nickel sulphides, Ni₃S₄ has attracted much less attention compared to other binary nickel sulphides due to the synthetic challenge in obtaining the single phase Ni₃S₄. Ni₃S₄ has a cubic spinel structure and is found in nature as the mineral polydymite. The problem associated with the synthesis of Ni₃S₄ is obtaining it in pure phase. Ni₃S₄ along with NiS and NiS₂ impurities was obtained through solid state reactions between Ni and S, NiS and S, or NiS and NiS₂ at 200–300 °C even after extending the reaction up to 6 months. Therefore, many properties of pure Ni₃S₄ are not completely known [108, 109, 110]. Manthiram and co-workers successfully synthesized Ni₃S₄ at room temperature using an aqueous nickel chloride in a sodium dithionite solution [99]. Ni₃S₄ has been also obtained by colloidal processes using elemental sulphur as a precursor in oleylamine at high temperature (180 °C) [100]. Alternatively, Ni₃S₄ has been found to appear as a by-product in a solvent-less synthesis of rhombohedral NiS nanorods and triangular nanoprisms or under hydrothermal conditions [101]. However, the synthetic approaches mentioned above produced either poor crystallinity or irregularly shaped particles. Much effort has been devoted to obtaining single-phase Ni₃S₄ efficiently in laboratories. Through a selective control in the reaction conditions, Ni precursor used or capping agents employed, it is possible to get single phase of Ni₃S₄. Recently, Tuna and co-

Introduction

workers reported the synthesis of Ni_3S_4 NPs with different shapes by thermolysis using a single-source of Ni precursor, ([bis(1,1,5,5-tetra-isopropyl-2-thiobiuret) nickel(II)]) in the presence of oleylamine, octadecene, or dodecanethiol [102]. Various methods of synthesis of nickel sulphides are listed in Table 1.7

Table 1.7. General synthetic methods for nickel sulphide nanoparticles

Author Name	Scheme
Y. Hayakawa et al., (45)	$\text{Ni}(\text{NO}_3)_2 \cdot 6\text{H}_2\text{O} + \text{S} + \text{oleylamine} \xrightarrow[1 \text{ h}]{210 \text{ }^\circ\text{C}} \text{NiS NPs}$
N. Revaprasadu et al., (111)	$\begin{array}{c} [\text{Ni}(\text{pip-dtc})_2] \\ \text{or} \\ [\text{Ni}(\text{thq-dtc})_2] \end{array} + \text{tri-n-octylphosphine (TOP)} \xrightarrow[190 \text{ }^\circ\text{C}, 2 \text{ h}]{\text{dodecylamine (DDA)}} \text{Ni}_3\text{S}_4 \text{ or } \text{Ni}_3\text{S}_2 \text{ NPs}$
M. Salavati-Niasari et.al., (112)	$[\text{Ni}(\text{sal})_2] + \text{S} + \text{oleylamine} \xrightarrow[60 \text{ min}]{120 \text{ }^\circ\text{C}} \text{NiS NPs}$
H. Zhanget al., (113)	$\text{NiCl}_2 \cdot 6\text{H}_2\text{O} + \text{DI water} + \text{EA} \xrightarrow[180 \text{ }^\circ\text{C}, 12 \text{ h}]{\text{thiourea}} \text{Ni}_7\text{S}_6 \text{ NPs}$ <p style="text-align: center;">(6 mL) (24 mL)</p> <p style="text-align: center;">EA = Ethanol amine</p>

1.3.6. Synthesis of ternary systems

The I-III-VI group based materials; mainly CuInS_2 and CuInSe_2 have large absorption coefficients and excellent photoconductivity [114]. The synthesis of non-toxic ternary chalcogenides semiconducting NPs (I-III-VI) such as CuInS_2 , CuInSe_2 , and $\text{CuIn}_x\text{Ga}_{1-x}\text{Se}_2$ gained much attention of researchers because they are considered to replace the expensive silicon-based solar cells. They are also

better than toxic semiconductors such as CdS, CdSe, CdTe, PbSe, etc. Another important class of ternary systems is the material based on I–IV–VI combinations as they have potential application in photovoltaic cells, electrochemical devices and photocatalytic material [115]. Among them, Cu–Sn–S (CTS) system is gaining importance because of the elements copper, tin and sulphur are nontoxic and abundant in the earth. In CTS systems, especially Cu_2SnS_3 and Cu_3SnS_4 are significant, and they have high absorption coefficient and tunable band gap which cover the optimal solar spectrum [116]. The band gap of these materials can be tuned by changing the particles size and composition, which offers the possibility of matching a specific region of the solar spectrum [117]. Various methods are available for the synthesis of CuInS_2 , CuInSe_2 (CIS/Se) and Cu_2SnS_3 (CTS) some of them are listed in Table 1.8.

Table 1.8. General synthetic methods for $\text{CI}(\text{S/Se})_2$ and CTS nanoparticles

Author Name	Scheme	
B. A. Korgel et al., (118)	$\text{CuCl} + \text{InCl}_3 + \text{Se}$	$\xrightarrow[240\text{ }^\circ\text{C, 4 h}]{\text{OLA}} \text{CuInSe}_2 \text{ NPs}$
B. A. Korgel et al., (66)	$\text{CuCl} + \text{InCl}_3 + (\text{NH}_2)_2\text{CSe}$	$\xrightarrow[240\text{ }^\circ\text{C, 1 h}]{\text{OLA}} \text{CuInSe}_2 \text{ NPs}$
B. Koo et al., (67)	$\text{CuCl}_2 + \text{InCl}_3 + (\text{NH}_2)_2\text{CS}$	$\xrightarrow[240\text{ }^\circ\text{C}]{\text{oleylamine}} \text{CuInS}_2 \text{ NPs}$
F. Bensebaa et al., (68)	$\text{CuCl}_2 \cdot 2\text{H}_2\text{O} + \text{InCl}_3 + \text{Na}_2\text{S/Na}_2\text{Se}$	$\xrightarrow[90\text{ }^\circ\text{C, 30 min}]{\text{MAA, Microwave}} \text{CuInSe}_2/\text{S}_2 \text{ NPs}$

Introduction

S. Dias et al., (119)	$2\text{CuCl}_2 \cdot 2\text{H}_2\text{O} + \text{SnCl}_2 \cdot 2\text{H}_2\text{O} + 3\text{Na}_2\text{S} \xrightarrow[12 \text{ h}]{180 \text{ }^\circ\text{C}} \text{Cu}_2\text{SnS}_3 \text{ NPs}$
J. Xu et al., (120)	$2\text{Cu}(\text{NO}_3)_2 + \text{SnCl}_4 + 3\text{S} \xrightarrow[240 \text{ }^\circ\text{C}, 1 \text{ h}]{\text{TEG}} \text{Cu}_2\text{SnS}_3 \text{ NPs}$
Q. Liu et al., (121)	$2\text{CuCl} + \text{SnCl}_2 + 3\text{S} \xrightarrow[240 \text{ }^\circ\text{C}, 1 \text{ h}]{\text{oleylamine}} \text{Cu}_2\text{SnS}_3 \text{ NPs}$

1.4. Role of capping agents and the stability of the nanoparticles

Capping agents are surfactant molecules used during the synthesis of NPs. They may or may not participate in the synthesis of NPs. Capping agent controls the growth of NPs by preventing them from aggregation and precipitation due to which the surface functionalization and stability of NPs are achieved. The capping agent should be bulk enough to prevent agglomeration and small enough to passivate the surface. The best capping agent would be the one with a balancing of passivation (quenching surface) and stabilization (prevent agglomeration) of NP surface. These capping agents create an inorganic-organic interface, and these interfaces influence the properties of the materials and subsequently the applications.

1.4.1. Architecture of capping agent

The capping agents are organic molecules which behave as Lewis bases. The skeleton of capping agents has a head group with elements having a lone pair of electrons and a tail group with a long alkyl chain (Figure. 1.9). Head groups passivate the surface of NPs and tail groups provide the solubility to the materials. Oleylamine, CTAB, octylamine, and pyridine are nitrogen based capping agents or surfactants [122]. The phosphorus-based capping agents are TOPA, TOPO, TPP, alkyl phosphonic acids and phosphazenes [123]. Long chain alcohols like octanol, oleyl alcohol are the oxygen based capping agents [124]. The sulphur based capping agents are long chain thiols, cysteine, and thiophenes [125].

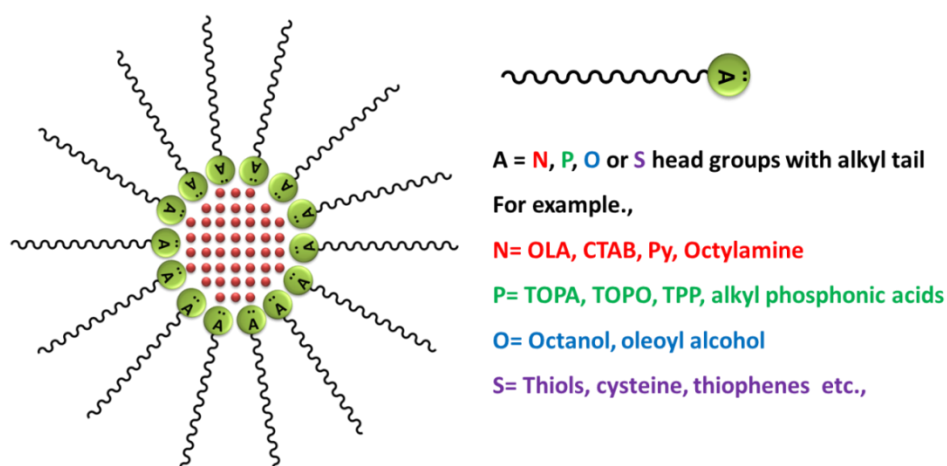


Figure 1.9. Systematic representation of the architecture of the capping agent.

1.4.2. Modes of stabilization

Three different modes of capping *viz.*, passivation, stabilization, and functionalization are usually practiced during the synthesis of NPs. The selection of specific mode capping will depend on the application aimed for [126].

Passivation

Complete quenching of the surface is called passivation. The maximum thermodynamic stability of NPs is possible in passivation which can obtain by surface coating of metals, metal oxides or any inorganic lattices.

Stabilization

Stabilizing agent prevents the agglomeration of NPs in the reaction medium by providing inter particle electrostatic and/or steric repulsions.

Functionalization

Functionalization of NPs can be achieved by tuning the structure of capping agent so that NPs can be used for a specific application. The general methods of surface modification are grafting thiolated surfactants or polymers, adsorption of charged surfactants, charged ligands or polymers, fullerenes, attachment of biological molecules such as DNA, peptides, proteins, and antigens [126].

Introduction

1.5. Definition of the problem

The majority of NPs are produced by colloidal synthetic method [127]. A typical reaction system for colloidal nanocrystals consists of three components: precursor, a reducing agent, organic surfactant, and solvent. In some of the syntheses, surfactants serve as solvents also. During synthesis of NPs, upon heating the reaction medium to a sufficiently high temperature, the precursor molecules chemically transform into active atomic or molecular species. These atomic or molecular species are building units of a material (substance), and they are known as nuclei. This process is called as nucleation. These nuclei then grow by incorporating additional building units still present in the reaction medium. The formation of NPs is governed by the relative rates of two competitive processes, i.e. (i) Nucleation and (ii) Growth of nuclei to form larger particles. The size of the particles obtained in a reaction is decided by the mechanism that predominates in a reaction.

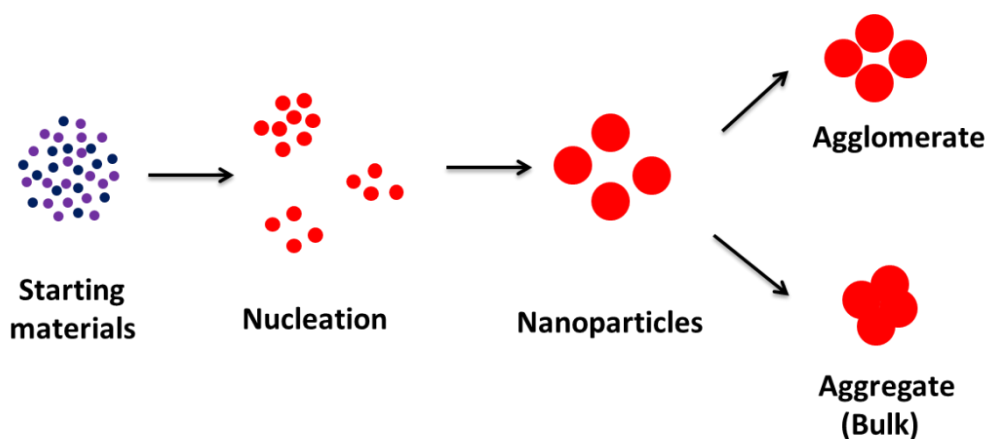


Figure 1.10. Schematic description of stages involved in colloidal synthesis.

The first step in the colloidal synthesis is to choose a temperature that is sufficient enough for the reaction to occur and a super saturated condition of growing nuclei. It is necessary to stop (cap) the growth of nucleated particles at the nanoscale, therefore capping agents play a role in adsorbing on the surface of the particles and preventing the uncontrolled growth. Otherwise, NPs undergo reversible agglomeration or irreversible aggregation (Figure 1.10 is adopted from

Ref. [125]). Therefore, the capping agents are used in the reaction to control the growth of particles. The surfactant molecules should be effective to stop at nano size as well as to prevent agglomeration or aggregation. Apart from the selection of capping agent, the selection of precursor materials and reagents, and their solubility are also important factors. Further, it is required to maintain the reaction mixture under reduced atmosphere to reduce metal/ sulphur source as well as to arrest/stop the growth of NPs in the reaction mixture by the assistance of surfactant/capping agent.

Organic surfactant molecules surround the NPs obtained by synthetic methods called as capping agent or stabilizing agents. The presence of these undesired capping agents hinders the chances of harnessing benefits of surface-dependent properties to their full potential. Some of the disadvantages of capping agent are;

- (i) Surrounding of chemically synthesized NPs by organic surfactant molecules or any other surface coating would affect surface-related processes such as surface recombination or charge transfer.
- (ii) The presence of organic surfactants around NPs hinders the mobility of charge carriers in the electronic devices such as solar cells, which cause the deficiency of devices fabricated using these materials.
- (iii) These molecules shield the active sites of catalyst imputing less catalytic activity than its potential.
- (iv) When NPs are intended to use in the biological or medicinal application; there is apprehension due to the toxicity of organic surfactant molecules.

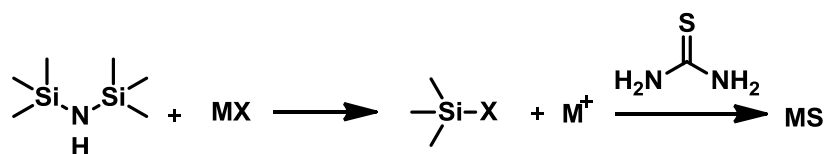
Another drawback in the synthesis of NPs is obtaining a specific stoichiometric product selectively in a pure form when various stoichiometric products of the material are available. As mentioned in Section 1.3, many methods including template-assisted synthesis and use of sensitive organometallic precursors have been developed. However, producing the rare phase of NPs of metal

Introduction

chalcogenides selectively in a simple bottom-up synthesis is remain as a challenge.

1.6. Scope of the thesis

As mentioned in Section 1.5, the capping agent stabilizes NPs but also affects other properties like optoelectronic properties, crystallinity, and catalytic application. These issues can be addressed by avoiding the organic surfactant molecules at pre-synthetic or post-synthetic conditions. In our group, the hexamethyldisilazane (HMDS) assisted synthesis was developed and has been used to produce few metal chalcogenides. Since the solubility of reactants plays a significant role in any reaction medium and decides the product(s) formation, the method needed an improvement to control the reaction products. Therefore, in the present work, we have modified the HMDS – assisted reaction changing the metal precursor, sulphur source and the reaction conditions. Metal chlorides were preferred over other metal sources due to their better solubility while thiourea was used instead of sulphur powder again due to the solubility. As determined earlier in our group, HMDS played multiple roles; as a solvent, reducing agent, and capping agent in arresting the growth of particles during syntheses.



Scheme 1.1. Synthetic methodology for modified HMDS - assisted synthesis.

At present, using the modified HMDS- assisted method, we have prepared a variety of binary metal chalcogenides viz., CuS, Cu₂S, CdS, Ni₃S₄, Bi₂S₃, and In₂S₃. The reaction was further extended to the synthesis of ternary metal chalcogenides. All those reactions yielded binary and ternary metal chalcogenide, semiconductor NPs without surrounding of any organic surfactant molecules. Since these materials had free or clean surfaces, it is important to study the effect of NPs with clean or bare surfaces on various applications. The detailed

discussion on the study of the effect of NPs with bare surfaces on catalysis, photocatalysis and photo-responsive behaviour is presented in this thesis. The various topics covered in the thesis are listed below, and the same is shown schematically in the Figure 1.11 below.

1. Organic functional group transformation using Ni_3S_4 NPs as catalysts
2. Photocatalytic degradation of organic dyes using CuS NPs
3. Photocatalytic reduction of Cr(VI) using CdS NPs
4. Photo-responsive behaviour of Bi_2S_3 NPs on exposure of light of varying intensity
5. Fabrication of solar cells using surfactant-free ternary metal sulphides

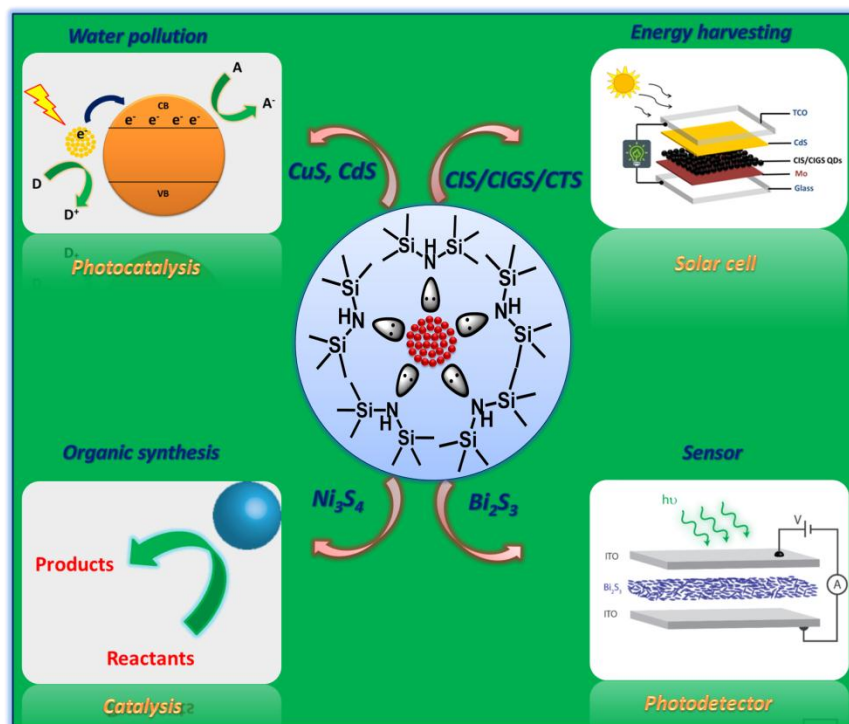


Figure 1.11. Systematic representation of the different applications of synthesized NPs.

Introduction

1.7. References

1. (a) C. Huan and S. Shu-Qing, *Chin. Phys. B.*, 2014, **23**, 1-14. (b) B. R. Taylor and S. M. Kauzlarich, *Chem. Mater.*, 1999, **11**, 2493-2500.
2. (a) M. Fernández-García and J. A. Rodríguez, *Encyclopedia of Inorganic and Bioinorganic Chemistry.*, 15 Dec 2011. (b) P. K. Stoimenov, R. L. Klinger, G. L. Marchin and K. J. Klabunde, *Langmuir*, 2002, **18**, 6679–6686.
3. (a) R. M. Crooks, M. Zhao, L. Sun, V. Chechik and L. K. Yeung, *Acc. of chem. Res.*, 2001, **34**, 181-190. (b) C. J. Murphy, T. K. Sau, A. M. Gole, C. J. Orendorff, J. Gao, L. Gou, S. E. Hunyadi and T. Li, *J. Phys. Chem. B.*, 2005, **109**, 13857-13870.
4. (a) M. S. Mauter and M. Elimelech, *Environmental Science & Technology*, 2008, **42**, 5843-5859. (b) C. Cha, S. R. Shin, N. Annabi, M. R. Dokmeci and A. Khademhosseini, *ACS Nano*, 2013, **7**, 2891-2897.
5. (a) T. Kietzke, D. Neher, K. Landfester, R. Montenegro, R. Güntner and U. Scherf, *Nature Materials*, 2003, **2**, 408–412. (b) J. P. Raoa and K. E. Geckeler, *Progress in Polymer Science*, 2011, **36**, 887–913.
6. C. Burda, X. Chen, R. Narayanan and M. A. El-Sayed, *Chem. Rev.*, 2005, **105**, 1025-1102.
7. V.V. Pokropivny and V.V. Skorokhod., *Materials Science and Engineering C*, 2007, **27**, 990–993.
8. (a) M. C. Daniel and D. Astruc, *Chem. Rev.* 2004, **104**, 293-346. (b) R. Kubo, *J. Phys. Soc. Jpn.* 1962, **17**, 975-986. (c) S. K. Ghosh and T. Pal, *Chem. Rev.*, 2007, **107**, 4797-4862.
9. a) Ph. Buffat and J. P. Borel, *Phys. Rev. A*, 1976, **13**, 2287-2298. (b) Q. Jiang, H. X. Shi and M. Zhao, *J. Chem. Phys.* 1999, **111**, 2176-2180. (c) K. J. Klabunde and R. M. Richards, *Nano scale materials in chemistry* John Wiley, 2nd Edition. (d) K. K. Nanda, S. N. Sahu and S. N. Behera, *Phys. Rev. A*, 2002, **66**, 013208-013216.
10. A. P. Alivisatos, *Science*, 1996, **271**, 933-937.

11. (a) H. Yu, J. Li, R. A. Loomis, L. Wang and W. E. Buhro, *Nat. Mat.*, 2003, **2**, 517-520. (b) H. Yu, J. Li, R. A. Loomis, P. C. Gibbons, L. Wang and W. E. Buhro, *J. Am. Chem. Soc.*, 2003, **125**, 16168-16169.
12. K. L. Kelly, E. Coronado, L. L. Zhao and G. C. Schatz, *J. Phys. Chem. B*, 2003, **107**, 668-677.
13. S. Eustis and M. A. El-Sayed, *Chem. Soc. Rev.*, 2006, **35**, 209-217.
14. (a) I. Gur, N. A. Fromer, M. L. Geier and A. P Alivisatos, *Science*, 2005, **310**, 462-465. (b) W. U. Huynh, X. G Peng and A. P. Alivisatos, *Adv. Mater.*, 1999, **11**, 923-927.
15. (a) P. O. Anikeeva, J. E. Halpert, M.G. Bawendi and V. Bulović, *Nano. Lett.*, 2009, **9**, 2532-2536. (b) S. Coe, W. K. Woo, M. Bawendi and V. Bulovic, *Nature*, 2002, **420**, 800-803.
16. G. Konstantatos and E. H. Sargent, *Nat. Nanotechnol.*, 2010, **5**, 391-400.
17. (a) R. Raja, T. Khimyak, J. M. Thomas, S. Hermans and B. F. G. Johnson, *Angew. Chem. Int. Ed.*, 2001, **40**, 4635-4638. (b) M. Shokouhimehr, Y. Piao, J. Kim, Y. Jang, and T. Hyeon, *Angew. Chem. Int. Ed.*, 2007, **46**, 7039-7043.
18. (a) M. Bruchez, M. Moronne, P. Gin, S. Weiss and A. P Alivisatos, *Science*, 1998, **281**, 2013-2016. (b) X. Michalet, F. F. Pinaud, L. A. Bentolila, J. M. Tsay, S. Doose, J. J. Li, G. Sundaresan, A. M. Wu, S. S Gambhir and S. Weiss, *Science*, 2005, **307**, 538-544.
19. P. Brousseau and C. J Anderson, *Propell. Explos. Pyrot.*, 2002, **27**, 300-306.
20. (a) Y. Engel, R. Elnathan, A. Pevzner, G. Davidi, E. Flaxer and F. Patolsky, *Angew. Chem., Int. Ed.*, 2010, **49**, 6830-6835. (b) A. Kolmakov, Y. Zhang, G. Cheng and M. Moskovits, *Adv. Mater.*, 2003, **15**, 997-1000. (c) V. V Sysoev, B. K. Button, K. Wepsiec, S. Dmitriev and A. Kolmakov, *Nano Lett.*, 2006, **6**, 1584-1588. (d) E. Brasola, F. Mancin, E. Rampazzo, P and Tecill, U Tonellato, *Chem. Commun.*, 2003, 3026-3027. (e) C. Y. Zhang, H. C. Yeh, M. T. Kuroki and T. H. Wang, *Nat. Mat.*, 2005, **4**, 826-831.
21. (a) B. M Reinhard, M. Siu, H. Agarwal, A. P Alivisatos and J. Liphardt, *Nano Lett.*, 2005, **5**, 2246-2252. (b) N. Liu, M. Hentschel, T. Weiss, A. P Alivisatos and H. Giessen, *Science*, 2011, **332**, 1407-1410.

Introduction

22. V. I. Klimov, A. A. Mikhailovsky, S. Xu, A. Malko, J. A. Hollingsworth, C. A. Leatherdale, H. J. Eisler and M. G. Bawendi, *Science*, 2000, **290**, 314-317.
23. D. N. Lambeth, E. M. T. Velu, G. H Bellesis, L. Lee and D. E Laughlin, *J. Appl. Phys.*, 1996, **79**, 4496-4501.
24. A. Tuxen, S. Carenco, M. Chintapalli, C. H. Chuang, C. Escudero, E. Pach, P. Jiang, F. Borondics, B. Beberwyck, A. P. Alivisatos, G. Thornton, W. F. Pong, J Guo, R. Perez, F. Besenbacher and M. Salmeron, *J. Am. Chem. Soc.*, 2013, **135**, 2273-2278.
25. A. S. Khanna, *Asian J. Exp. Sci.*, 2008, **21**, 25-34.
26. L. Amirav and A. P. Alivisatos, *J. Am. Chem. Soc.*, 2013, **135**, 13049-13053.
27. M. J. Choi, A. M. McDonagh, P Maynard and C. Roux, *Forensic Sci. Int.*, 2008, **179**, 87-97.
28. E. Boisselier and D. Astruc, *Chem. Soc. Rev.*, 2009, **38**, 1759-1782.
29. (a) L. Shi, H. Li, Z. Wang, X. Huang and L. Chen, *J. Mater. Chem.*, 2001, **11**, 1502-1505. (b) C. Kim, M. Noh, M. Choi, J. Cho and B. Park, *Chem. Mater.*, 2005, **17**, 3297-3301.
30. (a) T. Pradeep and Anshup, *Thin Solid Films* 2009, **517**, 6441-6478. (b) P. Jain and T. Pradeep, *Biotechnol. Bioeng.*, 2005, **90**, 59-63.
31. Y. Tachibana, L. Vayssieres and J. R Durrant, *Nat. Photonics*, 2012, **6**, 511-518.
32. <http://www.nanowerk.com/spotlight/spotid=18846.php>
33. (a) T. S. Ahmadi, Z. L. Wang, T. C. Green, A. Henglein and M. A. El-Sayed, *Science*, 1996, **272**, 1924-1926. (b) M. Moreno-Manas and R. Pleixats, *Acc. Chem. Res.* 2003, **36**, 638-643.
34. (a) R. Narayanan and M. A. El-Sayed, *J. Phys. Chem. B*, 2004, **108**, 5726-5733. (b) R. Narayanan and M. A. El-Sayed, *J. Phys. Chem. B*, 2005, **109**, 12663-12676. (c) G. A. Somorjai and J. Y. Park, *Top. Catal.*, 2008, **49**, 126-135.
35. (a) Johnson and F. G. Brian, *Top. Catal.* 2003, **24**, 1-4, 147-159. (b) B. Corain, P. Centomo, S. Lora and M. Kralik, *J. Mol. Catal. A: Chem.* 2003,

- 755**, 204-205. (c) A. K. Santra and D. W. Goodman, *Catal. Electrocatal. Nano. Surf.* 2003, 281-309. (d) M. Haruta, *Chem. Rec.* 2003, **3**, 75-87. (e) A. T. Bell, *Science*, 2003, **299**, 1688-1691. (f) J. M. Thomas, B. F. G. Johnson, R. Raja, G. Sankar and P. A. Midgley, *Acc. Chem. Res.* 2003, **36**, 20-30. (g) G. A. Somorjai and Y. G. Borodko, *Catal. Lett.* 2001, **76**, 1-2, 1-5. (h) G. Rupprechter and H. J. Freund, *Top. Catal.* 2000, **14**, 1-4, 3-14. (i) A. S. Eppler, G. Rupprechter, L. Guzzi and G. A. Somorjai, *J. Phys. Chem. B*, 1997, **101**, 48, 9973-9977.
36. (a) P. W. Jacobs, S. J. Wind, F. H. Ribeiro and G. A. Somorjai, *Surf. Sci.*, 1997, **372**, 1-3, L249-L253. (b) G. A. Somorjai, *Appl. Surf. Sci.*, 1997, **1**, 121-122, 1-19. (c) J. Grunes, J. Zhu, E. A. Anderson and G. A. Somorjai, *J. Phys. Chem. B*, 2002, **106**, 44, 11463-11468.
37. (a) Z. Liu, X. Y. Ling, X. Su and J. Y. Lee, *J. Phys. Chem. B*, 2004, **108**, 8234-8240. (b) D. A. Bulushev, I. Yuranov, E. I. Suvorova, P. A. Buffat and L. J. KiwiMinsker, *Catal.*, 2004, **224**, 8-17. (c) N. Lopez, T. V. W. Janssens, B. S. Clausen, Y. Xu, M. Mavrikakis, T. Bligaard and J. K. Norskov, *J. Catal.* 2004, **223**, 232-235. (d) S. Chen and A. Kucernak, *J. Phys. Chem. B*, 2004, **108**, 3262-3276. (e) Z. Liu, J. Y. Lee, W. Chen, M. Han and L. M. Gan, *Langmuir*, 2004, **20**, 181-187. (f) Z. Liu, X. Y. Ling, J. Y. Lee, X. Su and L. M. Gan, *J. Mater. Chem.*, 2003, **13**, 3049-3052. (g) K. Nakagawa, M. Yamagishi, H. Nishimoto, N. Ikenaga, T. Suzuki, T. Kobayashi, M. Nishitani-Gamo and T. Ando, *Chem. Mater.* 2003, **15**, 4571-4575. (h) E. R. Fachini, R. Diaz-Ayala, E. Casado-Rivera, S. File and C. R. Cabrera, *Langmuir*, 2003, **19**, 8986-8993. (i) Y. Takasu, H. Itaya, T. Kawaguchi, W. Sugimoto and Y. Murakami, *Stud. Surf. Sci. Catal.* 2003, **145**, 279-282. (j) F. Li, J. Zou and G. Yuan, *Catal. Lett.* 2003, **89**, 115-119. (k) L. Dubau, C. Coutanceau, E. Garnier, J-M. Leger and C. Lamy, *J. Appl. Electrochem.* 2003, **33**, 419-429. (l) S. Carrettin, P. McMorn, P. Johnston, K. Griffin, C. J. Kiely and G. Hutchings, *J. Phys. Chem. Chem. Phys.* 2003, **5**, 1329-1336.
38. (a) A. G. Boudjahem, S. Monteverdi, M. Mercy and M. M. Bettahar, *J. Catal.* 2004, **221**, 325-334. (b) K. Anderson, S. C. Fernandez, C. Hardacre and P. C.

Introduction

- Marr, *Inorg. Chem. Commun.* 2003, **7**, 73-76. (c) C. Yang, M. Kalwei, F. Schuth and K. Chao, *Appl. Catal. A: Gen.* 2003, **254**, 289-296. (d) A. Y. Khodakov, R. Bechara and A. Griboval-Constant, *Appl. Catal. A: Gen.* 2003, **254**, 273-288. (e) H. Lang, R. A. May, B. L. Iversen and B. D. Chandler, *J. Am. Chem. Soc.* 2003, **125**, 14832-14836. (f) T. Komatsu, K. Inaba, T. Uezono, A. Onda and T. Yashima, *Appl. Catal. A: Gen.* 2003, **251**, 315-326. (g) C. Bianchini, V. D. Santo, A. Meli, S. Moneti, M. Moreno, W. Oberhauser, R. Psaro, L. Sordelli and F. Vizza, *J. Catal.* 2003, **213**, 47-62. (h) S. G. Marchetti, M. V. Cagnoli, A. M. Alvarez, J. F. Bengoa, N. G. Gallegos, A. A. Yeramian and R. C. Mercader, *Hyperfine Interact.* 2002, **33**, 139/140 (1-4). (i) A. Horvath, A. Beck, Z. Koppany, A. Sarkany and L. Gucci, *J. Mol. Catal. A: Chem.* 2002, **295**, 182-183.
39. (a) I. Balint, A. Miyazaki and K. Aika, *Phys. Chem. Chem. Phys.* 2004, **6**, 2000-2002. (b) G. Marconi, P. Pertici, C. Evangelisti, A. M. Caporusso, G. Vitulli, G. Capannelli, M. Hoang and T. W. Turney, *J. Organomet. Chem.* 2004, **689**, 639-646. (c) C. Burda, X. Chen, R. Narayanan and M. A. El-Sayed, *Chemical Reviews*, 2005, **105**, 4, 1025-1102. (d) J. W. Yoo, D. J. Hathcock and M. A. El-Sayed, *J. Catal.* 2003, **214**, 1-7. (e) I. Balint, A. Miyazaki and K. Aika, *Chem. Commun.* 2002, **10**, 1044-1045. (f) I. Balint, A. Miyazaki and K. Aika, *J. Catal.* 2002, **207**, 66-75. (g) H. H. Ingelsten, J. Beziat, K. Bergkvist, A. Palmqvist, M. Skoglundh, Q. Hu, L. K. L. Falk and K. Holmberg, *Langmuir*, 2002, **18**, 1811-1818. (h) A. Miyazaki, I. Balint, K. Aika and Y. Nakano, *Chem. Lett.* 2001, **30**, 1332-1333. (i) J. W. Yoo, D. Hathcock and M. A. El-Sayed, *J. Phys. Chem. A*, 2002, **106**, 2049-2054.
40. (a) P. Konova, A. Naydenov, C. Venkov, D. Mehandjiev, D. Andreeva and T. Tabakova, *J. Mol. Catal. A: Chem.* 2004, **213**, 235-240. (b) K. Mallick and M. S. Scurrrell, *Appl. Catal. A: Gen.* 2003, **253**, 527-536. (c) L. Gucci, A. Beck, A. Horvath, Z. Koppany, G. Stefler, K. Frey, I. Sajo, O. Geszti, D. Bazin and J. Lynch, *J. Mol. Catal. A: Chem.* 2003, **545**, 204-205. (d) A. Ishiguro, T. Nakajima, T. Iwata, M. Fujita, T. Minato, F. Kiyotaki, Y. Izumi, K. Aika, M. Uchida, K. Kimoto, Y. Matsui and Y. Wakatsuki, *Chem. Eur. J.* 2002, **8**,

- 3260-3268. (e) M. Bowker, P. Stone, R. Bennett and N. Perkins, *Surf. Sci.* 2002, **511**, 435-448. (f) P. Claus and H. Hofmeister, *J. Phys. Chem. B*, 1999, **103**, 2766-2775.
41. (a) N. Toshima, M. Ohtaki and T. Teranishi, *React. Polym.* 1991, **15**, 135-145. (b) H. Hirai, M. Ohtaki and M. Komiyama, *Chem. Lett.* 1986, **15**, 269-272. (c) H. Hirai, M. Ohtaki and M. Komiyama, *Chem. Lett.* 1987, **16**, 149-152. (d) M. Ohtaki, N. Toshima, M. Komiyama and H. Hirai, *Bull. Chem. Soc. Jpn.* 1990, **63**, 1433-1440. (e) K. Suzuki, T. Yumura, M. Mizuguchi, Y. Tanaka, C-W. Chen and M. Akashi, *J. Appl. Polym. Sci.* 2000, **77**, 2678-2684. (f) C-W. Chen, M-Q. Chen, T. Serizawa and M. Akashi, *Chem. Commun.* 1998, 831-832. (g) C-W. Chen, T. Serizawa and M. Akashi, *Chem. Mater.* 1999, **11**, 1381-1389. (h) M. T. Greci, S. Pathak, K. Mercado, G. K. S. Prakash, M. E. Thompson and G. A. Olah, *J. Nanosci. Nanotechnol.* 2001, **1**, 3-6.
42. (a) M. L. Anderson, R. M. Stroud and D. R. Rolison, *Nano Lett.* 2002, **2**, 3, 235-240. (b) J. J. Pietron, R. M. Stroud and D. R. Rolison, *Nano Lett.* 2002, **2**, 5, 545-549. (c) J. W. Long, R. M. Stroud, K. E. Swider-Lyons and D. R. Rolison, *J. Phys. Chem. B*, 2000, **104**, 9772-9776. (d) J. T. Moore, J. D. Corn, D. Chu, R. Jiang, D. L. Boxall, E. A. Kenik and C. M. Lukehart, *Chem. Mater.*, 2003, **15**, 17, 3320-3325. (e) J. T. Moore, D. Chu, R. Jiang, G. A. Deluga and C. M. Lukehart, *Chem. Mater.*, 2003, **15**, 5, 1119-1124. (f) J. W. Long, R. M. Stroud, K. E. Swider-Lyons and D. R. Rolison, *J. Phys. Chem. B*, 2000, **104**, 9772-9776.
43. G. R. Chaudhary, P. Bansal and S. K. Mehta, *Chemical Engineering Journal*, 2014, **243**, 217-224.
44. F. Cao, R. Liu, L. Zhou, S. Song, Y-Q. Lei, W-D. Shi, F. Zhao and H. Zhang, *J. Mater. Chem.*, 2010, **20**, 1078-1085.
45. R. Karthikeyan, D. Thangaraju, N. Prakash and Y. Hayakawa, *CrystEngComm*, 2015, **17**, 5431-5439.
46. R. Narayanan and M. A. El-Sayed, *NanoLett.* 2004, **4**, 7, 1343-1348.
47. R. Narayanan and M. A. El-Sayed, *J. Phys. Chem. B*, 2004, **108**, 5726-5733.

Introduction

48. (a) H. W. Park, W. Y. Choi and M. R. Hoffmann, *J. Mater. Chem.*, 2008, **18**, 2379-2385. (b) Y. X. Li, G. Chen, C. Zhou and J. X. Sun, *Chem. Commun.*, 2009, 2020-2022. (c) C-H. Lai, M-Y. Lu and L-J. Chen, *J. Mater. Chem.*, 2012, **22**, 19–30.
49. (a) V. J. Gandubert, E. Torres and C. M. Niemeyer, *J. Mater. Chem.*, 2008, **18**, 3824-3830. (b) Q. F. Han, L. Chen, M. J. Wang, X. J. Yang, L. D. Lu and X. Wang, *Mater. Sci. Eng., B*, 2010, **166**, 118-121. (c) M. Muruganandham and Y. Kusumoto, *J. Phys. Chem. C*, 2009, **113**, 16144-16150.
50. P. Eskandari, F. Kazemi and Z. Zanda, *Journal of Photochemistry and Photobiology A: Chemistry*, 2014, **274**, 7–12.
51. B. Han, S. Liu, N. Zhang, Y-J. Xu and Z-R. Tang, *Applied Catalysis B: Environmental*, 2017, **202**, 298–304.
52. S. Liu, Z. Chen, N. Zhang, Z-R. Tang and Y-J. Xu, *J. Phys. Chem. C*, 2013, **117**, 8251–8261.
53. Z. Chen, S. Liu, M-Q. Yang and Y-J. Xu, *ACS Appl. Mater. Interfaces*, 2013, **5**, 4309–4319.
54. (a) R. Sasikala, A. Shirole, V. Sudarsan, T. Sakuntala, C. Sudakar, R. Naik and S. R. Bharadwaj, *International journal of hydrogen energy*, 2009, **34**, 3621–3630. (b) H. Gao, C. Liu, H. E. Jeong and P. Yang, *ACS Nano.*, 2012, **6**, 1, 234–240.
55. W. Wang, Y. Lu, Y. Xu, K. Wu, J. Huang, C. Ji and S. O. Ryu, *CrystEngComm*, 2016, **18**, 4681-4687.
56. W. Xu, S. Zhu, Y. Liang, Z. Li, Z. Cui, X. Yang and A. Inoue, *Scientific Reports*, **5**, 18125, DOI: 10.1038/srep18125.
57. J. Yu, J. Zhang and S. Liu, *J. Phys. Chem. C*, 2010, **114**, 13642–13649.
58. J-S. Hu, L-L. Ren, Y-G. Guo, H-P. A-M. Cao, L-J. Wan and C-L. Bai, *Angew. Chem.*, 2005, **117**, 1295–1299.
59. D. G. Shchukin and R. A. Caruso, *Chem. Mater.*, 2004, **16**, 2287-2292.
60. (a) J. Yu and X. Yu, *Environ. Sci. Technol.*, 2008, **42**, 4902–4907. (b) J. Das and D. Khushalani, *J. Phys. Chem. C*, 2010, **114**, 2544–2550. (c) A. McLaren,

- V-S. Teresa, G. Li and S. C. Tsang, *J. Am. Chem. Soc.*, 2009, **131**, 12540–12541.
61. (a) P. Xu, G. M. Zeng, D. L. Huang, C. L. Feng, S. Hu, M. H. Zhao, C. Lai, Z. Wei, C. Huang, G. X. Xi and Z. F. Liu, *Science of the Total Environment*, 2012, **424**, 1–10. (b) J. Yu, X. Yu, B. Huang, X. Zhang and Y. Dai, *Crystal Growth & Design*, 2009, **9**, 3, 1474–1480.
62. A. J. Nozik, *Nano Lett.* 2010, **10**, 2735–2741.
63. W. Shockley and H. J. Queisser, *J. Appl. Phys.*, 1961, **32**, 510-519.
64. (a) S. Bini, K. Bindu, M. Lakshmi, C. S. Kartha, K. P. Vijayakumar, Y. Kashiwaba and T. Abe, *Renew. Energy*, 2000, **20**, 405–413. (b) G-C. Park, H-D. Chung, C-D. Kim, H-R. Park, W-J. Jeong, J-U. Kim, H-B. Gu and K-S. Lee, *Solar Energy Materials and Solar Cells*, 1997, **49**, 365-374.
65. K. Ramanathan, M. A. Contreras, C. L. Perkins, S. Asher, F. S. Hasoon, J. Keane, D. Young, M. Romero, W. Metzger, R. Noufi, J. Ward and A. Duda, *Progr. Photovolt.: Res. Appl.*, 2003, **11**, 225-230.
66. B. Koo, R. N. Patel and B. A. Korgel, *J. Am. Chem. Soc.*, 2009, **131**, 3134–3135.
67. B. Koo, R. N. Patel and B. A. Korgel, *Chem. Mater.*, 2009, **21**, 1962–1966.
68. F. Bensebaa, L. Scoles, C. Durand, X. Du, D. Wang, A. Aouadou and Y. L. Page, *J. Nanopart. Res.*, 2010, **12**, 1897–1903.
69. (a) G. Xiao, Q. Dong, Y. Wang, Y. Sui, J. Ning, Z. Liu, W. Tian, B. Liu, G. Zou and B. Zou, *RSC Adv.*, 2012, **2**, 234-240. (b) G. Chen, Y. Yu, K. Zheng, T. Ding, W. Wang, Y. Jiang and Q. Yang, *Small*, 2015, **11**, 2848–2855. (c) G. Manna, R. Bose and N. Pradhan, *Angew. Chem. Int. Ed.*, 2014, **53**, 6743-6746.
70. (a) L. Cademartiri, R. Malakooti, P. G. O'Brien, A. Migliori, S. Petrov, N. P. Kherani and G. A. Ozin, *Angew. Chem., Int. Ed.*, 2008, **47**, 3814–3817. (b) J. Ota and S. K. Srivastava, *J. Phys. Chem. C*, 2007, **111**, 12260–12264. (c) J. Tang and A. P. Alivisatos, *Nano Lett.* 2006, **6**, 2701–2706.
71. (a) J. Kundu and D. Pradhan, *ACS Appl. Mater. Interfaces*, 2014, **6**, 1823–1834. (b) M. Basu, A. K. Sinha, M. Pradhan, S. Sarkar, Y. Negishi,

Introduction

- Govind and T. pal, *Environ. Sci. Technol.*, 2010, **44**, 6313–6318. (c) G. Henshaw, I. P. Parkin and G. A. Shaw, *J. Chem. Soc., Dalton Trans.*, 1997, 231–236. (d) W. Li, A. Shavel, R. Guzman, R-G. Javier, C. Flox, J. Fan, D. Cadavid, M. Ibanez, J. Arbiol, J. R. Morante and A. Cabot, *Chem. Commun.*, 2011, **47**, 10332–10334.
72. Y. Wu, C. Wadia, W. Ma, B. Sadtler and A. P. Alivisatos, *Nano Letters*, 2008, **8**, 2551-2555.
73. S. V. Bagula, S. D. Chavhanb and R. Sharma, *Journal of Physics and Chemistry of Solids*, 2007, **68**, 1623–1629.
74. (a) J. Kundu and D. Pradhan, *New J. Chem.*, 2013, **37**, 1470-1478. (b) S. Gorai, D. Ganguli and S. Chaudhuri, *Crystal Growth & Deign*, 2005, **5**, 3, 875-877.
75. M. Akhtar, Y. Alghamdi, J. Akhtar, Z. Aslam, N. Revaprasadu and M. A. Malik, *Materials Chemistry and Physics*, 2016, **180**, 404-412.
76. F. L. J. Wu, Q. Qin, Z. Li and X. Huang, *Powder Technology*, 2010, **198**, 267-274.
77. W. Du, X. Qian, X. Ma, Q. Gong, H. Cao and J. Yin, *Chem. Eur. J.*, 2007, **13**, 3241-3247.
78. Z. Liu, D. Xu, J. Liang, J. Shen, S. Zhang and Y. Qian, *J. Phys. Chem. B*, 2005, **109**, 10699-10704.
79. M. B. Sigman Jr., A. Ghezelbash, T. Hanrath, A. E. Saunders, F. Lee and B. A. Korgel, *J. Am. Chem. Soc.*, 2003, **125**, 16050-16057.
80. Y. Wu, W. C. Wadia, W. Ma, B. Sadtler and A. P. Alivisatos, *Nano Lett.*, 2008, **8**, 2551-2555.
81. X. Liu, X. Duan, P. Peng and W. Zheng, *Nanoscale*, 2011, **3**, 5090–5095.
82. Y. Xie, X. Zheng, X. Jiang, J. Lu, and L. Zhu, *Inorg. Chem.*, 2002, **41**, 387-392.
83. B. G. Kumar and K. Muralidharan, *Eur. J. Inorg. Chem.*, 2013, **32**, 2102 – 2108.
84. T. Mandal, V. Stavila, I. Rusakova, S. Ghosh and K. H. Whitmire, *Chem. Mater.* 2009, **21**, 5617–5626.

85. D. Xu, Z. Liu, J. Liang and Y. Qian, *J. Phys. Chem. B*, 2005, **109**, 14344–14349.
86. Z. Zhuang, X. Lu, Q. Peng and Y. Li, *J. Am. Chem. Soc.*, 2010, **132**, 1819–1821.
87. M. Chen, Y. N. Kim, C. Li and S. O. Cho, *Crystal Growth & Design*, 2008, **8**, 629–634.
88. A. L. Abdelhady, M. A. Malik, P. O'Brien and F. Tuna, *J. Phys. Chem. C*, 2012, **116**, 2253–2259.
89. V. Stavila, K. H. Whitmire and I. Rusakova, *Chem. Mater.*, 2009, **21**, 5456–5465.
90. Q. Liu, Z. Yan, N. L. Henderson, J. C. Bauer, D. W. Goodman, J. D. Batteas and R. E. Schaak, *J. Am. Chem. Soc.*, 2009, **131**, 5720–5721.
91. (a) H. Bao, X. Cui, C. M. Li, Y. Gan, J. Zhang and J. Guo, *J. Phys. Chem. C*, 2007, **111**, 12279–12283. (b) M. Nair and P. Nair, *Semicond. Sci. Technol.*, 1990, **5**, 1225–1230.
92. Z. Cui, S. Li, J. Zhou, J. Zhang, S. Ge and Z. Zheng, *NANO: Brief Reports and Reviews*, 2015, **10**, 2, 1550021–1550026.
93. S. Tamilvanan, G. Gurumoorthy, S. Thirumaran and S. Ciattini, *Polyhedron*, 2017, **123**, 111–121.
94. Q. Yang, C. Hu, S. Wang, Y. Xi and K. Zhang, *J. Phys. Chem. C*, 2013, **117**, 5515–5520.
95. Q. Li, M. Shao, J. Wu, G. Yu and Y. Qian, *Inorganic Chemistry Communications*, 2002, **5**, 933–936.
96. (a) L. Reijnen, B. Meester, A. Goossens and Schoonman, *J. Mater. Sci. Eng., C* 2002, **19**, 311–314. (b) Z-H. Ge, B-P. Zhang, Y-X. Chen, Z-X. Yu, Y. Liu and J-F. Li, *Chem. Commun.*, 2011, **47**, 12697–12699.
97. D. Yoon, H. Jin, S. Ryu, S. Park, H. Baik, S. Jaeoh, S. Haam, C. Joo and K. Lee, *CrystEngComm*, 2015, **17**, 4627–4631.
98. (a) Y. Wang, Q. Zhu, L. Tao and X. Su, *J. Mater. Chem.*, 2011, **21**, 9248–9254. (b) J. Yang, X. Duan, Q. Qin and W. Zheng, *J. Mater. Chem. A*, 2013, **1**, 7880–7884.

Introduction

99. (a) N. Mahmood, C. Zhang and Y. Hou, *Small*, 2013, **9**, 1321-1328. (b) X. Jiang, Y. Xie, J. Lu, L. Zhu, W. He and Y. Qian, *Adv. Mater.*, 2001, **13**, 1278-1281. (c) Y. Hu, J. Chen, W. Chen, X. Lin and X. Li, *Adv. Mater.*, 2003, **15**, 726-729.
100. L. Wang, J. Liu, L. L. Zhang, B. Dai, M. Xu, M. Ji, X. S. Zhao, C. Cao, J. Zhang and H. Zhua, *RSC Adv.*, 2015, **5**, 8422-8426.
101. (a) A. Manthiram and Y. U. Jeong, *J. Solid State Chem.*, 1999, **147**, 679–681. (b) Y. U. Jeong and A. Manthiram, *Inorg. Chem.*, 2000, **40**, 73–77.
102. (a) A. Ghezelbash and B. A. Korgel, *Langmuir*, 2005, **21**, 9451–9456. (b) H. T. Zhang, G. Wu and X. H. Chen, *Mater. Lett.*, 2005, **59**, 3728–3731.
103. (a) X. Chen, Z. Wang, X. Wang, J. Wan, J. Liu and Y. Qian, *Chem. Lett.*, 2004, **33**, 1294–1295. (b) C. An, Z. Zhang, X. Chen and Y. Liu, *Mater. Lett.*, 2006, **60**, 3631–3634.
104. (a) S-L. Yang, H-B. Yao, M-R Gao and S-H. Yu, *CrystEngComm*, 2009, **11**, 1383–1390. (b) H. Pang, C. Wei, X. Li, G. Li, Y. Ma, S. Li, J. Chen and J. Zhang, *Scientific Reports*, **4**, 3577, DOI: 10.1038/srep03577, 1-8. (c) Q. Xuefeng, L. Yadong, X. Yi and Q. Yitai, *Materials Chemistry and Physics*, 2000, **66**, 97–99. (d) L. Wang, Y. Zhu, H. Li, Q. Li and Y. Qian, *Journal of Solid State Chemistry*, 2010, **183**, 223–227.
105. (a) W. Zhou, X. Cao, Z. Zeng, W. Shi, Y. Zhu, Q. Yan, H. Liu, J. Wang and H. Zhang, *Energy Environ. Sci.*, 2013, **6**, 2216–2221. (b) P. A. Metcalf, P. Fanwick, Z. Kakol and J. M. Honig, *Journal of Solid State Chemistry*, 1993, **104**, 81-87. (c) J. Zhu, Y. Li, S. Kang, X-L. Wei and P. K. Shen, *J. Mater. Chem. A*, 2014, **2**, 3142–3147. (d) B. Zhang, X. Ye, W. Dai, W. Hou and Y. Xie, *Chem. Eur. J.*, 2006, **12**, 2337 – 2342.
106. X. Chen, Z. Wang, X. Wang, J. Wan, J. Liu and Y. Qian, *Chemistry Letters*, 2004, **33**, 10, 1294-1295.
107. (a) Y. Ruan, C. Wang and J. Jiang, *J. Mater. Chem. A*, 2016, **4**, 14509–14538. (b) T. Zhu, Z. Wang, S. Ding, J. S. Chen and X. Wen (David) Lou, *RSC Advances*, 2011, **1**, 397–400. (c) Z. Li, J. Han, L. Fan and R. Guo, *CrystEngComm*, 2015, **17**, 1952–1958. (b) F. Cao, R. Liu, L. Zhou, S. Song,

- Y. Q. Lei, W. D. Shi, F. Zhao and H. Zhang, *J. Mater. Chem.*, 2010, **20**, 1078–1085. (c) J-Z. Wang, S-L. Chou, S-Y. Chew, J-Z. Sun, M. Forsyth, D. R. MacFarlane and H-K. Liu, *Solid State Ionics*, 2008, **179**, 2379–2382.
108. N. J. Freymeyer, P. D. Cunningham, E. C. Jones, B. J. Golden, A. M. Wilttrout and K. E. Plass, *Cryst. Growth Des*, 2013, **13**, 4059–4065.
109. (a) M. Basu, A. K. Sinha, M. Pradhan, S. Sarkar, Y. Negishi and T. Pal, *Environ. Sci. Technol.*, 2010, **44**, 6313–6318. (b) J. Zhang, J. Yu, Y. Zhang, Q. Li and J. R. Gong, *Nano Lett.*, 2011, **11**, 4774–4779. (c) J. Liu and D. Xue, *J. Mater. Chem.*, 2011, **21**, 223–228. (d) G. Ku, M. Zhou, S. Song, Q. Huang, J. Hazle and C. Li, *ACS Nano*, 2012, **6**, 7489–7496. (e) S. Ramadan, L. Guo, Y. Li, B. Yan and W. Lu, *Small*, 2012, **8**, 3143–3150. (f) Y. Chen, C. Davoisne, J-M. Tarascon and C. Guery, *J. Mater. Chem.*, 2012, **22**, 5295–5299. (g) M. V. Ngo, S. D. Lopatin, S. K. Pangrle, N. H. Tripasa and H. T. Pham, *U.S. Patent*, **6,746**, 971 B1, June 8, 2004.
110. (a) A. Ghezelbash, M. B. Sigman, Jr., and B. A. Korgel, *Nano Lett.*, 2004, **4**, 537–542. (b) A. Ghezelbash and B. A. Korgel, *Langmuir*, 2005, **21**, 9451–9456. (c) R. D. Tilley and D. A. Jefferson, *J. Phys. Chem. B*, 2002, **106**, 10895–10901. (d) L. Zhang, J. C. Yu, M. Mo, L. Wu, Q. Li and K. W. Kwong, *J. Am. Chem. Soc.*, 2004, **126**, 8116–8117. (e) B. X. Jiang, Y. Xie, J. Lu, L. Zhu, W. He and Y. Qian, *Adv. Mater.*, 2001, **13**, 1278–1281. (f) A. Olivas, J. Cruz-Reyes, V. Petranovskii, M. Avalos and S. Fuentes, *J. Vac. Sci. Technol. A*, 1998, **16**, 3515–3520. (g) Y. Zhang, W. Sun, X. Rui, B. Li, H. T. Tan, G. Guo, S. Madhavi, Y. Zong and Q. Yan, *Small*, 2015, **11**, 3694–3702. (h) C. Jiang, Z. Shang and X. Liang, *ACS Catal.*, 2015, **5**, 4814–4818.
111. C. Gervas, S. Mlowe, M. P. Akerman, I. Ezekiel, T. Moyo and N. Revaprasadu, *Polyhedron*, 2017, **122**, 16–24.
112. S-N. Masoud, F. Davar and M. Mazaheri, *Materials Research Bulletin*, 2009, **44**, 2246–2251.
113. F. Cao, R. Liu, L. Zhou, S. Y. Song, Y. Q. Lei, W. D. Shi, F. Zhao and H. Zhang, *J. Mater. Chem.*, 2010, **20**, 1078–1085.

Introduction

114. (a) Y-H. Yang and Y-T. Chen, *J. Phys. Chem. B*, 2006, **110**, 17370-17374. (b) H. Zhong, Y. Li, M. Ye, Z. Zhu, Y. Zhou, C. Yang and Y. Li, *Nanotechnology*, 2007, **18**, 025602-025608. (c) P. M. Allen and M. G. Bawendi, *J. Am. Chem. Soc.*, 2008, **130**, 9240-9241. (d) H. Zhong, S. S. Lo, T. Mirkovic, Y. Li, Y. Ding, Y. Li and G. D. Scholes, *ACS Nano*, 2010, **9**, 5253-5262. (e) Q. Guo, S. J. Kim, M. Kar, W. N. Shafarman, R. W. Birkmire, E. A. Stach, R. Agrawal and H. W. Hillhouse, *Nano Lett.*, 2008, **8**, 2982-2987. (f) M. G. Panthani, V. Akhavan, B. Goodfellow, J. P. Schmidtke, L. Dunn, A. Dodabalapur, P. F. Barbara and B. A. Korgel, *J. Am. Chem. Soc.*, 2008, **130**, 16770-16777. (g) J. Tang, S. Hinds, S. O. Kelley and E. H. Sargent, *Chem. Mater.*, 2008, **20**, 6906-6910.
115. (a) J. Xu, X. Yang, T-L. Wong and C-S. Lee, *Nanoscale*, 2012, **4**, 6537-6542. (b) C. Wu, Z. Hu, C. Wang, H. Sheng, J. Yang and Y. Xie *Appl. Phys. Lett.* 2007, **91**, 143104-143107. (c) L. Zheng, Y. Xu, Y. Song, C. Wu, M. Zhang and Y. Xie, *Inorg. Chem*, 2009, **48**, 4003-4009. (d) P. A. Fernandes, P. M. P. Salome and A. F. Cunha, *J. Phys D: Appl Phys*, 2010, **43**, 215403-215414. (e) B. Qu, M. Zhang, D. Lei, Y. Zeng, Y. Chen, L. Chen, Q. Li, Y. Wang and T. Wang, *Nanoscale*, 2011, **3**, 3646-3651. (f) M. E. Norako, M. J. Greaney and R. L. J. Brutchey, *J. Am. Chem. Soc.*, 2012, **134**, 23-26.
116. (a) Y. Xiong, Y. Xie, G. Du and H. Su, *Inorg. Chem.* 2002, **41**, 2953-2959. (b) S. Okano, S. Takeshita and T. Isobe, *Mater. Lett.* 2015, **145**, 79-82. (c) J. Chang and E. R. Waclawik, *Chem. Eng. Commun.*, 2013, **15**, 5612-5619. (d) B. Li, Y. Xie, J. Huang and Y. Qian, *J. Solid State Chem.* 2000, **153**, 170-173.
117. (a) D. Pan, X. Wang, Z. H. Zhou, W. Chen, C. Xu and Y. Lu, *Chem. Mater.*, 2009, **21**, 2489-2493. (b) Y-H. A. Wang, X. Zhang, N. Bao, B. Lin, and A. Gupta, *J. Am. Chem. Soc.*, 2011, **133**, 11072-11075. (c) M-Y Chiang, S-H. Chang, C-Y. Chen, F-W. Yuan and H-Y. Tuan, *J. Phys. Chem. C*, 2011, **115**, 1592-1599.

118. M. G. Panthani, V. Akhavan, B. Goodfellow, J. P. Schmidtke, L. Dunn, A. Dodabalapur, P. F. Barbara and B. A. Korgel, *J. Am. Chem. Soc.*, 2008, **130**, 16770–16777.
119. S. Dias, K. Kumawat, S. Biswas and S. B. Krupanidhi, *Inorg. Chem.*, 2017, **56**, 2198–2203.
120. J. Xu, X. Yang, T-L. Wong and C-S. Lee, *Nanoscale*, 2012, **4**, 6537–6542.
121. Q. Liu, Z. Zhao, Y. Lin, P. Guo, S. Li, D. Pan and X. Ji, *Chem. Commun.*, 2011, **47**, 964–966.
122. (a) K. Aso, H. Kitauro, A. Hayashi and M. Tatsumisago, *J. Mater. Chem.*, 2011, **21**, 2987–2990. (b) G. Shen, D. Chen, K. Tang, C. An, Q. Yang and Y. Qian, *Journal of Solid State Chemistry*, 2003, **173**, 227–231.
123. (a) C. Graf, S. Dembski, A. Hofmann and E. Ruhl, *Langmuir*, 2006, **22**, 5604–5610. (b) P. Bao, C. Zhong, D. M. Vu, J. P. Temirov, R. B. Dyer and J. S. Martinez, *J. Phys. Chem. C*, 2007, **111**, 12194–12198. (c) A. Kairdolf, M. C. Mancini, A. M. Smith and S. M. Nie, *Anal. Chem.*, 2008, **80**, 3029–3034.
124. (a) G. Schmid and A. Lehnert, *Angew. Chem. Int. Ed. Engl.*, 1989, **28**, 780–781. (b) W. W. Weare, S.M. Reed, M.G. Warner and J. E. Hutchinson, *J. Am. Chem. Soc.*, 2000, **122**, 12890–12891. (c) L. R. Becerra, C. B. Murray, R. G. Griffin and M. G. Bawendi, *J. Chem. Phys.*, 1994, **100**, 3297–3300. (d) M. Green, *J. Mater. Chem.*, 2010, **20**, 5797–5809.
125. R. Nagarajan and T. A. Hatton, NPs: Synthesis, Stabilization and Functionalization, *ACS Symposium Series*, **2008**.
126. (a) A. Chastellain, A. Petri and H. Hofmann, *J. Colloid Interface Sci.*, 2004, **278**, 353–360. (b) C. P. Shah, M. Kumar and P. N. Bajaj, *Nanotechnology*, 2007, **18**, 385607–385613.
127. (a) C. B. Murray, D. J. Norris and M. G. Bawendi, *J. Am. Chem. Soc.* 1993, **115**, 8706–8715. (b) A. A. Guzelian, J. E. B. Katari, A. V. Kadavanich, U. Banin, K. Hamad, E. Juban, A. P. Alivisatos, R. H. Wolters, C. C. Arnold and J. R. Heath, *J. Phys. Chem.*, 1996, **100**, 7212–7219. (c) M. L. Steigerwald, A. P. Alivisatos, J. M. Gibson, T. D. Harris, R. Kortan, A. J. Muller, A. M. Thayer, T. M. Duncan, D. C. Douglass and L. E. Brus, *J. Am. Chem. Soc.*,

Introduction

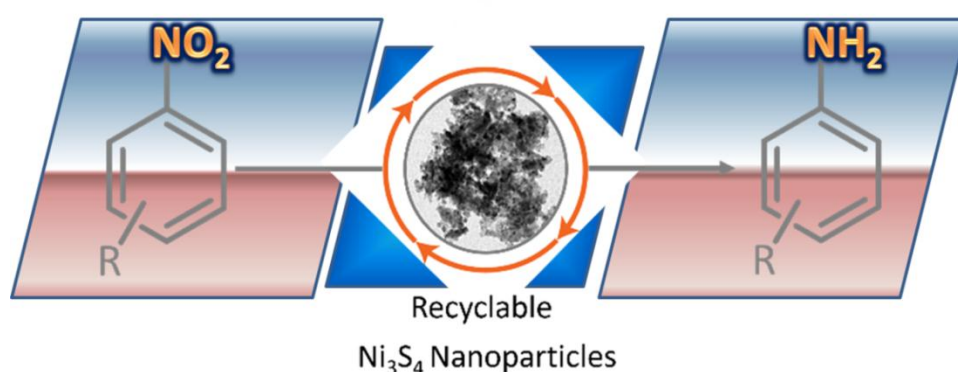
1988, **110**, 3046-3050. (d) T. Vossmeier, L. Katsikas, M. Giersig, I. G. Popovic, K. Diesner, A. Chemseddine, A. Eychmueller and H. Weller, *J. Phys. Chem.*, 1994, **98**, 7665-7673. (e) C. B. Murray, C. R. Kagan and M. G. Bawendi, *Annu. Rev. Mater. Sci.*, 2000, **30**, 545-610. (f) V. F. Puntès, K. M. Krishnan and A. P. Alivisatos, *Science*, 2001, **291**, 2115-2117. (g) L. Qu, Z. A. Peng and X. Peng, *Nano Lett.* 2001, **1**, 333-337. h) Z. A. Peng and X. Peng, *J. Am. Chem. Soc.*, 2002, **124**, 3343-3353. (i) C. L. Carnes, J. Stipp and K. J. Klabunde, *Langmuir*, 2002, **18**, 1352-1359. (j) Y. Sun and Y. Xia, *Science*, 2002, **298**, 2176-2179. k) X. Peng, L. Manna, W. Yang, J. Wickham, E. Scher, A. Kadavanich and A. P. Alivisatos, *Nature*, 2004, **404**, 59-61. (l) J. Tang, F. Red, Y. Zhu, T. Siegrist, L. E. Brus and M. L. Steigerwald, *Nano Lett.* 2005, **5**, 543-548. (m) C. N. R. Rao, A. Govindaraj and S. R. C. Vivekchand, *Annu. Rep. Prog. Chem.* 2006, **102**, 20-45. (n) J. Park, J. Joo, S. G. Kwon, Y. Jang and T. Hyeon, *Angew. Chem., Int. Ed.* 2007, **46**, 4630-4660. (o) W-K. Koh, A. C. Bartnik, F. W. Wise and C. B. Murray, *J. Am. Chem. Soc.*, 2010, **132**, 3909-3913. (p) S. R. Ghanta and K. Muralidharan, *Nanoscale*, 2010, **2**, 976-980. (q) M. Afzaal, M. Malik and P. O'Brien, *J. Mater. Chem.*, 2010, **20**, 4031-4040. (r) A. Abdelhady, M. Afzaal, M. Malik and P. O'Brien, *J. Mater. Chem.*, 2011, **21**, 18768-18775. (s) A. L. Abdelhady, K. Ramasamy, M. A. Malik, P. O'Brien, S. J. Haigh and J. Raftery, *J. Mater. Chem.*, 2011, **21**, 17888-17895. t) S. Malik, S. Mahboob, N. Haider, M. Malik and P. O'Brien, *Nanoscale*, 2011, **3**, 5132-5139. (u) Z. A. Peng and X. Peng, *J. Am. Chem. Soc.*, 2002, **124**, 3343-3353. (v) F. X. Redl, K. S. Cho, C. B. Murray and S. O'Brien, *Nature*, 2003, **423**, 968-971. (w) W. Wang, Y. Geng, P. Yan, F. Liu, Y. Xie and Y. Qian, *J. Am. Chem. Soc.*, 1999, **121**, 4062-4063. (x) L. Qu, Z. A. Peng and X. Peng, *Nano Lett.*, 2001, **1**, 333-337.

Chapter 2

Recyclable Ni_3S_4 nanocatalyst for hydrogenation of nitroarenes

Abstract

In this chapter, the synthesis of surface clean nanoparticles (NPs) of Ni_3S_4 , which is rare phase of nickel sulphides and its catalytic activity are discussed. NPs were synthesized in a single step via hexamethyldisilazane (HMDS)-assisted method using NiCl_2 and thiourea as starting materials. This synthetic method yielded phase pure, spherical Ni_3S_4 NPs of mean size $17 (\pm 4)$ nm having clean surfaces. The NPs were characterized thoroughly by PXRD, FTIR, EDAX, and TEM analyses. The catalytic behaviour of these particles was assessed by using it as a catalyst in the reduction reaction of aromatic nitro groups. The Ni_3S_4 NPs behaved as a versatile catalyst for the nitro hydrogenation of both activated and deactivated nitrobenzenes using hydrazine as a hydrogen source to yield corresponding amines in high yield ($\sim 90\%$). The heterogeneous catalyst, Ni_3S_4 NPs was recycled more than ten times without any change its activity. The enhanced catalytic activity of these Ni_3S_4 NPs was ascribed to their clean surfaces without any surfactant molecules around them.



Chapter 2

2.1. Introduction

NPs are the innovative class of catalytic materials having surface dependent catalytic properties [1-6]. Compared with the bulk materials, the high surface to volume ratio of NPs promotes the catalytic activity. Though, stabilizing or surfactant molecules cover the surfaces of NPs (Section 1.4). However, as mentioned in the Section 1.2, the presence of these undesired capping agents hinders the chances of harnessing benefits of surface-dependent properties to their full potential [7-11]. Hence, to enhance the catalytic activity, the capping agent might be removed from the surfaces of NPs. On the other hand, many successful nanocatalysts used in organic synthesis were prepared by elegant and intricate designs.

Nickel sulphide exists in various stoichiometries such as NiS, NiS₂, Ni₃S₂, Ni₆S₅, Ni₇S₆, Ni₃S₄, and Ni₉S₈. There are several efforts to synthesize nickel chalcogenides NPs [12-19], but many of them resulted in the formation mixture of sulphides. However, the challenge is to produce rare Ni₃S₄ phase in a simple bottom-up synthesis selectively. Since the formation of Ni₃S₄ is rare during the synthesis of nickel sulphides, and there is no commercial source available, many of its properties including the catalytic behaviour of Ni₃S₄ NPs are unexplored.

Aromatic nitro hydrogenation is an important process in academia, industry, and nature [20-22] because of the widespread occurrence of the nitro group in the natural products and biologically active molecules. Therefore, many catalyst were utilized in the hydrogenation. Some of the catalysts are Pt/carbon nanofibers, Fe₂O₃/Au, Fe(BF₄)₂, Fe₃O₄, Rh₃Ni, Fe, Co, Rh, Ni, Pd, Pt, Cu, Ag, Au, and Zn [23-35]. Though various catalysts are available for hydrogenation of nitroarenes, the performance of many of them still needs improvement. Also, some of the available reports did not mention TOF, which needed for complete understanding the catalytic performance.

Always there is a need for simplified method to produce catalyst, enhanced catalytic activity, recyclability of the heterogeneous catalyst, and versatility to use for various reactions. Many literatures indicated that the NPs as catalysts can be easily separated and recycled with retention of catalytic activity compared to their

bulk counterparts [36-39]. In the past years, many hierarchical nanostructures have been used in catalysis. However, the dearth of simplicity in the production of nanocatalyst compared with conventional bulk catalyst is a major hurdle for their use in catalysis.

It was well acknowledged that a high specific surface area was constructive for increasing the active sites. However, if the surfactant molecules block the active sites, the catalyst would show less activity than its potential. Therefore, in pursuit of finding a simple procedure for the synthesis of NPs, we have developed a novel HMDS-assisted method to produce NPs having clean surfaces. In this chapter, we have demonstrated a selective synthesis of Ni₃S₄ phase of nickel sulphide as NPs and their catalytic activity in hydrogenation of nitroarenes.

2.2. Experimental section

2.2.1. Materials

The chemicals used in the syntheses, NiCl₂, thiourea and hexamethyldisilazane [HN(SiMe₃)₂] (HMDS) were purchased from sigma-Aldrich and used without further purification. All solvents were purified using standard procedures.

2.2.2. Synthesis of nickel sulphide nanoparticles

In a typical procedure (Scheme 2.1), nickel chloride (0.2 g, 1.5 mmol) was reacted with thiourea (0.15 g, 2.0 mmol) and excess of 1,1,1,3,3,3-hexamethyldisilazane [HN(SiMe₃)₂] (HMDS) at 130 °C in a 50 mL round bottom flask equipped with a magnetic stirring bar and a condenser. The product started forming within 15 min but to complete the formation of Ni₃S₄ NPs; the reaction was continued up to 3 h. The colour of the reaction mixture was changing steadily from orange to black indicating the formation of nickel nanostructures. Unreacted HMDS and volatile side products were removed by applying high vacuum. The remnant was repeatedly washed with ethanol and acetone (10 ml × 3) to remove unreacted NiCl₂ and thiourea. The resultant nickel sulphide NPs were dried in a vacuum oven at a temperature of 120 °C for 4 h to remove the absorbed water or methanol for

Chapter 2

subsequent characterizations. The yield of the reaction was 80%. Throughout the reactions, inert conditions were maintained using Schlenk line technique.

2.2.3. Hydrogenation of the nitroarenes

In a typical reaction, nitroarenes (6 mmol), NH_2NH_2 (48 mmol), Ni_3S_4 (1 mol%, as catalysts) and ethanol (10 mL) were added into a 50 ml two neck round bottom flask equipped with a reflux condenser, where the second neck was closed after adding the compounds. The reaction mixture was stirred under atmospheric pressure at 125 °C. Progress of the reaction was monitored by a TLC, while the final products were confirmed by NMR spectral data (Figure. S1- S10). Turnover number (TON) of the catalyst was calculated by the ratio of moles of product and catalyst. $\text{TON} = \text{No of moles of product} / \text{No of moles of catalyst}$. Turnover frequency (TOF) was calculated from the ratio of TON and time (min).

2.2.4. Instruments and sample preparation

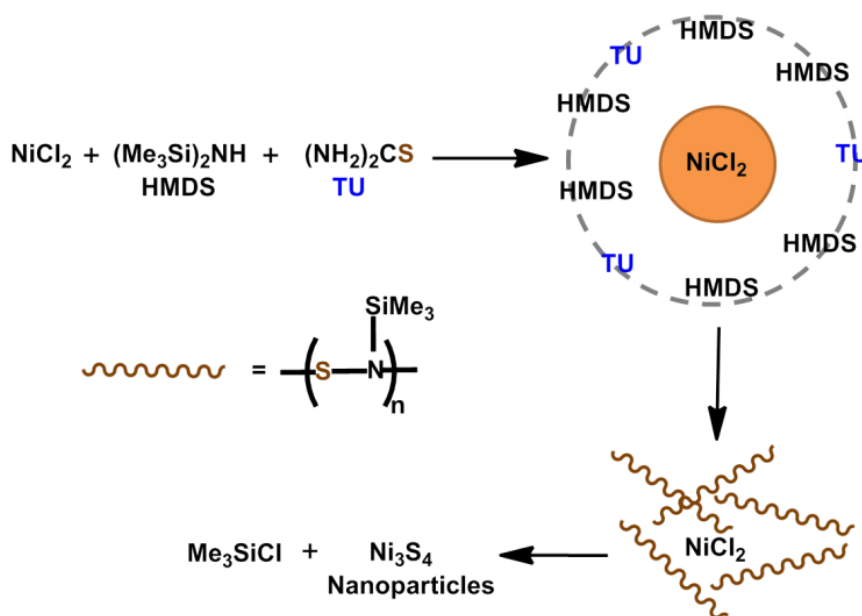
Powder X-ray diffraction (PXRD) patterns of obtained Ni_3S_4 nanocatalyst were recorded on a Bruker D8 X-ray diffractometer [λ (Cu- $\text{K}\alpha$) = 1.54 Å], employing a scan rate of 1° min^{-1} for the range of 20 to 80° . Field emission-scanning electron microscopy (FESEM) images and energy-dispersive X-ray spectroscopy (EDAX) were recorded using Ultra 55 Carl Zeiss instrument) operated at variable voltages. The NPs were dissolved in isopropanol and then dispersed on ITO plates to obtain FESEM micrographs. TEM images were acquired by using an FEI Technai G2 20 STEM instrument at an acceleration voltage of 200 kV. The NPs used for TEM measurements were dispersed in isopropanol and 1-2 drops of dispersion were dripped onto a carbon-coated copper grid (200 mesh). IR spectra were recorded with an Alpha FTIR spectrometer. The FTIR spectra of Ni_3S_4 nanocatalysts were subtracted from the spectrum of the substrate. The NMR spectra of compounds were obtained using a Bruker Avance 400 MHz FT-NMR spectrometer at room temperature with CDCl_3 as a solvent. The data are reported in parts per million (δ) with reference to tetramethylsilane. Chemical composition was analysed using a Varian Model Liberty Series Inductively Coupled Plasma-Optical Emission Spectrometer (ICP-OES) by dissolving the samples in nitric acid. Surface area and

pore size analysis were determined from the BET studies, which analyses were recorded by the Quantachrome instruments.

2.3. Results and discussion

2.3.1. Synthesis of Ni₃S₄ Nanocatalyst

We have demonstrated a novel HMDS-assisted method of synthesis of Ni₃S₄ nanocatalysts. The reaction shown in the Scheme 2.1 yielded phase pure Ni₃S₄ NPs at the reflux temperature (130 °C) without mixing of any other stoichiometric products. As a replacement to the organometallic precursors, we used simple starting materials to prepare the Ni₃S₄ NPs (nickel (II) chloride and thiourea). Synthesis at low temperature was possible because of the activation of metal by HMDS. Driving force of the reaction was the ability of HMDS to function as a capping agent, stabilizing surfactant molecule and solvent. During the reaction, two large trimethylsilyl groups of HMDS behaved as a surfactant and prevented the growth of Ni₃S₄ NPs while the lone pair of electrons on nitrogen atom effectively passivated the surface of NPs. Unreacted HMDS was removed from the surfaces of particles by high vacuum since it was a low boiling organic compound.



Scheme 2.1. Schematic representation of sequence of the reaction for nickel sulphide (Ni₃S₄) nanoparticles synthesis.

Chapter 2

In many reactions involving sulphur and nitrogen, albeit yielding the pure products, there is an ambiguity on the nature of intermediate steps. However, we have established the activation of HMDS-assisted syntheses of metal chalcogenides through the formation of an S-N intermediate, which was formed by the reaction of HMDS with sulphur [40- 42]. In the present study, thiourea has been used as a sulphide source instead of elemental sulphur due to its solubility at room temperature. Many reactions in organic and inorganic syntheses, thiourea has been used as a source of sulphide (S^{2-}). Similarly, it might have interacted with the HMDS and formed a similar S-N intermediate. This intermediate subsequently reacted with nickel chloride forming nickel sulphide and in turn released trimethylsilyl chloride as a side product [40-44]. The sequence of the reaction is shown in the Scheme 2.1.

Table 2.1: Controlled reactions for Ni_3S_4 nanoparticles synthesis

NO.	Reactions	Product
1.	$NiCl_2$ + Thiourea + Toluene	No reaction
2.	Thiourea + HMDS	S-N Intermediate
3.	$NiCl_2$ + Thiourea + HMDS	Ni_3S_4 nanoparticles

To confirm the sequence of reactions, we performed a few control reactions, which are shown in the Table 2.1. In our optimized reaction condition, there was no reaction between nickel chloride and thiourea in toluene. However, thiourea reacted with HMDS (reaction 2, Table 2.1) yielding a compound, which is similar to the one obtained in the reaction of S and HMDS. This observation was confirmed from the time dependent ^{29}Si NMR spectra (Figure. 2.1) of samples withdrawn from the reaction. The observed small multiplet peak around δ_{Si} 6.6 ppm corresponds to the probable S-N intermediate envisaged in the reaction S and HMDS (HMDS: δ_{Si} 2.3 ppm). After successfully synthesized and characterized Ni_3S_4 NPs we have studied the catalytic activity of as synthesized NPs for the hydrogenation of nitroarenes.

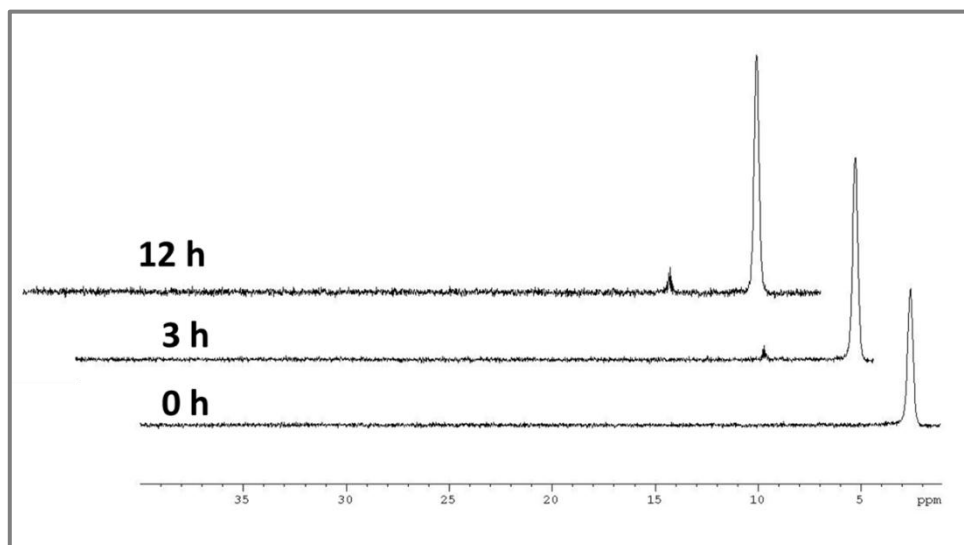


Figure 2.1. ^{29}Si NMR studies of the reaction mixture at different time intervals (HMDS δ_{Si} 2.3 ppm and intermediate δ_{Si} 6.6 ppm).

2.3.2. Characterization of Ni_3S_4 nanomaterial

The crystal structure and phase purity of just synthesized Ni_3S_4 NPs were established by powder X-ray diffraction studies (Figure. 2.2). The intensity and position of diffraction lines of NPs matched with the standard pattern of the cubical phase of Ni_3S_4 (JCPDS # 76-1813). There were no undesirable or additional peaks related to other phases of nickel sulphide. Clear PXRD pattern obtained signified the selectivity of the synthetic method. Further, any variation in the stoichiometry of reaction did not change the selectivity of nickel sulphide formation. Phase selectivity of the present method was further probed by a time-dependent PXRD study (Figure. 2.3). During the synthesis, NPs were isolated periodically, purified and analysed by PXRD. In the PXRD patterns, there was no signature of any other stoichiometry at any stage of the reaction. Thus, the time-dependent PXRD study supports the selective formation of Ni_3S_4 in the reaction from the beginning. EDAX spectra (Figure. 2.4) of the product obtained in our reactions showed no signature of starting materials (absence of chloride and silicon), while the atomic ratio was matching with Ni_3S_4 (Ni:S = 3:4) only. Hence, the HMDS- assisted method was phase specific and yielded only Ni_3S_4 NPs.

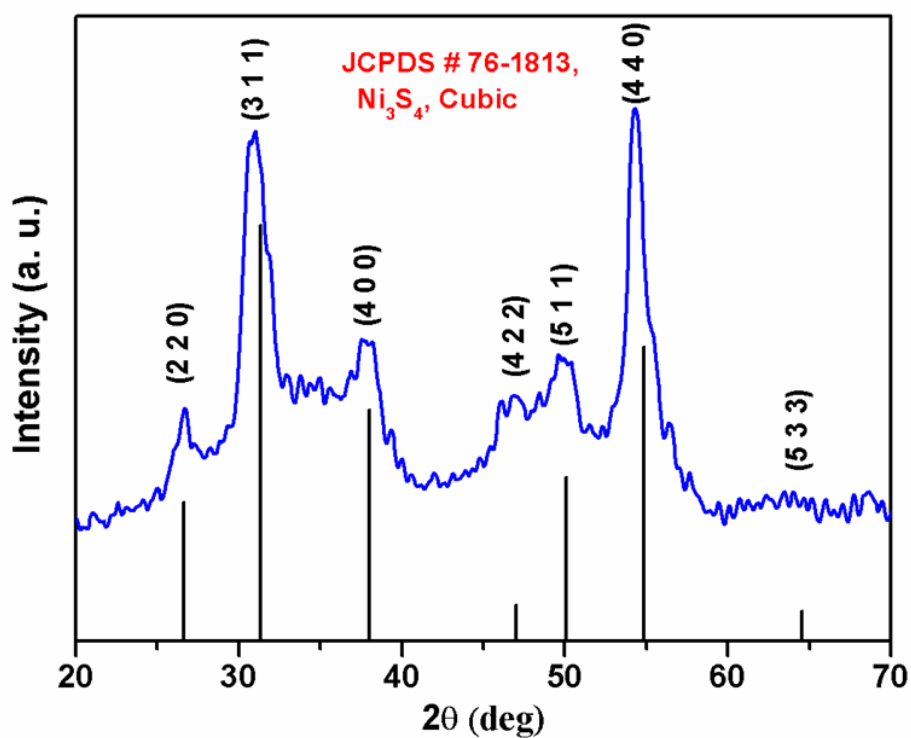


Figure 2.2. PXRD pattern of as synthesized Ni_3S_4 nanoparticles

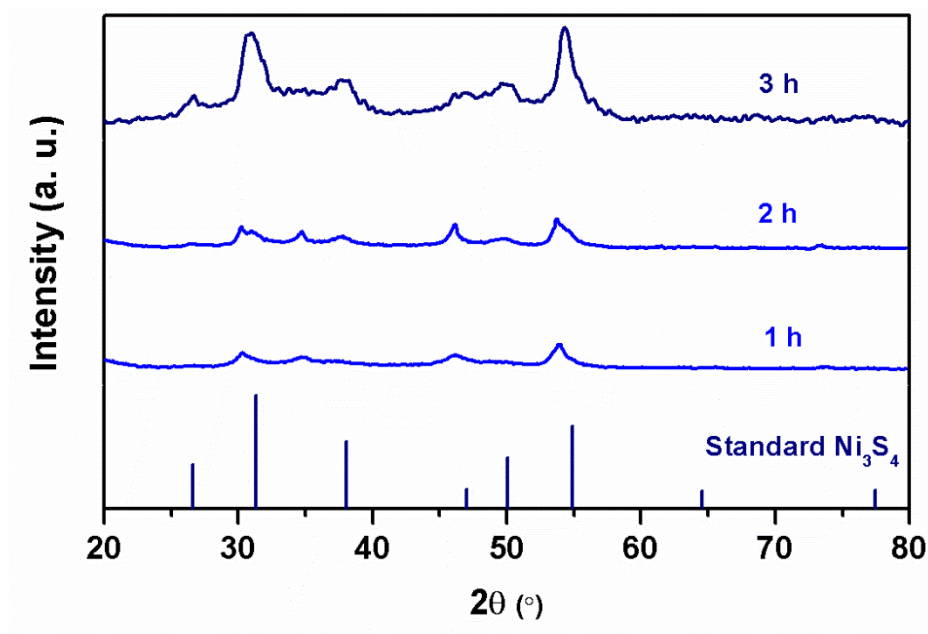


Figure. 2.3. Time dependent PXRD patterns of nanoparticles during the synthesis. The Ni_3S_4 phase selectivity was achieved from the initial stage of synthesis.

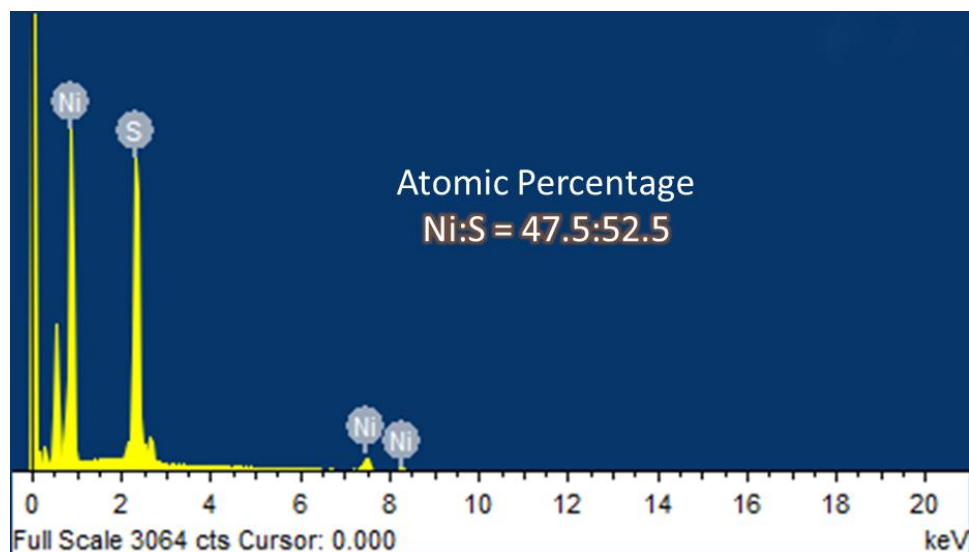


Figure 2.4. EDAX spectrum of as synthesized Ni_3S_4 nanoparticles

2.3.3. Microscopic investigation of Ni_3S_4 nanoparticles

TEM micrographs showed the aggregated spherical NPs having (Figure. 2.5) diameter of 8-29 nm and an average size of 17 ± 4 nm (Figure. 2.6). HRTEM micrographs showed the lattice spacing of 2.8 Å and 1.6 Å, which was corresponding to the inter-spacing of (3 1 1) and (4 4 0) planes of the standard pattern (Figure. 2.7). These planes were matching with the principal planes observed in the PXRD pattern of Ni_3S_4 NPs. A thorough analysis of surface by HRTEM (Figure. 2.7) showed no amorphous boundaries (signature of HMDS) on the surface of NPs indicating the complete removal of capping agents. Selected area diffraction showed a clear dotted pattern with (3 1 1) planes as dominating, which was indicative of the single-crystalline nature of Ni_3S_4 NPs (Figure. 2.7c). The SAED observations were consistent with the PXRD pattern of Ni_3S_4 NPs. FTIR spectrum did not have any signal of amine or alkane (HMDS) confirming the absence of capping agent on the surface (Figure. 2.8). Similarly, we did not observe the signal of silicon (HMDS) (Figure. 2.4) in the EDAX spectra. We obtained an ICP data and found no element other than Ni and S in our product. In summary, data from HRTEM, SAED, EDAX, ICP and FTIR analyses confirmed the capping agent free surfaces of NPs (Figure. 2.7 and 2.8).

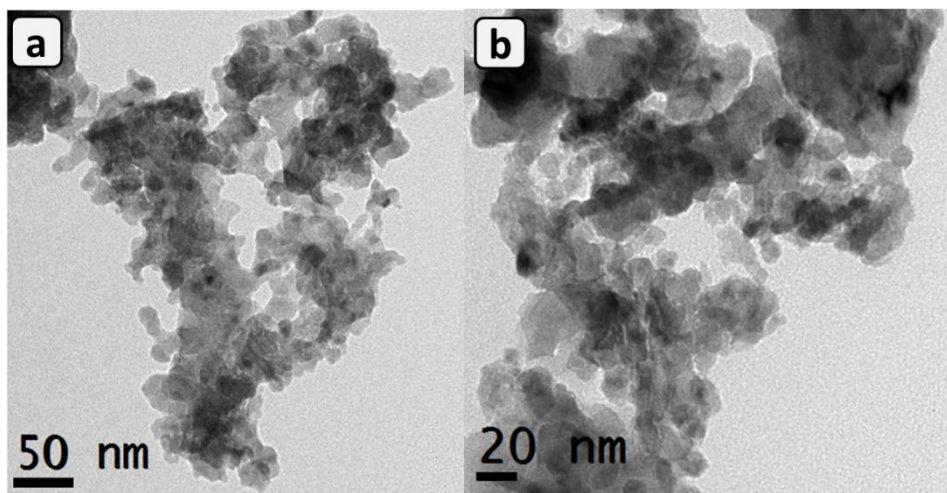


Figure 2.5. (a) and (b) are TEM micrographs of as synthesized Ni_3S_4 nanoparticles. Particles were well dispersed for effective catalytic activity.

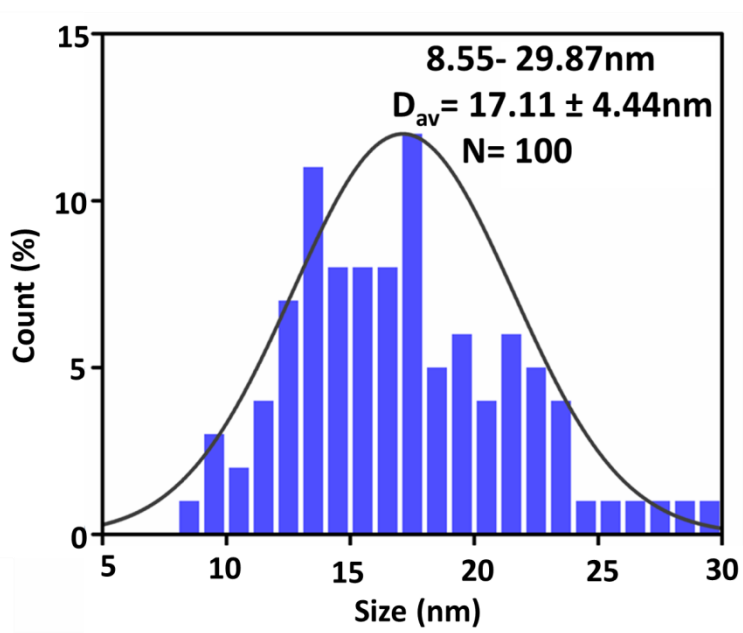


Figure 2.6. Particles distribution diagram from the TEM micrographs. Particles were mono dispersed with the average size of 17 ± 4 nm.

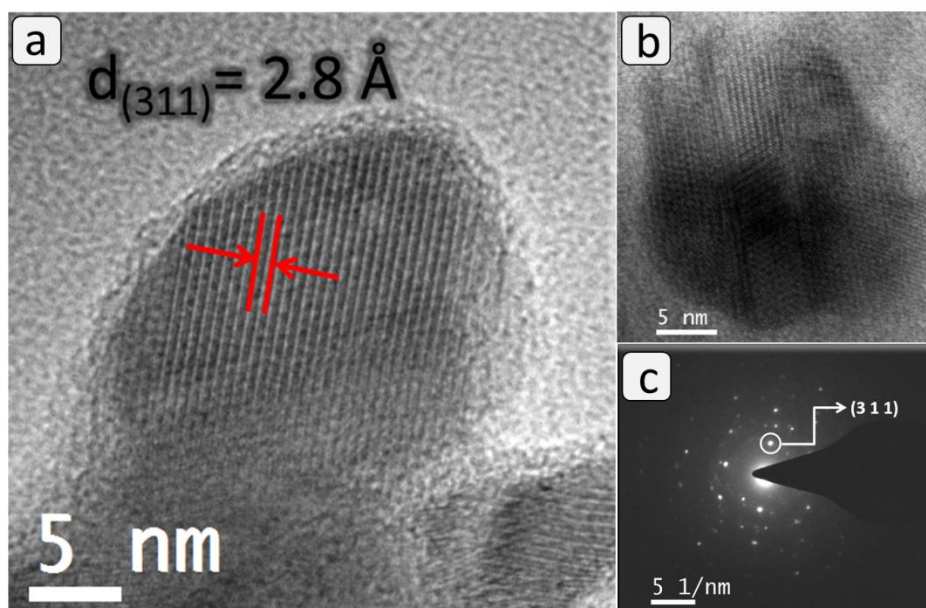


Figure 2.7. Surface characterization of the Ni_3S_4 nanocatalyst: (a) HRTEM micrograph of the nanoparticles. Particles were crystalline and dominant planes matched with PXRD pattern. (b) Individual nanoparticle (c) Selected area diffraction of the nanoparticles. Dominant plane is indicated by the circle which is complemented with the PXRD pattern. Dotted pattern represents the crystalline nature of the nanoparticles.

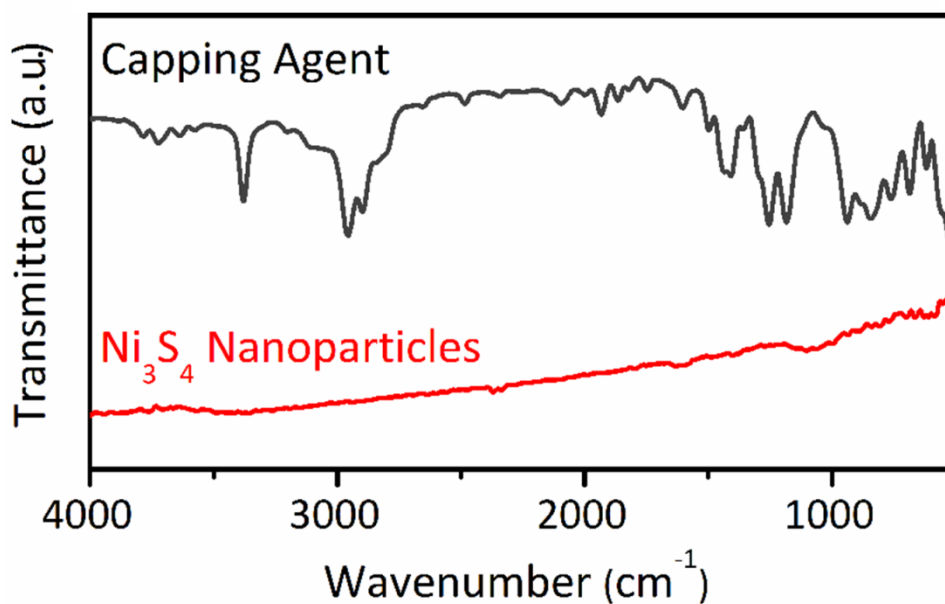
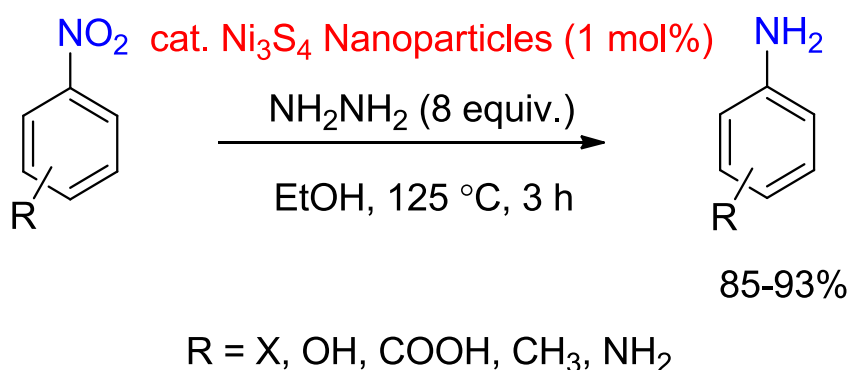


Figure 2.8. FTIR spectra of the Ni_3S_4 nanoparticles. Since there was no signal of the amine (HMDS), capping agent was completely removed from the surfaces.

Chapter 2

2.3.4. Ni₃S₄ nanoparticles as the catalyst

Since nickel sulphide obtained in our reaction had clean surfaces; we assessed the catalytic activity of Ni₃S₄ NPs using it as a catalyst in the reaction of hydrogenation of nitrobenzene (Table 2.2). The reduction of aromatic amines was chosen because of its important in the total synthesis of many organic molecules [22]. The Ni₃S₄ NPs displayed a remarkable catalytic activity towards the hydrogenation of nitrobenzene to aminobenzene under optimal conditions (Table 2.2). Reduction reactions were performed efficiently using 1 mol% of Ni₃S₄ NPs in ethanol using hydrazine as a hydrogen source. It was observed that under the optimized condition, 8 equivalents of hydrazine hydride was required to complete the reaction [19]. The maximum yield achieved under the optimized conditions was 88% with TOF of 111 min⁻¹.



Scheme 2.2. Reduction of the nitroarenes using the Ni₃S₄ nanoparticles as catalyst.

In control reactions, the hydrogenation of aminobenzene did not proceed either in the absence of Ni₃S₄ NPs or hydrazine in the reaction (Figure. 2.9). This observation confirmed the need for both these compounds to complete the reaction. The versatility of the catalyst was examined further in the reduction of substituted nitrobenzenes (O₂NC₂H₄R; R = X, CH₃, NH₂, COOH, OH) under optimized reaction condition, which is shown in the Scheme 2.2. The reactions successfully yielded corresponding aminobenzenes with high yields (85-93%). The products were confirmed by NMR spectral data (Figure. S1- S10). Various catalytic systems were used for the reduction of nitrobenzenes [23-35]. Few reports demonstrated the catalytic activity of different forms of nickel sulphides (except Ni₃S₄ phase) (Table 2.3). However, the present work is an elaborate study on catalytic activity of Ni₃S₄,

which showed the excellent result with high TOF and yield [41-43]. Thus, the study showed the effectiveness of Ni_3S_4 NPs as a catalyst towards the hydrogenation of various substituted nitrobenzenes.

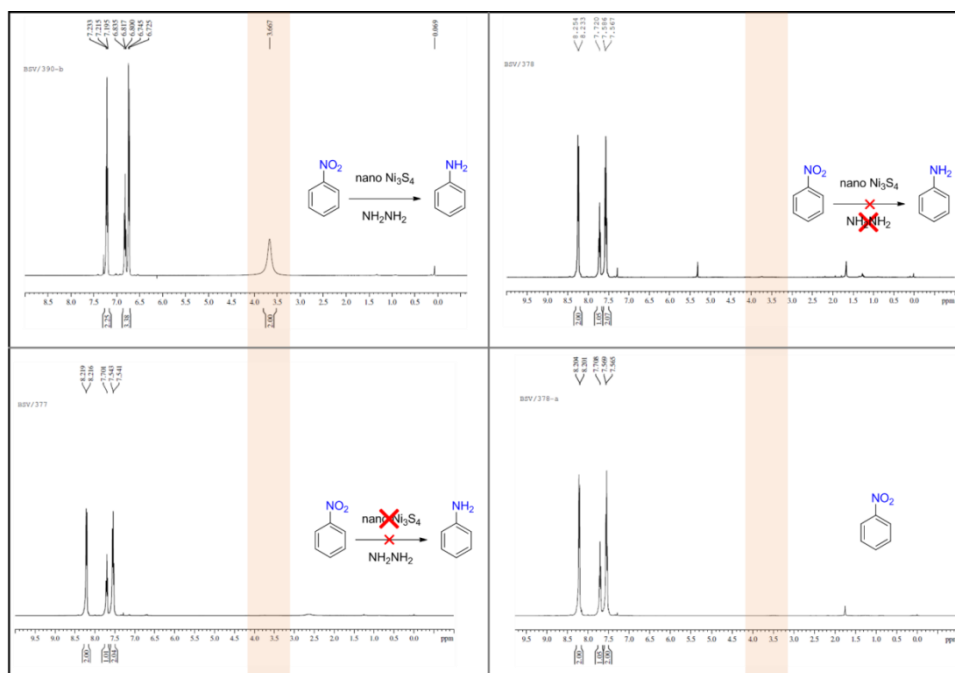
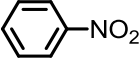
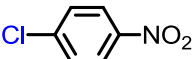
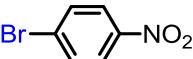
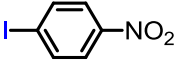


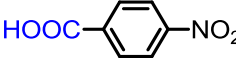

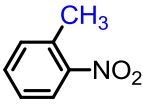
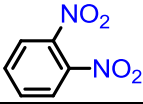


Figure 2.9. Controlled reaction to prove catalytic activity of Ni_3S_4 nanoparticles. Catalysis occurred only in presence of both Ni_3S_4 and hydrazine in the reaction.

Chapter 2

Table 2.2: Results of nickel sulphide catalyzed reduction of nitrobenzenes

Entry	Substrate	TOF(min ⁻¹)	Yield(%)
1		113	88
2		112	89
3		115	91
4		113	90
5		108	85
6		118	93
7		110	87
8		114	90
9		111	88
10		112	89

All the reactions were carried out under the optimal conditions. Reactant = 6 mmol; hydrazine = 48 mmol; temperature = 125 °C, catalyst = 1 mol %. Size of nanoparticles = 17 nm; Time = 3 h; solvent = ethanol, 10 ml.

Table 2.3. Comparison table of numerous catalysts with various nitroaromatics.

Catalyst	Substrate	Time	Yield (%)	TOF (min ⁻¹)	Reference
Pt/CNF	CNB	5h	99	610	23
Fe ₂ O ₃ /Au	NB	8h	90	--	24
Fe(BF ₄) ₂	NB	2h	89	--	25
Fe ₃ O ₄	PNP	8 min	99	--	26
Rh ₃ Ni	CNB	5h	97	--	27
Fe	NB	2-3h	95	--	28
Co	NB	15h	99	--	29
Rh	NB	10h	93	--	30
Ni	NB	4h	93	--	31
Pd	NB	1h	89	--	32
Pt	PNP	3h	99	--	33
Cu, Ag, Au	PNP	<10 min	--	--	34
Zn	NB	2.5h	99	--	35
Ni ₇ S ₆ (Ni ₃ S ₄)	NB	24h	--	--	37
NiS (Ni ₃ S ₄)	PNP	400 sec	--	--	38
NiS _{2+x} /g-C ₃ N ₄	NB	1h	--	--	39
Ni ₃ S ₄	NB	3h	88	113	Present work

CNB = Chloro nitrobenzene; NB = Nitrobenzene; PNP = p-Nitrophenol;

Chapter 2

In the reactions involving heterogeneous catalysis, the reacting molecules adsorb on the catalytically active solid surface. Then the chemical bonds are broken and formed on the surface, and finally the products are released. However, the catalytic activity of NPs depends on various factors such as particle size, surface area, structure-insensitivity/sensitivity, and the number of atoms/molecules in the surface that are available for catalytic activity [45]. We determined the surface area of Ni_3S_4 NPs by BET analysis as $6.49 \text{ m}^2/\text{g}$ (Figure. 2.10). In spite of less surface area, these Ni_3S_4 NPs showed a significant catalytic activity. Interestingly, Radek Zboril and co-workers [46] also observed high catalytic activity iron(III) oxide NPs at relatively lesser surface area for the decomposition of hydrogen peroxide. They ascribed the reason to the absence of an amorphous phase. In the present study, the surprisingly high catalytic activity of Ni_3S_4 NPs having less surface area can be attributed to the availability of more number of bare active sites at the surface since there was no other material surrounding the NPs. These free surfaces were possible because of the inherent advantage HMDS-assisted synthesis.

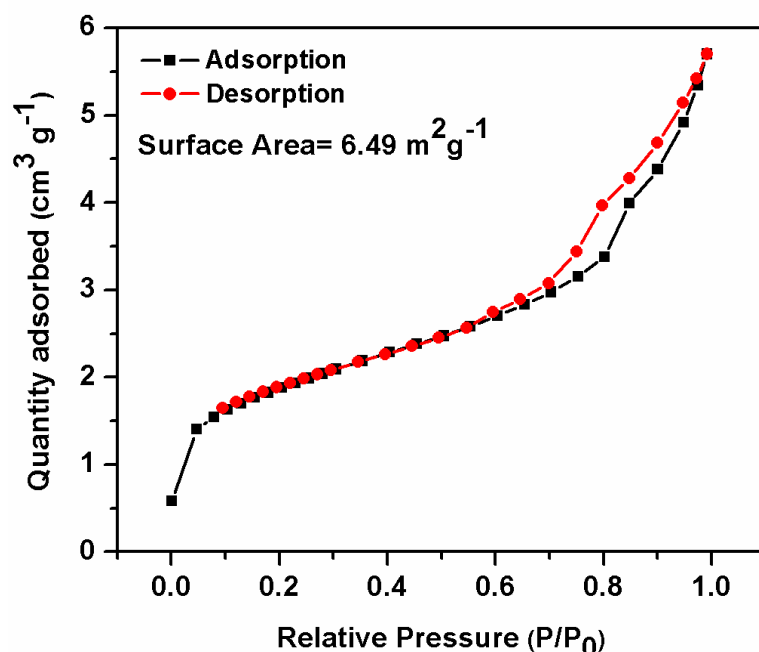


Figure 2.10. BET isotherm of as synthesized Ni_3S_4 nanoparticles.

Rioux et.al [47] observed a difference in the particle sizes polymer coated Pt determined by a chemisorption method and from PXRD lines. This observation was

explained based on the reduced exposed surface area due to the existence of unremoved polymer coated on the surface of Pt NPs which hindered the adsorption of gas. This observation also supported that not only the surface area or size of the NPs but also the availability of exposed active site at the surface are relevant to enhanced catalytic activity observed in this present study. However, any tangible evidence is needed for the prediction of a definite mechanism of the reaction.

2.3.5. Recyclability

For practical applications, recycling capability is desirable for any catalyst. Further, sulphur atoms often leach from sulphur-based compounds leading to the deactivation of their catalytic activity. Interestingly, the Ni₃S₄ NPs prepared in our reactions showed an excellent stability and recyclability in the reduction of nitrobenzenes. When the reaction mixture was filtered at hot condition, a minute solubility of Ni₃S₄ was observed. However, at room temperature, the catalyst precipitated from the solution. Therefore, we recovered and reused the catalyst more than ten times without any activation procedures (Figure. 2.11). After the each reaction, the catalyst was separated by centrifugation from organic layer and, washed, dried and reused. Throughout ten cycles, the reaction yield was almost constant; then there was a slight reduction in the yield (from 88% to 85%).

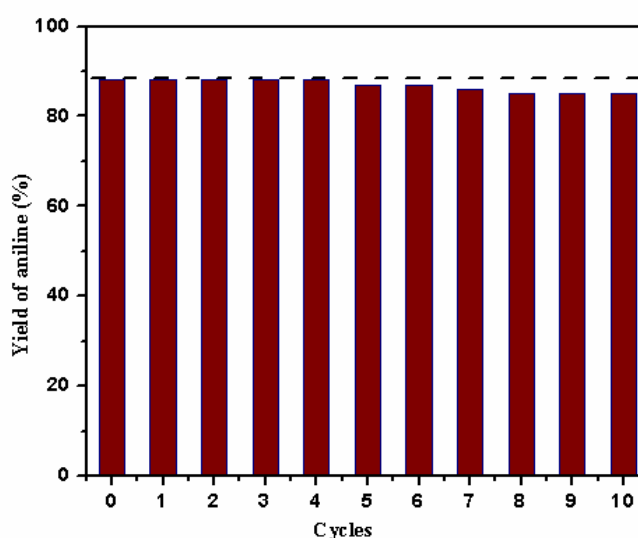


Figure 2.11. Stability of the catalyst. Recyclability analysis of the nickel sulphide. The yield of the aniline was not significantly reduced even after 10 cycles.

Chapter 2

Thermogravimetric analysis showed that NPs were stable approximately up to 200 °C and the catalytic activity did not destroy them (Figure. 2.12). A clear weight loss at 500 °C seen in the TGA plot was presumable due to loss of trapped HMDS or intermediate during the reaction. However, in the reused catalyst these trapped compounds would have dissolved into the reaction solvent and hence there was no sharp loss in weight.

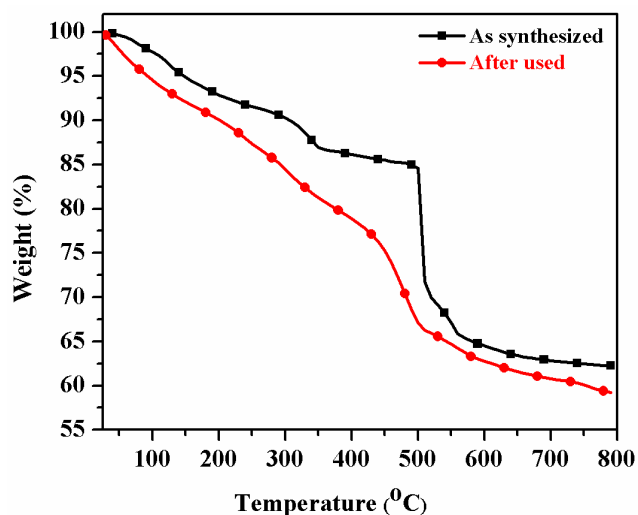


Figure 2.12. Thermal stability of the catalyst. TGA analysis of Ni₃S₄ nanoparticles. Potential use of catalyst at high temperature was explored.

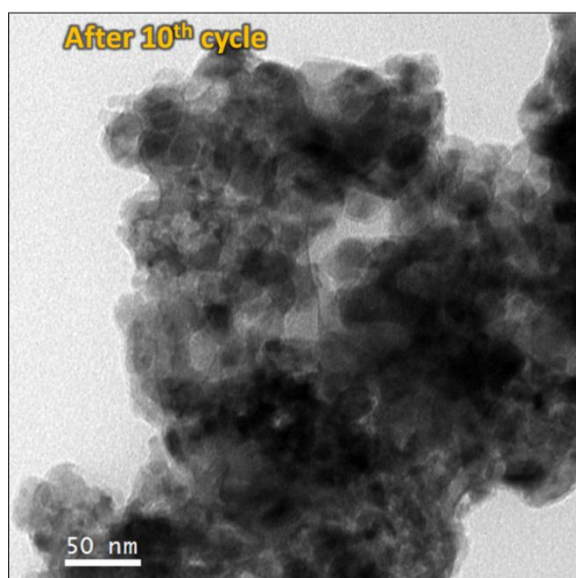


Figure 2.13. TEM micrograph of the reused Ni₃S₄ nanoparticles. Size of the particles were retained after catalysis.

Further, analysis of NPs by TEM after cycles of catalysis did not show any significant change in shape and size of the particles even after ten cycles (Figure. 2.13). Presumably, retaining of size and shapes of NPs ensured a constant catalytic activity for many cycles. In summary, the NPs were recyclable for many catalytic reactions due to their chemical stability and the preservation of the nano-regime.

2.4. Summary

In this chapter we have systematically explained the synthesis of Ni₃S₄ NPs and also successfully explained the catalytic activity of the synthesized Ni₃S₄ nanomaterials. We have developed a novel method for the production of a rare stoichiometric form of nickel sulphide (Ni₃S₄) NPs. The newly developed procedure was simple, single step and scalable for bulk preparation. The method yielded NPs with clean surfaces, which was characterized methodically by various techniques. We have demonstrated hitherto unexplored catalytic activity of Ni₃S₄ phase of nickel sulphide NPs in the hydrogenation of nitroarenes. The broad scope of substrates, easy recovery and recyclability highlight the potential of Ni₃S₄ as a catalyst. The high catalytic activity of Ni₃S₄ having less surface area is ascribed to the clean, surfactant free surface of NPs, which is an inherent advantage of HMDS-assisted synthesis.

2.5. References

- [1] R. Narayanan and M-A. El-Sayed, *Nano Lett.* 2004, **4**, 1343- 1348.
- [2] Z-C. Zhang, B. Xu and X. Wang, *Chem. Soc. Rev.* 2014, **43**, 7870- 7886.
- [3] Y. Zhang, X. Cui, F. Shi and Y. Deng, *Chem. Rev.* 2012, **112**, 2467- 2505.
- [4] M. B. Gawande, A. Goswami, F-X. Felpin, T. Asefa, X. Huang, R. Silva, X. Zou, R. Zboril and R. S. Varma, *Chem. Rev.* 2016, **116**, 3722- 3811.
- [5] R. Narayanan and M-A. El-Sayed, *J. Phys. Chem. B*, 2005, **109**, 12663- 12676.
- [6] E. Hariprasad and T. P. Radhakrishnan, *Chem. Eur. J.*, 2010, **16**, 14378- 14384.
- [7] H. Li, G. Chen, H. Yang, X. Wang, J. Liang, P. Liu, M. Chen and N. Zheng, *Angew. Chem. Int. Ed.*, 2013, **52**, 8368- 8372.
- [8] M. A. Boles, D. Ling, T. Hyeon and D. V. Talapin, *Nat. Mater.* **2016**, 15, 141- 153.
- [9] Z. Niu and Y. Li, *Chem. Mater.*, 2014, **26**, 72- 83.

Chapter 2

- [10] X. Chen, G. Wu, J. Chen, X. Chen, Z. Xie and X. Wang, *J. Am. Chem. Soc.*, 2011, **133**, 3693-3695.
- [11] J-J. Feng, A-Q. Li, Z. Lei and A-J. Wang, *ACS Appl. Mater. Interfaces*, 2012, **4**, 2570-2576.
- [12] A. Ghezelbash, M. B. Sigman and B. A. Korgel, *Nano Lett.*, 2004, **4**, 537- 542.
- [13] A. Ghezelbash and B. A. Korgel, *Langmuir*, 2005, **21**, 9451- 9456.
- [14] R. D. Tilley and D. A. Jefferson, *J. Phys. Chem. B*, 2002, **106**, 10895- 10901.
- [15] L. Zhang, J. C. Yu, M. Mo, L. Wu, Q. Li and K. W. Kwong, *J. Am. Chem. Soc.*, 2004, **126**, 8116- 8117.
- [16] B. X. Jiang, Y. Xie, J. Lu, L. Zhu, W. He and Y. Qian, *Adv. Mater.*, 2001, **13**, 1278- 1281.
- [17] A. Olivas, J. Cruz-Reyes, V. Petranovskii, M. Avalos and S. Fuentes, *J. Vac. Sci. Technol. A*, 1998, **16**, 3515- 3520.
- [18] Y. Zhang, W. Sun, X. Rui, B. Li, H. T. Tan, G. Guo, S. Madhavi, Y. Zong and Q. Yan, *Small*, 2015, **11**, 3694- 3702.
- [19] C. Jiang, Z. Shang and X. Liang, *ACS Catal.*, 2015, **5**, 4814- 4818.
- [20] R. Parry, S. Nishino and J. Spain, *Nat. Prod. Rep.*, 2011, **28**, 152- 167.
- [21] R. S. Downing, P. J. Kunkeler and H. V. Bekkum, *Catal. Today*, 1997, **37**, 121- 136.
- [22] (a) N. Ono, *The Nitro Group in Organic Synthesis*, Wiley-VCH, New York, 2001. (b) J. P. Adams, *J. Chem. Soc., Perkin Trans.*, 2002, **1**, 2586-2597.
- [23] M. Takasaki, Y. Motoyama, K. Higashi, S-H. Yoon, I. Mochida and H. Nagashima, *Org. Lett.*, 2008, **10**, 1601- 1604.
- [24] Q. Peng, Y. Zhang, F. Shi and Y. Deng, *Chem. Commun.*, 2011, **47**, 6476- 6478.
- [25] G. Wienhöfer, I. Sorribes, A. Boddien, F. Westerhaus, K. Junge, H. Junge, R. Llusar and M. Beller, *J. Am. Chem. Soc.*, 2011, **133**, 12875- 12879.
- [26] D. Cantillo, M. Baghbanzadeh and C. O. Kappe, *Angew. Chem. Int. Ed.*, 2012, **51**, 10190- 10193.
- [27] S. Cai, H. Duan, H. Rong, D. Wang, L. Li, W. He and Y. Li, *ACS Catal.*, 2013, **3**, 608- 612.

- [28] R. Dey, N. Mukherjee, S. Ahammed and B. C. Ranu, *Chem. Commun.*, 2012, **48**, 7982–7984.
- [29] (a) T. Schwob and R. Kempe, *Angew. Chem. Int. Ed.*, 2016, **55**, 15175–15179.
(b) L. Liu, P. Concepción and A. Corma, *Journal of Catalysis*, 2016, **340**, 1–9.
- [30] (a) R. G. D. Noronha, C. C. Romao and A. C. Farnandes, *J. Org. Chem.*, 2009, **74**, 6960–6964; (b) A. B. Taleb and G. Jenner, *J. Mol. Catal.*, 1994, **91**, 149–153. (c) H. Berthold, T. Schotten and H. Honig, *Synthesis*, 2002, 1607–1610.
- [31] S. K. Mahapatra, S. U. Sonavane, R. V. Jayaram and P. Selvam, *Org. Lett.*, 2002, **4**, 4297–4300.
- [32] (a) Ronald J. Rahaim, Jr. and Robert E. Maleczka, Jr., *Org. Lett.*, 2005, **7**, 22 5087-5090. (b) B. Sreedhar, P. Surendra Reddy and D. Keerthi Devi, *J. Org. Chem.*, 2009, **74**, 8806–8809.
- [33] Y. Motoyama, K. Kamo and H. Nagashima, *Org. Lett.*, 2009, **11**, 1345- 1348.
- [34] N. Pradhan, A. Pal and T. Pal, *Langmuir*, 2001, **17**, 1800- 1802.
- [35] C. Boix and M. Poliakoff, *J. Chem. Soc., Perkin Trans.*, 1999, **1**, 1487–1490.
- [36] P. S. Rathore, R. Patidar, T. Shripathic and S. Thakore, *Catal. Sci. Technol.*, 2015, **5**, 286–295.
- [37] F. Cao, R. Liu, L. Zhou, S. Song, Y. Lei, W. Shi, F. Zhao and H. Zhang, *J. Mater. Chem.* 2010, **20**, 1078–1085.
- [38] R. Karthikeyan, D. Thangaraju, N. Prakash and Y. Hayakawa, *CrystEngComm* 2015, **17**, 5431-5439.
- [39] Y-N. Zhang, X-H. Li, Y-Y. Cai, L-H. Gong, K-X. Wang and J-S. Chen, *RSC Adv.* 2014, **4**, 60873–60877.
- [40] B. G. Kumar and K. Muralidharan, *J. Mater. Chem.*, 2011, **21**, 11271- 11275.
- [41] B. G. Kumar and K. Muralidharan, *Eur. J. Inorg Chem*, 2013, 2102- 2108.
- [42] B. G. Kumar and K. Muralidharan, *RSC Adv*, 2014, **4**, 28219- 28224.
- [43] B. G. Kumar, B. Srinivas, M. D. Prasad and K. Muralidharan, *J. Nanopart. Res.* 2015, **17**, 325- 335.
- [44] B. Srinivas, B. G. Kumar and K. Muralidharan, *J. Mol. Catal. A: Chem.*, 2015, **410**, 8- 18.

Chapter 2

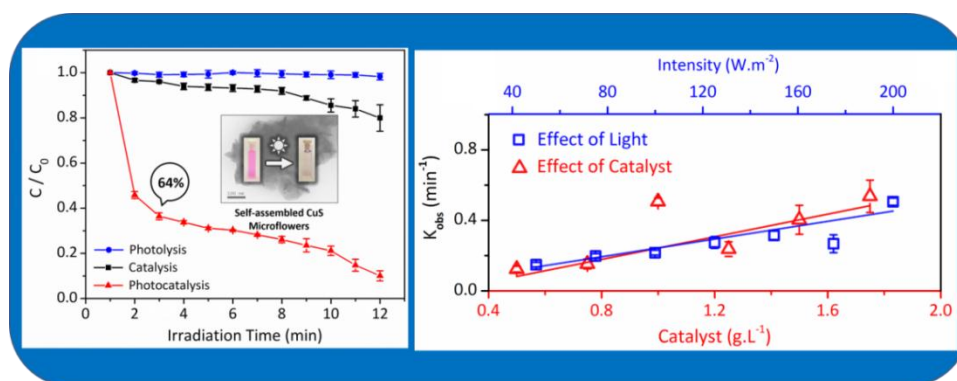
- [45] (a) M. Boudart, *J. Mol. Catal.*, 1985, **30**, 27 – 38. (b) S. Chaturvedi, P. N. Dave and N. K. Shah, *J. Saudi Chem. Soc.*, 2012, **16**, 307–325. (c) F. Yang, D. Deng, X. Pan, Q. Fu and X. Bao, *Natl. Sci. Rev.*, 2015, **2**, 183–201.
- [46] C. Gregor, M. Hermanek, D. Jancik, J. Pechousek, J. Filip, J. Hrbac and Radek Zboril, *Eur. J. Inorg. Chem.*, 2010, 2343–2351.
- [47] R. M. Rioux, H. Song, J. D. Hoefelmeyer, P. Yang and G. A. Somorjai, *J. Phys. Chem. B*, 2005, **109**, 2192-2202.

Chapter 3

Stabilizer free copper sulphide nanostructures for rapid photocatalytic decomposition of rhodamine B

Abstract

In this chapter hexamethyldisilazane (HMDS)- assisted synthesis of CuS and Cu₂S nanostructures and photocatalytic activity of the synthesized nanostructures were discussed. These nanostructures were synthesized by modified HMDS assisted synthetic method at 130 °C. The reaction yielded hexagonal CuS NPs with average size of 22 ± 6 nm and cubic Cu₂S NPs with average size of 52 ± 10 nm. The CuS microflowers were constructed by self-assembly of nanoflakes which was grown through anisotropic growth of (1 0 3) planes. We have demonstrated an efficient photocatalytic activity of CuS nanostructures through photocatalytic decomposition of Rhodamine B dye. The CuS flowers rapidly decomposed Rhodamine B in solution (12 min). The efficient catalytic activity is explained by invoking clean surfaces of NPs. We have also demonstrated the influence of illumination intensity on the efficiency of catalyst and the recyclability.



3.1. Introduction

Colloidal syntheses of NPs have provided accesses to the complex nanostructures like flowers [1, 2], dandelions [3], wafers [4], heterodimers [5], core-shell particles [6], fibrous materials [7], porous materials [8] and other hierarchical nanostructures. However, the reaction conditions and reagents used in the chemical syntheses decide the dimensions and properties of the complex structures. Microflowers are 3D-superstructures of intermediate size with remarkable properties [9–15]. Microflowers have a unique morphology; being in microscale but constructed by nanoscale flakes and therefore ensemble the properties of individual nanoflakes too. Thus, the structure helps in harnessing entire size dependent properties all at the same time. Photocatalysis was one among many fields benefitted from the flower morphology [16–20]. Other than contribution of the nano size, flower morphology provides porous cavities for photocatalytic activity [21]. Among various photocatalytic materials, copper sulphide gained attention because of the low cost, abundance and tunability. Recently, copper sulphide nanostructures showed improved photocatalytic performance [22–30].



Figure 3.1. Pictorial representation of the water pollution by the organic dyes from textile industries.

Chapter 3

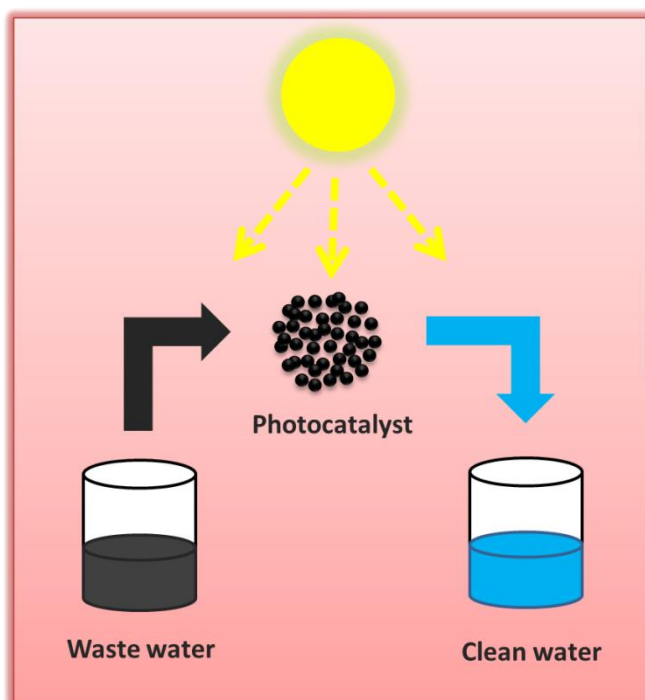


Figure 3.2. Pictorial representation of the photocatalytic degradation of the waste water.

In the field of environmental contamination caused by dyes (Figure. 3.1), the heterogeneous photocatalytic process (Figure. 3.2) is an authentic technique, which can be successfully used to oxidize the organic pollutants present in the aqueous system [36]. During the advance oxidation process, the pollutants or organic matters are completely converted to carbon dioxide or to less harmful compounds based on the stability of those intermediates. Experimental observations indicate that almost complete mineralization of organic compounds to carbon dioxide, water and inorganic anions have taken place in the photocatalytic process. Mostly, the semiconducting nanomaterials such as ZnO and TiO₂ are often used as catalyst in the photocatalytic process because of their high stability, low costs, high efficiency and nil toxicity. However, wide band gap of the TiO₂ and ZnO made them active only in the UV range and show less photocatalytic efficiency in visible region.

The major research is going on to find a suitable semiconducting material which is active in visible region to achieve higher photocatalytic activity towards the dye degradation. As mentioned in the Section 1.2., the surfactants/capping agents that are present around/on the surfaces of NPs unfavourably modify the properties of

Synthesis of Copper Sulphide Nanostructures

the nanostructures. Case in point, most of the potential catalytic centres in the NPs are protected by the capping agents. However, synthesizing NPs for catalysis, without organic surfactants but utilizing less energy, simple starting materials and simple purification procedures is a challenging task [31, 32]. Herein, we have developed a direct synthesis of CuS microflowers assisted by HMDS and their photocatalytic activity. It was determined that the nanoflakes constructed these microflowers. Using the same procedure, but by tailoring the stoichiometry of reaction, Cu₂S NPs were also synthesized. HMDS used in these syntheses is a multifunctional reagent with capping and reducing abilities [33–35].

In this chapter, an efficient photocatalytic activity of CuS microflowers by photocatalytic degradation (within 12 min) of the Rhodamine B solution is demonstrated. We have investigated the influences of illumination intensity, amount of catalyst and flower morphology on the photocatalytic activity and quantified through rate constant measurements. We have also analysed the reason for the enhanced photocatalytic activity of CuS microflowers compared to the similar studies reported in literature [22–30].

3.2. Experimental section

3.2.1. Materials

The chemicals used in the syntheses, copper chloride (CuCl₂), thiourea and hexamethyldisilazane [HN(SiMe₃)₂] (HMDS) were purchased from Sigma-Aldrich and used without further purification. All solvents were purified using standard procedures. Instrumentation and sample preparation are similar to the one discussed in Chapter 2 and Section 2.2.4.

3.2.2. Synthesis of CuS microflowers

In a typical synthesis (Scheme 3.1), a reaction flask containing copper (II) chloride (0.18 g, 1.4 mmol) and thiourea (0.10 g, 1.4 mmol) was degassed and flushed with dry nitrogen gas and then 1,1,1,3,3,3-bis(trimethylsilyl) amine (HMDS) (5 mL, 23.8 mmol) was injected into the flask. The reaction mixture was stirred at around reflux temperature (~130 °C) under inert condition. Although the formation of copper sulphide was instantaneous, the reaction

Chapter 3

mixture was refluxed for 3 h to achieve uniform flower distribution. At the end of reaction hour, a black precipitate was isolated. The side products and unreacted HMDS were removed by vacuum. Then the black precipitate was washed with methanol ($20\text{ mL} \times 3$) followed by acetone ($20\text{ mL} \times 3$) at ambient temperature to remove unreacted copper (II) chloride and thiourea respectively. The final product was dried at $120\text{ }^{\circ}\text{C}$ for 3 h before analysis. Using synthetic procedure discussed here, we have synthesized copper sulphide NPs up to 2.5 g, which showed the potential ease of method to scale up for commercial production.

3.2.3. Synthesis of Cu_2S nanoparticles

Synthetic procedure of Cu_2S NPs was same as the CuS flowers except for the reaction stoichiometric ratio (Scheme 3.1). Stoichiometry was set as 1: 0.5 excess for CuCl_2 (0.2 g, 1.4 mmol), thiourea (0.053 g, 0.7 mmol) and HMDS (capping agent, 5 mL, 23.8 mmol) respectively. Since an excess of HMDS was present in the reaction, the mole ratio of HMDS was maintained constant for all reactions. The reaction mixture was stirred for 3h at room temperature to avoid local concentration differences in the reaction mixture. A black precipitate of Cu_2S NPs was obtained after 3 h of reflux. Modification of reaction time or temperature did not have any noticeable change in the product.

3.2.4. Photocatalysis

Decomposition of Rhodamine B in aqueous solution was studied in the presence of CuS microflowers as photocatalyst. All photocatalytic decomposition experiments were conducted in a cylindrical pyrex cell which was kept $\sim 10\text{ cm}$ away from the light source to avoid thermal effect. In a standardized procedure, 60 mg of photocatalyst was added into the pyrex cell containing 60 mL aqueous solution of Rhodamine B of 3 M (1 g. L^{-1}) concentration. Since it was a heterogeneous catalysis, CuS was added according to the weight ratio (60 mg of CuS per 60 mL of 3 M of RhB). The solution was stirred before illumination under dark to create adsorption and desorption equilibrium (15 min). Blue LED controlled by Zahner Zennium

Synthesis of Copper Sulphide Nanostructures

electrochemical workstation (Zahner, Germany) illuminated the reaction mixture (454 nm, 200 W. m⁻²). The reaction mixture was bubbled by constant flow of atmospheric oxygen. Analysing environments were maintained cool to avoid thermal assistance in photocatalysis.

The Rhodamine B concentration was monitored by colorimetry. During the photocatalysis, samples (5 mL) were withdrawn periodically (1 min) using syringes. Then the samples were centrifuged to remove residual catalyst particulates. This centrifugation process also avoided the scattering of UV light by CuS particles in analysis. Absorption spectra were collected until no changes were observed in the absorption maximum. Rhodamine B concentrations in each sample were calculated by Beer Lambert law [$c = A/(\epsilon \times l)$], where, A = absorbance of dye at 553 nm, ϵ = molar absorption coefficient [37] of Rh B (= 87,000 M⁻¹cm⁻¹), l = path length of cuvette (1 cm). All absorption profiles were normalised for visual comparison. Rate constants were calculated from the slopes of plot $-\ln(C/C_0)$ versus irradiation time (t). Rate constants were expressed in inverse minutes. To ensure consistency, all analyses were repeated three times and standard errors were calculated. To confirm recyclability, the catalyst was recovered by centrifugation after every cycle. The recovered catalyst was purified by washing with methanol (10 mL \times 5) and acetone (10 mL \times 2) and dried under vacuum for 2 h to obtain in powder form, which was used for recycling experiments and SEM analyses. Recycling experiments were also conducted under the standardized conditions mentioned above.

3.3. Results and discussion

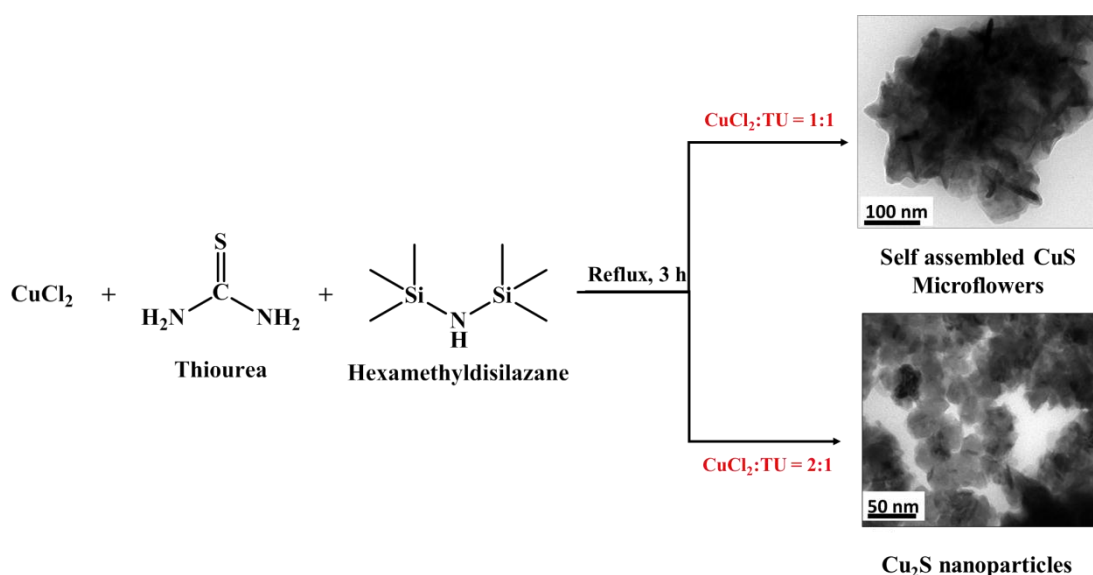
3.3.1. Modified HMDS-assisted synthetic method

It is known that the solubility of reactants play an important role in any reaction and decides the product(s) formed from the reaction [34, 35]. We have developed a modified HMDS-assisted method [31–33] to synthesize CuS microflowers wherein easily soluble thiourea was used as the source of sulphur rather than elemental sulphur. Elemental sulphur was soluble in HMDS only at high reaction temperature. In this reaction, copper (II) chloride

Chapter 3

was reacted with thiourea (1:1) in HMDS to obtain CuS microflowers (Scheme 3.1). Since thiourea was a soluble form of sulphur source at room temperature and its removal after the synthesis was easy. Solubility of thiourea provided control in the present reaction and improved the quality of the materials obtained and further provided favourable condition to perform many reactions by adjusting the stoichiometry. While varying the stoichiometry of the reaction, Cu₂S NPs were obtained when copper (II) chloride to thiourea ratio in the reaction was 2:1. Thus, the “modified HMDS-assisted synthesis” afforded a methodology for the production of both CuS microflowers and Cu₂S NPs.

To explain the role of the HMDS in these reactions, a controlled reaction (CuCl₂ + thiourea) was performed. In this reaction, no copper sulphide was formed in the absence of HMDS explaining the necessity of HMDS to activate thiourea in the reaction. Dual role of HMDS as solvent and its involvement in arresting the growth of particles during syntheses in the HMDS-assisted methodology was explained clearly in the previous reports from our laboratory [33–35]. HMDS is presumed to play similar roles in this modified HMDS-assisted synthetic methodology for the production of metal sulphide nanomaterials.



Scheme 3.1. Schematic illustration of synthesis of CuS and Cu₂S nanoparticles.

3.3.2. Characterization of CuS nanomaterial

The synthesized products CuS and Cu₂S NPs were initially characterized by PXRD. The PXRD analysis confirmed the formation of CuS nanostructures and its crystal structure (Figure. 3.3). In PXRD pattern obtained, the peak positions were resolved and broadened. Two dominant planes (1 0 3) and (1 1 0) were observed. Similar to the products obtained in other synthetic procedures, (1 1 0) CuS plane grew higher than standard pattern [13, 34]. Comparing with the standard diffraction pattern, it was concluded that CuS flowers had covellite crystal structure (JCPDS# 06-0464; hexagonal) and no other stoichiometric copper sulphide phases were identified in the PXRD pattern. To confirm the composition of copper sulphide, EDAX (Figure. 3.4) spectrum was obtained, which showed the atomic ratio of flowers as Cu:S = 1:1. The absence of chlorine (CuCl₂) and carbon signals in the spectrum confirmed complete removal of starting materials in the product and its purity.

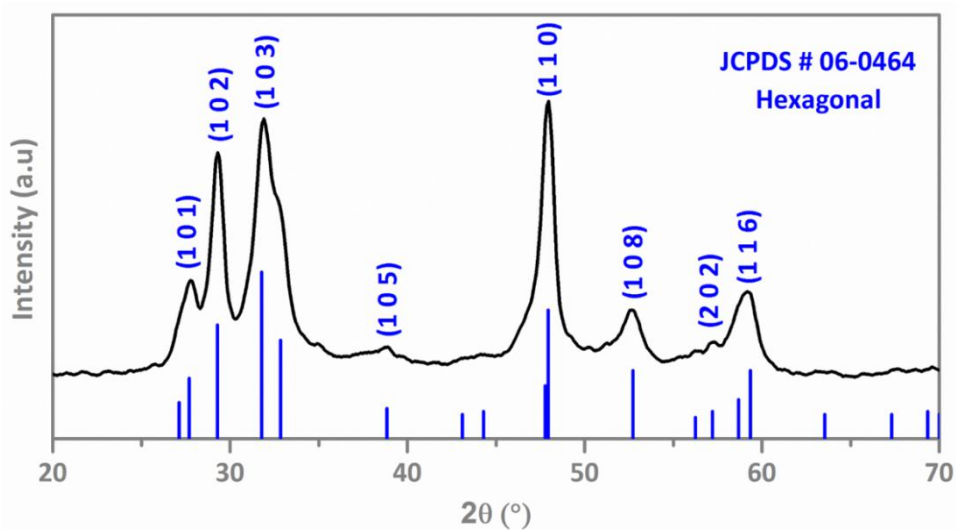


Figure 3.3. Powder X-ray diffraction pattern of copper sulphide nanostructures. The vertical lines represent standard diffraction pattern from JCPDS library. CuS flowers had bulk hexagonal crystal structure.

Chapter 3

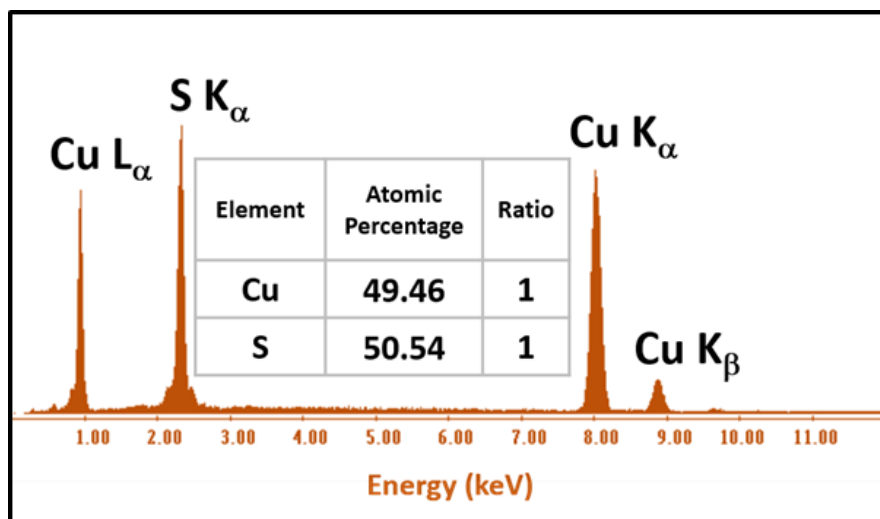


Figure 3.4. EDAX spectrum of CuS nanostructures. Peaks are labelled according to the energy values. Atomic ratio was 1:1. Peaks corresponding to starting materials, capping agent and carbonaceous materials were not observed.

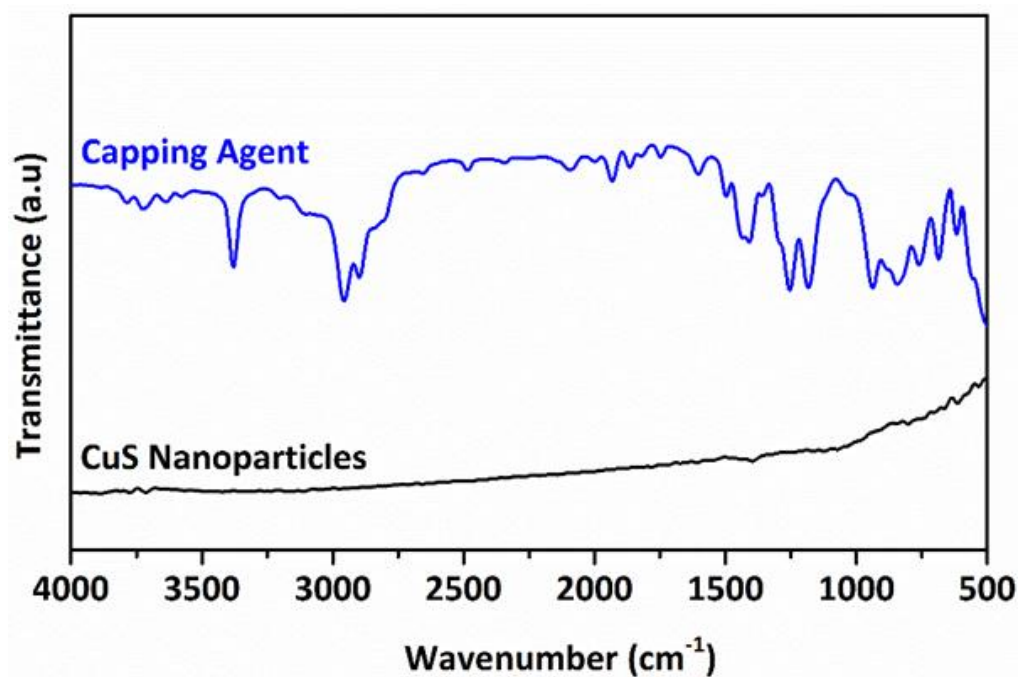


Figure 3.5. FTIR spectrum of copper sulphide nanostructures. FTIR spectrum of HMDS is presented for visual comparison. Absence of capping agent in CuS nanostructures was confirmed.

Synthesis of Copper Sulphide Nanostructures

The absence of signal of silicon and carbonaceous species in EDAX spectrum and no absorbance in IR region (Figure. 3.5) relating any organic moieties confirmed the clean surfaces of CuS flakes. Moreover, HRTEM micrographs did not show any signature of capping agent (amorphous layer) on the surface of nanoflakes (Figure. 3.7a). Since there was no capping agent on the surfaces of particles, the peak broadening in PXRD pattern was only due to the tiny sizes of particles. Although no capping agent (HMDS) was on the surfaces of NPs, there was no agglomeration of NPs and they were stable against oxidation. HMDS arrested the growth of nucleus formed during reaction but was removed in post synthetic process.

3.3.3. Dimensions and flower morphology of CuS particles

Dimensions and morphology of CuS particles formed in the present synthesis were analysed by transmission electron microscope. TEM micrographs showed a flower like architecture of CuS particles (Figure. 3.6a, b and c). Low magnification images showed abundance and distribution of flowers. High magnification images showed that the flowers were constructed by nanoscale flake shaped particles (Figure. 3.6a). Numerous flakes associated to construct three-dimensional architectures of flowers while the number of nanoflakes constructing flowers was not constant. Flower like structures were stable and not dissociated by sonication or concentration variation. Flower architecture was obtained in all reactions independent of variation in solvents and substrates.

The width of the flakes that constituted the flower like architecture was between 9 and 35 nm with the average of 22 ± 6 nm (Figure. 3.6d). The flakes had a constant width along the entire length of flakes. Flake widths were monodisperse and length varied according to the flower size. Polydispersity in length of flakes created polydispersity in the sizes of the flowers. Selected area diffraction (SAED) analysis of flowers showed a bright dotted pattern (Figure. 3.6e). The bright dots were indexed as (1 0 3), (2 0 2) and (1 1 0) planes of the bulk covellite structure. The dotted SAED pattern attributed to the crystalline

Chapter 3

nature of flakes. The obtained selected area diffraction pattern was consistent with powder diffraction pattern.

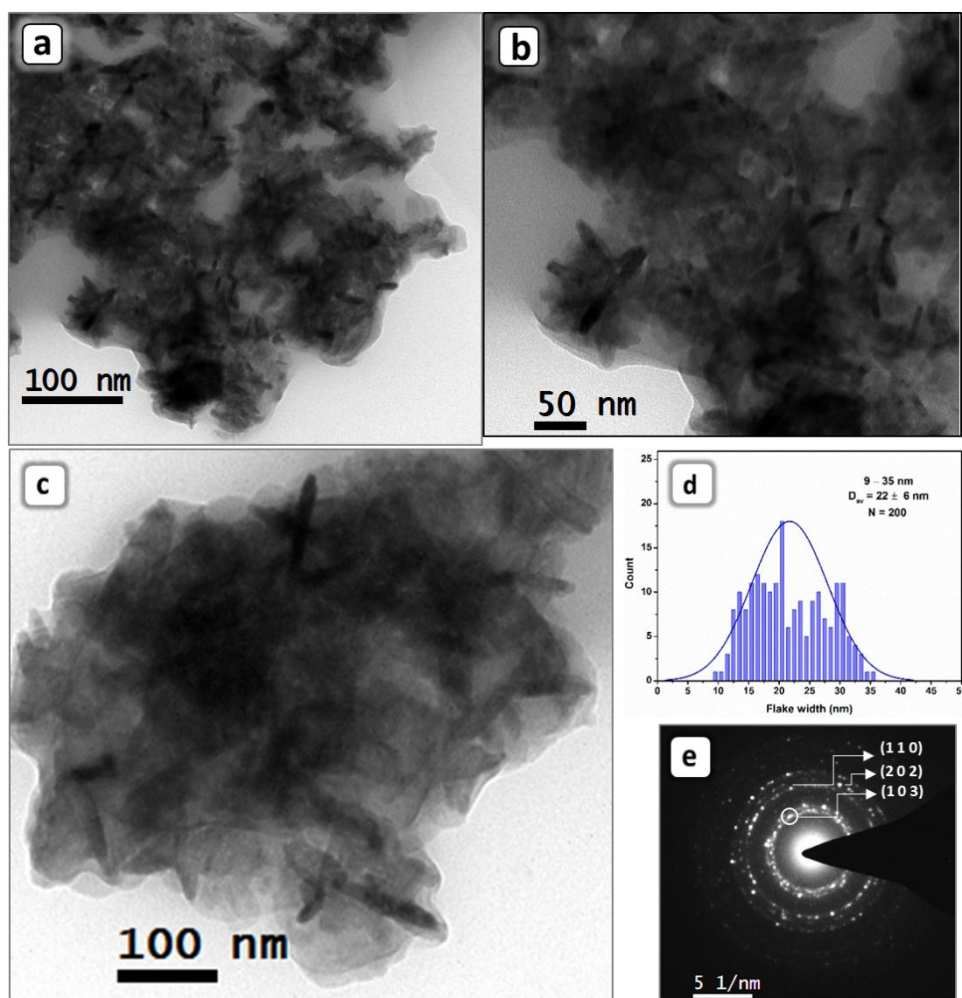


Figure 3.6. (a), (b) and (c) are TEM micrograph of copper sulphide nanostructures. The flower was constructed by flake shaped nanoparticles. (d) Distribution diagram of CuS flowers. Flake widths were 9–35 nm ($D_{av} = 22 \pm 6$ nm) and length of flakes varied with the size of the flowers. (e) Selected area diffraction pattern of flowers. Dotted pattern indicated the crystalline nature of flowers. Dominant (1 0 3) CuS plane is highlighted by a circle.

3.3.4. Anisotropic growth of (1 0 3)_{CuS} planes: self-assembly of nanoscale flakes

To understand the flake formation and their construction, inter-planar distances of a flake present in the periphery of a flower were measured by HRTEM (Figure. 3.7a). Lattice measurements of the flake showed lattice fringe of 2.8 Å (Figure. 3.7b), which corresponds to (1 0 3) planes of covellite structure. All the flakes possessed homogenous (1 0 3) planes irrespective to

Synthesis of Copper Sulphide Nanostructures

the size of the flowers. The (1 0 3) planes have grown parallel to the flakes. Hence, an anisotropic growth of (1 0 3) planes was responsible for flake like shape. This observation was consistent with PXRD pattern. HRTEM images showed that flakes were crystalline without visual defects. Further, the flakes were magnified to the atomic level (Figure. 3.7c) and corresponding two-dimensional fast Fourier transformation (FFT) was obtained (Figure. 3.7d). FFT patterns were matching with patterns of PXRD and SAED.

All flakes seen in the TEM micrographs were uniform and without side arms. This observation eliminated the possibility of lower formation from the branching of single flake. There were no appreciable defective interfaces or twins detected in high magnification TEM images of the flakes (Figure. 3.7c). Thus, the flower formation did not originate from oriented attachment of smaller NPs [38]. In all micrographs, no flakes were interfaced with other flakes in flowers. All flakes existed individually in flowers. Hence, the flakes were the basic building blocks of flowers. Moreover, HRTEM image of flakes did not have amorphous layer on the surfaces (Figure. 3.7a). Hence, the capping agent was absent on the surface of nanoflakes. To minimize the surface energy, nanoflakes self-assembled and constructed the flowers [10, 34].

Chapter 3

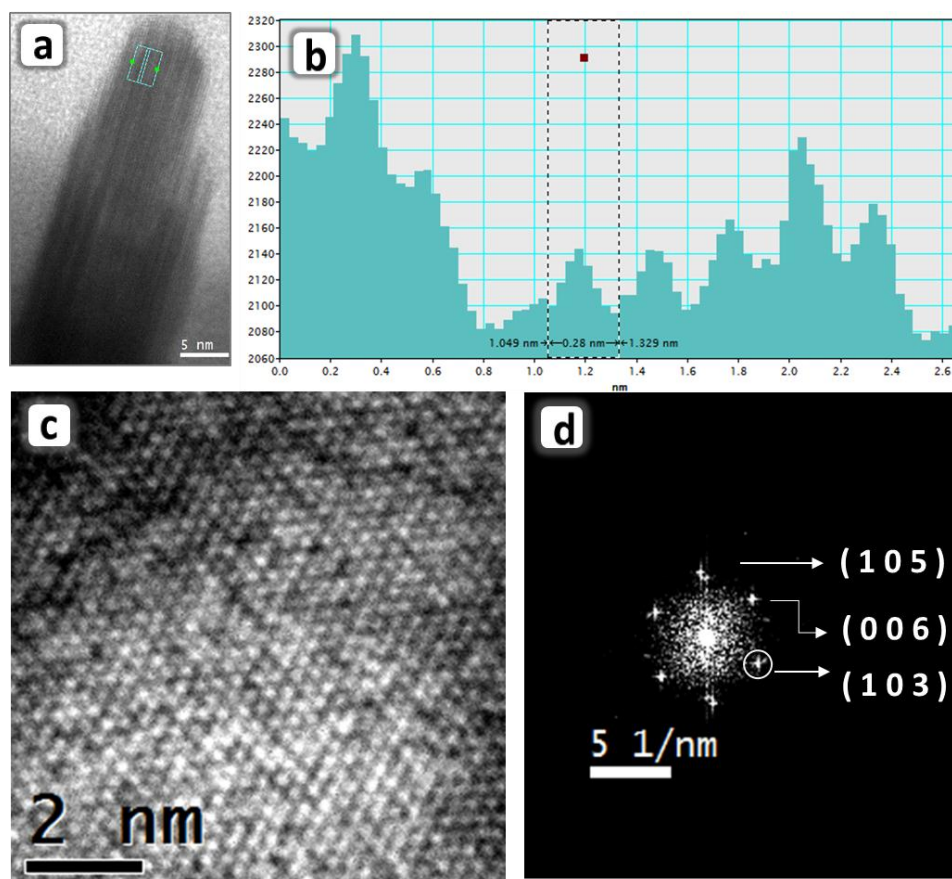


Figure 3.7. (a) TEM image of a flake with width size of 16 nm. (b) Lattice profile of the flake. The flake grew parallel to (1 0 3) CuS plane. (c) HRTEM image of a flake. Lattices indicated the crystalline nature of the nanoflake. Lattices were free from defects. (d) Two dimensional fast Fourier transformation of image (c). Dominant (1 0 3) plane is highlighted by a circle.

3.3.5. Stoichiometric modification-Cu₂S nanoparticles formation

Since copper sulphides exist in different stable stoichiometries, the reaction stoichiometric ratio was modified to understand the change in the product formation. When the stoichiometric ratio of CuCl₂: TU in the reaction is 2:1, Cu₂S NPs were formed (Figure 3.8). Other stoichiometric variations yielded the same Cu₂S NPs. PXRD and EDAX analyses (Figure 3.9 and 3.10) confirmed successful synthesis of Cu₂S NPs. PXRD pattern showed reflections of phase pure cubic Cu₂S (JCPDS # 65-2980). No traces of other stoichiometric compounds were found. Peaks position and relative intensities were matching with standard pattern. EDAX spectrum showed Cu to S stoichiometric ratio in the product as 2:1. The absence of silicon signal in the

Synthesis of Copper Sulphide Nanostructures

EDAX spectrum and the absence of signature of HMDS in FTIR spectrum (Figure 3.11) confirmed the complete removal of capping agent on the surfaces of Cu_2S NPs.

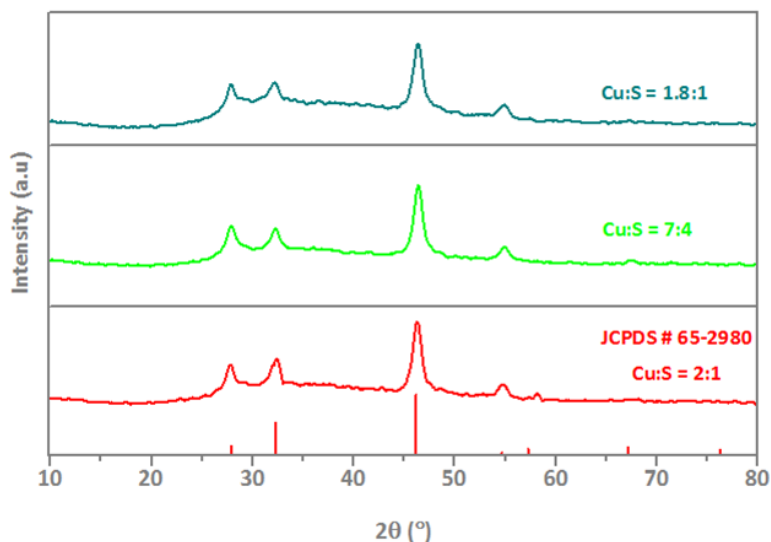


Figure 3.8. PXR D patterns of stoichiometric variation. All attempted variations given the pattern of Cu_2S nanoparticles (65-2980)

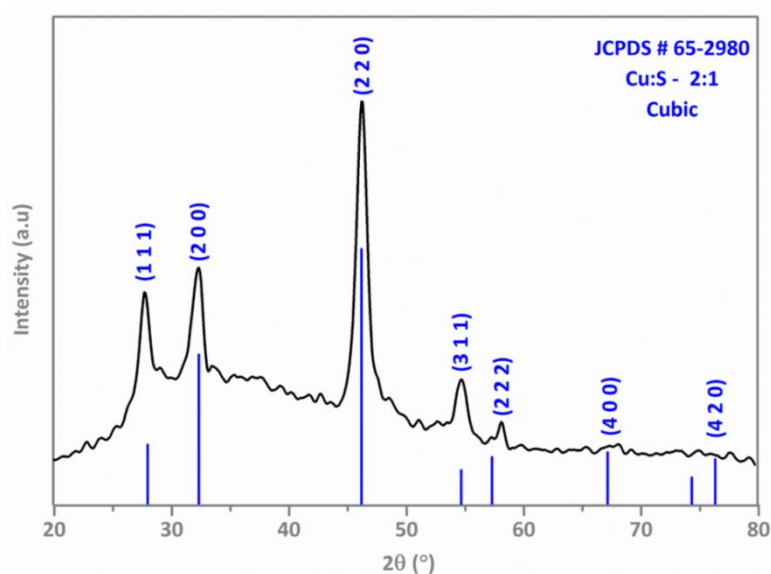


Figure 3.9. Powder X-ray diffraction pattern of Cu_2S nanoparticles. The vertical blue lines are the peak positions from JCPDS library. Cu_2S nanoparticles had bulk cubic-crystal structure.

Chapter 3

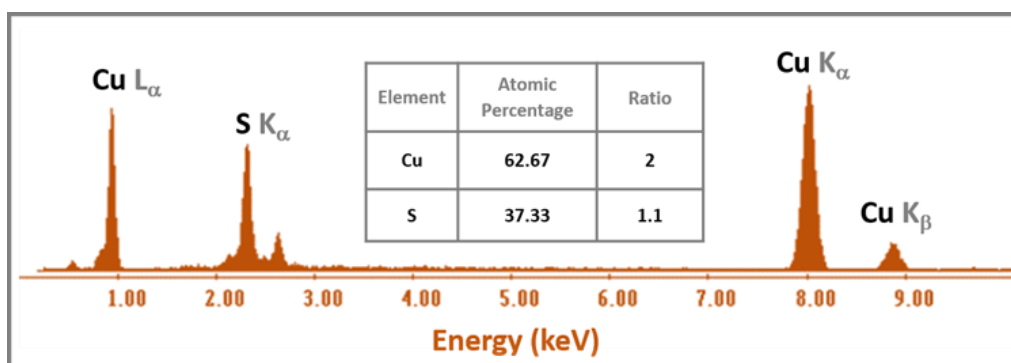


Figure 3.10. EDAX spectrum of Cu_2S nanoparticles. Atomic ratio was calculated as Cu:S = 2:1.1.

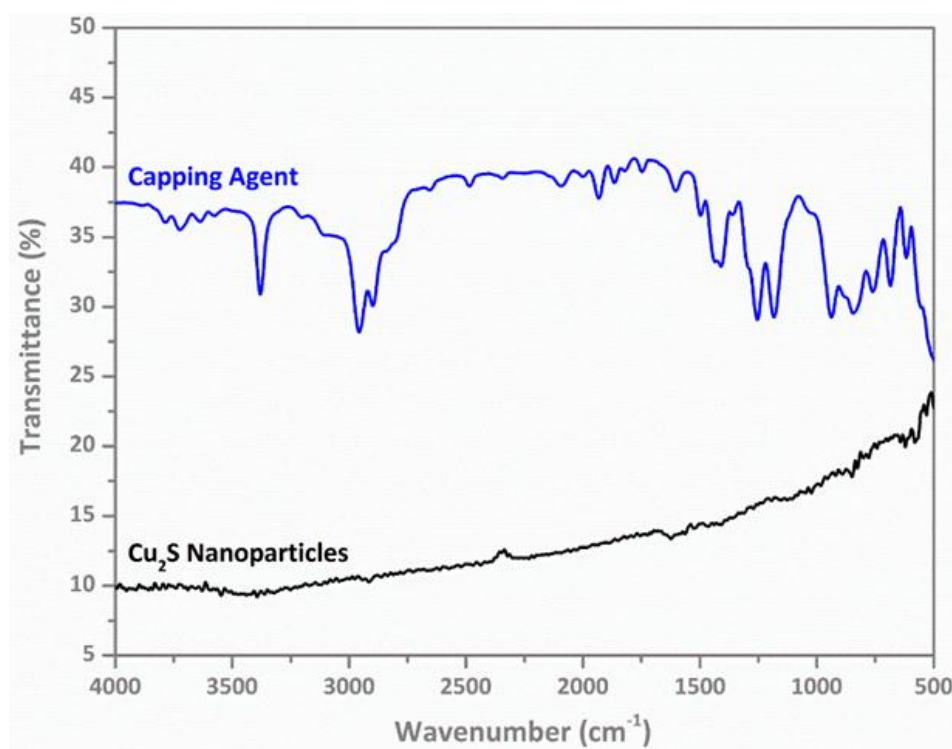


Figure 3.11. FTIR spectrum of Cu_2S nanoparticles. Absence of capping agent on the surfaces of nanoparticles was confirmed.

Synthesis of Copper Sulphide Nanostructures

Morphology of Cu_2S NPs was investigated by TEM analysis (Figure. 3.12a-d). Cu_2S particles had a spherical shape with the diameter of 29–75 nm ($D_{\text{av}} = 52 \pm 10$ nm) (Figure. 3.12e). SAED pattern of Cu_2S NPs showed a clear dotted pattern (Figure. 3.12f) confirming the crystalline nature of NPs.

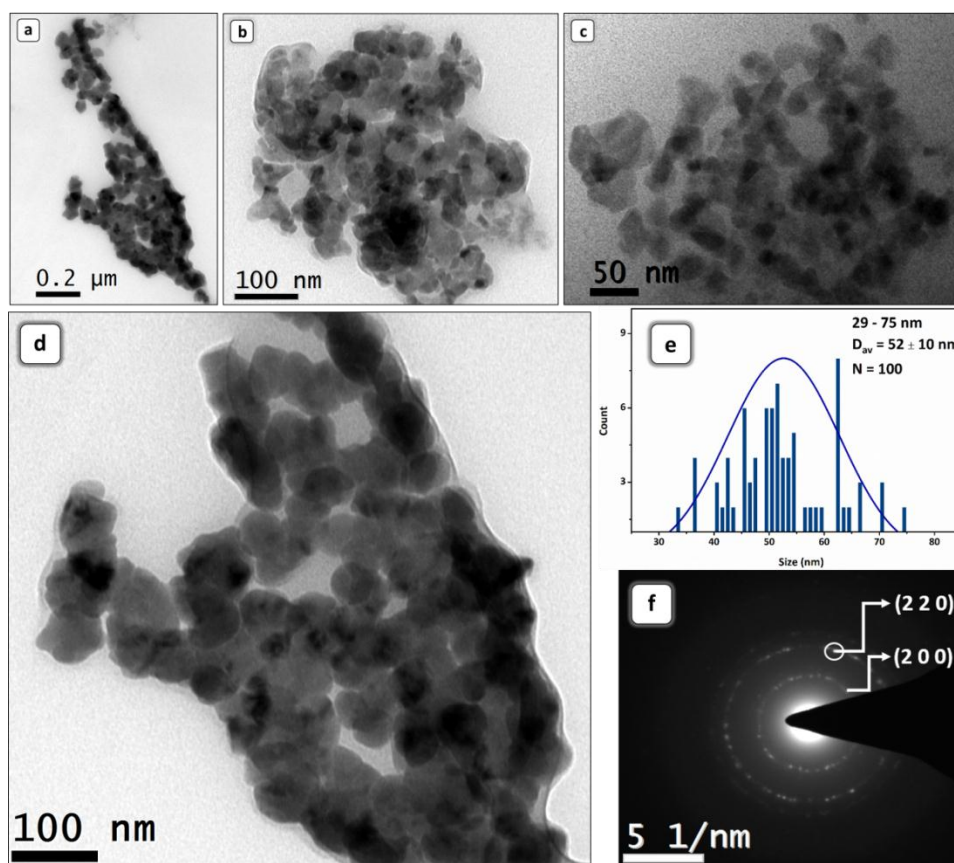


Figure 3.12. (a, b, c and d) are TEM images of Cu_2S nanoparticles with different magnifications. Abundance of particles was high. Particles had nearly spherical shape. (e) Particle size distribution diagram. Cu_2S particles had a size of 29–75 nm with $D_{\text{av}} = 52 \pm 10$ nm. (f) SAED pattern of Cu_2S nanoparticles. Dominant plane is highlighted by a circle.

HRTEM micrographs (Figure. 3.13a, c) showed one of the dominant planes (2 0 0). The information obtained from PXRD, SAED and HRTEM regarding crystallinity and inter planar distances were consistent with each other. Further, two-dimensional fast Fourier transformation acquired Cu_2S NPs at higher magnification (Figure. 3.13c and d) were matching with the standard diffraction pattern. Defect free particles confirmed single crystalline nature of

Chapter 3

the Cu_2S NPs (Figure. 3.13d). In summary, Cu_2S NPs were synthesized by stoichiometric modification in the CuS synthesis and characterised completely.

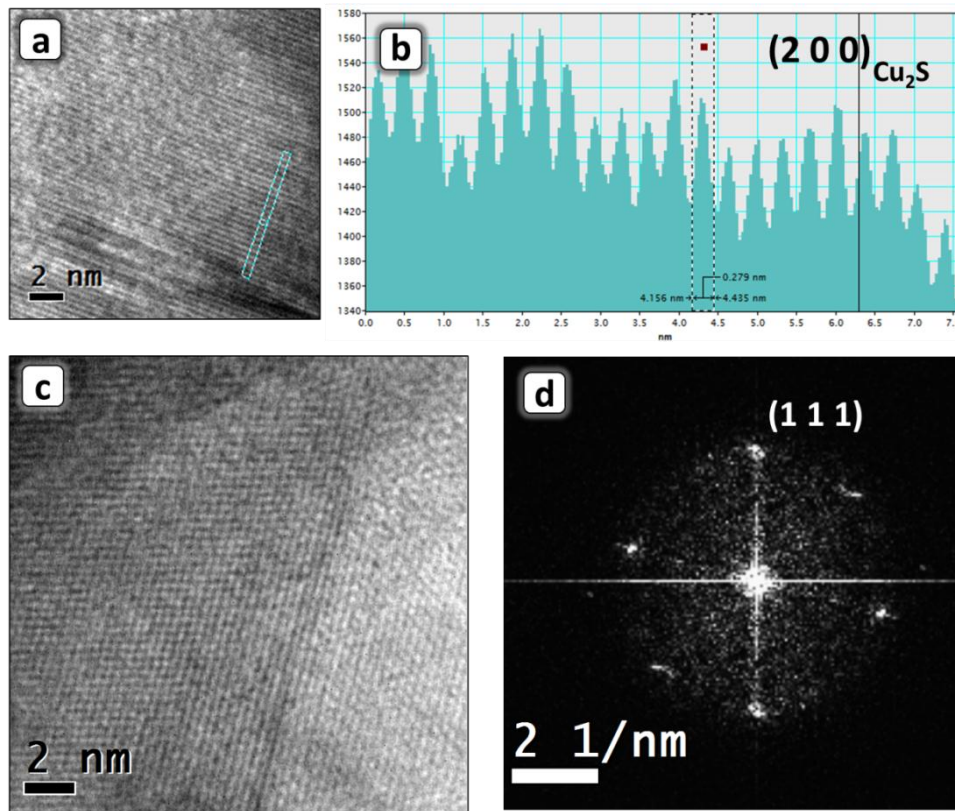


Figure 3.13. (a) HRTEM micrograph of a Cu_2S nanoparticle. (b) Lattice profile of selected region of image. (a) Plane (2 0 0) of Cu_2S was observed. (c) HRTEM image showing continuous lattice points. Clear lattice points denoted the crystalline nature of nanoparticles. The lattices were free from defects. (d) Two dimensional fast Fourier transformation of image (c).

3.3.6. Optical properties

Optical properties of CuS and Cu_2S NPs were examined by UV–Vis spectroscopy. Solid-state spectra were recorded to understand the optical properties since complete removal of capping agent on the surface of NPs reduced the solubility of these materials. Solid-state UV spectrum of the CuS flowers showed a broad reflectance, but the shape of the spectrum was similar to the spectra reported earlier [13]. The spectrum of Cu_2S NPs had a broad reflectance peak centred on 586 nm (Figure. 3.14a). The band gap calculations of the as synthesized CuS and Cu_2S NPs were made from the absorption

Synthesis of Copper Sulphide Nanostructures

spectral data, and the band gap of CuS microflowers was 2.81 eV and Cu₂S NPs was 1.97 eV (Figure. 3.14b and c).

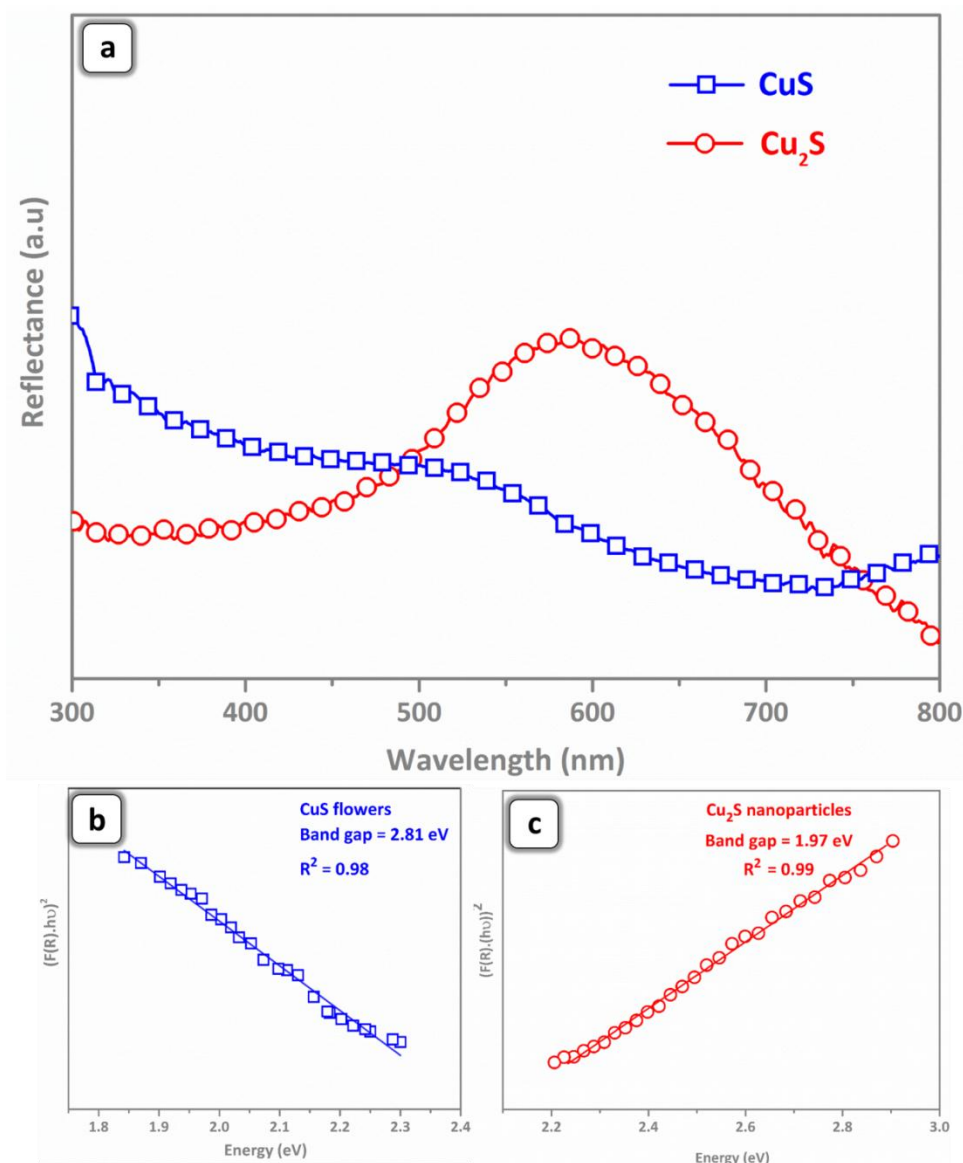


Figure 3.14. (a) Solid UV–visible reflectance spectrum of CuS and Cu₂S nanostructures. (b, c) are optical band gap spectrum of CuS and Cu₂S nanostructures.

3.3.7. CuS flowers as photocatalyst

Photocatalytic activities of CuS and Cu₂S NPs were examined by following the photocatalytic degradation of Rhodamine B (Rh B) dye in solution. CuS flowers exhibited photocatalytic activity under illumination by visible light (blue, 454 nm, 200 W. m⁻²). During analyses, colour of the solution was changing gradually from bright pink to colourless (12 min, Figure. 3.15a inset)

Chapter 3

in the presence of CuS. The decolouration explained that the structure of Rh B was destroyed during photocatalysis [39, 40]. This observation can be attributed to the oxidative degradation of the Rh B in analytical solution [41].

Degradation of Rh B (Structure of Rh B in Figure 3.16) in aqueous solution (60 mL of 3 M) in the presence of CuS microflowers (60 mg) was monitored by observing the change in Rh B concentration through absorption spectra (Figure. 3.15a and b). The Figure. 3.15a illustrates that the absorbance maxima of Rh B ($\lambda_{\text{max}} = 553 \text{ nm}$) was decreasing rapidly without any shift and no new absorption peak was appearing. Hence, the concentration changes and relative concentration (C/C_0) of Rh B were calculated from the absorbance maxima. Figure. 3.15b shows temporal progression of degradation of Rh B under various conditions. Photocatalytic degradation (decolouration) was practically instantaneous. Within 3 min, CuS flowers decomposed $\sim 64\%$ of Rh B solution. Complete photodegradation ($\sim 99\%$) of Rh B occurred within 12 min. Subsequent absorption visualized in the UV spectrum originated from the residual fragments in analytical solution [42]. Initial phase degradation was faster compared to the final phase of degradation. We attribute this observation to the lack of availability of catalyst in the final phase of reaction. This rapid photocatalytic degradation of Rh B solution showed the effectiveness of CuS flowers as photocatalysts. Photons alone (photolysis) did not decompose the Rh B (circles) and catalyst alone (catalysis) did not decompose Rh B (squares). Both photons and catalyst synergistically decomposed Rh B (triangles). Error bars were calculated from three independent measurements. Plots of absorbance versus time is given in the Figure. 3.17.

Synthesis of Copper Sulphide Nanostructures

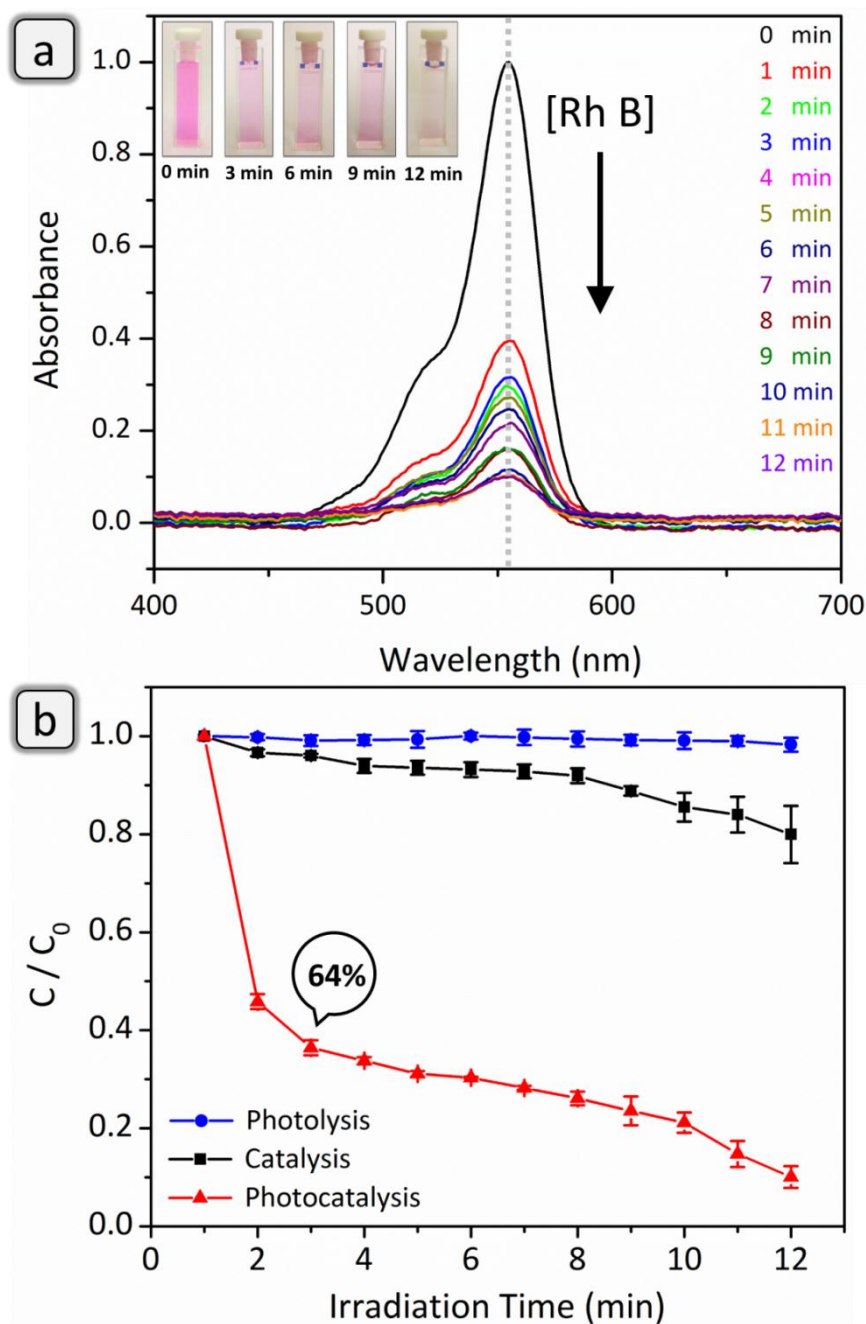


Figure 3.15. Photocatalytic activity of the CuS Flowers. (a) Optical absorption profile of decomposition of Rh B aqueous solution. Changes in the concentration can be seen at 553 nm. Inset shows digital images of colour change during the decomposition. (b) Controlled reactions were described using the relative concentration of the Rh B (C/C_0).

Chapter 3

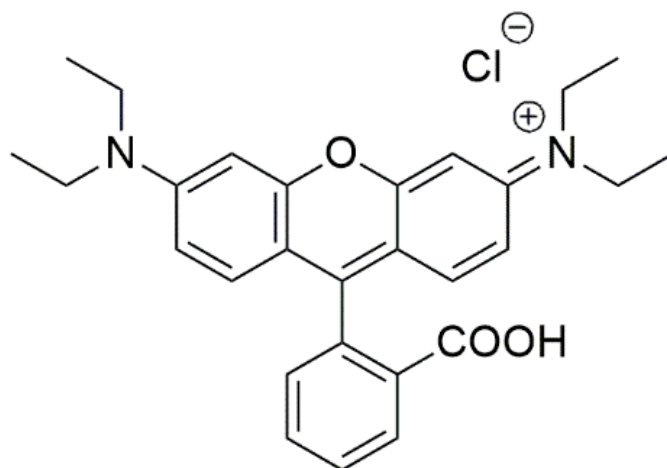


Figure 3.16. Structure of Rhodamine B dye. It is a toxic colorant in textile industry and cosmetic products. It is a common organic pollutant in water.

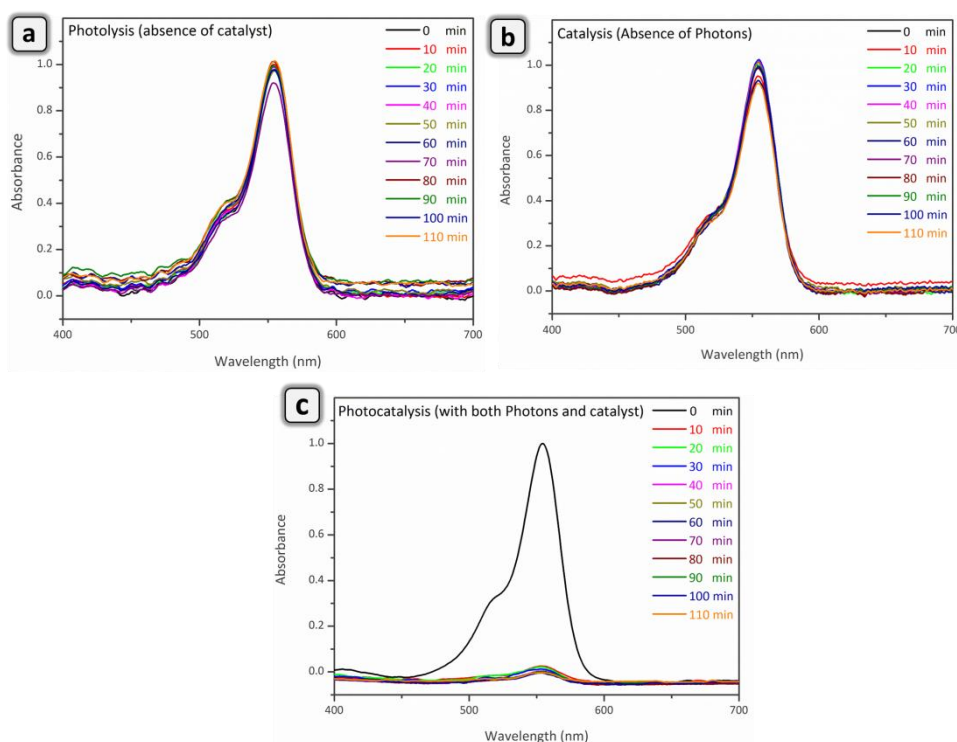


Figure 3.17. Normalized profiles of absorption. (a) Absorption kinetics of photolysis. Decomposition of Rh B was carried out in the absence of copper sulphide catalyst. Photons alone did not decompose Rh B aqueous solution. (b) Absorption kinetics of catalysis. Decomposition of Rh B was carried out in the absence of light. Catalyst alone did not decompose Rh B aqueous solution. (c) Absorption kinetics of photocatalysis. Decomposition of Rh B was carried out in the presence of both photons and catalyst. Degradation of Rh B is self-evident from the plot.

Synthesis of Copper Sulphide Nanostructures

To confirm photocatalytic activity as only the reason for degradation of Rh B, separate catalysis and photolysis were performed. Observation from the UV spectrum showed that changes in Rh B concentration were negligible in both photolysis and catalysis (Figure. 3.15b). There was no appreciable decrease in maxima of RhB in both the process even after extended reaction time (120 min, Figure. 3.17c). Hence, it was clear that the visible light irradiation alone did not decompose Rh B (Figure. 3.15b, circles and Figure. 3.17a) and thus the failure of direct photolysis (without CuS) excluded the possibility of Rh B degradation by self-sensitisation. There was a slight decrease in the dye concentration when CuS (without UV irradiation) was added to the reaction mixture (Figure. 3.15b, squares and Figure. 3.17b). This may be due the decomposition of dye or adsorption dye on the surfaces of catalyst particles. Both results confirmed that independent photolysis (with photons and without catalyst) and catalysis (with catalyst and without photons), did not influence the decomposition of Rh B. Decomposition of Rh B was accelerated only when both catalyst and photons were present (Figure. 3.15b, triangles). Hence, both catalysis and photolysis synergistically influenced the decomposition of Rh B. CuS nanostructures effectively couple photons and catalytic activity to decompose the Rh B solution. In brief, controlled reactions clarified that CuS flowers degraded the Rh B solution through photocatalysis.

To quantify the photocatalytic activity, the rate constant of the photocatalytic degradation was calculated. Initial phase of the degradation (within first three minutes) fitted well in pseudo first order kinetics [$-\ln(C/C_0) = k.t$] [43, 44]; where C and C_0 are reaction and the initial concentrations of Rh B, respectively, t is the irradiation time, k is the apparent reaction rate constant. Since major degradation occurred within three minutes, the rate constant (k_{obs}) observed at initial stage was used for all performance analyses [45]. The calculated rate constant was $0.50 \pm 0.02 \text{ min}^{-1}$. Larger rate constant value revealed the effectiveness of catalyst.

To check the catalytic activity of as synthesized Cu_2S NPs, we have done an experiment for the photocatalytic degradation of Rhodamine B dye under identical conditions which are maintained for the CuS NPs. Unexpectedly, the

Chapter 3

Cu₂S NPs showed very less activity and there was no reproducibility of results. This unexpected behaviour is may be because of morphology of synthesized NPs.

3.3.8. Effect of amount of catalyst and intensity of photons

When the amount (between 0.5 and 1.75 g. L⁻¹) of CuS was varied there was increment in photocatalytic performance. The rate constants showed, the amount of catalyst had a linear relationship with the rate constant (Figure. 3.18a). At initial variation, there may not be enough photocatalyst to enhance the degradation. The increasing amount of catalyst will provide more catalytic centres and hence more absorption of photons. At 1.75 g. L⁻¹, rate constant was 4.2 times higher than the initial value. At the higher concentrations, larger errors were observed in measurements. This observation was due to scattering of light and opaqueness of the solution. Results suggested that the photocatalytic activity of CuS flowers could be enhanced by increasing the amount of catalyst.

We observed that photocatalytic performance of microflowers increased with increasing intensity of light. Hence, we conducted the intensity dependent studies on CuS photocatalyst by varying the intensity of the light at constant intervals (25 W. m⁻²). Other experimental conditions were unchanged. Photocatalyst amount was maintained as 1 g. L⁻¹. Rapid decolouration of Rh B was observed along with the increasing intensity of photons. The degradation was duly monitored by rate constant measurements. The rate constant had a direct relationship with intensity of light (Figure. 3.18b). Variation in rate constant along with light intensity confirmed that decomposition of Rh B had photon assistance. At 200 W· m⁻², rate constant was 3.3 times higher than the initial value. This observation attributed to the fact that higher degree of illumination would generate more carriers in photocatalyst. Hence, the contribution of light in photocatalysis was more. In summary, photocatalytic performance of CuS flowers can be improved by increasing the intensity of light.

Synthesis of Copper Sulphide Nanostructures

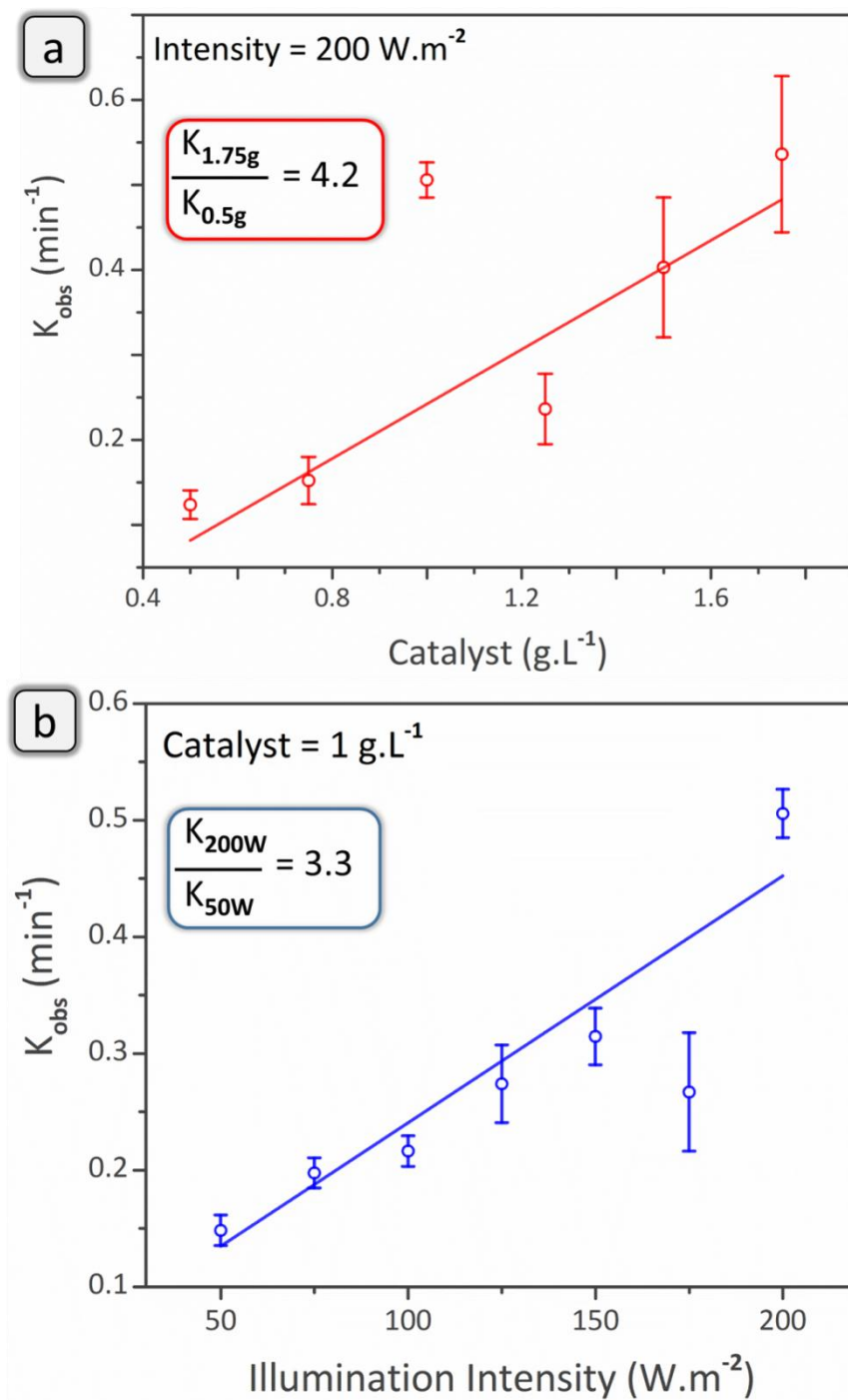


Figure 3.18. Influence of photons (a) and catalyst (b) in the photocatalysis. Both influences had a linear relationship with the rate constant. Lines represent linear fit of the data. Error bars were calculated from three independent measurements.

Chapter 3

3.3.9. Recyclability

To highlight CuS microflowers as a reusable photocatalyst, we have conducted recyclability studies. Under identical conditions, three catalytic cycles were consecutively performed (Figure. 3.19a). We fixed the concentrations of photocatalyst (1 g. L^{-1}) and Rh B ($3 \text{ }\mu\text{M}$) in the analysis. Once Rh B degraded completely, microflowers were recovered and then used for another fresh catalytic reaction. Since the photocatalyst was denser than the analytical solution, it was recovered by centrifugation without impurities. The heterogeneous nature of CuS catalyst was the key to the photocatalysis and it simplified the recycling process. After every cycle, photocatalyst was reused without activation. Recyclability was monitored using absorption spectra through C/C_0 plots (Figure. 3.19a). Compared to the first cycle (12 min), both second (17 min) and third cycles of decomposition had taken longer time (31 min) for completion. This observation indicated the deterioration of photocatalytic activity.

To compare cycles, recyclability was followed by rate constant calculations (Figure. 3.19b and Figure. 3.20). Results showed that rate constants decreased after each cycle of photocatalysis. The third cycle rate was 3.6 times smaller than first cycle. The smaller rate constant value indicated the slower degradation rate of Rh B. Hence, CuS photocatalyst was stable up to two cycles. It should be noted that stability of photocatalyst was moderate for recyclability. Reason for the decreased photocatalytic activity is explained in following section. Recyclability studies showed that the photocatalytic performance of the CuS microflowers reduced after every cycle.

Synthesis of Copper Sulphide Nanostructures

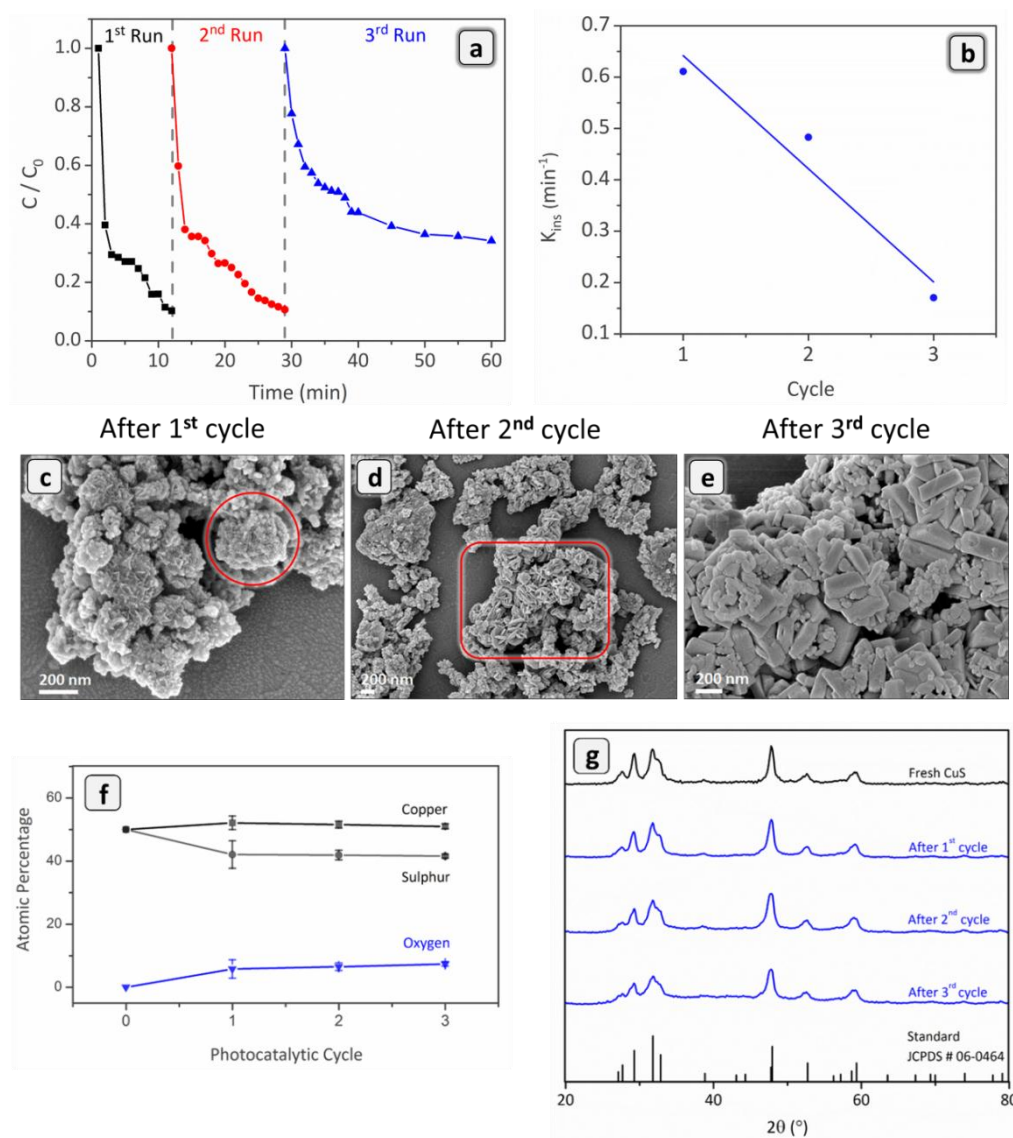


Figure 3.19. Recyclability of CuS photocatalyst. (a) Recyclability is explained by C/C_0 measurements ($1 \text{ g cat} \cdot \text{L}^{-1}$). (b) Trend of rate constants during recyclability of photocatalyst. After every cycle, rate constant decreased. (c) SEM micrographs after every cycle. (d) Flower structure disrupted after each cycle. Highlighted area shows major changes in the morphology. (e) After third cycle, nanoflakes transformed to bulk rods. (f) Atomic ratios measurements from EDAX analysis. Atomic ratios were compared at each cycle. Oxide formation was observed after first cycle. (g) PXRD pattern after each cycle. The CuS phase was retained after three consecutive cycles. Copper oxide signature was absent and it might be due to the uneven oxidation or detection limit of PXRD measurements.

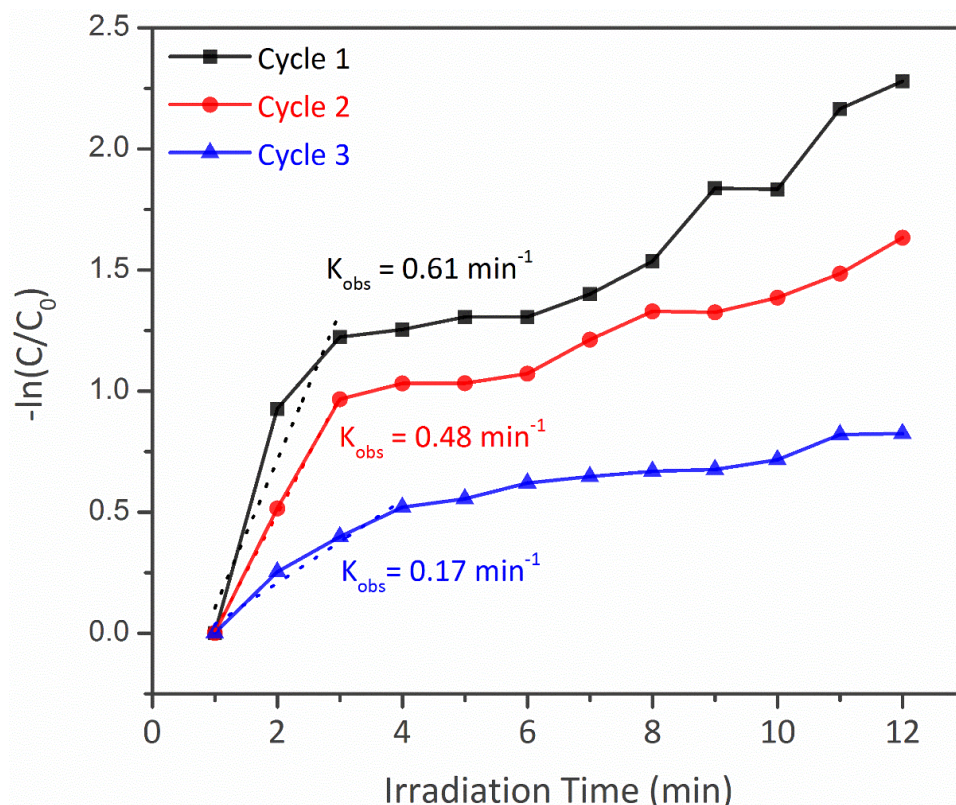


Figure 3.20. Rate constant measurements during recycling process. Standard conditions were utilized (1 g of CuS catalyst for 1 L of Rh B aqueous solution; light intensity 200 W. m^{-2}). Decreasing trend of rate constant was observed.

To explore the issues of recyclability, we investigated structural stability of the photocatalysts. After every cycle, photocatalyst was purified and subjected to SEM analysis (Figure. 3.19c–e). SEM studies indicated that photocatalytic activity was sensitive to the structural change of the flowers. The stability of flower architectures was weak and disrupted over cycles. Density of nanoflakes gradually decreased after the first cycle (Figure. 3.19a and b). After the second cycle, nanoflakes were separated and started growing as bulk particles. After third cycle, the nanoflakes transformed to the bulk rods (Figure. 3.19e). Rods were with a length of $266 \pm 62 \text{ nm}$ and width of $105 \pm 26 \text{ nm}$. Clearly, nano regime was lost during the photocatalysis. Hence, structural degradation was a reason for moderate recyclability.

Along with structural stability, we have duly followed the stability of copper sulphide phase during the photocatalysis. After every cycle, copper sulphide was subjected to the EDAX and PXRD analyses (Figure. 3.19f and

Synthesis of Copper Sulphide Nanostructures

3.19g). EDAX analysis showed that oxide formation (~8%) occurred during the photocatalysis. Every sulphur released from CuS was quantitatively replaced by oxygen. However, PXRD patterns did not show any oxide formation. This observation may be attributed to uneven regional oxidation on the surfaces of NPs and the detection limit of PXRD measurements. Hence, the chemical instability of CuS also deteriorated the activity of the catalyst. In summary, we identified that copper sulphide and its flower architectures collectively contributed to photocatalytic activity.

3.3.10. Clean surfaces and enhancement of photocatalytic activity

The following factors explained the origin of structure dependence of photocatalytic activity. Porous cavities (Figure. 3.6a-c) among the nanoflakes in flowers behaved as additional catalytic centres [21]. Those nano cavities could have accommodated more RhB than individual flakes and hence showed increment in the photodegradation. Moreover, these porous nature influences the absorbed light by multiple reflections [21, 46]. These reflections enhance the photon harvesting capability of photocatalyst. Therefore, higher number of photogenerated electrons and holes would be generated. This process enhanced the photocatalytic efficiency of CuS flowers. The effective photocatalysis also owed to self-assembly of nanoflakes forming flowers. These flowers could efficiently harvest photogenerated charges from all constituted nanoflakes [47]. These arguments were in accordance with recyclability studies; once the flower architectures were lost, catalytic activity of copper sulphide decreased (Figure. 3.19b). Based on these observations, we propose that the efficient photocatalytic was due to the large surface area, porous structures and self-assembly.

EDAX and TEM analyses confirmed that capping agent was absent on the surfaces of NPs (Figure. 3.4 and Figure. 3.6). Since photocatalytic reactions occur on the surfaces of photocatalyst, clean surfaces could facilitate the photocatalytic activity of CuS nanostructures. NPs that were obtained using modified HMDS-assisted synthetic method were free from capping agents and hence all potential catalytic surfaces would be readily available for

Chapter 3

photocatalysis [48]. Moreover, capping agent-free surfaces would create dangling bonds and trap states on the surfaces and thus could induce charges on photoexcitation of the catalyst [49–52]. These charges promoted more Rh B molecules approaching the surfaces of the photocatalyst. This was leading to the increased degradation of Rh B solution. The whole process collectively enhanced the photocatalytic activity of the CuS flowers. Based on observations, we concluded that photocatalytic enhancement was due to clean surfactant free surfaces of CuS flowers.

3.4. Summary

In this chapter, we have thoroughly explained the synthesis of both CuS and Cu₂S nanostructures and also successfully explained the photocatalytic activity of the synthesized materials. The described methodology enables synthesis of both CuS microflowers and Cu₂S NPs from same starting materials. Cu₂S NPs were synthesized by tuning the stoichiometry of the reaction. The NPs were free from capping agent on the surfaces. Cu₂S NPs had spherical shape and CuS NPs had flower architecture. The flower nanostructures were synthesized without any linkers or post-modification process. Nanoflakes were a basic building block of flower architectures. Anisotropic growth of (1 0 3) planes was responsible for flake shape. Nanoflakes self-assembled and constructed flower architectures. We demonstrated that CuS microflowers could serve as a photocatalyst and rapidly degraded Rh B solution (12 min). Recyclability studies showed that photocatalyst could be recycled upto three times. SEM analysis confirmed that flower architectures are responsible for photocatalytic activity. Our results also suggested that higher amount of catalyst and higher illumination intensity enhanced the photocatalytic activity of flowers. An enhanced photocatalytic activity was due to unique flower morphology and clean surfaces. Facile synthesis, ease of removal of capping agent and photocatalytic activity may influence possible applications of copper sulphide NPs.

3.5. References

1. Z. Yang, Z. H. Lin, C. Y. Tang and H. T. Chang, *Nanotechnology*, 2007, **18**, 255606.
2. B. I. Kharisov, *Recent Pat. Nanotechnol.*, 2008, **2**, 190.
3. T. K. Yong, L. Hyunjoo, J. K. Hyoung and H. L. Tae, *Chem. Commun.*, 2010, **46**, 2085.
4. P. Jiang and M. J. McFarland, *J. Am. Chem. Soc.*, 2004, **126**, 13778.
5. G. Hongwei, Z. Rongkun, X. Z. Xi and X. Bing, *J. Am. Chem. Soc.*, 2004, **126**, 5664.
6. O. Hooisweng, R. L. Daniel, S. Mamta, A. B. Barbara, W. W. Watt and W. Ulrich, *Nano Lett.*, 2005, **5**, 113.
7. L. Mei and M. Stephen, *Langmuir*, 2000, **16**, 7088.
8. J. Peng, C. Joel, F. B. Jane and L. C. Vicki, *J. Am. Chem. Soc.*, 1999, **121**, 7957.
9. Q. Wang, X. Cui, W. Guan, W. Zheng, J. Chen, X. Zheng, X. Zhang, C. Liu, T. Xue, H. Wang, Z. Jin and H. Teng, *J. Phys. Chem. Solids*, 2013, **74**, 1470.
10. C. Zhiguo, W. Shaozhen, W. Qian and G. Baoyou, *Cryst. Eng. Comm.*, 2010, **12**, 144.
11. M. S. Akhtar, M. A. Khan, M. S. Jeon and O. B. Yang, *Electrochim. Acta*, 2008, **53**, 7869.
12. R. Wahab, S. G. Ansari, Y. S. Kim, H. K. Seo, G. S. Kim, G. Khang and H. S. Shin, *Mat. Res. Bull.*, 2007, **42**, 1640.
13. L. Benxia, X. Yi and X. Yi, *J. Phys. Chem. C*, 2007, **111**, 12181.
14. P. Kumar, M. Gusain, R. Nagarajan, *Inorg. Chem.*, 2011, **50**, 3065.
15. Z. Cheng, S. Wang, Q. Wang and B. Geng, *Cryst. Eng. Comm.*, 2010, **12**, 144.
16. L. Zhang, W. Wang, Z. Chen, L. Zhou, H. Xu and W. Zhu, *J. Mater. Chem.*, 2007, **17**, 2526.
17. B. Li and Y. Wang, *J. Phys. Chem. C*, 2010, **114**, 890.

Chapter 3

18. Y. Guo, J. Wang, L. Yang, J. Zhang, K. Jiang, W. Li, L. Wang and L. Jiang, *Cryst. Eng. Comm.*, 2011, **13**, 5045.
19. Y. Zheng, K. L. Lv, X. F. Li, K. J. Deng, J. Sun, L. Q. Chen, L. Z. Cui and D. Y. Du, *Chem. Eng. Technol.*, 2011, **34**, 1630.
20. J. Zhang, Y. Wang, J. Zhang, Z. Lin, F. Huang and J. Yu, *ACS Appl. Mater. Interfaces*, 2013, **5**, 1031.
21. X. Meng, G. Tian, Y. Chen, R. Zhai, J. Zhou, Y. Shi, X. Cao, W. Zhou and H. Fu, *Cryst. Eng. Comm.*, 2013, **15**, 5144.
22. Z. Cheng, S. Wang, Q. Wang and B. Geng, *Cryst. Eng. Comm.*, 2010, **12**, 144.
23. M. Basu, A. K. Sinha, M. Pradhan, S. Sarkar, Y. Negishi, Govind and T. Pal, *Environ. Sci. Technol.*, 2010, **44**, 6313.
24. X. Meng, G. Tian, Y. Chen, R. Zhai, J. Zhou, Y. Shi, X. Cao, W. Zhou and H. Fu, *Cryst. Eng. Comm.*, 2013, **15**, 5144.
25. B. Li, Y. Xie and Y. Xue, *J. Phys. Chem. C*, 2007, **111**, 12181.
26. M. Tanveer, C. Cao, I. Aslam, Z. Ali, F. Idrees, M. Tahir, W. S. Khan, F. K. Butta and A. Mahmood, *RSC Adv.*, 2014, **4**, 63447.
27. Z. K. Yang, L. X. Song, Y. Teng and J. Xia, *J. Mater. Chem. A*, 2014, **2**, 20004
28. M. Tanveer, C. Cao, Z. Ali, I. Aslam, F. Idrees, W. S. Khan, F. K. But, M. Tahir and N. Mahmood, *Cryst. Eng. Comm.*, 2014, **16**, 5290.
29. J. Kundu and D. Pradhan, *ACS Appl. Mater. Interfaces*, 2014, **6**, 1823.
30. Z. Li, L. Mi, W. Chen, H. Hou, C. Liu, H. Wang, Z. Zheng and C. Shen, *Cryst. Eng. Comm.*, 2012, **14**, 3965.
31. B. G. Kumar and K. Muralidharan, *J. Mater. Chem.*, 2011, **21**, 11271.
32. B. G. Kumar and K. Muralidharan, *Eur. J. Inorg. Chem.*, 2013, 2102.
33. B. G. Kumar and K. Muralidharan, *RSC Adv.*, 2014, **4**, 28219.
34. M. Yuan, K. W. Kemp, S. M. Thon, J. Y. Kim, K. W. Chou, A. Amassian and E. H. Sargent, *Adv. Mater.*, 2014, **26**, 3513.
35. D. K. Harris and M. G. Bawendi, *J. Am. Chem. Soc.*, 2012, **134**, 20211.
36. S. Dong, J. Feng, M. Fan, Y. Pi, L. Hu, X. Han, M. Liu, J. Sun and J. Sun, *RSC Adv.*, 2015, **5**, 14610–14630.

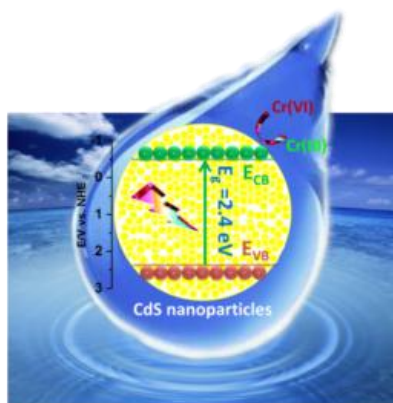
37. R. L. Penn and J. F. Banfield, *Science*, 1998, **281**, 969.
38. O. Ma, M. Lavertu, J. Sun, S. Nguyen, M. D. Buschmann, F. M. Winnik and C. D. Hoemann, *Carbohydr. Polym.*, 2008, **72**, 616.
39. X. Li, N. Kikugawa and J. Ye, *Chem. Eur. J.*, 2009, **15**, 3538.
40. X. Li, N. Kikugawa and J. Ye, *Adv. Mater.*, 2008, **20**, 3816.
41. J. Zhao, T. Wu, K. Wu, K. Oikawa, H. Hidaka, and N. Serpone, *Environ. Sci. Technol.*, 1998, **32**, 2394.
42. T-J. Kuo, C. -N. Lin, C-L. Kuo, and M. H. Huang, *Chem. Mater.*, 2007, **19**, 5143.
43. H. U. Lee, S. C. Lee, Y-C. Lee, B. Son, S. Y. Park, J. W. Lee, Y.-K. Oh, Y. Kim, S. Choi, Y-S. Lee, and J. Lee, *Sci. Rep.*, 2014, **4**, 6740.
44. H. U. Lee, S. C. Lee, S. H. Choi, B. Son, S. J. Lee, H. J. Kim and J. Lee, *Appl. Catal. B- Environ.*, 2013, **129**, 106.
45. F. Pincella, K. Isozaki and K. Miki, *Light Sci. Appl.*, 2014, **3**, e133.
46. L. Zhang and J. C. Yu, *Chem. Commun.*, 2003, 2078.
47. A. G. Kanaras, C. Sonnichsen, H. Liu and A. P. Alivisatos, *Nano Lett.*, 2005, **5**, 2164.
48. H. Tong, S. Ouyang, Y. Bi, N. Umezawa, M. Oshikiri and J. Ye, *Adv. Mater.*, 2012, **24**, 229.
49. S. Li, L. Zhang, H. Wang, Z. Chen, J. Hu, K. Xu and J. Liu, *Sci. Rep.*, 2013, **4**, 3978
50. W-N. Wang, W-J. An, B. Ramalingam, S. Mukherjee, D. M. Niedzwiedzki, S. Gangopadhyay and P. Biswas, *J. Am. Chem. Soc.*, 2012, **134**, 11276.
51. A. L. Linsebigler, G. Lu and J. T. Yates, *Chem. Rev.*, 1995, **95**, 735.
52. J. F. Hamilton, *Photogr. Sci. Eng.*, 1974, **18**, 493.

Chapter 4

Facile preparation of surfactant or support material free CdS nanoparticles with enhanced photocatalytic activity

Abstract

This chapter describes the production of organic surfactant molecules or support material free CdS nanoparticles (NPs) and its efficient photocatalytic activity for the reduction of toxic Cr(VI) to the less toxic and much less mobile form of Cr(III). We have synthesized the template free CdS NPs by adopting the solution phase hexamethyldisilazane (HMDS)-assisted chemical synthetic method using CdCl_2 and thiourea as the precursors. The NPs were characterized by powder X-ray diffraction (PXRD), field emission scanning electron microscopy (FESEM), and transmission electron microscopy (TEM). We have demonstrated an excellent photocatalytic performance of as prepared CdS NPs under visible light illumination for the reduction of Cr(VI) to Cr(III) at acidic pH. The enhanced catalytic activity of CdS NPs was explained by the availability of clean surfaces in the absence of insulating organic molecules as stabilizing agents. The efficient separation of photo excited electron-hole pairs was confirmed by the observed stable transient photocurrent response during transient studies, which was further confirmed through the experienced less resistance to the interfacial charges in the electrochemical impedance spectra (EIS). The catalyst also showed good photocatalytic stability and reusability, that made it as an excellent candidate for waste water treatment.



Chapter 4

4.1. Introduction

Nanoporous materials exhibit improved properties over their bulk counterparts because of increased surface area [1]. The surface of the semiconductor NPs influences the photocatalytic activity since reactants interact with the photocatalyst surface, where the catalytic reaction takes place. Surrounding of chemically synthesized NPs by organic surfactant molecules or any other surface coating would affect surface-related processes such as surface recombination or charge transfer. However, as mentioned in the Section 1.2., these molecules shield the active sites of catalyst imputing less catalytic activity than its potential. Therefore, it is of great importance to research not only how to produce the catalyst in some simple processes efficiently, but also how to provide it with clean and active surfaces.

Cadmium sulphide (CdS) is one of the important II–VI semiconductors and an essential technological material. It has attracted significant interest because of its appropriate band gap energy of around 2.4 eV, visible light response, excellent stability and abundant availability [2-11]. Cadmium sulphide has been explored for applications in many fields such as solar cells, bioimaging [12], photoconductivity [13], chemiluminescence [14, 15] and sensing applications [16]. It is also used extensively as a promising visible-light driven photocatalyst. However, CdS photocatalyst has restrictions due to the photo-corrosion problem, the facile recombination of electron–hole pairs and the less surface reaction efficiency. Therefore, the development of stable CdS-based photocatalysts with efficient charge separation and high photocatalytic activity is crucial to increase their potential for practical applications.

Several hierarchical nanostructures of CdS are prepared by various methods such as microwave assisted synthesis [17, 5], chemical vapour deposition [18], hydrothermal route [19], chemical bath deposition (CBD) [4], UV irradiation technology [20] and electrochemical and chemical synthesis [21-24]. Some of the nanostructures obtained by these methods have been used in catalysis. Much research efforts are on incorporating CdS on support materials to overcome the constraint of its poor adsorption properties and photochemical instability when used as a photocatalyst. These substrate-supported CdS NPs have shown improved catalytic properties [3, 17, 25-27]. Though the available chemical methods are

capable of preparing composite semiconductors with hetero-interfaces for charge transfer, there is a need to produce efficient semiconductor nanomaterials with suitable surfaces to provide more active sites for catalytic reactions. Further, it is of interest to understand the effect of surfactant free surfaces of semiconductor NPs on photocatalysis.

Hexavalent chromium compounds, Cr(VI), are highly toxic, carcinogenic and a contaminant frequently found in wastewater from industrial processes such as electroplating, pigments, metal cleaning, leather tanning, mining, and chromate production (Figure 4.1) [28-31]. The widely recognized, promising way for the treatment of wastewater containing hexavalent chromium compounds is semiconductor-based photocatalytic (In Chapter 3, Figure 3.2) reduction using CdS based materials [3, 25-27]. These materials have exceptional advantages, such as low cost, direct use of clean and safe solar energy, and reusability [4, 5, 32, 33].

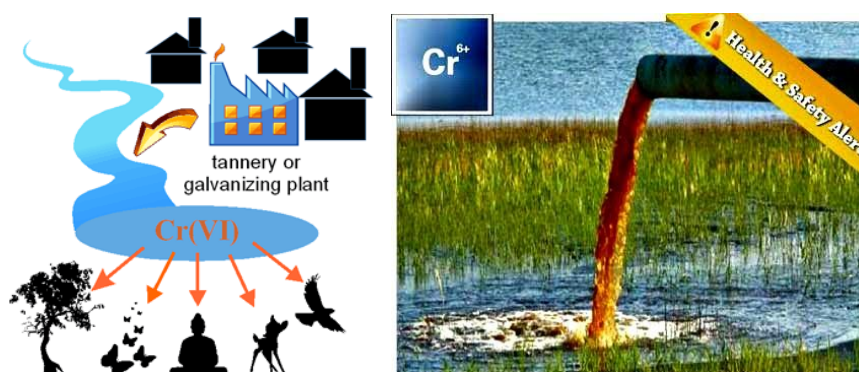


Figure 4.1. Pictorial representation of the water pollution by the Cr(VI) from heavy metal industries.

In this chapter, we have discussed a facile synthesis of template free pure CdS and the enhanced photocatalytic activity of NPs with clean surfaces. The photocatalytic activity of unsupported and unprotected CdS was tested for the reduction of Cr(VI) to the less toxic and much less mobile form of Cr(III). Besides, we have shown the recyclability and stability of CdS NPs. In this study, we have synthesized template free CdS NPs by adopting the solution phase HMDS-assisted chemical synthetic method using CdCl₂ and thiourea as the precursors.

Chapter 4

4.2. Experimental section

4.2.1. Materials

The chemicals used in the syntheses, cadmium chloride (CdCl_2), thiourea and hexamethyldisilazane (HMDS) were purchased from Sigma-Aldrich and used as received. All solvents were purified using standard procedures. Instrumentation and sample preparation are similar to the one discussed in Chapter 2 and Section 2.2.4.

4.2.2. Synthesis of surfactant free CdS nanoparticles

All the chemicals used in the synthesis were purchased from Aldrich and used without further purification. The reactions were performed under inert atmosphere using standard Schlenk techniques. In a typical synthesis (Scheme 4.1) the reaction flask (two-necked round-bottomed flask) containing CdCl_2 (0.188 g, 1.4 mmol), thiourea (0.106 g, 1.4 mmol) were placed and then deoxygenated 1,1,1,3,3,3-bis(trimethylsilyl)amine or hexamethyldisilazane (HMDS) (capping agent, 5 mL, 23.85 mmol) was introduced into the flask. The reaction mixture was refluxed for 3 h, and yellow precipitate of CdS NPs was observed after the completion of the reaction. The side products and unreacted HMDS were removed by applying high vacuum. The obtained yellow precipitate was subsequently washed with methanol (3×20 mL) followed by acetone (3×20 mL) to remove unreacted CdCl_2 and thiourea respectively, and the final product was dried at 120°C for 3 h before analysis. This synthetic procedure was easy to scale up, and we have synthesized up to 2.5 g of cadmium sulphide NPs.

4.2.3. Photocatalytic activity test

The photocatalytic activity of the CdS was evaluated by conducting the experiment of Cr (VI) reduction under visible light (sun light). Typically, a 30 mg photocatalyst was suspended in a 60 mL of Cr(VI) solution ($\text{K}_2\text{Cr}_2\text{O}_7$, 50 mg L^{-1}) under constant stirring. Before irradiation, the suspension was magnetically stirred in the dark for 30 min to ensure adsorption equilibrium of the Cr (VI) on the catalyst surface. After that, the reaction vessel was moved to expose to sun light. At specific time intervals, 3 mL aliquots were taken and centrifuged to remove the catalyst. The reduced

solutions were examined spectrophotometrically by measuring the absorbance at 349 nm on a UV-Vis spectrometer (JASCO- V770). All photocatalytic measurements were repeated three times to make sure the reliability of the results.

4.2.4. Electrochemical activity test

Transient measurements were conducted using Zahner-Zennium electrochemical workstation with three electrode system, where a Pt wire as the counter electrode, Ag/AgCl as the reference electrode and the prepared sample on the FTO as the working electrode. Working electrodes were prepared as follows: 25 mg of CdS NPs were dispersed in toluene and the mixture was dispersed ultrasonically for 30 min, then the homogeneous mixture was dispersed on $1\text{ cm} \times 1\text{ cm}$ area of a cleaned FTO glass plate. Finally, 20 μL of Nafion (10%) solution was dispersed on the coated area. The remaining part of the FTO glass was sealed with the Teflon tape and then allowed to dry at room temperature condition for slow evaporation, and the as-prepared electrode was further annealed at $60\text{ }^{\circ}\text{C}$ in a vacuum oven overnight to remove the resin and to obtain a uniform coating on electrodes. 1 M phosphate buffer solution (pH 7) was used as the electrolyte. Photocurrent-time curves were recorded at open circuit potential with 20 sec light on/off cycles. To perform electrochemical impedance measurements (EIS), we have taken 200 mg of CdS NPs and made it into a pellet form by using pelletiser by applying 3 ton pressure. The prepared pellet was sandwiched between the two gold coated Cu electrodes and carried out the impedance measurements by two- probe method. The measurements were performed over the frequency range 1–100 kHz at the open-circuit potential and the amplitude of the applied sinusoidal voltage was 10 mV.

4.2.5. Recycling test

The recyclability studies were conducted under identical conditions described above. Five catalytic cycles were consecutively performed. For all recyclability studies, a fixed concentrations of catalyst (0.5 g. L^{-1}) and pollutant (50 mg. L^{-1}) were used for analysis. Since, the process is heterogeneous catalysis, the catalyst was easily separable by centrifugation after each cycle and purified by washing with 0.5 M HCl

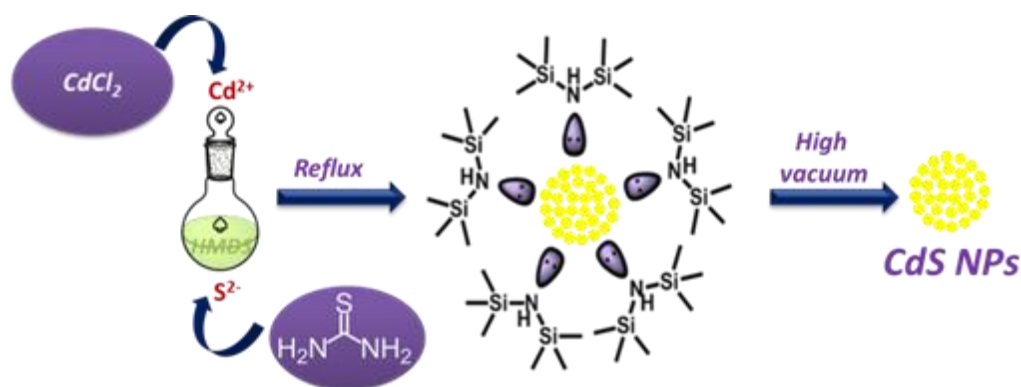
Chapter 4

solution, water and acetone for several times and dried under vacuum at 60 °C for 2 h.

4.3. Results and discussion

4.3.1. Surfactant free CdS nanoparticles

The solubility of reactants plays a significant role in any reaction medium and decides the product(s) formation. We have utilized the modified HMDS-assisted method [34] to synthesize CdS NPs using CdCl_2 as a metal source and thiourea as a sulphur source (mole ratio = 1:1) (Scheme 4.1). Both these precursors were soluble in HMDS at room temperature. To highlight the role of the HMDS in the reaction, we performed controlled reactions where the reaction of CdCl_2 and thiourea did not proceed without HMDS. These results explained the necessity of HMDS to activate thiourea in the reaction. HMDS played multiple roles; as a solvent, reducing agent, and capping agent in arresting the growth of particles during syntheses.



Scheme 4.1. Schematic illustration of synthesis of surfactant free CdS NPs.

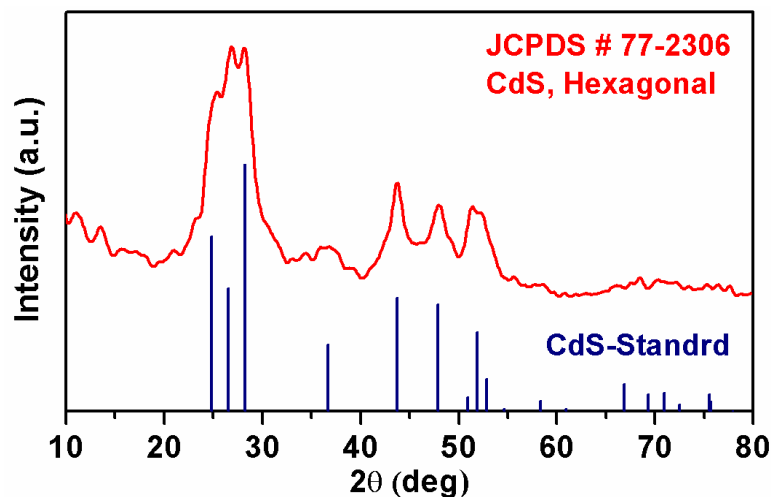


Figure 4.2. PXRD spectrum of as synthesized surfactant free CdS NPs.

The crystallographic structure and phase purity of the as-prepared CdS NPs were established by powder X-ray diffraction (XRD). In the XRD patterns (Figure. 4.2) all characteristic peaks were indexed to the hexagonal structure of CdS (JPCDS No. 77-2306). The strong and sharp peaks clearly suggest that the CdS NPs were well-crystallized. Since no other crystalline impurities were detected, the synthesized CdS had single phase, and no crystal phase impurity existed in it. The EDS analysis (Figure. 4.3) also showed only Cd and S with 1: 1 ratio (atomic percentage = 51.55: 48.45) indicating the purity of synthesized nanocatalyst without any impurity from the precursor.

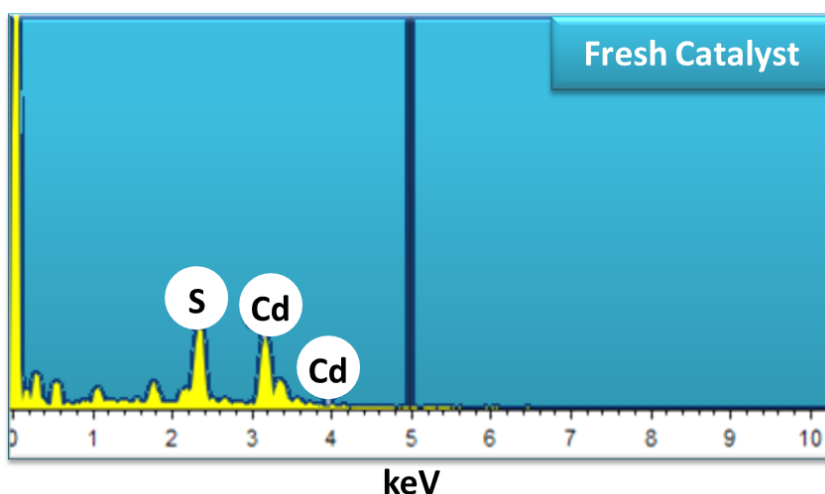


Figure 4.3. Elemental analysis by the energy dispersive X-ray spectroscopy. Atomic ratios were matched with the theoretical values. EDAX spectrum of fresh CdS catalyst.

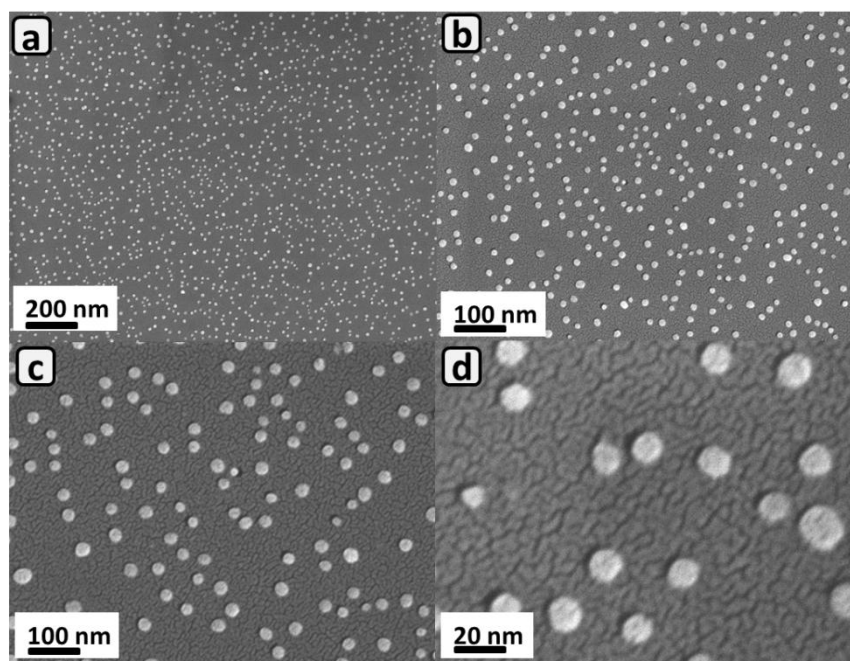


Figure 4.4. Morphological study of surfactant free CdS nanocatalyst. (a) to (d) are FESEM micrographs of CdS nanoparticles at different magnifications.

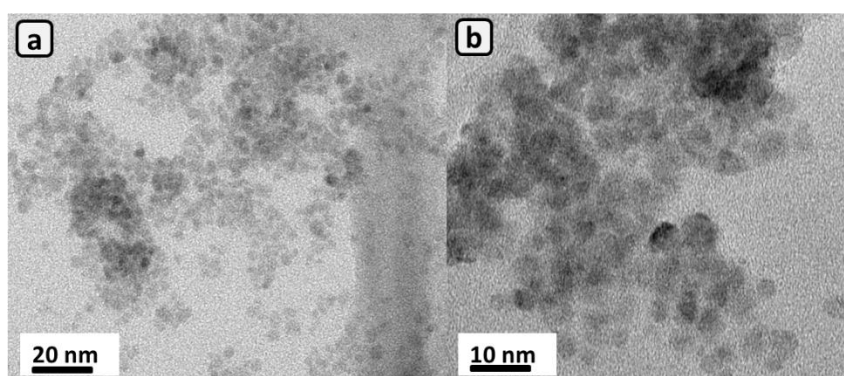


Figure 4.5. (a) and (b) TEM micrographs of as synthesized CdS NPs.

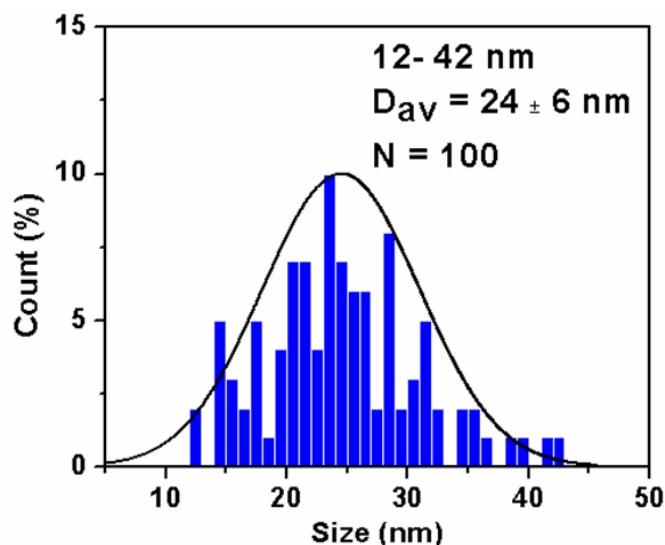


Figure 4.6. Particles distribution diagram from the FESEM micrographs. Particles were mono dispersed with the average size of $24 \pm 6 \text{ nm}$.

Figure 4.4 and 4.5 show the morphology of CdS NPs observed by the field emission scanning electron microscopy (FESEM) and transmission electron microscopy (TEM). FESEM images show an overview of the spherical shape of NPs of size about 12–42 nm in diameter with an average $24 \pm 6 \text{ nm}$ which is expressed in Figure.4.6. The TEM images also revealed the spherical shape of CdS NPs. The precisely observed fringe spacing of 3.1 \AA in the HRTEM image (Figure. 4.7 and Figure. 4.8) was in agreement with the separation of (1 0 1) lattice plane of hexagonal Wurtzite structure (JPCDS No. 77-2306) of the CdS. And the associated selected area electron diffraction (SAED) rings (Figure. 4.8b) identified the (1 0 1), (1 1 2) and (1 1 0) planes. The circle indicated the dominating planes and those planes matched well with the XRD pattern of the hexagonal phase of CdS (JPCDS No. 77-2306). Further, these results showed crystalline nature of as-prepared CdS NPs.

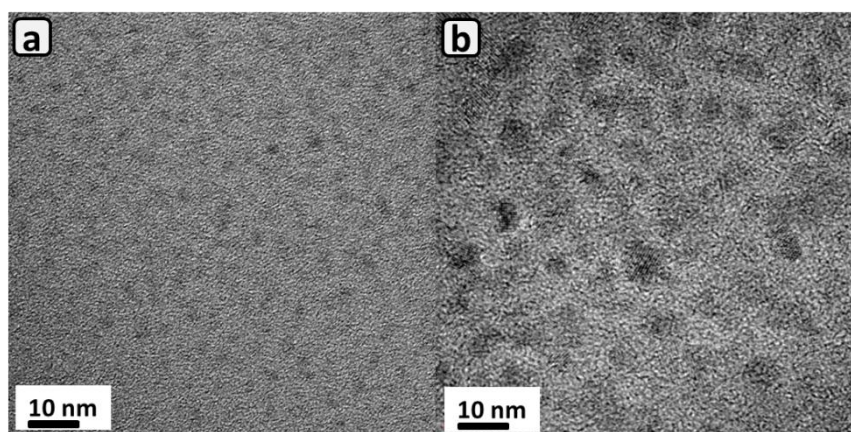


Figure 4.7. (a) and (b) are HRTEM micrograph of as synthesized CdS NPs.

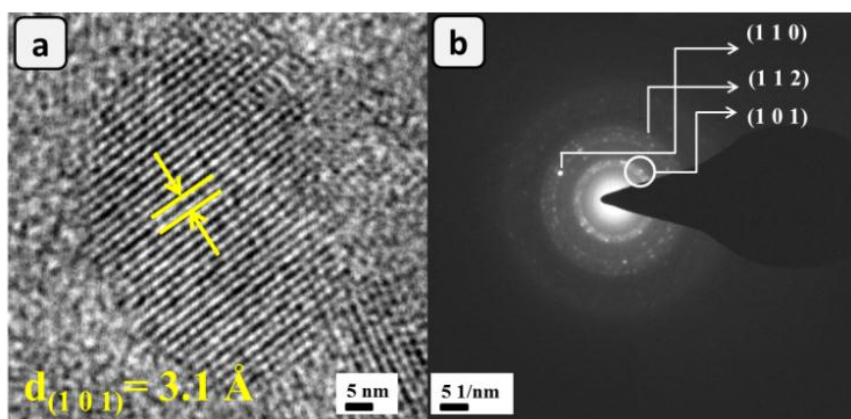


Figure 4.8. Surface characterisation of the CdS nanocatalyst (a) HRTEM micrograph of the nanoparticles. Particles were crystalline and dominant planes matched with XRD pattern. (b) Selected area diffraction of the nanoparticles. Dominant plane is indicated by the circle which is matched with the XRD pattern. Dotted pattern represents the crystalline nature of the nanoparticles.

For catalytic applications, the catalyst surface must be clean from any hindrance. In FT-IR spectrum of as-prepared CdS (Figure 4.9) NPs showed no signal for any organic moieties confirming the absence of any organic molecules covering the particles. Thus, our reactions yielded NPs without any surfactants surrounding them. Our recent work [34] proved the stability of NPs even without surfactant. We also observed that metal sulphide NPs did not agglomerate readily. The UV-Vis diffuse reflectance spectra (DRS) were used to determine the optical properties of the sample. Figure. 4.10 shows the UV-vis diffuse reflectance spectra (DRS) of CdS NPs. Freshly prepared samples exhibited strong absorption in the visible region [35]. Besides, the DRS spectrum indicated that the CdS NPs could be photoexcited by

visible-light irradiation, by which chemical redox reactions could be triggered. The surface area of CdS NPs was determined from the BET analysis (Figure. 4.11) as $6.55 \text{ m}^2/\text{g}$.

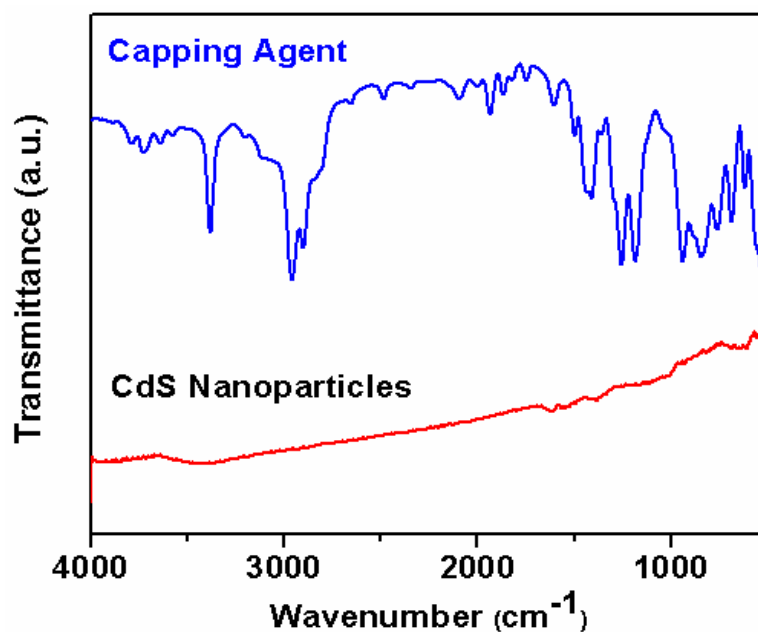


Figure 4.9. FTIR spectra of the nanoparticles. Since there was no signal of the amine (HMDS), capping agent was completely removed from the surfaces.

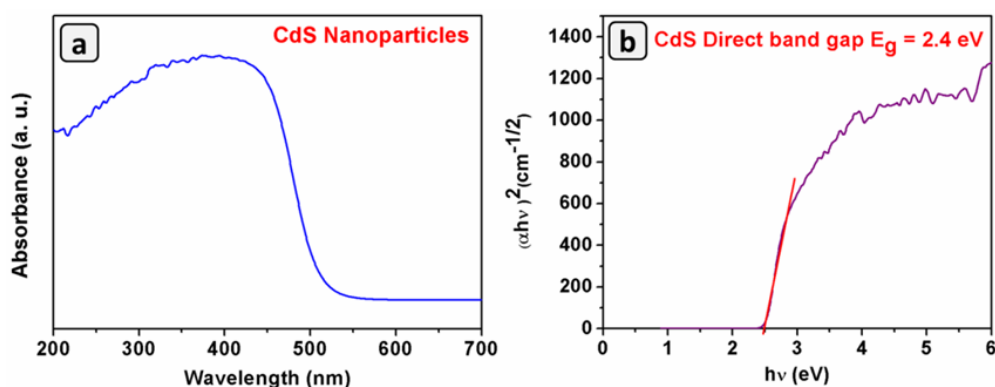


Figure 4.10. (a) UV-vis diffuse reflectance spectra (DRS) of CdS NPs and (b) Band gap image of the CdS NPs.

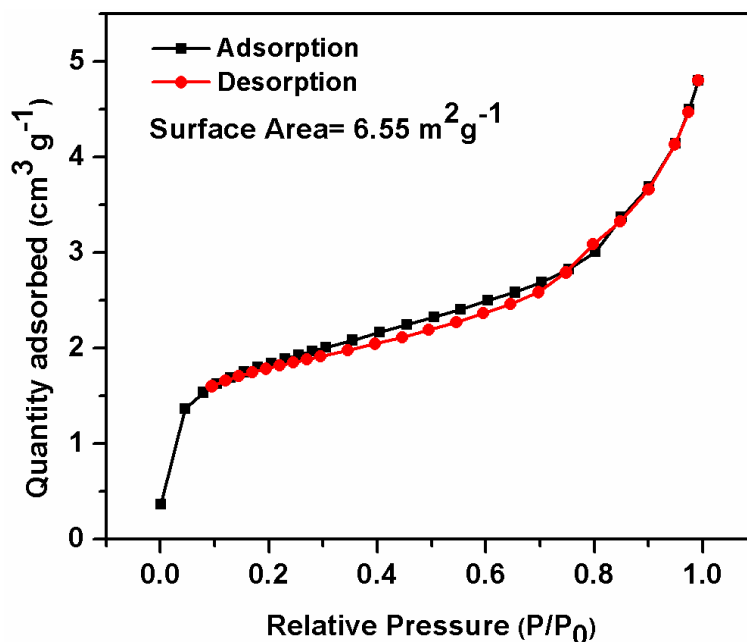


Figure 4.11. BET surface area analysis of CdS NPs. Nitrogen adsorption-desorption isotherm.

4.3.2. Photocatalytic performance

Due to its high toxicity and high mobility in water, the hexavalent chromium is a priority pollutant requiring attention. Many approaches have been developed to treat Cr(VI) ions [17, 36-39], but the most common remediation strategy is the photocatalytic reduction of Cr(VI) ions to a less toxic form of Cr(III) using semiconductor nanomaterials. Therefore, we have evaluated the photocatalytic activity of the surfactant-free CdS NPs obtained using HMDS-assisted synthesis in the photocatalytic reduction of Cr(VI) under visible light irradiation. A solution of $K_2Cr_2O_7$ in deionized water was used as a model solution as a source of Cr(VI). The time-dependent UV-Vis spectra (Figure. 4.12a) exemplify a steady decrease in the intensity of absorption maxima of Cr(VI) confirming its reduction.

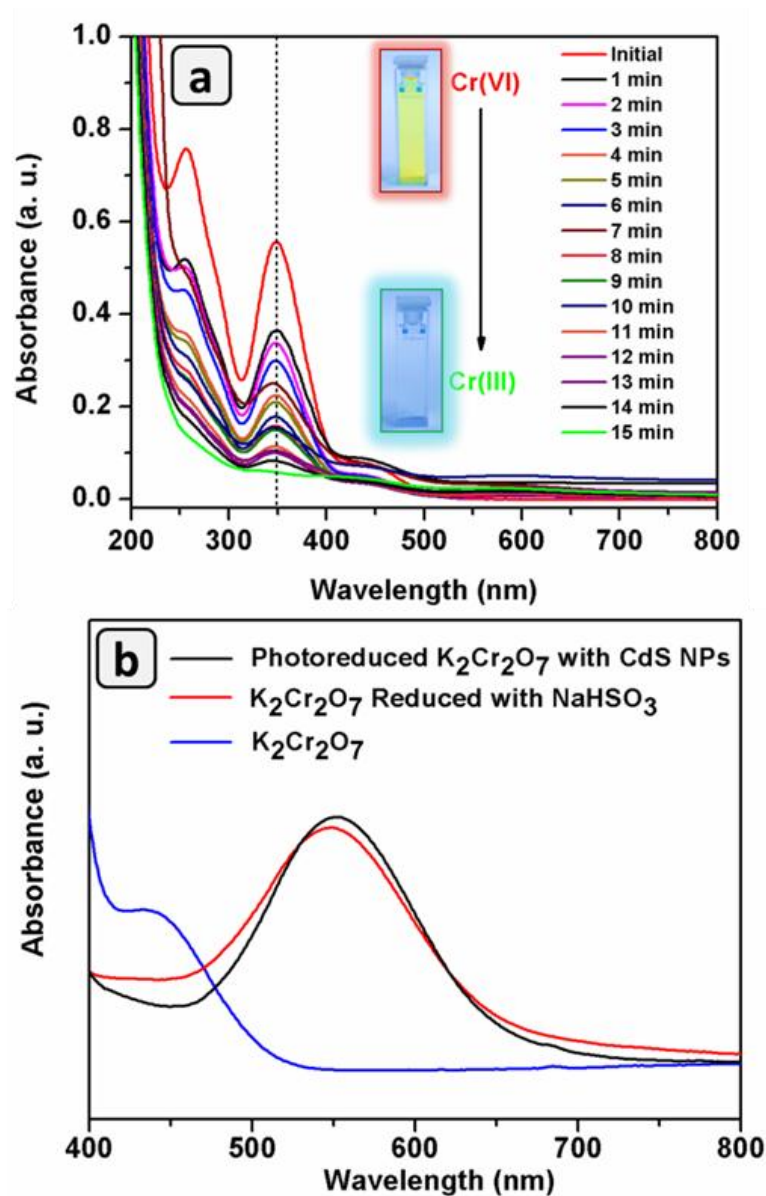


Figure 4.12. Photocatalytic activity of the CdS nanoparticles. (a) Optical absorption profile of reduction of Cr(VI) aqueous solution. Changes in the concentration can be seen at 349 nm. (b) UV-visible spectra of PDCA treated solutions of K₂Cr₂O₇, K₂Cr₂O₇ reduced with NaHSO₃, and photoreduced K₂Cr₂O₇ with nanoparticles.

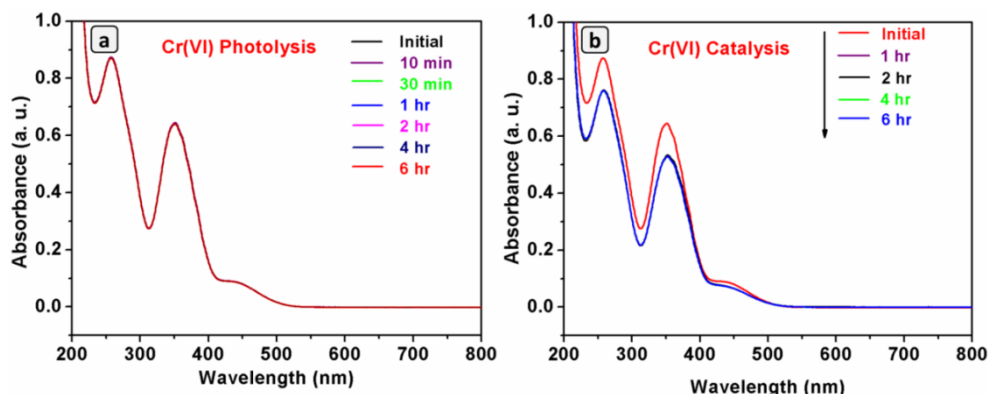


Figure 4.13. Controlled reactions of Cr(VI) reductions, a) Photolysis and b) Catalysis.

To explain the importance of the photocatalytic effect and to confirm the reduction product, we have carried out few control reactions separately (Figure. 4.13). In these control reactions, if either catalyst or light source was absent there was no reduction of Cr(VI) to Cr(III). Further, the reduction of Cr(VI) to Cr(III) by CdS was confirmed by forming a metal complex with 2,6-pyridine dicarboxylic acid (PDCA). The PDCA was known to form a unique violet colour complex with Cr(III) specifically [40, 41]. We have also prepared a $K_2Cr_2O_7$ solution (50 mg. L^{-1}) and reduced it using $NaHSO_3$, followed by heating the resultant solution with PDCA for about 30 min. Both these solutions displayed a light violet colour, which was analysed by UV-Vis spectrophotometer (Figure. 4.12b). Both the photoreduced as well as $NaHSO_3$ reduced samples exhibited the light absorption in the range of 550–555 nm. Finally to cross check the oxidation state of chromium we conducted a negative control reaction, in which a non-reduced $K_2Cr_2O_7$ solution did not show any absorption band in this wavelength range after treatment with PDCA. The obtained results confirmed the successful conversion of Cr(VI) to Cr(III) under the photoreduction conditions.

4.3.3. Significance of surface clean CdS nanoparticles

We have analysed the photocatalytic Cr(VI) reduction to Cr(III) using template free CdS NPs alone (without any support) as a catalyst. Table 4.1 displays the data about the Cr(VI) reduction by using CdS coupled with other moieties such as TiO_2 , RGO, ZnS, etc. It is apparent from the table that the CdS NPs obtained from HMDS-assisted synthesis worked as a suitable photocatalyst.

Table 4.1. Comparisons between the CdS nanoparticles and previously reported photocatalytic reduction of Cr(VI) in the presence of other CdS hetero-structures.

Photo-catalytic materials	Catalytic amount	Amount of $K_2Cr_2O_7$	Required time	Ref.
CdS/N-rGO	3.5 mg	20 ml of Cr(VI) solution (10 mg. L^{-1})	25 min	3
RGO–CdS	(0.0025 g L^{-1})	100 ml of $K_2Cr_2O_7$, $1.0 \times 10^{-5} \text{ M}$	80 min	4
CdO–CdS core–shell nanoboxes	7 mg	20 mL Cr(VI) solution (10 mg. L^{-1})	30 min	5
CdS–reduced graphene oxide composites	10 mg	1 g. L^{-1}	250 min	17
RGO–CdS	100 mg	100 mL of 10 ppm Cr(VI) solution	120 min	25
ZnS(en)0.5–CdS	50 mg	200 mL of 100 ppm of $K_2Cr_2O_7$ (0.4 mM)	--	26
CdS(QDs) sensitized TiO_2	--	100 mL Cr(VI) solution (10 mg. L^{-1})	240 min	27
CdS–grapheme nanocomposites	10 mg	30 mL Cr(VI) solution (20 mg. L^{-1})	20 min	32
CdS@ TiO_2 Core-Shell Nanocomposites	10 mg	40 mL Cr (VI) suspensions (20 mg. L^{-1})	30 min	33
Hetero-system $CuFe_2O_4/CdS$	50 mg	50 mL of $5 \times 10^{-4} \text{ M}$	250 min	39
TiO_2 Layer Coated-CdS Spheres	15 mg	40 mL of Cr(VI)solution (10 mg. L^{-1}).	60 min	44
$CdS/\alpha\text{-Fe}_2O_3$	50 mg	200 mL of Cr(VI) solution (50 mg L^{-1})	120 min	45
CdS NP's	30 mg	60 mL of Cr(VI) solution (50 mg. L^{-1})	15 min	Present work

Chapter 4

The photoelectrochemical performance of semiconductors primarily hinges on the generation of the photoinduced electron, separation of electron–hole pairs and efficiency of charge carrier transfer. Since the surface of the semiconductor NPs has an influence on photocatalytic activity and the presence of organic insulators surrounding the NPs as surfactant molecules, the charge transfer process is impeded. Therefore, it is interesting to study photocurrent generation in the organic surfactant free CdS NPs obtained through HMDS-assisted synthesis. The photocatalytic activity of material can be directly echoed by the transient photocurrent generated under light illumination. An electrochemical system (Zahner Zennium) was employed to measure the photocurrents and electrochemical impedance spectroscopy (EIS).

The transient photocurrent response of the products was measured using a standard three-electrode system under visible light irradiation (LED light) of wavelength 450 nm. The as-prepared CdS NPs were drop-casted on FTO conductive glass and coated with Nafion polymer to produce photoelectrode (working electrode). FTO glass was used as the current collector. The Pt counter electrode and Ag/AgCl reference electrode were other two electrodes in the cell. The 1 M phosphate buffer (pH 7) solution was used as the electrolyte solution.

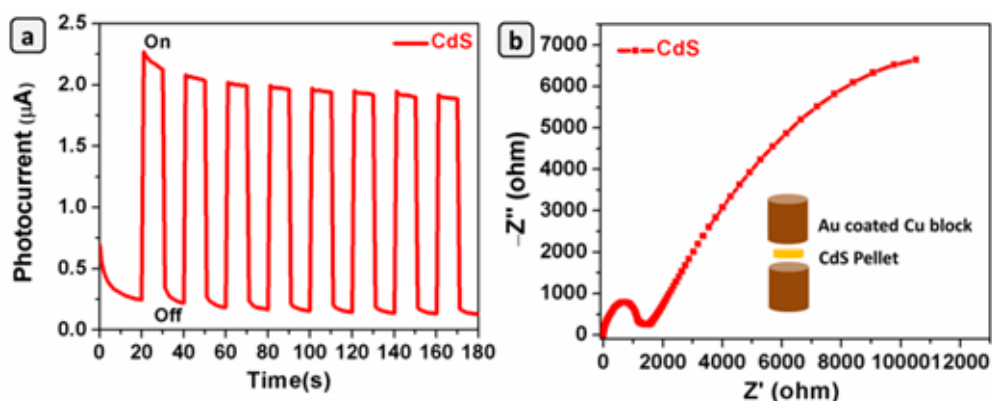


Figure 4.14. (a) Transient photocurrent responses of template free CdS nanoparticles under visible light irradiation in 1 M PBS (pH 7) aqueous solution. (b) Nyquist plot obtained for template free CdS nanoparticles by two probe method.

No photocurrent was observed for CdS in the dark, for the blank FTO, while the organic surfactant free CdS showed appreciable photocurrents under visible light irradiation. As shown in Figure. 4.14a, the spikes of the transient photocurrent responses of CdS over on–off cycles of intermittent light irradiation were observed with no breakage for multiple times. The fast and uniform transient photocurrent response of the products indicates an efficient separation of photoexcited electron–hole pairs from the as-prepared template free CdS under visible light irradiation. The intensity of photocurrent was stable and comparable to that reported in the literature for the particles without supports [42, 43]. The increased photocurrent was due to the clean surfaces of the CdS and was achieved without any support materials.

The effective electron transfer and recombination processes at the electrolyte and electrode interfacial surface were investigated further by the electrochemical impedance spectra (EIS). The spectra were obtained at the frequency of 100 kHz and alternating current (AC) voltage amplitude of 10 mV with an open circuit potential of 1 V. The results are represented as Nyquist plot (Z imaginary vs. Z real) in Figure. 4.14b. All the Nyquist plots contain a linear part at low frequencies that is associated with the diffusion process and a semicircle portion at high frequencies, which corresponds to the electron transfer limited process. It is evident from the Figure. 4.14b that as-prepared CdS NPs showed a lower resistance on interfacial charge transfer compared to the CdS materials that were prepared with support/surfactants. This observation confirmed the efficient separation of photoexcited electron–hole pairs from the surfactant and support material free CdS NPs under visible light irradiation. The surfactant-free structure of CdS NPs might have provided a path for free run of electrons and favoured the separation and transfer of charges. The obtained result was in agreement with the order of photocatalytic activity because the generation of photogenerated carriers is a critical step in photocatalytic reactions.

4.3.4. Stability of photocatalyst and recyclability

The stability of the photocatalyst (CdS) during the reaction is critical for practical application. The recycling usability of five cycles for the photoreduction of Cr(VI) to Cr(III) (Figure. 4.15) was carried out. The catalyst was recovered after every cycle by centrifugation. The recovered catalyst was purified by washing with 0.5 M HCl

Chapter 4

solution, deionized water, and acetone for several times and then dried under vacuum for 2 h to obtain as a powder. The re-born NPs were used to check the recyclability and stability of the catalyst. The recyclable nature of the catalyst was tested in the new solution of Cr(VI) under the same experimental conditions as mentioned above. There was no noticeable decrease in the photocatalytic efficiency up to three cycles. In the first three cycles, reduction of Cr(VI) to Cr(III) by CdS was occurring in 15- 24 min, after that the catalytic activity was decreasing slowly. Reduction of Cr(VI) required nearly 42 min at the fifth cycle.

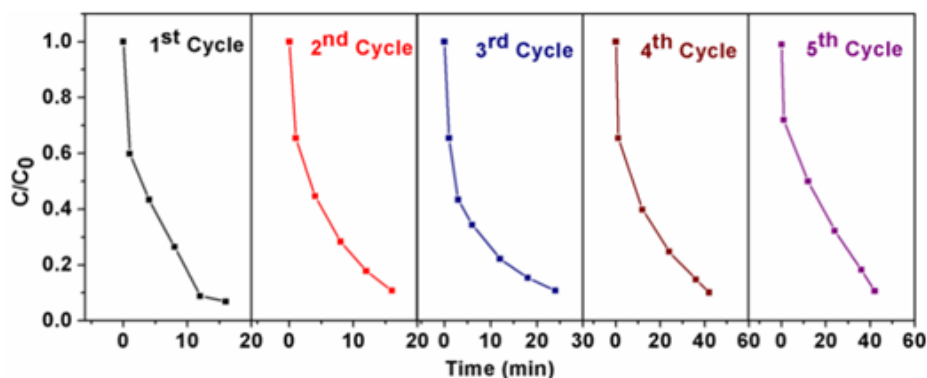


Figure 4.15. Photocatalytic activity of the CdS nanoparticles. Recyclability studies. The catalyst was stable up to 3 cycles and the activity was decreased at the 5th cycle.

It is well known that the CdS cannot sustain water oxidation reaction and suffers severe photo-corrosion. There is no sacrificial hole acceptor present in our system and this condition could lead to a degradation of catalyst. Therefore, we have performed XRD, FESEM and EDS analyses of the recovered CdS catalyst after every cycle of photo reduction. The XRD pattern was found to be same as that of as-synthesized catalyst and thus confirmed that there was no change in the crystal structure before and after photo reduction (Figure. 4.16). The EDS analyses (Figure. 4.17) also revealed that the elemental composition of the catalyst remained unchanged even after five cycles. However, the FESEM image showed that the morphology of NPs was changing slowly (Figure. 4.18). After the first cycle of reduction, the morphology of NPs was retained, while it changed slightly after the third cycle. After fifth cycles, the particles agglomerated fully into large particles. These observations have proved the deactivation of photocatalyst under the reaction conditions.

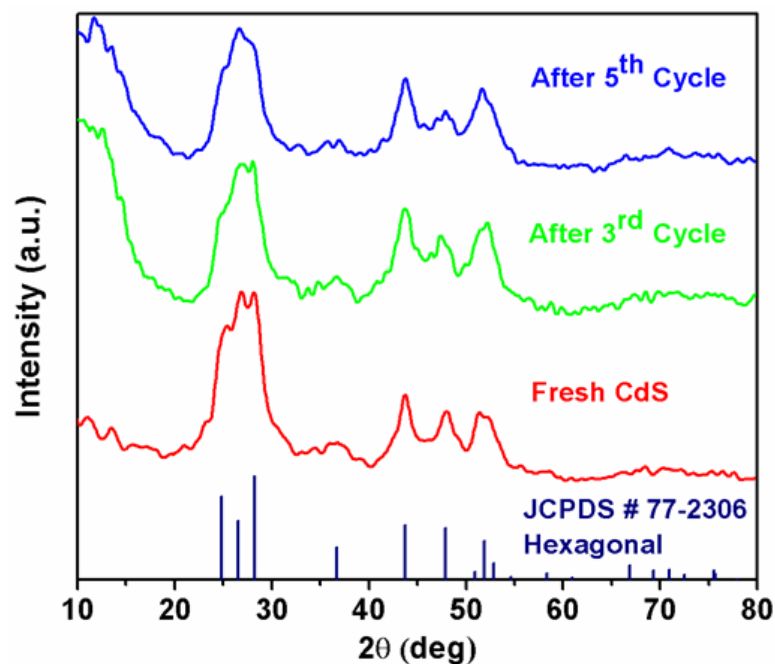


Figure. 4.16. XRD pattern of as synthesized and recycled CdS nanoparticles. The CdS phase was retained after five consecutive cycles.

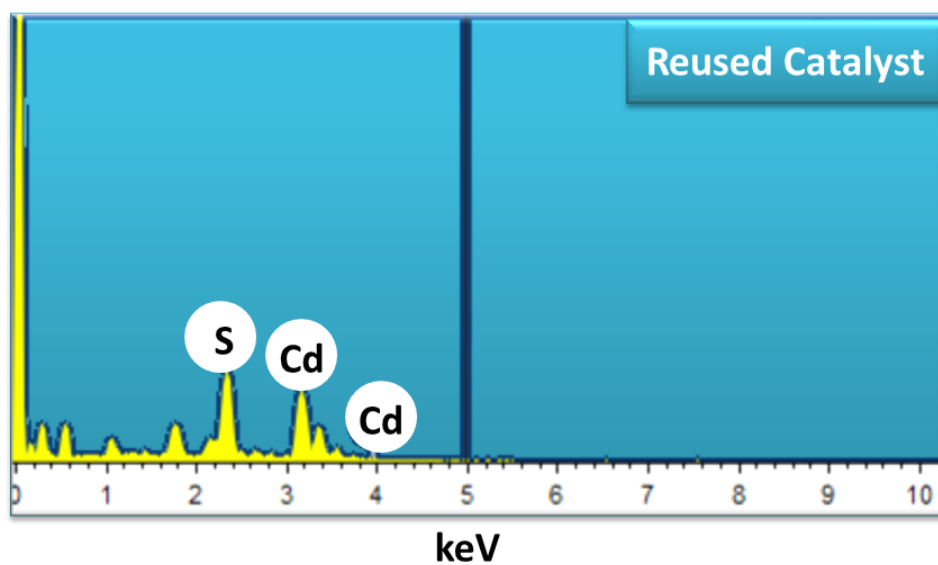


Figure 4.17. Elemental analysis by the energy dispersive X-ray spectroscopy. Atomic ratios were matched with the theoretical values. EDAX spectrum of reused CdS catalyst.

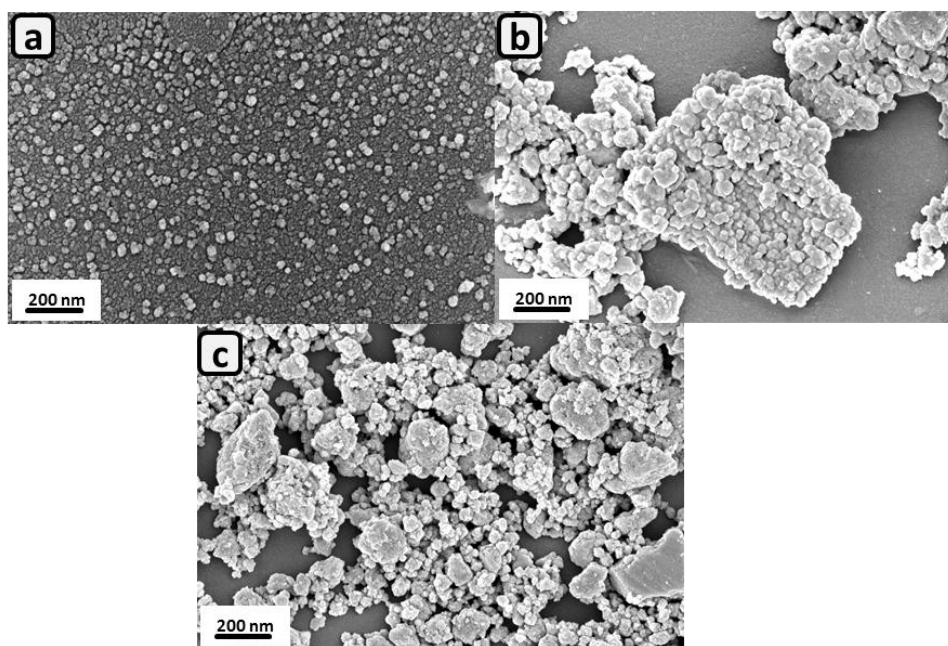


Figure. 4.18. FESEM micrographs of the reused CdS NPs. (a) FESEM micrographs after 1st cycle. (b) After 3rd cycle, spherical of particles was slightly agglomerated. (c) After 5th cycle, spherical shape of particles was transformed into bulky shapes.

4.4. Summary

In this chapter, the HMDS-assisted synthetic methodology was tested for the synthesis of surfactant free CdS NPs. The method was useful for the synthesis of CdS in 2-3 g scale. We have utilized the bare CdS NPs as catalyst for Cr(VI) remediation in aqueous solution at acidic pH under visible light ($\lambda > 420$ nm) irradiation, and showed that the HDMS-based synthesis leads to highly active CdS NPs, rivalling with common CdS-supported catalyst. The photocatalytic activity was explained by the availability of clean surfaces without any organic surfactant molecules surrounding the CdS NPs, which supported a fast separation of photoexcited electrons under visible light illumination.

The fast charge separation was evaluated by transient photocurrent responses over on–off cycles of intermittent light irradiation and by electrochemical impedance spectra (EIS). The observed rapid and uniform transient photocurrent response indicated an efficient separation of photoexcited electron–hole pairs from the as-prepared CdS NPs under visible light irradiation. The intensity of photocurrent was significantly higher than that reported in the literature for the particles without

support materials. A semicircle portion of small diameter at high frequencies in Nyquist plot showed the lowest resistance to the interfacial charge transfer. This observation confirmed the efficient separation of photoexcited electron–hole pairs from the surfactant and support material free CdS NPs under visible light irradiation. To the best of our knowledge, this is the first report of effective reduction of Cr(VI) by CdS NPs without any surfactant molecules in surrounding or support materials.

4.5. References

1. C.M.A. Parlett, K. Wilson and A.F. Lee, *Chem. Soc. Rev.* 2013, **42**, 3876–3893.
2. Z-R. Tang, B. Han, C. Han and Y-J. Xu, *J. Mater. Chem. A*, 2017, **5**, 2387–2410.
3. S. Wang, J. Li, X. Zhou, C. Zheng, J. Ning, Y. Zhonga and Y. Hu., *J. Mater. Chem. A*. 2014, **2**, 19815–19821.
4. R. C. Pawar and C. S. Lee, *Materials Chemistry and Physics*. 2013, **141**, 686–693.
5. W. Yang, Y. Liu, Y. Hu, M. Zhou and H. Qian, *J. Mater. Chem.* 2012, **22**, 13895–13898.
6. M. Gratzel, *Nature*, 2001, **414**, 338–344.
7. A. Olea and P.J. Sebastian, *Sol. Energy Mater. Sol. Cells*, 1998, **55**, 149–156.
8. D.H. Xiang, Y.B. Zhu, C.J. Cai, Z.J. He, Z.S. Liu, D.G. Yin and J. Luo, *Phys. E*. 2011, **44**, 733–737.
9. Q. Li, B.D. Guo, J.G. Yu, J.G. Ran, B.H. Zhang, H.J. Yan and J.R. Gong, *J. Am. Chem. Soc.* 2011, **133**, 10878–10884.
10. Y. Guo, J. Wang, Z. Tao, F. Dong, K. Wang, X. Ma, P. Yang, P. Hu, Y. Xu and L. Yang, *CrystEngComm* 2012, **14**, 1185–1188.
11. J. Frenzel, J-O. Joswig and G. Seifert, *J. Phys. Chem. C*, 2007, **111**, 10761–10770.
12. L-W. Liu, S-Y. Hu, Y. Pan, J-Q. Zhang, Y-S. Feng, X-H. Zhang and *Beilstein J. Nanotechnol.* 2014, **5**, 919–926.
13. Q. Li and R.M. Penner, *Nano Letters*. 2005, **5**, 1720–1725.

Chapter 4

14. Y-M. Fang, J. Song, R-J. Zheng, Y-M. Zeng and J-J. Sun, *J. Phys. Chem. C*, 2011, **115**, 9117–9121.
15. J.R. Lakowicz, I. Gryczynski, Z. Gryczynski and C.J. Murphy, *J. Phys. Chem. B*, 1999, **103**, 7613-7620.
16. R. Demir, S. Okur and M. Seker, *Ind. Eng. Chem. Res.* 2012, **51**, 3309–3313.
17. X. Liu, L. Pan, T. Lv, G. Zhu, Z. Sun and C. Sun, *Chem. Commun.* 2011, **47**, 11984–11986.
18. K. Ramasamy, M.A. Malik, M. Helliwell, J. Raftery and P. O'Brien, *Chem. Mater.* 2011, **23**, 1471–1481.
19. M. Chen, Y.N. Kim, C. Li and S.O. Cho, *Crystal Growth & Desin.* 2008, **8**, 629–634.
20. S. D. Wu and Z. Zhu, *Mater. Sci. Eng. B*, 2002, **90**, 206- 208.
21. S. Gorer, J. A. Ganske, J. C. Hemminger and R. M. Penner, *J. Am. Chem. Soc.* 1998, **120**, 9584-9593.
22. D. Xi, H. Zhang, S. Furst, B. Chen and Q. Pei, *J. Phys. Chem. C*, 2008, **112**, 19765–19769.
23. M. A. Anderson, S. Gorer and R. M. Penner, *J. Phys. Chem. B*, 1997, **101**, 5895-5899.
24. (a) K. Kandasamy, H.B. Singh and S.K. Kulshreshtha, *J. Chem. Sci.*, 2009, **121**, 3, 293–296. (b) G. Hemakanthi, B.U. Nair and A. Dhathathreyan, *Proc. Indian Acad. Sci. (Chem. Sci.)*, 2000, **112**, 2, 109–118.
25. F. T. Johra and W-G. Jung, *Applied Surface Science*, 2014, **317**, 1015–1021.
26. H-G. Agileo, F. Tzompantzi, R. Gomez and C-B. Hector, *Materials Letters*, 2014, **115**, 147–150.
27. X. Liu, L. Pan, T. Lv and Z. Sun, *Journal of Alloys and Compounds*, 2014, **583**, 390–395.
28. P. R. Wittbrodt and C. D. Palmer, *Environ. Sci. Technol.* 1995, **29**, 255–263.
29. W. Wang, M. O. Tade and Z. P. Shao, *Chem. Soc. Rev.* 2015, **44**, 5371–5408.
30. Z. H. Wang, R. T. Bush, L. A. Sullivan and J. S. Liu, *Environ. Sci. Technol.* 2013, **47**, 6486–6492.
31. W. J. Jiang, M. Pelaez, D. D. Dionysiou, M. H. Entezari, D. Tsoutsou and K. O'Shea, *Chem. Eng. J.* 2013, **222**, 527–533.

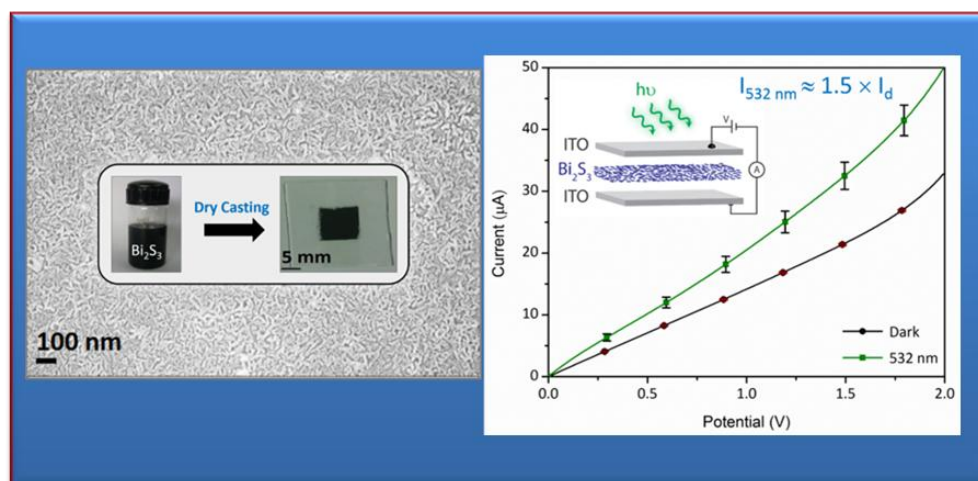
32. N. Zhang, M-Q. Yang, Z-R. Tang and Y-J. Xu, *Journal of Catalysis*. 2013, **303**, 60–69.
33. S. Liu, N. Zhang, Z-R. Tang and Y-J. Xu, *ACS Appl. Mater. Interfaces*, 2012, **4**, 6378–6385.
34. (a) B.G. Kumar and K. Muralidharan, *J. Mater. Chem.* 2011, **21**, 11271-11275. (b) B. G Kumar and K. Muralidharan, *Eur. J. InorgChem*, 2013, 2102-2108. (c) B. G Kumar and K. Muralidharan, *RSC Adv*, 2014, **4**, 28219-28224. (d) B. G. Kumar, B. Srinivas, M. D. Prasad and K. Muralidharan, *J. Nanopart. Res.* 2015, **17**, 325-336. (e) B. Srinivas, B. G. Kumar and K. Muralidharan, *J. Mol. Catal. A: Chem.* 2015, **410**, 8-18. (f) B. Srinivas, B. G. Kumar and K. Muralidharan, *ChemistrySelect*, 2017, **2**, 4753–4758.
35. W. Zhao, C. Liu, L. Cao, X. Yin, H. Xu and B. Zhang, *RSC Adv.* 2013, **3**, 22944–22948.
36. Y. C. Zhang, J. Li, M. Zhang and D. D. Dionysiou, *Environ. Sci. Technol.* 2011, **45**, 9324–9331.
37. B. Weng, S. Liu, N. Zhang, Z. R Tang and Y. J. Xu, *J. Catal.* 2014, **309**, 146–155.
38. B. Weng, X. Zhang, N. Zhang, Z. R. Tang and Y. J. Xu, *Langmuir*, 2015, **31**, 4314–4322.
39. N. Nasrallah, M. Kebir, Z. Koudri and M. Trari, *Journal of Hazardous Materials*. 2011, **185**, 1398–1404.
40. Ch. Swapna, N. Ravikiran, G. Ramakrishnan and S. Roy, *ACS Sustainable Chem. Eng.* 2016, **4**, 974–982.
41. Z. Chen, R. Naidu and A. Subramanian, *J. Chromatogr. A*, 2001, **927**, 219–227.
42. W. Wang, Y. Lu, Y. Xu, K. Wu, J. Huang, C. Ji and S.O. Ryu, *CrystEngComm* 2016, **18**, 4681-4687.
43. C. Song, Y. Feng, W. Shi and C. Liu, *CrystEngComm* **2016**, *18*, 7796-7804.
44. Z. Chen and Y-J. Xu, *ACS Appl. Mater. Interfaces*, 2013, **5**, 13353–13363.
45. S. Zhang, W. Xu, M. Zeng, J. Li, J. Xu and X. Wang, *Dalton Trans.* 2013, **42**, 13417-13424.

Chapter 5

Photo-responsive Bi_2S_3 nanoflakes: Synthesis and device fabrication at ambient conditions

Abstract

This chapter describes hexamethyldisilazane (HMDS) assisted syntheses of Bi_2S_3 nanoflakes and its photo-responsive properties. Since the optoelectronic devices consist multicomponent interfaces, the synthesis of NPs and fabrication of devices play a significant role in quality, cost and fast fabrication of devices. The wet chemical synthesis holds a great promise of controlling these factors. Herein, we have developed a wet chemical method for the synthesis of one-dimensional Bi_2S_3 nanoflakes and demonstrated its photo-responsivity by fabricating prototype device by dry-casting of Bi_2S_3 suspensions on the electrodes. A key advantage of the present approach was the synthesis and fabrications were carried out under ambient conditions.



Chapter 5

5.1. Introduction

Material processing technology is a key industrial component for the mass production of optoelectronic devices [1-12]. The solution processing technology offers an advantage of making the devices at ambient conditions because of the possibility of making devices from solution using any of the following techniques; spray coating [1, 2], mist coating [3], spin coating [4, 5], dry casting [6, 7], dip coating [8, 9], roll-to-roll printing [10] and inkjet printing [11, 12]. Furthermore, these processing methods allow the fabrication of flexible modern electronics by integrating nanomaterials with any substrates. Thus, the nanomaterials prepared by wet chemical methods offer the way for cheap and fast processing technology.

Photodetectors have received much attention as an important class of optoelectronic devices owing to their extensive use in electronic eyes [13-15], night vision devices [16], tumour detection [17], imaging [18, 19] and quality control of industrial products [20]. Photodetectors made out of inorganic materials will have tunable absorption, stability, and high quantum yield. Bi_2S_3 is a useful photo-responsive material with a direct band gap of 1.3 eV [21] and a large absorption coefficient [22]. The high availability of sulphide and bismuth in the earth crust is also an important factor for the use of Bi_2S_3 for optoelectronic applications. While a significant work on the Bi_2S_3 based photodetector is known [23-32], there are still a need for the search for the best synthetic methods [33-48] and simplicity in processing methods.

In this work, we have demonstrated a novel synthesis of Bi_2S_3 (bismuth sulphide) NPs using the HMDS-assisted method. Interestingly, the Bi_2S_3 nanoflakes have been synthesized in a short duration (3 h) using readily available bismuth chloride and thiourea as starting materials. The Bi_2S_3 nanoflakes had width 15-82 nm with the average 48 ± 15 nm and the length up to few microns and are obtained in a high morphological yield (~98%). The reaction produced one-dimensional nanoflakes without any seeds or shape selection procedures and they were free from the capping agents.

To understand the photo-responsive properties of Bi₂S₃ nanoflakes, we have fabricated a prototype of photodetectors with a configuration of ITO/Bi₂S₃/ITO, by dry-casting the Bi₂S₃ suspensions. The devices showed a green light-induced conductivity that had a linear response to the intensity of the light. Further, the transient measurements established a reversible "on" and "off" switching phenomena with the rise-and-decay time as 1.11 ± 0.10 ns and 2.06 ± 0.21 ns. Herein, we present the synthesis and photo-responsive study of organic surfactant free Bi₂S₃ nanoflakes.

5.2. Experimental section

5.2.1. Materials

The chemicals used in the syntheses, bismuth (III) chloride (BiCl₃), thiourea and hexamethyldisilazane (HMDS) were purchased from Sigma-Aldrich and used as received. All solvents were purified using standard procedures. Instrumentation and sample preparation are similar to the one discussed in Chapter 2 and Section 2.2.4.

5.2.2. Synthesis of Bi₂S₃ nanoflakes

We have used the HMDS-assisted method to synthesize Bi₂S₃ nanoflakes. [49, 50, 51] In a typical method, bismuth(III) chloride (0.20 g, 0.63 mmol) and thiourea (0.072 g, 0.94 mmol) were added to the reaction flask. Then, HMDS (5.0 mL, 23.8 mmol) was injected into the flask and stirred for the homogeneity. Then the reaction mixture was heated to reflux and maintained for 3 h. The black precipitate was obtained at the end of the reaction. The reaction mixture was smelly, and the precipitate was separated out by the filtration. (Caution: intermediate is smelly and will widely diffuse in the air). Then the precipitate was washed with methanol (20 mL \times 3) and acetone (20 mL \times 2) by centrifugation (3500 rpm, 5 min). Purification procedures were carried out under ambient conditions. The product was dried under high vacuum (120 °C, 1 h) and the fine black powder was obtained. The reaction procedure was reproducible, and yield was $62 \pm 4\%$.

Chapter 5

5.2.3. Electronic measurements

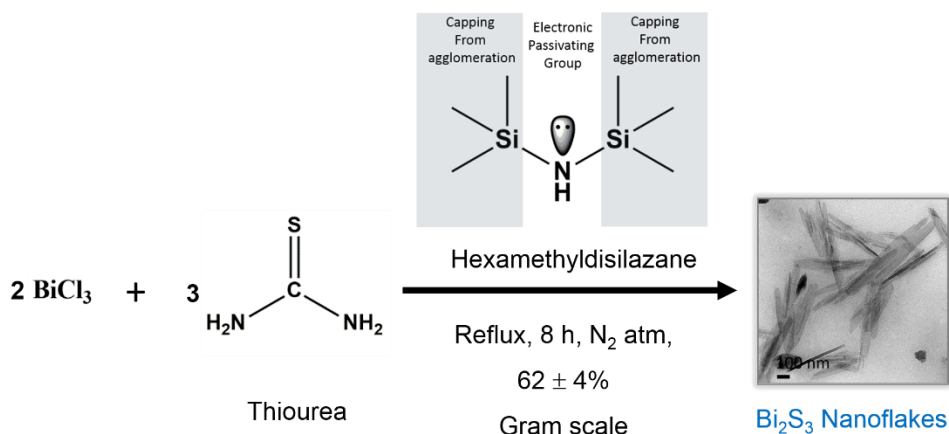
Device configuration was ITO/Bi₂S₃/ITO. The prototype photodetector devices are made from dry casting the samples on surface of the ITO plates. Conductive indium tin oxide glass plates were used (resistance = 60 $\Omega \cdot \text{sq}^{-1}$). The active area of the device was 1 cm \times 1 cm. Before the coating, ITO plates were washed with a detergent solution followed by the ultrasonication in acetone. Electrode area of the device was directed by masking with teflon tape. Then etching of the device was performed on the other ITO plate (10% of HCl solution; 3 h). Then plates were washed with IPA solution, and the sample was coated with isopropyl alcohol suspension of Bi₂S₃ nanoflakes (40 mg in 1.5 mL). The coated samples were air-dried for a uniform active layer. Finally, devices were made by binding the coated plate with other ITO by binder clips. Two-probe method was used to study the optoelectronic properties. The photoconductivity of the device was analysed by I-V measurements. Green LED (532 nm, 122 W. m⁻², bandwidth = 22 nm) was utilized for the illumination of the device. Green LED was controlled by Zahner Zennium electrochemical workstation (Zahner, Germany). In transient studies, the light intensity of 90 W. m⁻² was used. Reproducibility of the devices was confirmed by three different batches of the synthesis and device making. All the analytical data were plotted with standard error. Device measurements were conducted under ambient conditions. For the energy level diagram, energy values were adopted from the literature [65].

Impedance measurements were carried out in Zahner Zennium electrochemical workstation and procedures are mentioned below. Two-probe analytical method was utilized for the impedance measurements. The Bi₂S₃ was made as a pellet under pressure (3 ton) with pellet dimensions of radius = 0.8 cm and thickness = 0.062 cm. The resistance was calculated from the impedance spectroscopy. We utilised frequency range from 100 Hz to 4 MHz with AC amplitude of 20 mV. The temperature was stabilized for 30 min before the measurements. Measurements were repeated three times and standard error was reported in this chapter. Bulk resistance was calculated from the real axis intercept of the semicircle in the Nyquist plot.

5.3. Results and discussion

5.3.1. Synthesis of Bi₂S₃ nanomaterials

We have successfully synthesized organic-free Bi₂S₃ nanoflakes by the HMDS-assisted method with yield of $62 \pm 4\%$. We have used soluble thiourea in the present procedure as a sulphur source due to the prospect of easy handling in pre and post-synthetic manipulations. In these reactions, HMDS performed dual role as a capping agent as well as a solvent. Bulk trimethylsilyl group of HMDS acted as capping group and avoided the agglomeration of NPs (Scheme 5.1) during their formation. Hence, HMDS stabilized the NPs and yielded quantum confined one-dimensional Bi₂S₃ nanoflakes. The key advantage of the method was that capping agent (HMDS) could be removed from the NPs efficiently by high vacuum. Thus, NPs were free from insulating organic layer. Because of mild reaction conditions and simple purification procedure, the present synthetic design is worthy for scale up. Thus, we have produced 2 g of nanoflakes and used it for device fabrication. Therefore, the current synthetic procedure is robust for large scale synthesis also offers quantum confined Bi₂S₃ nanoflakes.



Scheme 5.1. The modified HMDS-assisted synthesis of Bi₂S₃ nanoflakes.

5.3.2. Structure and composition of Bi_2S_3 nanoflakes

Primarily, the acquired powder X-ray diffraction patterns (Figure 5.1) confirmed the formation of Bi_2S_3 in our reaction. Intensities and position of observed lines were matching with the standard pattern of orthorhombic structure bulk Bi_2S_3 (JCPDS Library; Card # 84-0279); but with a preferred orientation of (1 1 1) and (1 2 1) planes. Supported by HRTEM images (Figure 5.7a), we have identified (1 2 1) planes as responsible for the flake shape. The absence of signature of secondary amines or any other signals related to organic compounds in the FTIR spectrum (Figure 5.2) ruled out the possibility of broadening of lines by organic impurities. Therefore, broadening of lines in diffraction patterns was attributed only to the nano-regime of the Bi_2S_3 flakes. Thus, the absence of the capping agent (HMDS) on the surface of the Bi_2S_3 nanoflakes was self-evident.

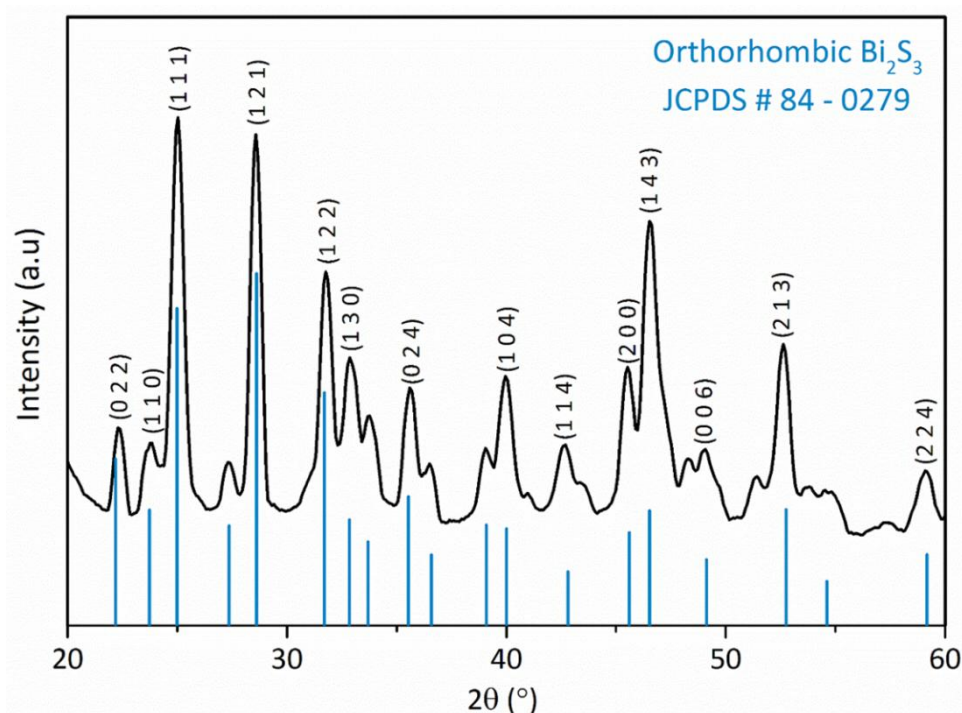


Figure 5.1. Primary characterization of Bi_2S_3 nanoparticles. (a) PXRD pattern of the nanoflakes. We observed that the obtained pattern matched with orthorhombic Bi_2S_3 (JCPDS # 84-0279).

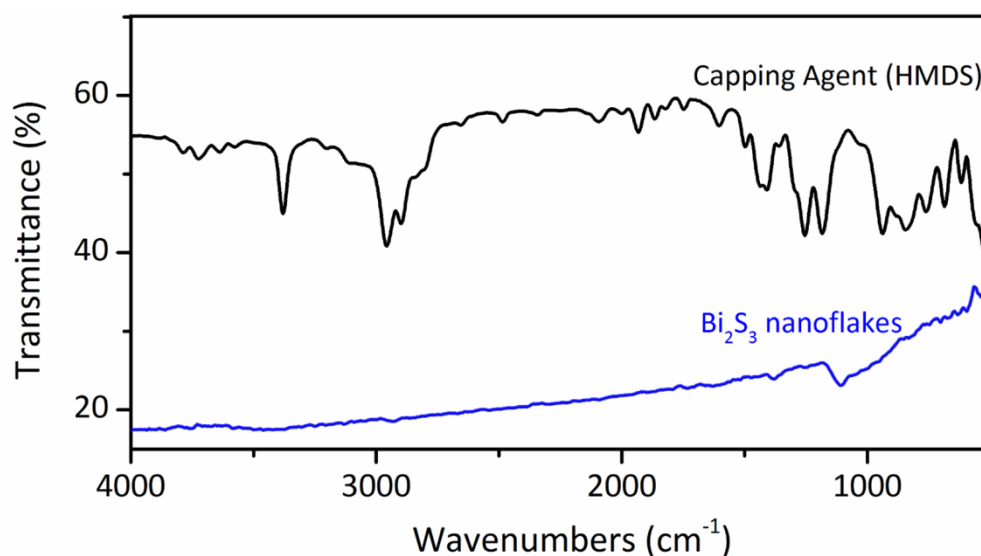


Figure 5.2. Primary characterization of Bi_2S_3 nanoparticles. FTIR spectrum of the nanoflakes. HMDS spectrum was plotted for the visual comparison.

Scanning electron microscopy images of Bi_2S_3 (Figure 5.3) showed a uniform distribution of particles of size ranging up to 2 μm , but with a high morphological yield of nanoflakes ($\sim 98\%$). Any change in reaction parameters like temperature, stoichiometry, and solvents did not alter the morphology and dimensions of NPs obtained. EDAX measurements showed the stoichiometric ratio of Bi:S as 1.7: 3 which clearly showed 3% bismuth deficiency in NPs obtained from our reactions (Figure 5.4). Bismuth ratio was not improving even after the addition of excess BiCl_3 . However, the bismuth deficiency did not influence the properties of Bi_2S_3 nanoflakes or fabricated devices. EDAX did not have the signature of Si and Cl, which showed the purity of NPs and the absence of the capping agent. This observation explained that nanoflakes were free from the insulating organic layer on the surface of the NPs. Surprisingly, even in the absence of the capping agent, nanoflakes were well separated and we did not observe agglomeration. Thus, the growth or stoichiometry of the NPs and morphological yield was insensitive to the experimental parameters.

Chapter 5

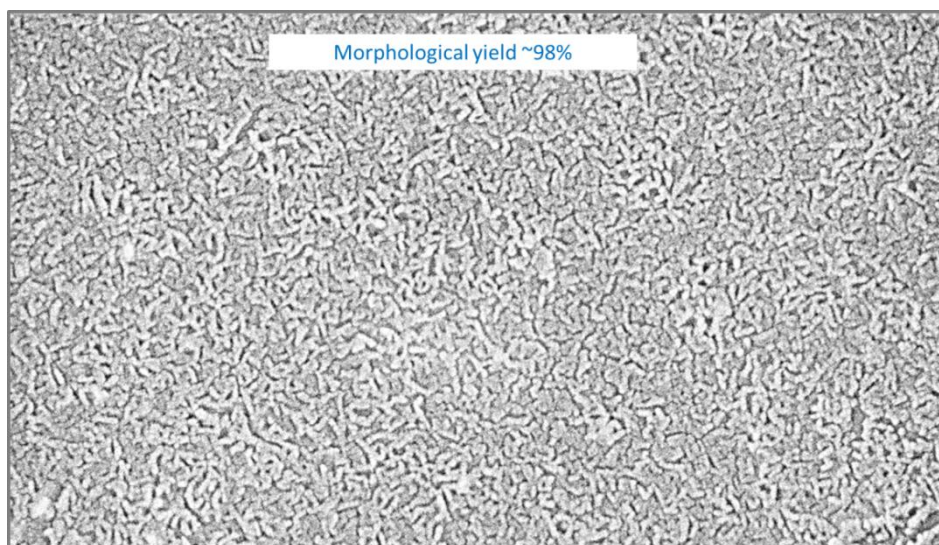


Figure 5.3. Primary characterization of Bi_2S_3 nanoparticles. FESEM micrographs of the nanoparticles.

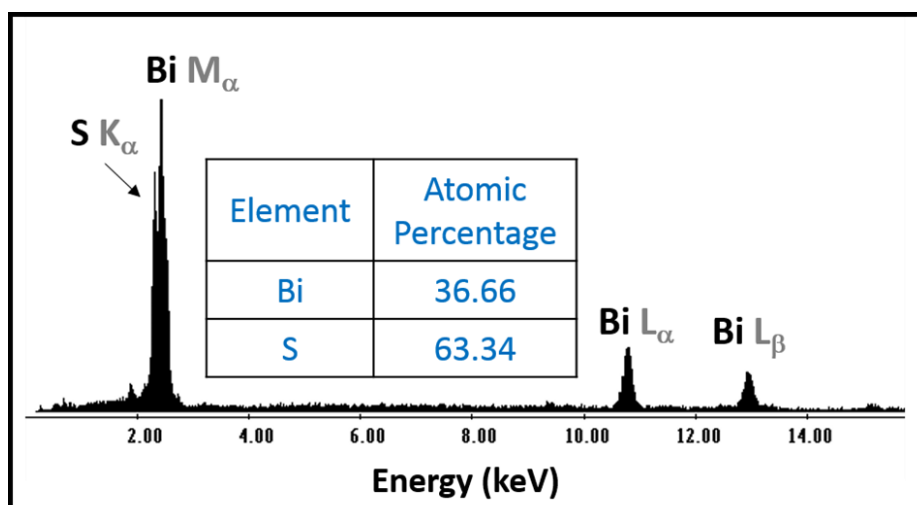


Figure 5.4. Primary characterization of Bi_2S_3 nanoparticles. EDAX spectrum of the nanoflakes. Atomic ratio showed that obtained product was slightly bismuth deficient (3%).

TEM micrographs confirmed the flake shape of the NPs obtained from the present procedure (Figure 5.5a and 5.6a, b). TEM micrographs also showed the high abundance of NPs (Figure 5.5a). The nanoflakes had the width of 15-82 nm with average of 48 ± 15 nm (Figure 5.5b). Also the nanoflakes had the length up to few micrometers. Since the width of few flakes was less than Bohr radius of Bi₂S₃ (~30 nm) [52], weak confinement along the width was observed (spectrally determined band gap = 1.40 eV; Figure 5.8b). The width of the flakes was constant along the length but the edges were sharp. The observed modification at the edges might be to tolerate the strain in growth [50]. Selected area diffraction (SAED) showed a clear dotted pattern which was indicative of the single-crystalline nature of NPs (Figure 5.6c) and we did not observe rings characteristic of amorphous organic capping agents indicating their absence.

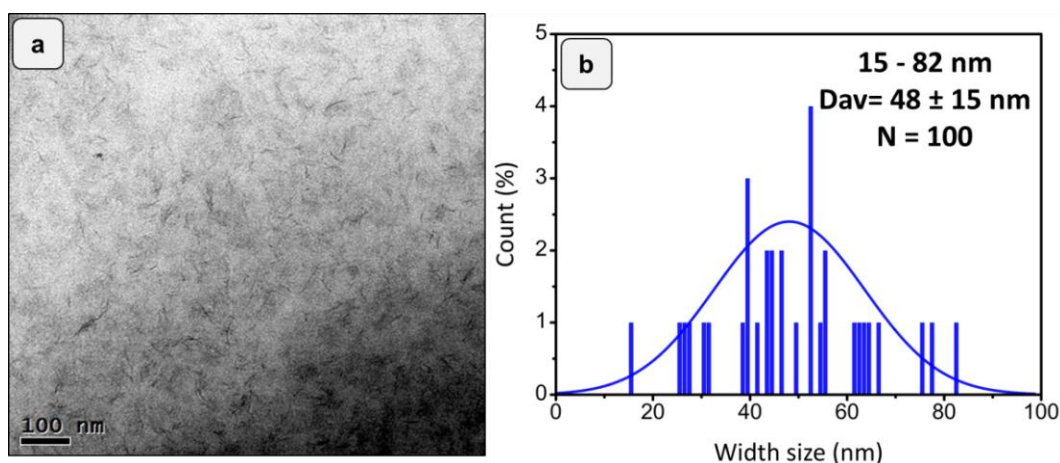


Figure 5.5. (a) Large area TEM image of the Bi₂S₃ nanoflakes. Abundance of the flakes was high. Flakes were thin and less visible in the low magnification. (b) Particle distribution diagram of the Bi₂S₃ nanoflakes.

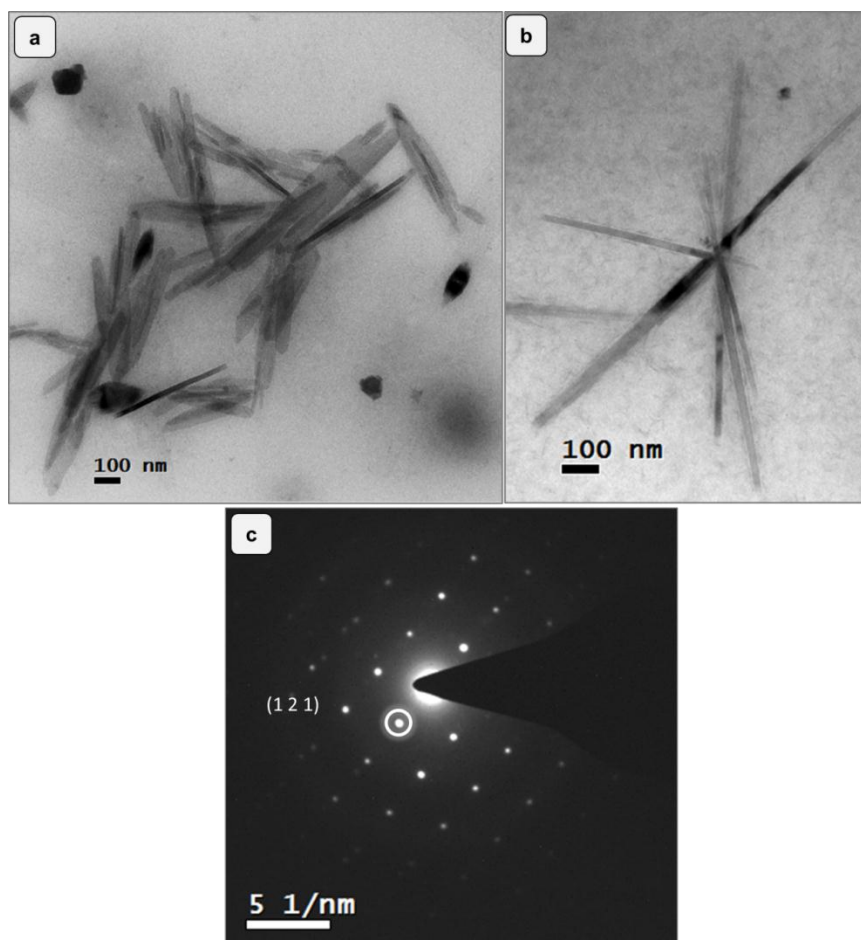


Figure 5.6. (a, b) are TEM micrographs of the Bi₂S₃ nanoparticles. (c) SAED pattern of the flake. The circle indicates dominant (1 2 1) planes.

Parallel to the observation in the PXRD pattern, the HRTEM micrographs (Figure 5.7a) showed (1 2 1) as dominating planes. Two-dimensional FFT (Figure 5.7b) also confirmed construction of nanoflakes by principal (1 2 1) and (1 3 0) planes. Moreover, we have not observed any dislocation, distortion, and twins in lattices of nanoflakes. Hence, the oriented growth mechanism did not influence the flake shape of the NPs [53]. Since there was no capping agent on the surfaces to minimize the surface energy of the particles, the planes might have grown to flake shape. Nanoflakes were crystalline along the whole length of the axis as confirmed by HRTEM studies. A curious observation is the high crystallinity was achieved using a moderate reaction temperature. Altogether the HRTEM observations suggested that nanoflakes were single crystals and structurally constructed to flakes by (1 2 1) and (1 3 0) planes.

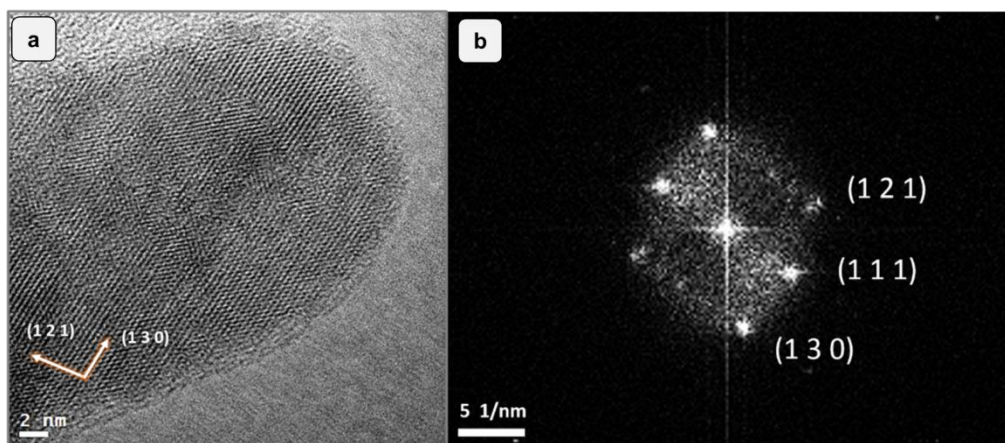


Figure 5.7. (a) HRTEM micrograph of the Bi_2S_3 nanoparticles. (b) FFT analysis of whole flake in the image (a).

5.3.3. Optical properties

The solid state optical spectrum showed broad characteristic absorption of the Bi_2S_3 NPs with the maxima positioned at ~ 602 nm (Figure 5.8a). Due to the poor solubility of Bi_2S_3 NPs solid phase spectrum was recorded. The band gap of Bi_2S_3 was calculated from the absorption spectra (Figure 5.8b) using the Kubelka-Munk method by assuming Bi_2S_3 as a direct band gap material [54]. We determined band gap as 1.40 eV which was slightly higher than that reported for bulk band gap (1.3 eV) [21]. Since the width size of fewer flakes is lower than the Bohr radius (~ 30 nm), we attributed the minor blue shift to weak confinement of carriers in the width of the nanoflakes.

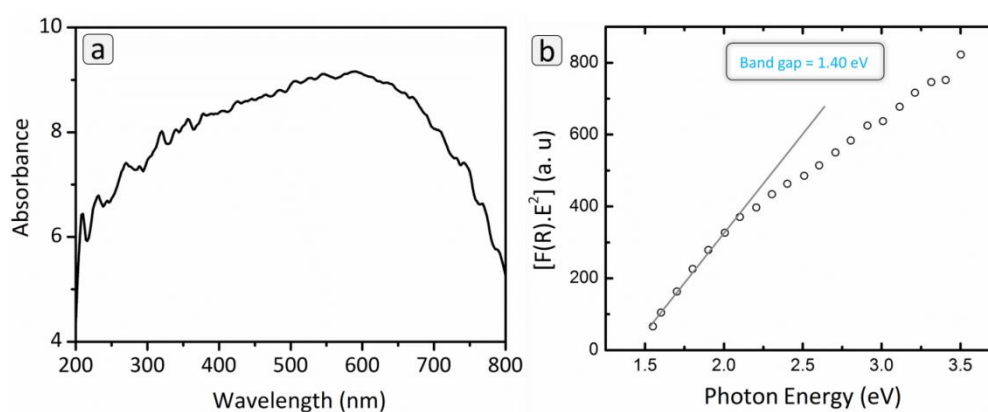


Figure 5.8. (a) Solid state UV analysis of the Bi_2S_3 flakes. The broad absorption spectrum spanning the entire UV-Visible region. (b) Band gap calculation by Kubelka-Munk method. Straight line represents the fit with $R^2 = 0.99$.

Chapter 5

5.4. Electronic properties

5.4.1. Device construction

The capping agent free NPs are critical for efficient optoelectronic applications [55, 56], since these capping agents will create an insulating barrier on every NP and decrease the efficiency of the devices. Hence, we have synthesized organic-free Bi_2S_3 nanoflakes and built a prototype device of the photodetector (Figure. 5.9). Among the various processing techniques, dry-casting is an attractive laboratory-friendly technique to fabricate the devices with small substrates (~ 1 cm). Moreover, the dry-casting technique does not require any costly equipment. The thickness of the active layer in the device can be controlled by the concentration of the NPs. We fabricated the devices by binding the dry-casted Bi_2S_3 active layer between two ITO electrodes with instrument configuration of ITO/ Bi_2S_3 /ITO, and the active area was $1\text{ cm} \times 1\text{ cm}$.

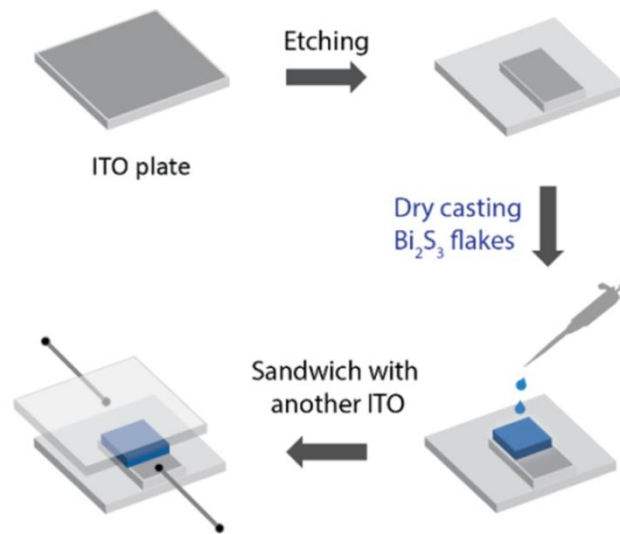


Figure 5.9. (a) Device making from the dry casting. Devices were made by binding the active layer between ITO electrodes. Active area of the device was $1\text{ cm} \times 1\text{ cm}$.

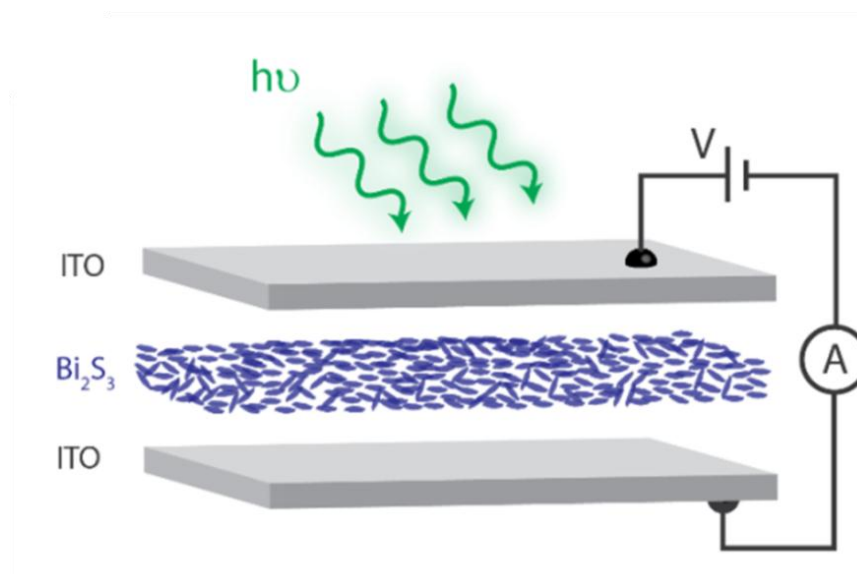


Figure 5.10. Cross sectional view of the device with circuits.

Figure 5.9 illustrates the fabrication process of the device at ambient conditions. At first, the active layer was made by the dry-casting of the suspension of Bi_2S_3 nanoflakes (40 mg in 1.5 mL) on the etched ITO substrate. The non-active area of ITO plates was etched to avoid shorting of the circuit while binding. We observed the dewetting of the Bi_2S_3 layer from the ITO substrates when more concentration than the specified in experimental section was used for casting. Slow evaporation of Bi_2S_3 suspension of the NPs helped in achieving a high-quality active layer. Then, another ITO plate was sandwiched with binder clips to make the final device. An identical parallel ITO electrode structure was used to support the charge collection (Figure 5.10). Figure 5.11 explains the working principle of the device. Illumination by light generated a photocurrent while charge separation occurred in ITO junctions. Three devices were analysed to check the reproducibility of performance. The performance of the device was stable in air and no degradation was observed after two months.

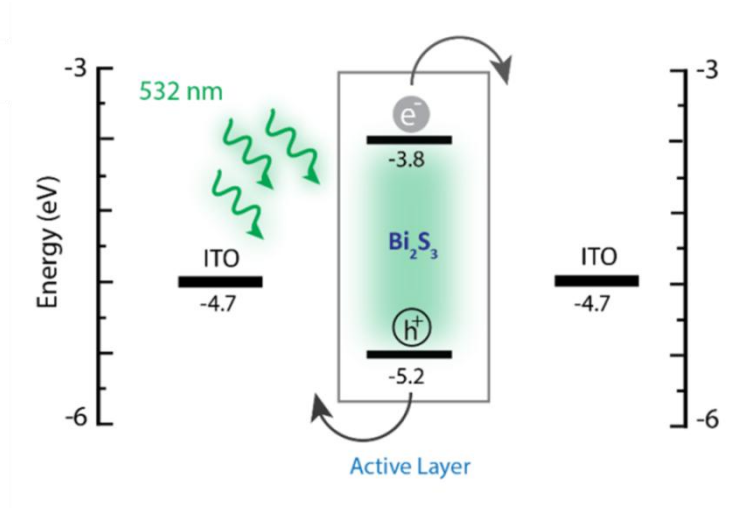


Figure 5.11. Energy level diagram of the device components.

5.4.2. I-V Studies

We evaluated I-V characteristics of the devices made from Bi₂S₃ nanoflakes. Figure 5.12 shows the representative I-V curves of devices under dark and illuminated conditions. Illumination of device by green light (532 nm, 122 W. m⁻²) showed the enhanced photoconductivity compared to dark condition ($I_{532 \text{ nm}} \approx 1.5 \times I_d$). Both dark and illuminated conditions exhibited a linear response. The linear behaviour indicated that Ohmic contact was established between the nanoflakes and the ITO [57]. The change in slope of the curves between dark and illuminated conditions specified increase in current with the illumination which indicates high sensitivity. We have observed photoexcited current of 50 μA at the bias voltage of 2 V. Compared to the photocurrent (46 μA) generated by the device of similar Bi₂S₃ architecture reported earlier [23], we have achieved slightly higher photocurrent of 50 μA at the increased voltage (2 V). Thus, the capping agent free nature of the NPs enhanced the photocurrent. The observed photocurrent generation even below 1 V can be attributed to the low resistance of the devices. Above 1 V, the difference between the dark current and photocurrent increased because the higher voltages enhanced the separation of photogenerated electrons and holes. The error bar in the I-V curves exemplified the stability of the device and the reproducibility of data. Even though ITO plates were bound physically, there was no breakdown of the device during measurements. All these findings indicated that the capping agent free

Bi₂S₃ nanoflakes exhibit considerable photoresponse under the green light illumination.

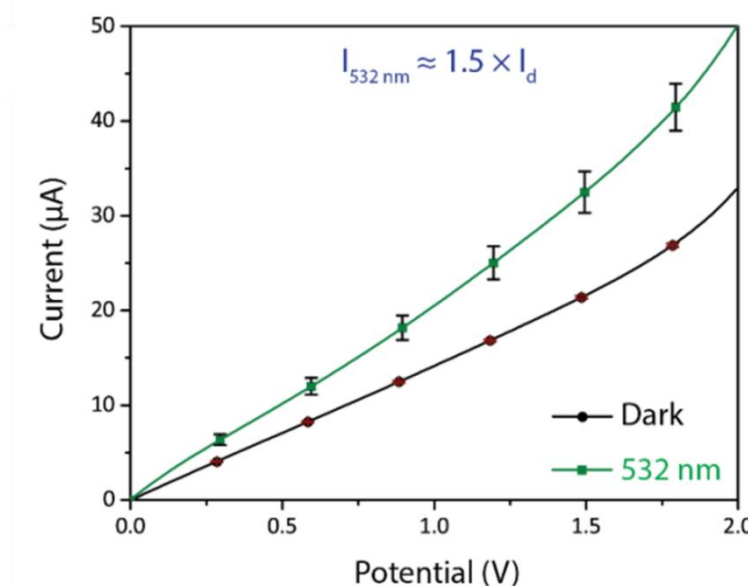


Figure 5.12. Two probe I-V measurements (532 nm, 122 W. m⁻²).

It is to be mentioned that considerable dark current was observed in the devices which can be attributed to trap-assisted current [58-62] and minimal resistance (Section 5.4.5). Since the NPs did not have capping agent on the surfaces, there were more surface traps and less resistance [57-61]. The charges might be trapped in the devices and contribute to the current in dark conditions. It seems that the capping agent free surfaces generated more surface traps leading to moderate device performance. However, we have accomplished the workable photoconductor with a simple device design. Hence, the synthetic method or fabrication procedure requires modification to achieve a balance between surface traps and better conductivity.

5.4.3. Intensity dependent studies

We examined the effect of illumination on the photocurrent (Figure 5.13) by exposing the device to green light of varying intensity but at a fixed wavelength. Interestingly, the photocurrent increased linearly with the intensity of illuminated light according to the power law $I \propto P^{0.070}$. It was observed that photocurrent rose from 37 μA (at dark) and reached a maximum of 44 μA at the 50 W. m⁻². The linear

Chapter 5

increase in the current with the green light indicates more carrier generation in the device. Compared with a standard Bi_2S_3 based photodetectors ($I \propto P^{0.77}$) [27], we have observed little power dependence in the present system. The low responsiveness may be attributed to the reflective ITO glass substrates [63] and surface trap based recombination centers [64]. We have tested the device up to 50 W. m^{-2} without damaging the device performance. These findings indicated the stability of device without any break-down and the robust nature of the Bi_2S_3 nanoflakes at an incident light of high intensity. In summary, the high-intensity illumination can improve the photoresponse of the Bi_2S_3 nanoflakes.

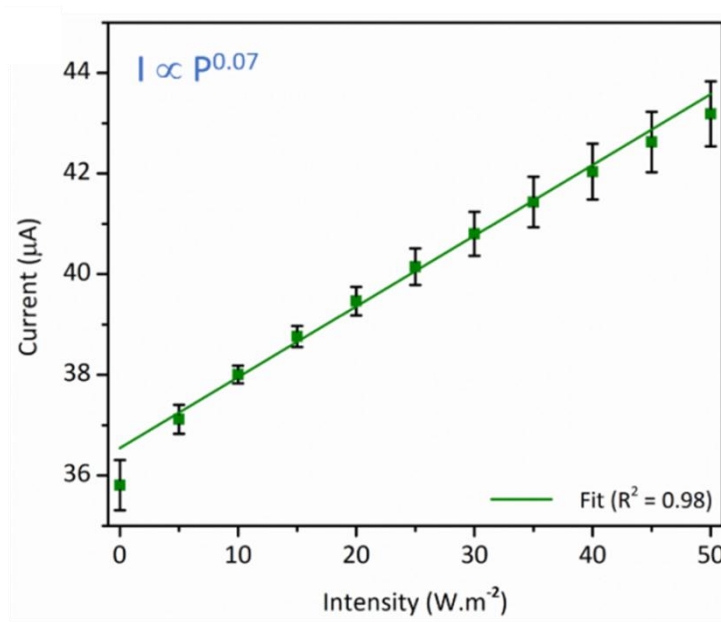


Figure 5.13. Intensity-dependent measurement of the device.

5.4.4. Transient studies

We next evaluated the use of Bi_2S_3 as a photodetector by transient state measurements (Figure 5.14). Square wave pulse of 50 W. m^{-2} with the interval of 40 s was given as an input optical signal to the device and output current was measured. While turned on, the pulse photocurrent increased from 4.5 nA to 5.6 nA. The photocurrent reached the steady state and sustained until it is switched off. The photocurrent curves replicated the pattern of input optical signals. The rise time of the device was calculated as $1.11 \pm 0.10 \text{ s}$ and decay time was $2.06 \pm 0.21 \text{ s}$ (Figure 5.15 and Table 5.1). Rise time was calculated from the interval of 10-90% of its

peak value while the decay time was calculated from the range of 90-10% of its peak value. Since the rise and fall curves are symmetric, the device can produce reliable photodetection. The photocurrent was almost constant during all the cycles. The photocurrent On: Off switching current ratio was 1:1.3. Every cycle was identical and reproducible without any detectable degradation in the device performance. Photocurrent was switchable to the on-off ratio even after the 700 s. Reversibility and stability of photocurrent in the transient studies exemplified the performance of the devices. It is to be mentioned that we have achieved the rise and decay time without any device structure optimization. All these observations indicated that response and decay time were in seconds and the device can detect the fast varying optical signals.

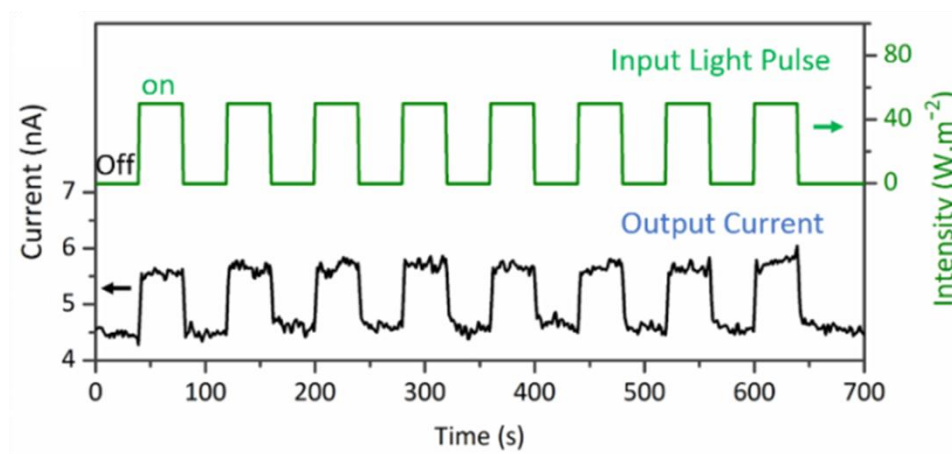


Figure 5.14. Optoelectronic properties of the devices. Transient measurements of the device. For the comparison, Input square pulse is also shown.

Chapter 5

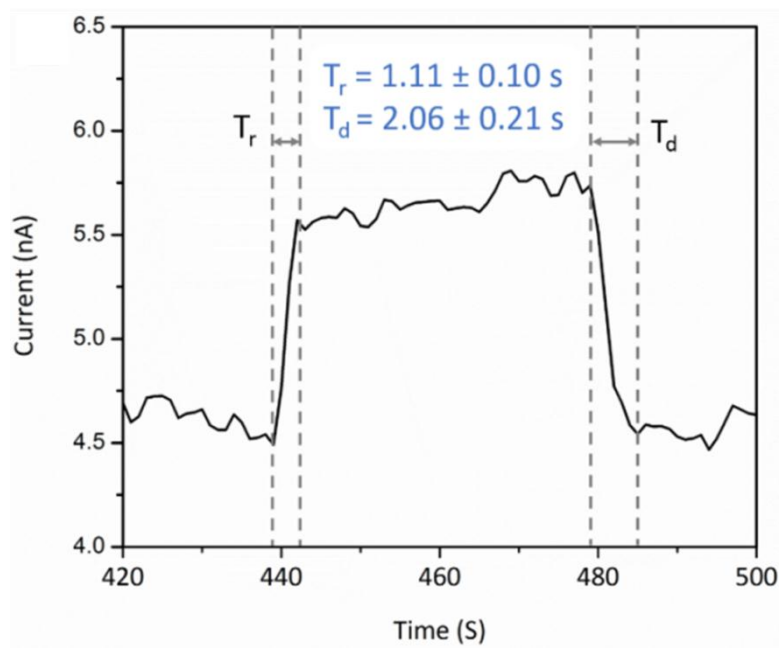


Figure 5.15. Optoelectronic properties of the devices. A magnified cycle of the transient studies.

Table 5.1. Transient studies of Bi_2S_3 photodetector. Values measured from Figure. 5.15.

Cycle	T_r (s)	T_d (s)
1	0.82	2.02
2	1.78	1.40
3	1.01	2.96
4	0.99	2.88
5	1.04	1.76
6	1.01	1.49
7	1.19	2.14
8	1.05	1.89
Mean	1.11	2.06
Standard deviation	0.10	0.21

5.4.5. Impedance analysis

With the intention of making electronic grade nanomaterials, we designed the HMDS-assisted method for making capping agent free NPs [49, 50, 51]. Organic impurity-free NPs expected to have better carrier mobility and hence good conductivity [55]. Hence, impedance analysis was carried out to analyse the effect of the absence of the capping agent on the surfaces. Impedance measurements were performed using the two probe method. Fully expressed semicircles were observed in the analyses (Figure 5.16). The resistance was directly measured by extrapolating the semicircle at the lower frequencies in the Nyquist plot and was found to be $3.15 \pm 0.02 \text{ k}\Omega$. It was in the optimal range of the device operation. There were no other types of resistances (semicircles) observed in the measurements. The small resistance was also responsible for good ohmic contact and linear response in I-V studies. Thus, present synthetic procedure yielded low-resistance NPs for a better optoelectronic application.

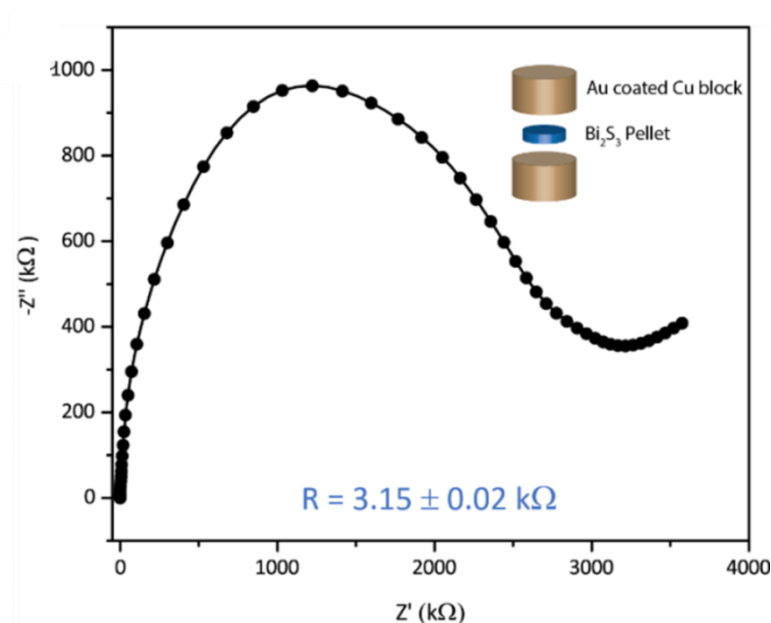


Figure 5.16. Nyquist plot of Bi_2S_3 nanoflakes. Dots are experimental data, and the solid lines are trend line. Inset showing the measurement design (exploded view) of the impedance analysis.

Chapter 5

5.5 Summary

We have developed a solution phase synthetic method for the synthesis of Bi_2S_3 NPs with the capping agent free surfaces to enhance the photoresponse. Using the HMDS-assisted method, 2 g of the Bi_2S_3 nanoflakes was produced. The method was a straight forward and scalable method for synthesis of Bi_2S_3 flakes. A prototype device photodetector was fabricated from Bi_2S_3 nanoflakes using dry casting method. The device exhibited a linear response to the intensity of light under illumination and had repose time of 1.1 s. We found that higher light illumination can enhance photoresponse of the present system. Further, Bi_2S_3 nanoflakes had a resistance of $3.15 \pm 0.02 \text{ k}\Omega$ which was in the optimal range photodetector operation. Altogether, we have demonstrated simplicity in the synthesis, processing and device making. We have also shown that synthesis and device making can be achieved using a minimum energy under ambient conditions.

5.6. References

- [1] K-J. Chen, H-C. Chen, K-A. Tsai, C-C. Lin, H-H. Tsai, S-H. Chien, B-S. Cheng, Y-J. Hsu, M-H. Shih, C-H. Tsai, H-H. Shih and H-C. Kuo, *Adv. Funct. Mater.*, 2012, **22**, 5138–5143.
- [2] I. J. Kramer, J. C. Minor, G. M. Bautista, L. Rollny, P. Kanjanaboos, D. Kopilovic, S. M. Thon, G. H. Carey, K. W. Chou, D. Zhitomirsky, A. Amassian and E. H. Sargent, *Adv. Mater.*, 2015, **27**, 116–121.
- [3] T. Zhu, K. Shanmugasundaram, S. C. Price, J. Ruzyllo, F. Zhang, J. Xu, S. E. Mohny, Q. Zhang and A. Y. Wang, *Appl. Phys. Lett.*, 2008, **92**, 023111.
- [4] J. Zhao, J. A. Bardecker, A. M. Munro, M. S. Liu, Y. Niu, I-K. Ding, J. Luo, B. Chen, A. K. Y. Jen and D. S. Ginger, *Nano Lett.* 2006, **6**, 463-467.
- [5] G. Konstantatos, I. Howard, A. Fischer, S. Hoogland, J. Clifford, E. Klem, L. Levina and E. H. Sargent, *Nature*, 2006, **442**, 180-183.
- [6] Q. Guo, H. W. Hillhouse and R. Agrawal, *J. Am. Chem. Soc.*, 2009, **131**, 11672.

- [7] M. G. Panthani, V. Akhavan, B. Goodfellow, J. P. Schmidtke, L. Dunn, A. Dodabalapur, P. F. Barbara and B. A. Korgel, *J. Am. Chem. Soc.*, 2008, **130**, 16770-16777.
- [8] M. Law, L. E. Greene, J. C. Johnson, R. Saykally and P. Yang, *Nat. Mater.*, 2005, **4**, 455 – 459.
- [9] X. Wang, L. Zhi, K. Müllen, *Nano Lett.*, 2008, **8**, 323-327.
- [10] J. Leppäniemi, T. Mattila, T. Kololuoma, M. Suhonen and A. Alastalo, *Nanotechnology*, 2012, **23**, 305204.
- [11] V. Wood, M. J. Panzer, J. Chen, M. S. Bradley, J. E. Halpert, M. G. Bawendi and V. Bulović, *Adv. Mater.*, 2009, **21**, 2151–2155.
- [12] H. M. Haverinen, R. A. Myllylä and G. E. Jabbour, *Appl. Phys. Lett.*, 2009, **94**, 073108.
- [13] D. Floreano, R. P. Camara, S. Viollet, F. Ruffier, A. Brückner, R. Leitel, W. Buss, M. Menouni, F. Expert, R. Juston, M. K. Dobrzynski, G. L'Eplattenier, F. Recktenwald, H. A. Mallot and N. Franceschini, *Proc. Natl. Acad. Sci.*, 2013, **23**, 9267-9272.
- [14] I. Jung, J. Xiao, V. Malyarchuk, C. Lu, M. Li, Z. Liu, J. Yoon, Y. Huang and J. A. Rogers, *Proc. Natl. Acad. Sci.*, 2011, **108**, 1788.
- [15] H. C. Ko, M. P. Stoykovich, J. Song, V. Malyarchuk, W. M. Choi, C–J. Yu, J. B. Geddes III, J. Xiao, S. Wang, Y. Huang and J. A. Rogers, *Nature*, 2008, **454**, 748-753.
- [16] M. Ettenberg, *Adv. Imag.*, 2005, **20**, 29–32.
- [17] X. Gao, Y. Cui, R. M. Levenson, L. W. K. Chung and S. Nie, *Nature Biotechnol.*, 2004, **22**, 969–976.
- [18] M. Caria, L. Barberini, S. Cadeddu, A. Giannattasio, A. Rusani, A. Sesselego, A. Lai, S. D'Auria and F. Dubecky, *Appl. Phys. Lett.*, 2002, **81**, 1506-1508.
- [19] J. Wang, M. S. Gudiksen, X. Duan, Y. Cui and C. M. Lieber, *Science*, 2001, **293**, 1455-1457.
- [20] A. Abuazza, D. Brabazon and M. A. El-Baradie, *J. Mater. Process. Tech.*, 2003, **143–144**, 875–879.

Chapter 5

- [21] H. Bao, X. Cui, C. M. Li, Y. Gan, J. Zhang and J. Guo, *J. Phys. Chem. C*, 2007, **111**, 12279-12283.
- [22] M. Nair and P. Nair, *Semicond. Sci. Technol.*, 1990, **5**, 1225–1230.
- [23] G. Xiao, Q. Dong, Y. Wang, Y. Sui, J. Ning, Z. Liu, W. Tian, B. Liu, G. Zou and B. Zou, *RSC Adv.*, 2012, **2**, 234-240.
- [24] M. T. S. Nair and P. K. Nair, *Semicond. Sci. Technol.*, 1990, **5**, 1225.
- [25] T. W. Case, *Phys. Rev.*, 1917, **9**, 305.
- [26] R. Suarez, P. K. Nair and P. V. Kamat, *Langmuir*, 1998, **14**, 3236–3241.
- [27] G. Konstantatos, L. Levina, J. Tang and E. H. Sargent, *Nano Lett.*, 2008, **8**, 4002-4006.
- [28] G. Chen, Y. Yu, K. Zheng, T. Ding, W. Wang, Y. Jiang and Q. Yang, *Small*, 2015, **11**, 2848–2855.
- [29] H. Li, J. Yang, J. Zhang and M. Zhou, *RSC Adv.*, 2012, **2**, 6258-6261.
- [30] R. Li, J. Yang, N. Huo, C. Fan, F. Lu, T. Yan, Z. Wei and J. Li, *Chem. Phys. Chem.*, 2014, **15**, 2510-2516.
- [31] Yi. Xi, C. Hu, X. Zhang, Y. Zhang and Z. L. Wang, *Solid State Commun.*, 2009, **149**, 1894-1896.
- [32] G. Manna, R. Bose and N. Pradhan, *Angew. Chem. Int. Ed.*, 2014, **53**, 6743-6746
- [33] L. Cademartiri, R. Malakooti, P. G. O'Brien, A. Migliori, S. Petrov, N. P. Kherani and G. A. Ozin, *Angew. Chem., Int. Ed.*, 2008, **47**, 3814–3817.
- [34] L. Tian, T. H. Yao and J. Vittal, *J. Cryst. Growth Des.*, 2008, **8**, 734–738.
- [35] Q. F. Han, J. Chen, X. J. Yang, L. Lu and X. Wang, *J. Phys. Chem. C*, 2007, **111**, 14072–14077.
- [36] W. Lou, M. Chen, X. Wang and W. Liu, *Chem. Mater.*, 2007, **19**, 872–878.
- [37] X-P. Shen, G. Yin, W-L. Zhang and Z. Xu, *Solid State Commun.*, 2006, **140**, 116–119.
- [38] A. K. Jain, V. Sharma, R. Bohra, A. A. Sukumar, V. S. Raju, J. E. Drake, M. B. Hursthouse and M. E. Light, *J. Organomet. Chem.*, 2006, **691**, 4128–4134.
- [39] G. Xie, Z. P. Qiao, M. H. Zeng, X. M. Chen and S. L. Gao, *Cryst. Growth Des.*, 2004, **4**, 513–516.

- [40] P. Boudjouk, M. P. Remington, D. G. Grier, B. R. Jarabek and G. McCarthy, *J. Inorg. Chem.*, 1998, **37**, 3538–3541.
- [41] L. S. Li, N. J. Sun, Y. Y. Huang, Y. Qin, N. Zhao, J. N. Gao, M. X. Li, H. H. Zhou and L. M. Qi, *Adv. Funct. Mater.*, 2008, **18**, 1194–1201.
- [42] A. Alemi and M. Dolatyari, *Rad. Eff. Def. Sol.*, 2008, **163**, 123–130.
- [43] W. H. Li, *Mater. Lett.*, 2008, **62**, 243–245.
- [44] J. Ota and S. K. Srivastava, *J. Phys. Chem. C*, 2007, **111**, 12260–12264.
- [45] J. Xu, N. Petkov, X. Wu, D. Iacopino, A. J. Quinn, G. Redmond, T. Bein, M. A. Morris and J. D. Holmes, *Chem. Phys. Chem.*, 2007, **8**, 235–240.
- [47] A. K. Jain and R. Bohra, *Appl. Organomet. Chem.*, 2006, **20**, 411–415.
- [48] J. Tang and A. P. Alivisatos, *Nano Lett.*, 2006, **6**, 2701–2706.
- [49] B. G. Kumar and K. Muralidharan, *J. Mater. Chem.*, 2011, **21**, 11271.
- [50] B. G. Kumar and K. Muralidharan, *Eur. J. Inorg. Chem.*, 2013, 2102.
- [51] B. G. Kumar and K. Muralidharan, *RSC Adv.*, 2014, **4**, 28219.
- [52] B. Pejova and I. Grozdanov, *Mater. Chem. Phys.*, 2006, **99**, 39–49.
- [53] R. L. Penn, *J. Phys. Chem. B*, 2004, **108**, 12707–12712.
- [54] J. B. M. Goodall, S. Kellici, D. Illsley, R. Lines, J. C. Knowles and J. A. Darr, *RSC Adv.*, 2014, **4**, 31799–31809.
- [55] M. V. Kovalenko, M. Scheele and D. V. Talapin, *Science*, 2009, **324**, 1417.
- [56] D. V. Talapin, J.-S. Lee, M. V. Kovalenko and E. V. Shevchenko, *Chem. Rev.*, 2010, **110**, 389–458.
- [57] L. Li, Y. Yu, G. J. Ye, Q. Ge, X. Ou, H. Wu, D. Feng, X. H. Chen and Y. Zhang, *Nat. Nanotechnol.*, 2014, **9**, 372–377.
- [58] T. Zhai, X. Fang, M. Liao, X. Xu, L. Li, B. Liu, Y. Koide, Y. Ma, J. Yao, Y. Bando and D. Golberg, *ACS Nano*, 2010, **4**, 1596–1602.
- [59] M. B. Jarosz, V. J. Porter, B. R. Fisher, M. A. Kastner and M. G. Bawendi, *Phys. Rev. B*, 2004, **70**, 195327.
- [60] D. S. Ginger and N. C. Greenham, *J. Appl. Phys.*, 2000, **87**, 1361.
- [61] O. L. Sanchez, D. Lembke, M. Kayci, A. Radenovic and A. Kis, *Nat. Nanotechnol.*, 2013, **8**, 497.
- [62] J. P. Clifford, K. W. Johnston, L. Levina and E. H. Sargent, *Appl. Phys. Lett.*, 2007, **91**, 253117.

Chapter 5

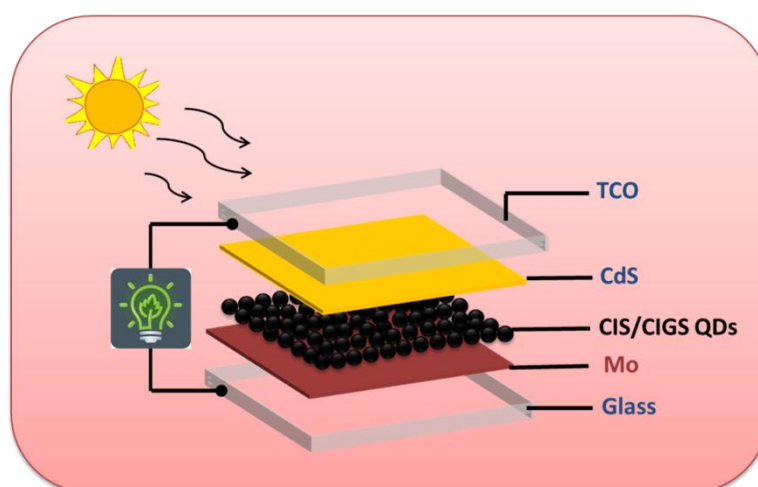
- [63] A. W. Blakers, A. Wang, A. M. Milne, J. Zhao and M. A. Green, *Appl. Phys. Lett.*, 1989, **55**, 1363.
- [64] Y. Jin, J. Wang, B. Sun, J. C. Blakesley and N. C. Greenham, *Nano Lett.*, 2008, **8**, 1649–1653.
- [65] H-C. Liao, M-C. Wu, M-H. Jao, C-M. Chuang, Y-F. Chend and W-F. Su, *Cryst. Eng. Comm.*, 2012, **14**, 3645–3652.

Chapter 6

Synthesis of ternary metal chalcogenide nanoparticles for solar cell device fabrication

Abstract

Ternary metal sulphide nanoparticles (NPs), CuInS_2 , Cu_2SnS_3 , and Cu_3SnS_4 , were synthesized using the modified hexamethyldisilazane (HMDS) - assisted synthetic method. The structure, shape and the composition of these nanomaterials were investigated with powder X-ray diffraction (XRD), Field Emission Electron Microscopy (FESEM) and Energy Dispersive X-ray Analysis (EDX). The PXRD pattern of CuInS_2 showed tetragonal structure. FESEM images of CuInS_2 NPs showed 10-20 nm particle of spindle-shaped morphology. PXRD patterns of Cu_2SnS_3 and Cu_3SnS_4 showed tetragonal and orthorhombic structures respectively. FESEM images of Cu_2SnS_3 and Cu_3SnS_4 depicted particles having a cauliflower-like morphology with the sizes ranging 30-50 nm. The EDAX analysis of CuInS_2 , Cu_2SnS_3 , and Cu_3SnS_4 disclosed no signal for any organic moieties confirming the purity of the materials. A preliminary attempt was made to fabricate solar cell devices by drop casting using these ternary metal chalcogenides and their efficiency was measured. Based on the initial analysis, the fabricated devices were showing some response, but the fabrication procedure needs to be optimized.



Chapter 6

6.1. Introduction

The band gap of semiconductor NPs can be tuned by varying the particle size or by tuning constituent stoichiometries in alloyed NPs. However, the size dependent properties will disappear once the NPs are deposited onto a thin film and undergo thermal process for different applications. In contrast, composition control is a possible route to fabricate semiconductor NPs with tunable band gaps. Furthermore, various band gaps can be conveniently achieved through variation of composition in multicomponent NPs even under a fixed size. For example, the use of two different metals allow access to the band gaps and not accessible to binary metal chalcogenides [1-3].

The typical ternary metal chalcogenide system possesses two metals each with oxidation states of +1 and +3 in permutation with a pair of chalcogens each in oxidation state -2. This system is described as an I-III-VI₂. Hence, recently researchers have turned their attention towards ternary nontoxic I-III-VI₂ materials such as CuInS₂ and CuInSe₂ NPs [4]. Among the various, I-III-VI₂ compounds, CuInS₂ is a promising material for photovoltaic applications owing to its high absorption coefficient, also the direct band gap of 1.53 eV, which is well matched with the solar spectrum [5]. The latest report shows the potential use of CuInS₂ NPs in solar cell devices with power conversion efficiencies reaching ~5%. Very recent reports have demonstrated high-efficiency green QDSC based on CISZ QD sensitizer. These solar cells show an unprecedented champion cell efficiency of 7.04% and a certified efficiency of 6.66% [6]. Also CuInS₂ NPs are important in biolabeling [7] and light-emitting diodes [8] due to their size-tunable emission in the red to the near-infrared region (550–850 nm) [9].

Another important class of ternary systems is I-IV-VI combination. They have potential applications in photovoltaic cells, electrochemical devices and photocatalytic material [10]. Among them Cu-Sn-S (CTS) system is a P-type semiconductor having a high absorption coefficient (10^5 cm^{-1}) and tunable band gap (1.1-1.5 eV), which covers the optimal solar spectrum [11]. They have many crystal structures namely cubic, tetragonal, wurtzite, orthorhombic, mohite, triclinic and

anorthic [12]. Among these structures, tetragonal is the stable structure, while zinc blende and wurtzite are metastable structures. The CTS system includes Cu_2S – SnS_2 , Cu_2SnS_3 [13, 14], Cu_4SnS_4 [15], $\text{Cu}_4\text{Sn}_7\text{S}_{16}$ [14] and Cu_4SnS_6 [16] system.

It was observed that, efficiency of CTS based solar cells varied depending on the adopted synthetic method. From Table 6.1, it is quite clear that there is much greater scope to improve PCE of CTS solar cells further. However, very few reports describe the bulk synthesis of these compositions.

Table 6.1. Reported efficiencies for the CTS based solar cells.

Method of preparation	Efficiency (PCE) (%)	Reference
electrodeposition	0.94	17
milling process	1.94	18
direct liquid coating(DLC)	2.00	19
coevaporation	3.66	20
coevaporation	4.63	21

Various methods like solvothermal, elemental hydrothermal methods, single-source molecular precursor, microwave irradiation and hot injection technique are available for the synthesis of ternary metal chalcogenides like CuInS_2 [22-26] and CTS [17, 27-33]. These synthetic methods usually require high temperature, more reaction time, special devices, and some of them use highly toxic materials. Hence, to overcome these problems, we have developed a simple methodology for the synthesis of suitable ternary metal chalcogenides. Similar to the discussion in Chapter 1 (Section 1.5), it is necessary to synthesize the quantum dot NPs without any organic molecules surrounding it as capping agents. The present chapter describes synthesis of ternary metal chalcogenides such as CuInS_2 , Cu_2SnS_3 and Cu_3SnS_4 NPs by solution phase without using any surfactants or templates.

Chapter 6

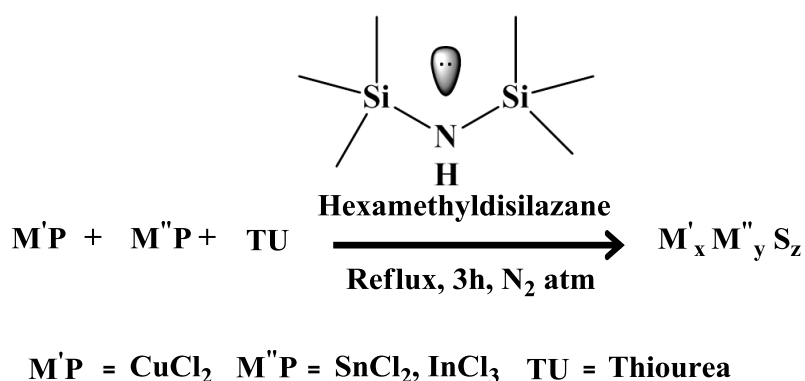
6.2. Experimental section

6.2.1. Materials and instruments

The chemicals CuCl_2 , InCl_3 , SnCl_2 and thiourea were purchased from Sigma-Aldrich and used as such without further purification. Solvents were purified according to standard literature procedures. The reactions were carried out using a standard Schlenk line technique. Instrumentation and sample preparation are similar to the one discussed in Chapter 2 and Section 2.2.4.

6.2.2. Common synthetic procedure for In_2S_3 , CuInS_2 , Cu_2SnS_3 and Cu_3SnS_4 nanoparticles

Metal sources (metal halides), thiourea and excess of 1,1,1,3,3,3-hexamethyldisilazane $[\text{HN}(\text{SiMe}_3)_2]$ (HMDS) were added into a 50 mL round bottom flask and the reaction mixture was refluxed at 130 °C (Scheme 6.1) for 3 h. It was observed that the reaction mixture turned to black. The unreacted HMDS and volatile side products were removed by applying high vacuum. The remnant was repeatedly washed with methanol, tetrahydrofuran (THF), ethanol and acetone ($10 \text{ mL} \times 3$) to remove unreacted precursors. The resultant NPs were dried in a vacuum oven at a temperature of 120 °C for 4 h before characterization. Mole ratio and exact quantity used to synthesize various ternary metal chalcogenide are listed in Table 6.2.



Scheme 6.1. Generalised reaction of synthesis of ternary metal chalcogenides.

Table 6.2. Experimental details for the synthesis of metal chalcogenides

Nanoparticle	Chemical	Ratio (M'P : M''P : TU)	Moles (mmol)	Weight (g)
In ₂ S ₃	InCl ₃	2	0.90	0.20
	Thiourea	3	1.30	0.10
CuInS ₂	CuCl ₂	1	1.40	0.20
	InCl ₃	1	1.40	0.30
	Thiourea	2	2.80	0.21
Cu ₂ SnS ₃	CuCl ₂	2	1.40	0.20
	SnCl ₂	1	0.46	0.13
	Thiourea	3	1.80	0.16
Cu ₃ SnS ₄	CuCl ₂	3	1.40	0.20
	SnCl ₂	1	0.70	0.09
	Thiourea	4	2.10	0.14

6.2.3. Fabrication of device

Following steps are involved in device fabrication,

I. Etching of the substrate:

Commercially available ITO/glass substrates which are having surface sheet resistance $\sim 10 \text{ } \Omega/\text{square}$ and 1.1 mm thickness were used in the solar cell device fabrications. They were cut into pieces of $15 \times 15 \text{ mm}$ using a glass cutter. To prevent short circuits between electrodes, some part of ITO was removed by etching, while the other portion was covered by adhesive tape. The exposed portion of ITO substrate was kept in an acidic mixture, containing 9 parts concentrated hydrochloric acid, 1 part nitric acid and 10 parts of water for more than 30 min to remove the metallic layer. Then adhesive tape was detached, and the etched substrates were cleaned with distilled water.

II. Cleaning the substrate:

Samples of suitable size were cleaned in acetone for 5 min, then in absolute ethanol. Subsequently, substrates were rinsed with plenty of deionized water, after that substrates were dried under a nitrogen flow. The samples were stored in glass containers, which were cleaned using the similar procedure.

III. Fabrication:

We have fabricated the device as follows. A CuInS₂/PEDOT:PSS nanocomposite counter electrode (CIS(or)CTS/PEDOT:PSS CE) was prepared by dispersing CuInS₂

Chapter 6

(CIS) powder (0.2 g) in a PEDOT:PSS aqueous solution (0.40 g) and sonicating for 30 min to form a well-dispersed composite solution. The composite solution was drop-cast onto ITO glass, naturally dried to evaporate water, and subsequently sintered at 70 °C for 2 h at an ambient atmosphere. Another layer of CdS was prepared by drop casting 0.1 g mL⁻¹ of a CdS NPs dispersion (in toluene) on ITO conductive glass followed by drying to remove solvent (toluene) and annealing at 120 °C for 30 min at an ambient atmosphere. Al sheet was used as a back contact counter electrode. The thickness of Al sheet was about 200 nm. A analogous procedure was used for CTS also.

6.3. Results and discussion

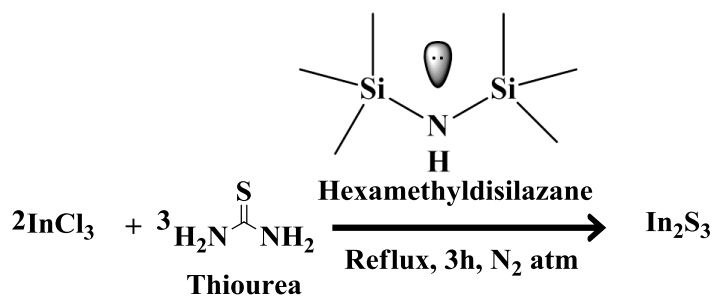
6.3.1. Synthesis and characterization

In order to prepare ternary metal chalcogenides without capping agents, we considered following factors while designing the reaction methodology.

- Compared to binary metal chalcogenide NPs, ternary or higher order metal chalcogenide NPs synthesis needs particular attention to control the reactivity of two or three cationic precursors. Thus, finding a suitable reaction condition to avoid the formation of undesirable side products are more complicated than binary compounds synthesis.
- During the synthesis of ternary and higher order metal chalcogenide NPs, there is a chance to form corresponding binary metal chalcogenides due to the difference in rates of reactions and metal precursors. For example, during the synthesis of CuInS₂, CuS or Cu₂S and In₂S₃ phases are also formed.
- To attain finest crystallinity for the ternary or higher order metal chalcogenides NPs, we need to maintain slow growth rate.

Initially, we have identified (Chapter 3) reaction condition suitable for the synthesis of copper chalcogenides from CuCl₂ by reacting with thiourea in the presence of HMDS. In next step, to understand the suitable condition for the formation of In₂S₃, InCl₃ was reacted with thiourea in HMDS at reflux temperature. Interestingly, In₂S₃ was formed within 3 hours (Scheme 6.2). The product obtained in this reaction was characterized by powder X-ray diffraction pattern, EDAX

analysis (Figure 6.1) and FESEM (Figure 6.2 showing particles size 20-50 nm). Thus, the precise understanding of reactivities of various metal sources in the synthesis of binary metal chalcogenides provided a reasonable extension of developed methodology for the synthesis of ternary metal chalcogenides.



Scheme 6.2. Synthesis of In_2S_3 nanoparticles.

With the aim of producing organic free CuInS_2 , Cu_2SnS_3 , and Cu_3SnS_4 NPs, we chose reacting thiourea with metal sources in HMDS at reflux temperature. The generalized reaction of synthesis of ternary metal chalcogenides is shown in Scheme 6.1, while the stoichiometric ratios are depicted in Table 6.2. Interestingly, all these reactions yielded individual products in good yields within 3 h without using any template or surfactant. Presumably, since the reactivities of CuCl_2 , InCl_3 , and SnCl_2 with HMDS were similar, it was possible to obtain the targeted products easily.

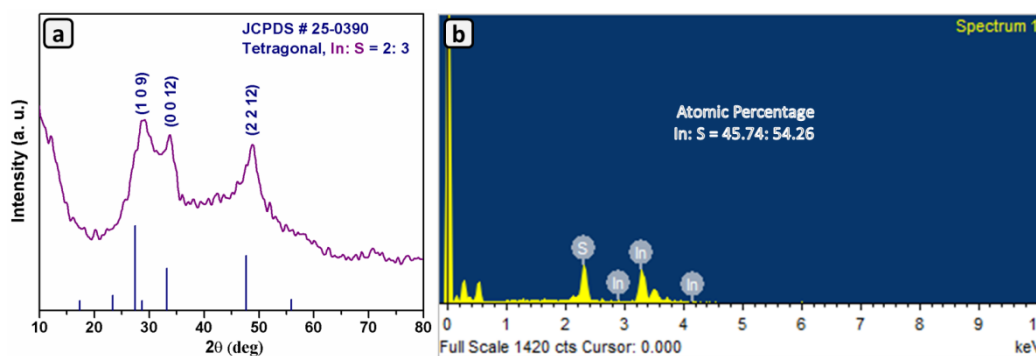


Figure 6.1. (a) PXRD of In_2S_3 nanoparticles. (b) EDX spectrum of In_2S_3 nanoparticles.

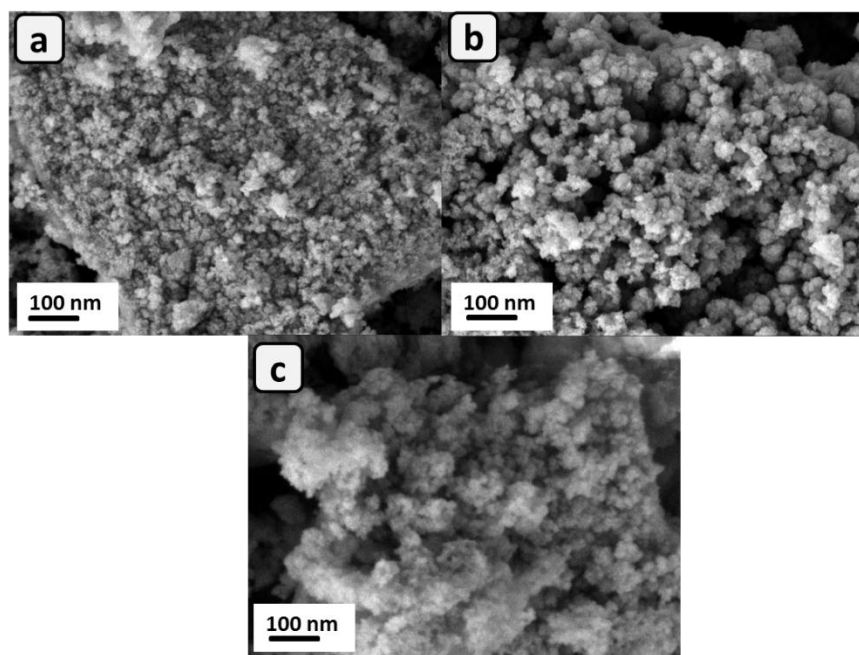


Figure 6.2. (a, b and c) FESEM images of In_2S_3 nanoparticles at high magnification levels.

In the previous chapters, we obtained surfactant/capping agent free binary NPs. By following the similar strategy, we have synthesized ternary metal chalcogenides NPs without any capping agent. The present standardized reaction conditions yielded tetragonal phase of CuInS_2 , Cu_2SnS_3 and orthorhombic phase of Cu_3SnS_4 NPs. While literature showed the use of vigorous reaction condition for the synthesis of higher order metal chalcogenides, we obtained the ternary metal chalcogenides NPs by maintaining simpler reaction condition.

The synthesized products were characterized using Powder X-ray Diffraction (PXRD) Pattern, Energy Dispersive X-ray analysis (EDAX), Field Emission Scanning Electron Microscopy (FESEM) and Fourier Transform Infrared Spectroscopy (FT-IR). The PXRD pattern of CuInS_2 NPs is shown in Figure 6.3, which showed the obtained product had tetragonal crystal structure with body-centred lattice (JCPDS # 89-6095). The broad diffraction peaks were detected at $2\theta = 27.8, 32.3, 46.3$ and 54.7 that correspond to $(1\ 1\ 2)$, $(2\ 0\ 0)$, $(2\ 2\ 0)$ and $(3\ 1\ 2)$ planes of the tetragonal structure. Figure 6.4 depicts the PXRD pattern of Cu_2SnS_3 NPs, which showed that product had tetragonal body-centred crystal structure (JCPDS # 89-4714). The obtained broad diffraction peaks at $2\theta = 28.6, 47.3, 56.1$ correspond to $(1\ 1\ 2)$, $(2\ 2\ 0)$ and $(3\ 1\ 2)$ planes of tetragonal structure. Figure 6.5

represents the PXRD pattern of Cu_3SnS_4 NPs, which showed that product had orthorhombic phase primitive crystal structure (JCPDS # 36-0218). The obtained broad diffraction peaks at $2\theta = 28.6, 47.5, 56.7$ correspond to (2 2 2), (0 4 4) and (2 6 2) planes of the orthorhombic structure.

Examination of PXRD pattern of CuInS_2 , Cu_2SnS_3 and Cu_3SnS_4 showed the absence of any other characteristic peaks corresponding to copper chloride, CuS , copper oxides (CuO , Cu_2O), indium sulphide (In_2S_3) and tin sulphide (SnS). There was no other phase of copper indium sulphide (CuInS_2) and copper tin sulphide (Cu_2SnS_3 and Cu_3SnS_4) present. This observation was showing the phase purity of products. It is interesting to observe that HMDS assisted reaction had perfect control to produce required stoichiometric products ($\text{Cu}_2\text{SnS}_3/\text{Cu}_3\text{SnS}_4$) selectively.

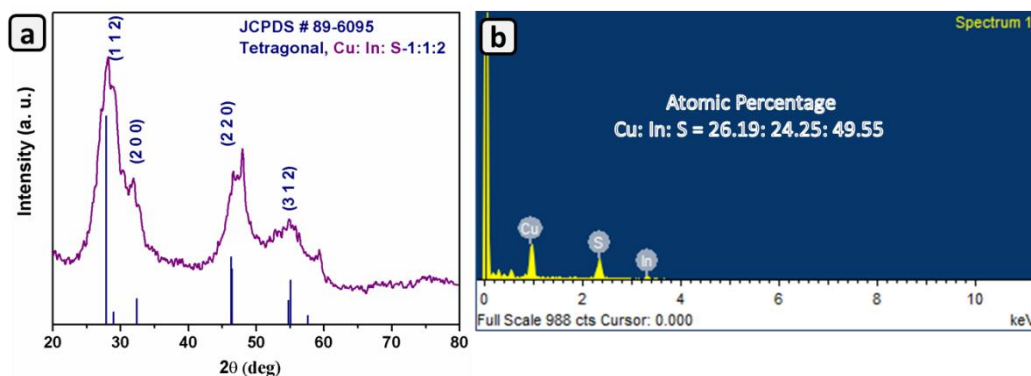


Figure 6.3. (a) PXRD of CuInS_2 nanoparticles. (b) EDX of CuInS_2 nanoparticles

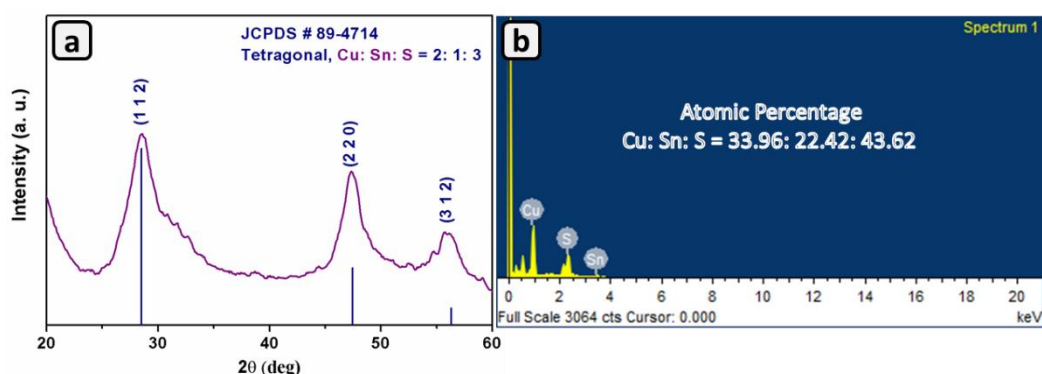


Figure 6.4. (a) PXRD of Cu_2SnS_3 nanoparticles. (b) EDX of Cu_2SnS_3 nanoparticles

Chapter 6

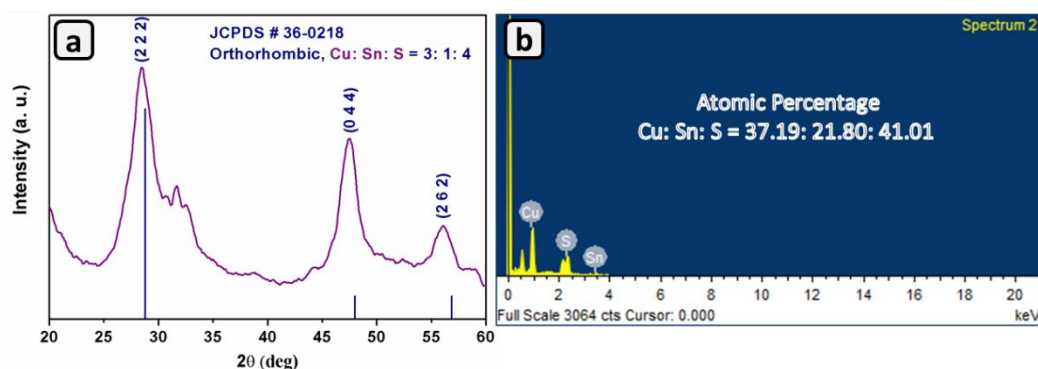


Figure 6.5. (a) PXRD of Cu_3SnS_4 nanoparticles. (b) EDX of Cu_3SnS_4 nanoparticles

The samples of ternary systems were analysed in Field Emission Scanning Electron Microscopy to investigate on morphologies. FESEM images of CuInS_2 (Figure 6.6a, b and c) showed spindle-shaped morphology with the size of 10-20 nm. In case of Cu_2SnS_3 (Figure 6.7a, b, and c) and Cu_3SnS_4 (Figure 6.8a, b, and c) FESEM depicted cauliflower like morphology for NPs of sizes varying from 30 to 50 nm.

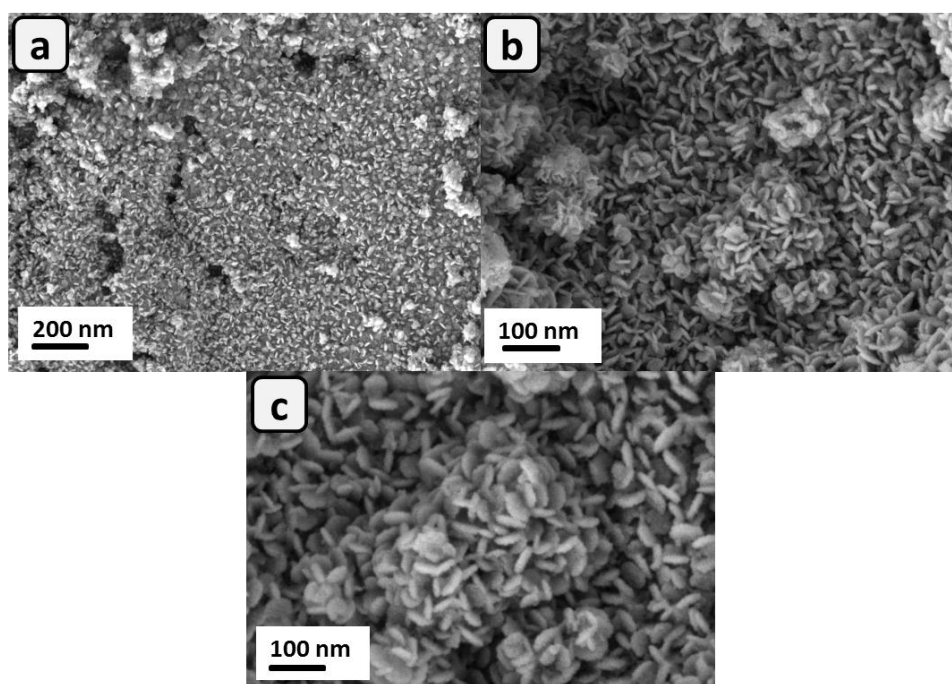


Figure 6.6. (a, b and c) FESEM images of CuInS_2 nanoparticles at high magnification levels

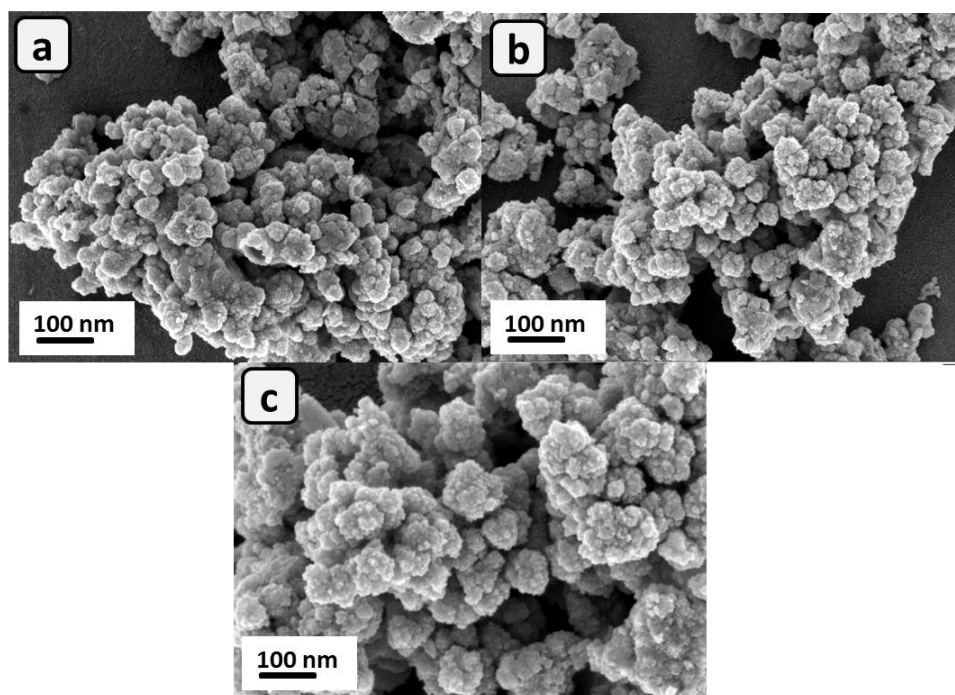


Figure 6.7. (a, b and c) FESEM images of Cu_2SnS_3 nanoparticles at high magnification levels

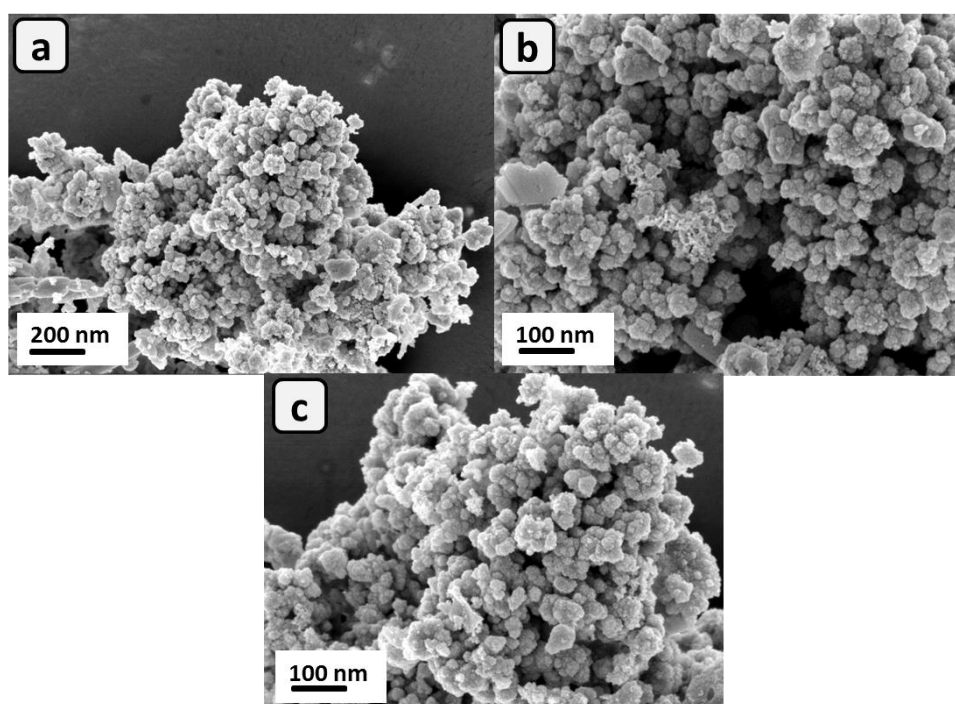


Figure 6.8. (a, b and c) FESEM images of Cu_3SnS_4 nanoparticles obtained from the different regions of the sample

Chapter 6

Figures 6.3.b, 6.4.b and 6.5.b are showing the Energy Dispersive X-ray analysis (EDAX) spectra of CuInS_2 , Cu_2SnS_3 and Cu_3SnS_4 NPs respectively. The elemental analyses from various samples of all the three samples of CuInS_2 , Cu_2SnS_3 and Cu_3SnS_4 NPs were consistent. The analyses proved the presence of elements Cu: In: S and Cu: Sn: S only, no other elements including carbon was absent. This observation confirmed the absence of any carbonaceous mass in CuInS_2 , Cu_2SnS_3 and Cu_3SnS_4 NPs. The purity of products was investigated by FTIR spectra of obtained NPs. The FTIR spectra of (Figure 6.9, 6.10 and 6.11) synthesized CuInS_2 , Cu_2SnS_3 , and Cu_3SnS_4 NPs showed no signal corresponding to any organic molecules, confirming their absence around the particles. It indicated the purity of product.

Absorbance and band gap are the two important factors that decide the future and application of the material. Solid UV–Vis diffused reflectance spectra were recorded for the synthesized ternary systems of CuInS_2 , Cu_2SnS_3 and Cu_3SnS_4 NPs (Figure 6.12 to Figure 6.14). The absorption maxima and the band gap of surfactant-free CuInS_2 , Cu_2SnS_3 , and Cu_3SnS_4 NPs are listed in Table 6.3. All these ternary systems have broad absorption spanning up to NIR region. The band gaps of these materials are also suitable for their use in solar cells.

Table 6.3. The absorption maxima and band gap values of the synthesized ternary systems

Material	Absorption maxima (nm)	Band gap (eV)
CuInS_2	500	1.40
Cu_2SnS_3	550	1.40
Cu_3SnS_4	600	1.15

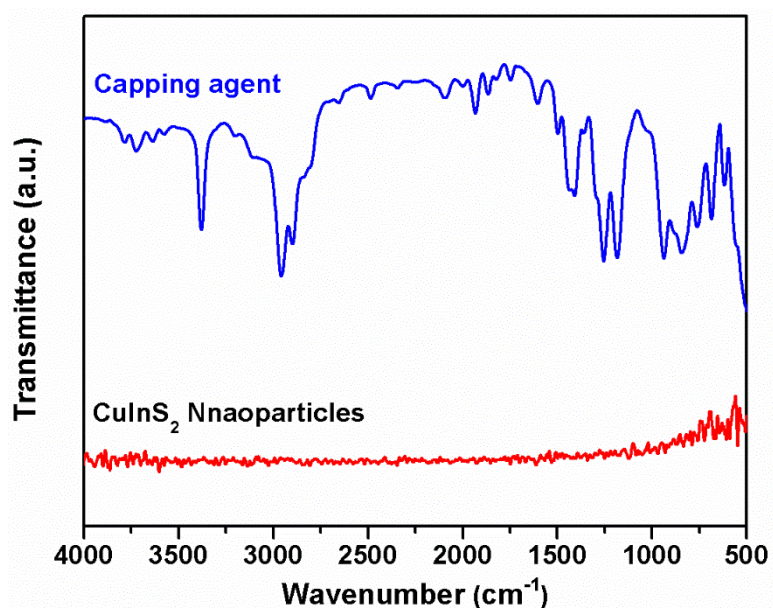


Figure 6.9. FT-IR spectrum of CuInS₂

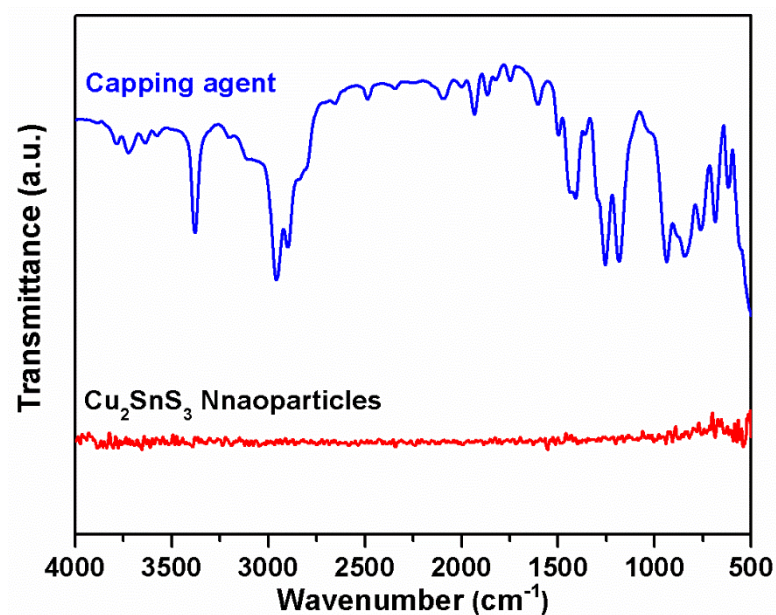


Figure 6.10. FT-IR spectrum of Cu₂SnS₃

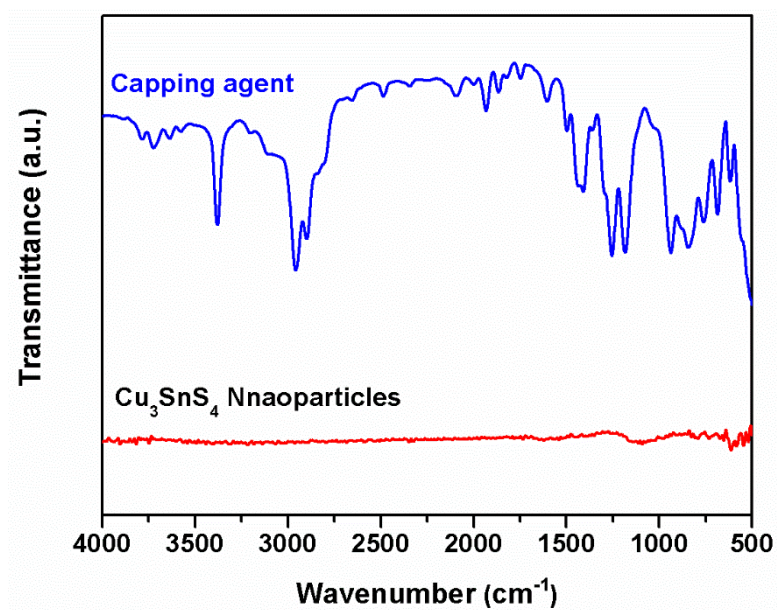


Figure 6.11. FT-IR spectrum of Cu_3SnS_4

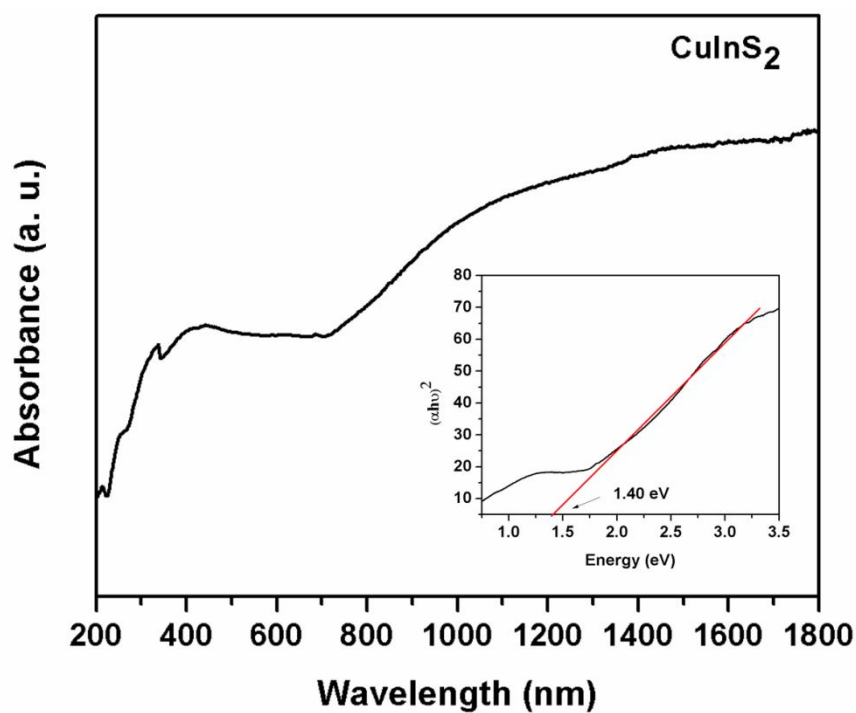


Figure 6.12. UV-Vis-NIR spectrum of as prepared CuInS_2 . Inset: band gap (1.40 eV)

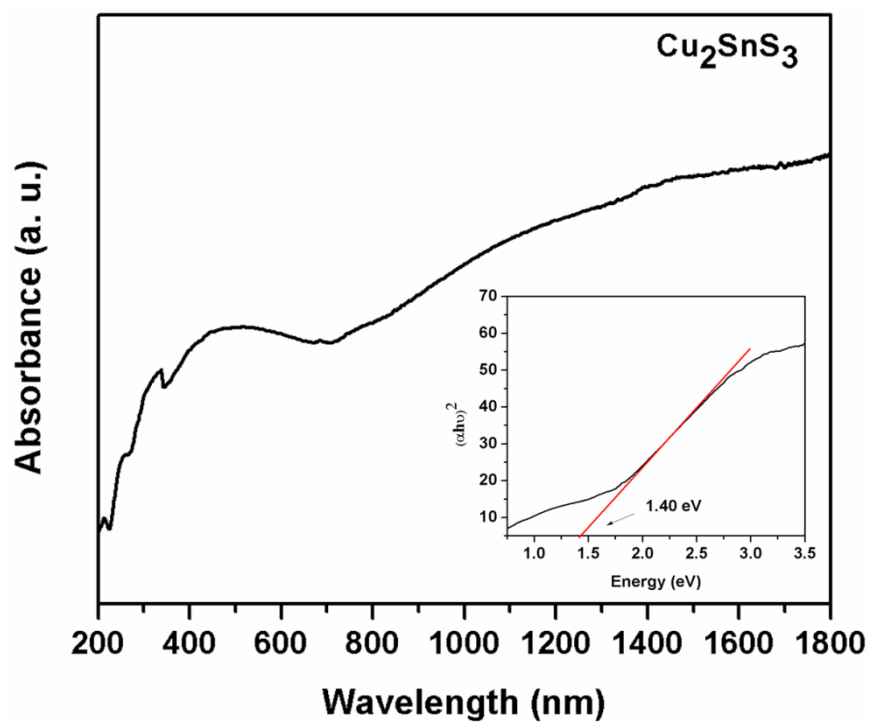


Figure 6.13. UV–Vis–NIR spectrum of as prepared Cu_2SnS_3 . Inset: band gap (1.40 eV)

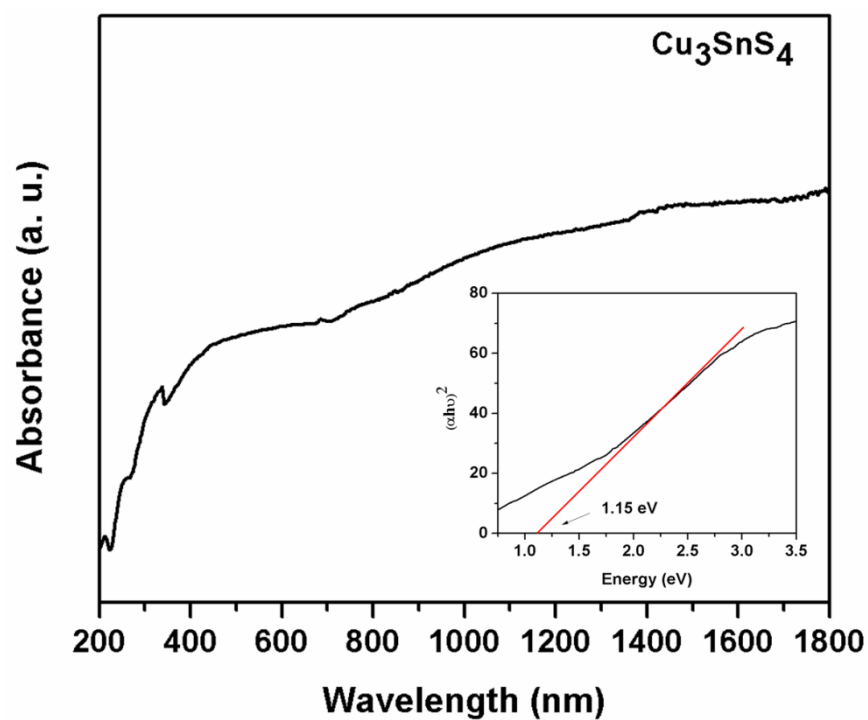


Figure 6.14. UV–Vis–NIR spectrum of as prepared Cu_3SnS_4 . Inset: band gap (1.15 eV)

6.4. Fabrication of CIS/CTS based solar cell and device performance

The standard structure of solar cells based on metal chalcogenides is shown in Figure 6.15. These devices consist of a glass substrate, front contact electrode, absorbing layer and back contact electrode [34]. Generally, CdS is used as buffer layer in CIS and CTS based solar cells. Molybdenum is back contact because of the matching of its work-function with active layer. However, we have Al foils instead of Mo due to the ease of fabrication (Sputtering unit is required to produce Mo layer).

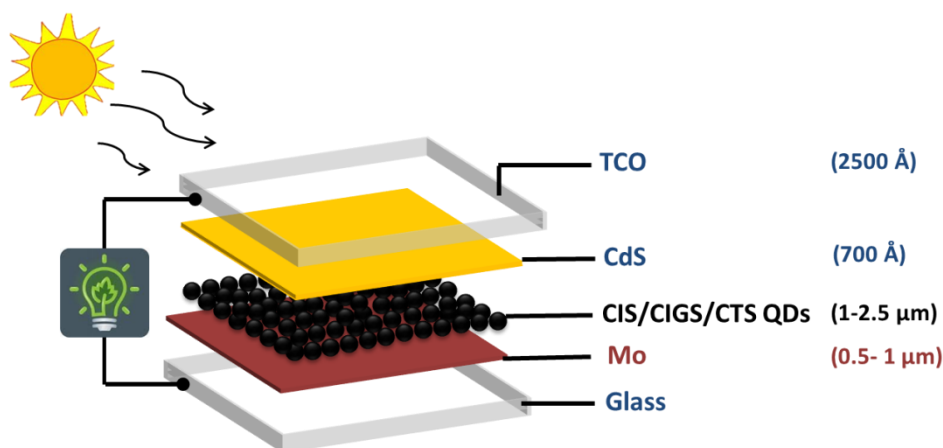


Figure 6.15. Schematic illustration of a typical CIS/CIGS/CTS photovoltaic device. Sunlight enters through the top layer of the device (the transparent conducting oxide)

The organic molecules surrounding the chemically synthesized NPs are insulators, i.e. they hinder the mobility of electrons. This hurdle would decrease the efficiency of solar cells fabricated using those NPs surrounded by insulating organic molecules. Therefore, to understand the effect of organic surfactant free NPs on the efficiency of CIS and CTS based solar cells, we have made preliminary attempt to fabricate devices. As prepared surfactant molecules free ternary systems, CIS and CTS NPs were used to fabricate the solar cell device of the structure of glass/ITO/PEDOT:PSS/CIS (or) CTS/CdS/Al. We have fabricated the devices in different sizes as shown in Figure 6.16. The active area of the solar cell was prepared by keeping all deposited materials on a defined area and by scratching out all material from all other parts of ITO substrate.

Ternary metal sulphide NPs

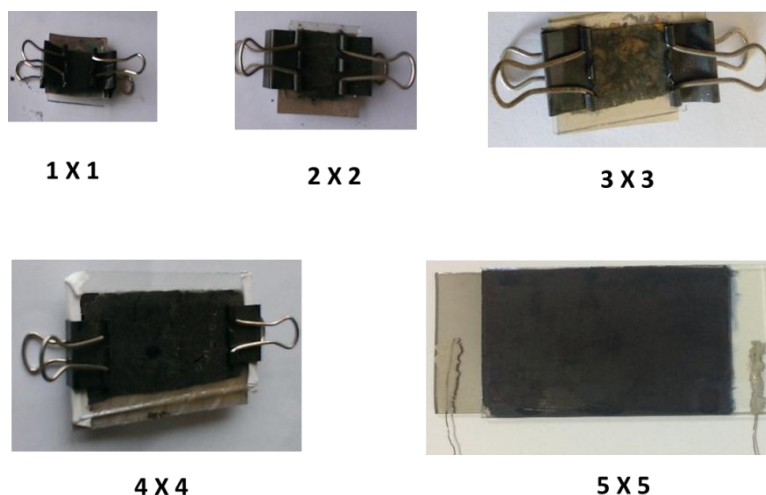


Figure 6.16. Photographs of solar cells in different sizes fabricated using CIS and CTS materials that are synthesised during present work.

Adhesion of materials in layers is the primary requirement for the success of device making. If there are no proper layers of materials, overlapping of materials will occur, leading to short-circuit in the cell. Figures 6.17 and 6.18 represents the cross-sectional view and elemental mapping of the fabricated device obtained from the investigation by FESEM. From the picture, it is visible that materials are sticking to each other in layers.

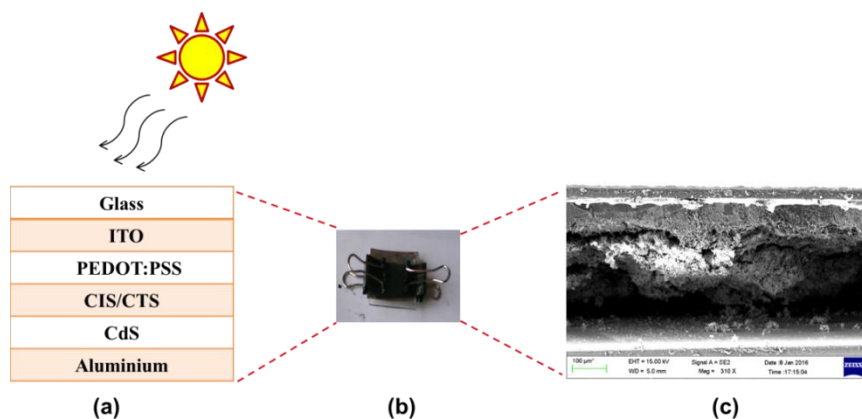


Figure 6.17. (a) Pictorial representation of structure of the solar cell device. (b) Image of the fabricated device ($1 \times 1 \text{ cm}^2$ area cell). (c) Cross sectional view of the device.

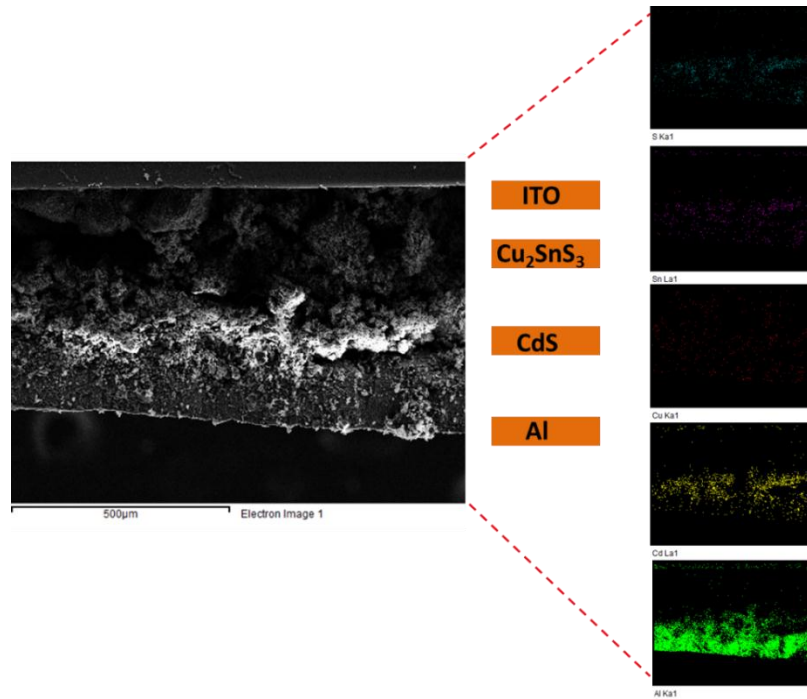


Figure 6.18. Cross sectional view and elemental mapping of the device (solar cell).

The performance of devices are analyzed using standard I-V characteristics under AM 1.5 solar simulator (polychromatic light intensity of 100 mWcm^{-2} obtained using a 150W Xe; Science Tech) coupled with electrochemical workstation (Zahanner Zenium). Each device was placed under AM 1.5 illuminations and I-V curves were obtained by connecting ITO and Al electrodes of assembled device to the electrochemical workstation. The I-V curves obtained from the fabricated CIS and CTS based devices are shown in Figures 6.19 and 6.20 respectively. The extracted short-circuit current (I_{sc}), open circuit voltage (V_{oc}) and fill factor (FF) values for the device are listed in Table 6.4.

Among the CIS and CTS based devices, the CIS-based one had considerable FF of 70% while others showed FF of 25-26% under our laboratory condition. From the data obtained from preliminary device fabricated in our lab, it is observed that the device performance was poor and procedure of fabrication is required to be standardized.

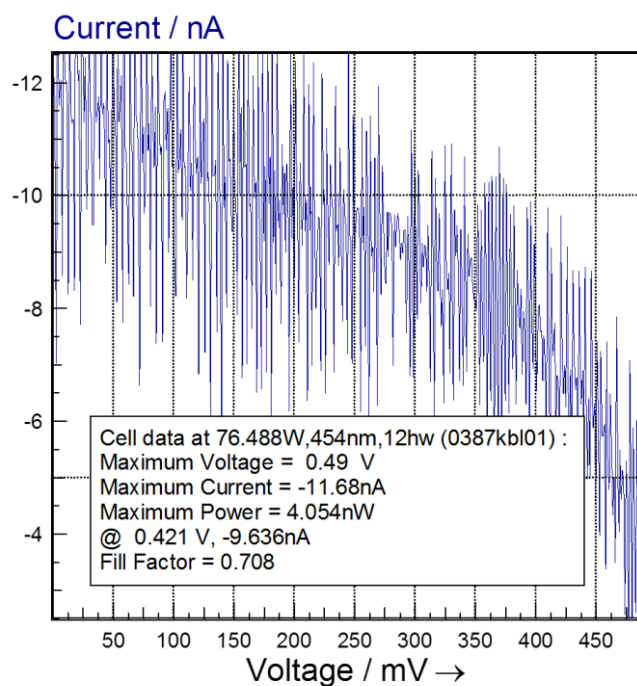


Figure 6.19. Current- voltage (I-V) curve determined after measurement of a CuInS_2 (CIS) fabricated device.

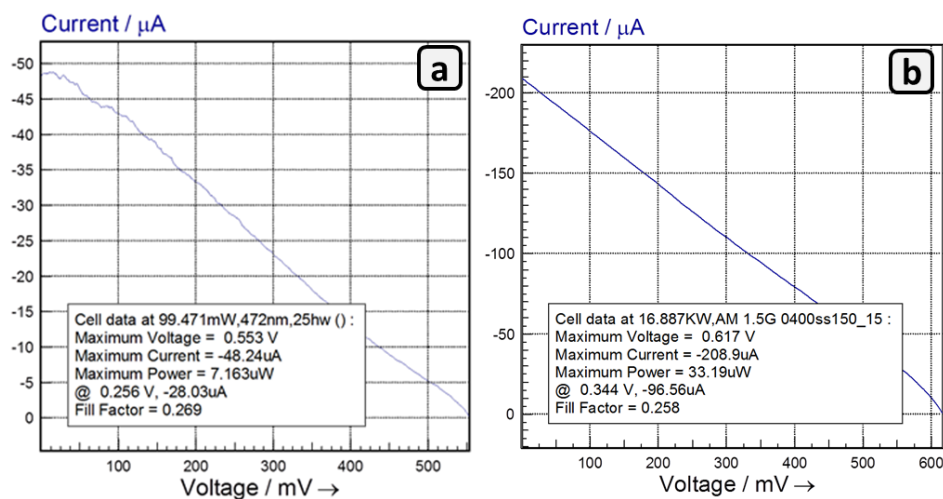


Figure 6.20. Current- voltage (I-V) curve determined after measurement of CTS based (a) Cu_2SnS_3 and (b) Cu_3SnS_4 fabricated device.

Chapter 6

Table 6.4. I-V characteristics of fabricated devices

Sample	Isc (μ A)	Voc (mV)	FF (%)
CuInS ₂	0.011	0.49	70
Cu ₂ SnS ₃	48.24	0.55	26
Cu ₃ SnS ₄	208.9	0.61	25

6.4.1. Future plan for the fabrication of device

For achieving the efficiency of the ternary systems fully, it is required to change the architecture of the device in the following fashion; Glass/ITO/CdS/CIS (or) CIGS (or) CTS/Mo/glass. The back contact electrode, i.e. Mo layer is to be coated by the sputtering process. The thickness of the metal (Mo) layer/film should be about 100 nm.

6.5. Summary

(1) We have explored the synthesis of surfactant/template free ternary metal chalcogenides, CuInS₂, Cu₂SnS₃ and Cu₃SnS₄ NPs by modified HMDS- assisted synthetic method. FT-IR spectra and EDAX analyses proved the absence of organic surfactant molecules as the capping agent.

(2) The synthesized products were characterized by PXRD, EDAX, FESEM, UV–Vis and FT-IR data. FESEM images of CuInS₂ showed 10-20 nm size of spindle-shaped morphology. In case of Cu₂SnS₃ and Cu₃SnS₄ NPs of size ranging 30-50 nm and cauliflower like morphology were obtained.

(3) The preliminary attempt of devices fabrication showed that the materials synthesized in the present work were active in the photovoltaic phenomenon. However, the procedure needs to be optimized to improve the performance of solar cells and to understand the effect of surfactant free NPs on the efficiency of solar cell.

6.6. References

- [1] (a) X. Peng, *Acc. Chem. Res.* 2010, **43**, 1387. (b) R. C. Somers, M. G. Bawendi and D. G. Nocera, *Chem. Soc. Rev.* 2007, **36**, 579. (c) C. Burda, X. Chen, R. Narayanan and M. A. El-Sayed, *Chem. Rev.* 2005, **105**, 1025. (d) M. G. Panthani, V. Akhavan, B. Goodfellow, J. P. Schmidtke, L. Dunn, A. Dodabalapur, P. F. Barbara and B. A. Korgel, *J. Am. Chem. Soc.* 2008, **130**, 16770. (e) N. Tessler, V. Medvedev, M. Kazes, S. H. Kan and U. Banin, *Science*, 2002, **295**, 1506. (f) X. Michalet, F. F. Pinaud, L. A. Bentolila, J. M. Tsay, S. Doose, J. Li, G. Sundaresan and A. Wu, *Science* 2005, **307**, 538. (g) W. Zhang and X. Zhong, *Inorg. Chem.* 2011, **50**, 4065–4072.
- [2] (a) M. A. El-Sayed, *Acc. Chem. Res.*, 2004, **37**, 326–333. (b) I. Moreels, F. Vanhaecke, K. Lambert, D. D. Muynck, T. Nollet, J. C. Martins, F. Vanhaecke, A. Vantomme, C. Delerue, G. Allan and Z. Hens, *ACS Nano*, 2009, **3**, 3023–3030.
- [3] (a) Y-H. Yang and Y-T. Chen, *J. Phys. Chem. B*, 2006, **110**, 17370–17374. (b) H. Zhong, Y. Li, M. Ye, Z. Zhu, Y. Zhou, C. Yang and Y. Li, *Nanotechnology*, 2007, **18**, 025602–025608. (c) P. M. Allen and M. G. Bawendi, *J. Am. Chem. Soc.*, 2008, **130**, 9240–9241. (d) H. Zhong, S. S. Lo, T. Mirkovic, Y. Li, Y. Ding, Y. Li and G. D. Scholes, *ACS Nano*, 2010, **9**, 5253–5262. (e) Q. Guo, S. J. Kim, M. Kar, W. N. Shafarman, R. W. Birkmire, E. A. Stach, R. Agrawal and H. W. Hillhouse, *Nano Lett.*, 2008, **8**, 2982–2987. (f) M. G. Panthani, V. Akhavan, B. Goodfellow, J. P. Schmidtke, L. Dunn, A. Dodabalapur, P. F. Barbara and B. A. Korgel, *J. Am. Chem. Soc.*, 2008, **130**, 16770–16777. (g) J. Tang, S. Hinds, S. O. Kelley and E. H. Sargent, *Chem. Mater.*, 2008, **20**, 6906–6910.
- [4] P. D. Matthews, P. D. McNaughter, D. J. Lewis and P. O'Brien, DOI: 10.1039/x0xx00000x.
- [5] (a) P. M. Allen and M. G. Bawendi, *J. Am. Chem. Soc.*, 2008, **130**, 9240–9241. (b) Q. Guo, G. M. Ford, H. W. Hillhouse and R. Agrawal, *Nano Lett.*, 2009, **9**, 3060–3065. (c) Q. Guo, S. J. Kim, M. Kar, W. N. Shafarman, R. W. Birkmire, E. A. Stach, R. Agrawal and H. W. Hillhouse, *Nano Lett.*, 2008, **8**, 2982–2987. (d) M. G. Panthani, V. Akhavan, B. Goodfellow, J. P. Schmidtke, L. Dunn, A.

Chapter 6

- Dodabalapur, P. F. Barbara and B. A. Korgel, *J. Am. Chem. Soc.*, 2008, **130**, 16770–16777.
- [6] (a) Z. Yang, C-Y. Chen, C-W. Liu, C-L. Li and H-T. Chang, *Adv. Energy Mater.*, 2011, **1**, 259-263. (b) P. Zhenxiao, M-S. Iván, Q. Shen, H. Zhang, Y. Li, K. Zhao, J. Wang, X. Zhong and J. Bisquert, *J. Am. Chem. Soc.* 2014, **136**, 9203–9210.
- [7] (a) J. Y. Lee, D. H. Nam, M. H. Oh, Y. Kim, H. S. Choi, D. Y. Jeon, C. B. Park and Y. S. Nam, *Nanotechnology*, 2014, **25**, 175702-175712. (b) L. Li, T. J. Daou, I. Texier, T. T. K. Chi, N. Q. Liem and P. Reiss, *Chem. Mater.*, 2009, **21**, 2422–2429.
- [8] (b) W-S. Song and H. Yang, *Chem. Mater.*, 2012, **24**, 1961-1967. (b) H. Zhong, Z. Wang, E. Bovero, Z. Lu, F. C. J. M. van Veggel and G. D. Scholes, *J. Phys. Chem. C*, 2011, **115**, 12396-12402.
- [9] Z. Tan, Yu. Zhang, Ch. Xie, H. Su, J. Liu, C. Zhang, N. Dellas, S. E. Mohnney, Y. Wang, J. Wang and J. Xu, *Adv. Mater.*, 2011, **23**, 3553–3558.
- [10] (a) J. Xu, X. Yang, T-L. Wong and C-S. Lee, *Nanoscale*, 2012, **4** 6537. (b) C. Wu, Z. Hu, C. Wang, H. Sheng, J. Yang and Y. Xie, *Appl. Phys. Lett.* 2007, **91**, 143104. (c) L. Zheng, Y. Xu, Y. Song, C. Wu, M. Zhang and Y. Xie, *Inorg. Chem.*, 2009, **48** 4003. (d) P. A. Fernandes, P. M. P. Salome and A. F. Cunha, *J. Phys D: Appl Phys*, 2010, **43**, 215403. (e) B. Qu, M. Zhang, D. Lei, Y. Zeng, Y. Chen, L. Chen, Q. Li, Y. Wang and T. Wang, *Nanoscale*, 2011, **3**, 3646. (f) M. E. Norako, M. J. Greaney and R. L. J. Brutchey, *J. Am. Chem. Soc.*, 2012, **134**, 23.
- [11] (a) Y. Xiong, Y. Xie, G. Du and H. Su, *Inorg. Chem.* 2002, **41**, 2953-2959. (b) S. Okano, S. Takeshita and T. Isobe, *Mater. Lett.* 2015, **145**, 79-82. (c) J. Chang and E. R. Waclawik, *Chem. Eng. Commun.*, 2013, **15**, 5612-5619. (d) B. Li, Y. Xie, J. Huang and Y. Qian, *J. Solid State Chem.* 2000, **153**, 170-173.
- [12] (a) S. Okano, S. Takeshita and T. Isobe, *Mater. Lett.* 2015, **145**, 79-82. (b) Q. Liu, Z. Zhao, Y. Lin, P. Guo, S. Li, D. Pan and X. Ji, *Chem. Commun.* 2011, **47**, 964-966. (c) X. Liu, X. Wang and M. T. Swihart, *Chem. Mater.* 2015, **27**, 1342-1348. (d) L. Yi, D. Wang and M. Gao, *Chem. Eng. Commun.*, 2012, **14**, 401-404. (e) J. Chang and E. R. Waclawik, *Chem. Eng. Commun.*, 2013, **15**, 5612-5619.

- (f) H. Wu, D. Liu, H. Zang, C. Wei, B. Zeng, J. Shi and S. Yang, *Carbon*, 2012, **50**, 4847-4855. (g) Y. Tan, Z. Lin, W. Ren, W. Ren, W. Long, Y. Wang and X. Ouyang, *Mater. Lett.* 2012, **89**, 240-242.
- [13] N. Li, Y. Xie, J. Huang and Y. Qian, *J. Solid State Chem.* 2000, **153**, 170.
- [14] X. Chen, H. W. Sato and M. Mieno, *J. Solid State Chem.* 1998, **139**, 144.
- [15] S. Jaulmes, J. Rivet and P. Laruelle, *Acta Crystallogr. B* 1977, **33**, 540.
- [16] X. Chen and W. H. Sato, *Mater. Res. Bull.* 1999, **34**, 239.
- [17] D. M. Berg, R. Djemour, L. Gutay, G. Zoppi, S. Siebentritt and P. J. Dale, *Thin Solid Films* 2012, **520**, 291-6294.
- [18] Q. Chen, X. Dou, Y. Ni and S. Zhuang, *J. Colloid Interface Sci.* 2012, **376**, 327-330.
- [19] D. Tiwari, T. K. Chaudhuri, T. Shripathi, U. Deshpande and R. Rawat, *Sol. Energy Mater. Sol. Cells.* 2013, **113**, 165- 170.
- [20] A. Kanai, H. Araki, A. Takeuchi and H. Katagiri, *Phys. Status Solidi B*, 2015, **252**, 1239–1243.
- [21] (a) M. Nakashima, J. Fujimoto, T. Yamaguchi and M. Izaki, *Appl. Phys. Express*, 2015, **8**, 042303. (b) U. V. Ghorpade, M. P. Suryawanshi, S. W. Shin, I. Kim, S. K. Ahn, J. H. Yun, C. Jeong, S. S. Kolekar and J. H. Kim, *Chem. Mater.* 2016, **28**, 3308–3317.
- [22] (a) J. Xiao, Y. Xie, R. Tang and Y. Qian, *J. Solid State Chem.*, 2001, **161**, 179-183. (b) Y. Jiang, Y. Wu, X. Mo, W. Yu, Y. Xie and Y. Qian, *Inorg. Chem.*, 2000, **39**, 2964-2965.
- [23] (a) Y. Jiang, Y. Wu, S. Yuan, B. Xie, S. Zhang and Y. Qian, *J. Mater. Res.*, 2001, **16**, 2805-2809. (b) A. Pein, M. Baghbanzadeh, T. Rath, W. Haas, E. Maier, H. Amenitsch, F. Hofer, C. O. Kappe and G. Trimmel, *Inorg. Chem.*, 2011, **50**, 193–200.
- [24] (a) C-C. Wu, C-Y. Shiau, D. W. Ayele, W-N. Su, M.-Y. Cheng, C-Y. Chiu and B-J. Hwang, *Chem. Mater.*, 2010, **22**, 4185–4190. (b) S. L. Castro, S. G. Bailey, R. P. Raffaele, K. K. Banger and A. F. Hepp, *Chem. Mater.*, 2003, **15**, 3142-3147.
- [25] (a) K. K. Banger, M. H. C. Jin, J. D. Harris, P. E. Fanwick and A. F. Hepp, *Inorg. Chem.*, 2003, **42**, 7713-7715. (b) S. L. Castro, S. G. Bailey, R. P.

Chapter 6

- Raffaella, K. K. Banger and A. F. Hepp, *J. Phys. Chem. B*, 2004, **108**, 12429-12435.
- [26] (a) B. Koo, R. N. Patel and B. A. Korge, *J. Am. Chem. Soc.*, 2009, **131**, 3134–3135.
- [27] Z. Su, K. Sun, Z. Han, F. Liu, Y. Lai, J. Li and Y. Liu, *J. Mater. Chem.*, 2012, **22**, 16346-16352.
- [28] G. M. Ilari, C. M. Fella, C. Ziegler, A. R. Uhl, Y. E. Romanyuk and A. N. Tiwari, *Sol. Energy Mater. Sol. Cells.*, 2012, **104**, 125-130.
- [29] M. Bouaziz, M. Amlouk and S. Belgacem, *Thin Solid Films*, 2009, **517**, 2527-2530.
- [30] W. Wang, H. Shen and J. Li, *Mater. Lett.* 2013, **111**, 5-8.
- [31] J. Park, M. Song, W. M. Jung, W. Y. Lee, H. Kim, Y. Kim, C. Hwang and W. Shim, *Dalton Trans.*, 2013, **42**, 10545-10550.
- [32] D. Tiwari, T. K. Chaudhuri and T. Shripathi, *Appl. Surf. Sci.*, 2014, **297**, 158–166.
- [33] S. Dias, B. Murali and S. B. Krupanidhi, *Sol. Energy Mater. Sol. Cells*, 2015, **143**, 152–158.
- [34] (a) <https://www.nrel.gov/pv/copper-indium-gallium-diselenide-solar-cells.html> (b) J. Pettersson, T. Torndahl, Ch. Platzer-Bjorkman, A. Hultqvist, and M. Edoff, *IEEE Journal of Photovoltaics*, 2013, **3**, 1376-1382. (c) T. K. Todorov, O. Gunawan, T. Gokmen and D. B. Mitzi, *Prog. Photovolt: Res. Appl.* 2013, **21**, 82–87. (d) M. Yuan, D. B. Mitzi, W. Liu, A. J. Kellock, S. J. Chey and V. R. Deline, *Chem. Mater.* 2010, **22**, 285–287.

Chapter 7

Summary and conclusions

Organic surfactant molecules (known as capping agents or stabilizing agents) surround the NPs obtained by synthetic chemical methods. The presence of these unwanted capping agents hampers the chances of harnessing benefits of surface-dependent properties to their full potential. Therefore, we have developed a novel and single step HMDS-assisted synthesis to produce surfactant free binary and ternary metal chalcogenide NPs. The method was a modification of the synthesis developed in our lab earlier. Since the solubility of reactants plays a significant role in any reaction medium and decides the product(s) formation, we have modified the HMDS – assisted reaction changing the metal precursor, sulphur source and the reaction conditions. Overall, hexamethyldisilazane played multiple roles as capping agent, reductant, and solvent.

Using this synthetic method, we have produced CuS, Cu₂S, CdS, Bi₂S₃ and Ni₃S₄ NPs, which had clean surfaces. We have also synthesised surfactant/template free ternary metal chalcogenides, CuInS₂, Cu₂SnS₃ and Cu₃SnS₄ NPs by modified HMDS- assisted synthetic method. The method was utilised in the synthesis of a specific stoichiometric product selectively in a pure form when various stoichiometric products of the material are known. The rare phases of metal chalcogenides NPs were produced selectively in a simple bottom-up synthesis without using any template or sensitive organometallic precursors. All these NPs were stable for several months as confirmed by time-dependent PXRD analyses. This result indicated that stabilization by capping agent is not required after NP formation for metal chalcogenides.

The rare phase of nickel sulphide family, Ni₃S₄ was prepared in the pure form without mixing of any other stoichiometry by modified- hexamethyldisilazane assisted synthesis. The reactions yielded phase pure spherical NPs of the size ranging 8- 29 nm. We have demonstrated Ni₃S₄ NPs as a versatile catalyst for nitro hydrogenation of both activated and deactivated nitrobenzene. The NPs were reused

Chapter 7

ten times without loss of their catalytic activity. These Ni_3S_4 NPs showed enhanced catalytic activity because of their clean surfaces without any surfactant molecules around them.

CuS and Cu_2S nanostructures were synthesized in stoichiometry controlled reactions using the modified HMDS-assisted synthesis. This method yielded hexagonal CuS NPs with average size of 22 ± 6 nm and cubic Cu_2S NPs with average size of 52 ± 10 nm. We have established an efficient photocatalytic activity of CuS nanostructures through photocatalytic degradation of Rhodamine B dye. It was observed that the CuS flowers rapidly decomposed Rhodamine B in solution (12 min). The productive catalytic activity was rationalized by invoking clean surfaces of NPs. We have also confirmed the influence of illumination intensity on the efficacy of the catalyst. Recyclability studies showed that photocatalyst could be recycled up to three times. SEM analysis confirmed that flower architectures responsible for the photocatalytic activity.

Template-free cadmium sulphide NPs were synthesised by modified HMDS-assisted synthesis. This method yielded hexagonal crystal structure of CdS NPs with the size of 12- 42 nm. The synthesized materials were employed for the reduction of aqueous Cr(VI) under visible light ($\lambda > 420$ nm) irradiation. The prepared CdS NPs demonstrated better performance for Cr(VI) removal at acidic pH. It was observed that the photocatalytic activity of CdS NPs in aqueous suspension exhibited immense removal capacity for toxic Cr(VI) , due to its smaller particle size and well dispersibility.

Orthorhombic Bi_2S_3 NPs were synthesized by modified HMDS-assisted synthesis. This method yielded orthorhombic crystal structure of Bi_2S_3 NPs with the size of 15- 82 nm. Bi_2S_3 nanoflakes were synthesized by the wet chemical method and demonstrated its photo-responsivity through the fabrication of prototype device by dry-casting of Bi_2S_3 suspensions on the electrodes. The device exhibited a linear response to the intensity of light under illumination and had the repose time of 1.1 s. We found that the higher light illumination can enhance photoresponse of the present system. Further, Bi_2S_3 nanoflakes had the resistance of 3.15 ± 0.02 k Ω which was in

the optimal range photodetector operation. A key advantage of the present synthetic approach is the synthesis and fabrications were carried out in the ambient conditions.

Surfactant/template free ternary metal chalcogenides like CuInS_2 , (CIS) Cu_2SnS_3 and Cu_3SnS_4 (CTS) NPs were synthesized by modified HMDS-assisted synthetic method. The reaction yielded CuInS_2 NPs of size 10-20 nm having spindle-shaped morphology. Through this synthetic method, Cu_2SnS_3 and Cu_3SnS_4 NPs of size 30-50 nm having a cauliflower-like morphology were obtained. We have attempted to fabricate the solar cell using CIS and CTS NPs so as to understand the effect of surfactant free NPs on the efficiency. However, the assembled device had photovoltaic performances of relatively low current densities (CIS $0.011 \mu\text{A cm}^{-2}$ and for CTS up to $208 \mu\text{A cm}^{-2}$) and open circuit voltage (CIS 0.49 mV and for CTS up to 0.55-0.61 mV). From these observations, we have concluded device fabrication needs to be standardised to achieve high efficiency.

The solubility of NPs was a prominent issue in the present synthetic procedure of HMDS-assisted synthesis. All the obtained materials were insoluble making it difficult in the fabrication, but the same made it suitable to function as heterogeneous catalysts. Hence current method has to be improved for the better passivation of surface and solubility.

Supplementary material

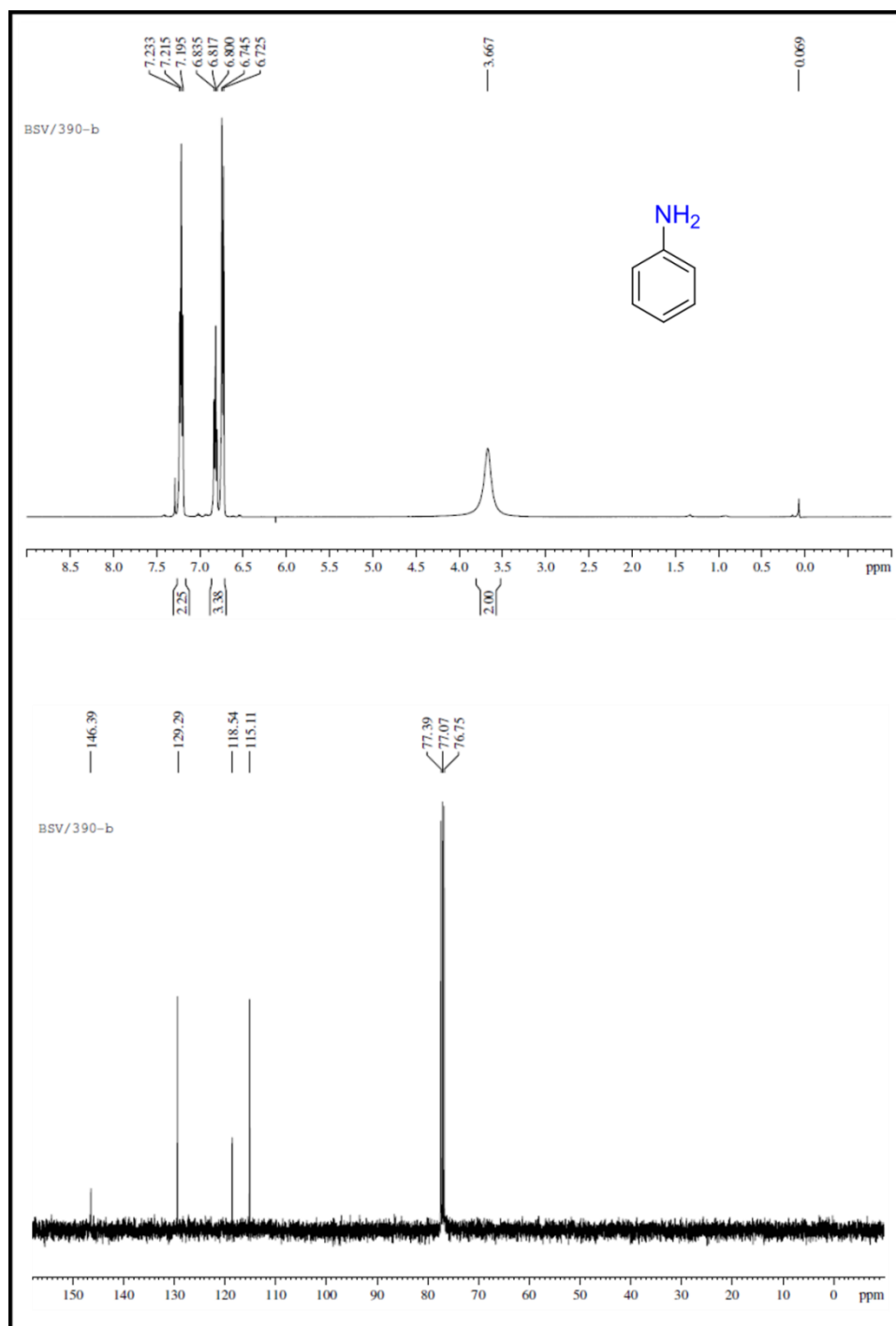


Figure S1. ^1H and ^{13}C NMR spectra of aniline

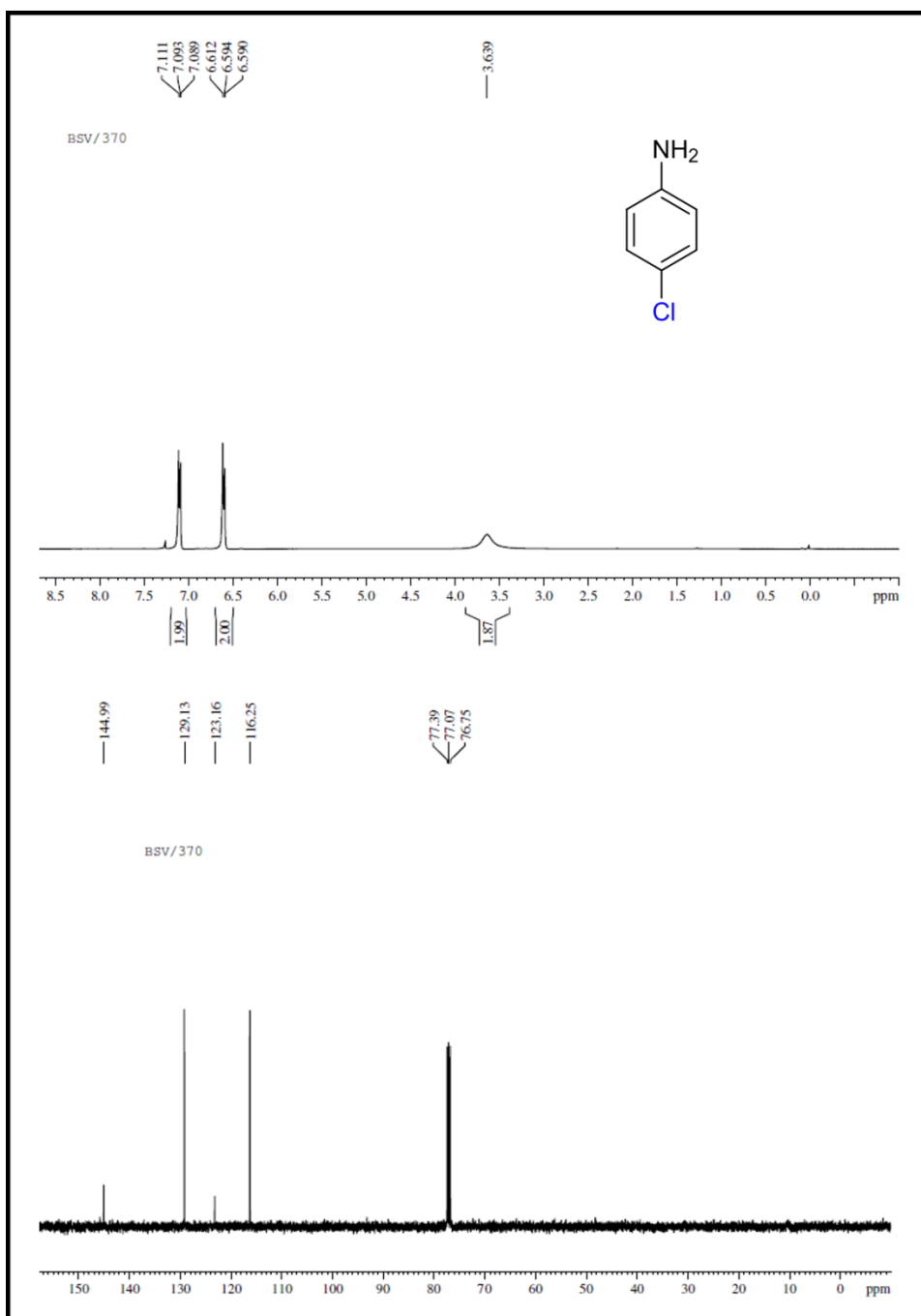


Figure S2. ^1H and ^{13}C NMR spectra of 4-chloroaniline

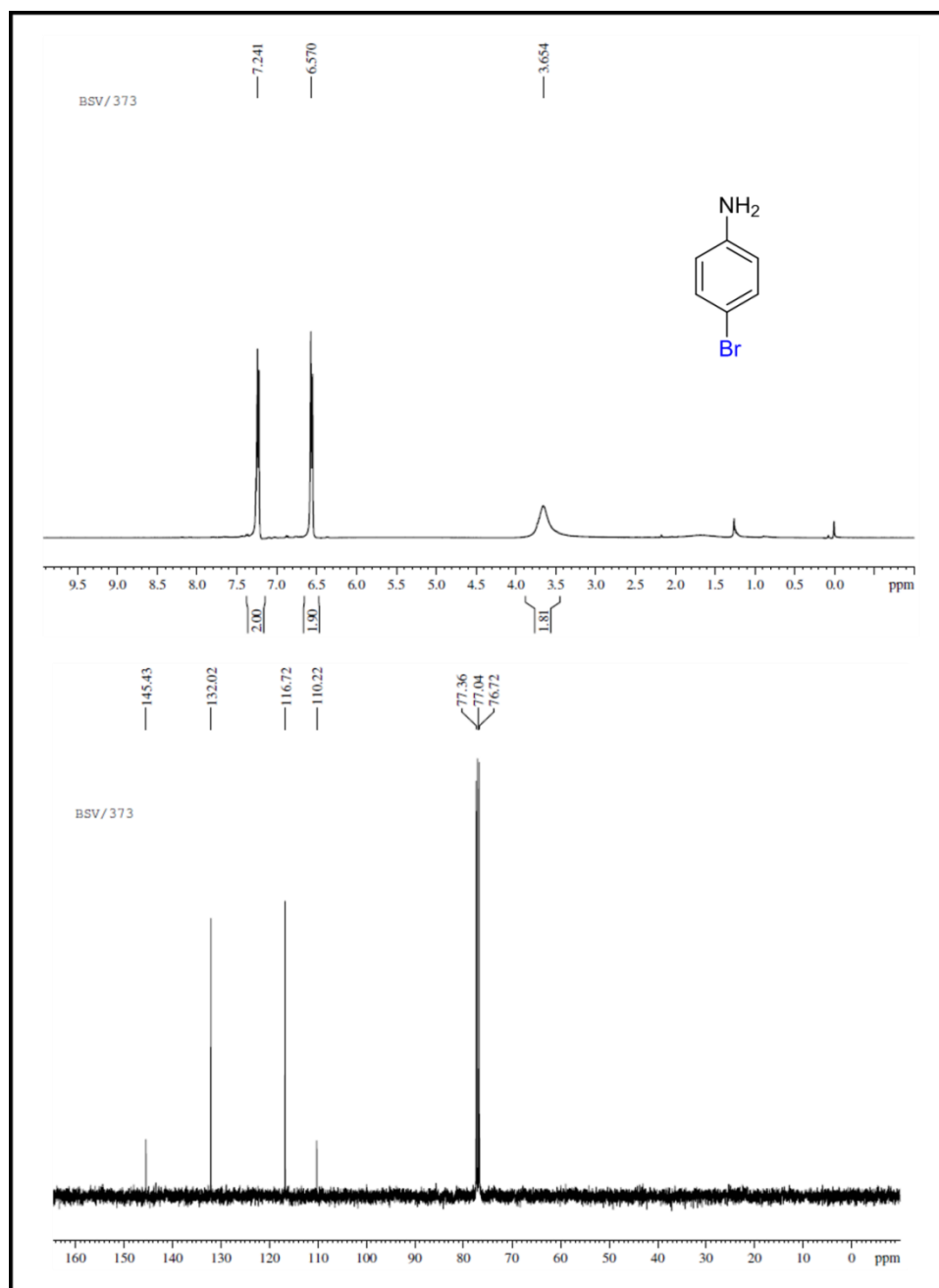


Figure S3. ^1H and ^{13}C NMR spectra of 4-bromoaniline

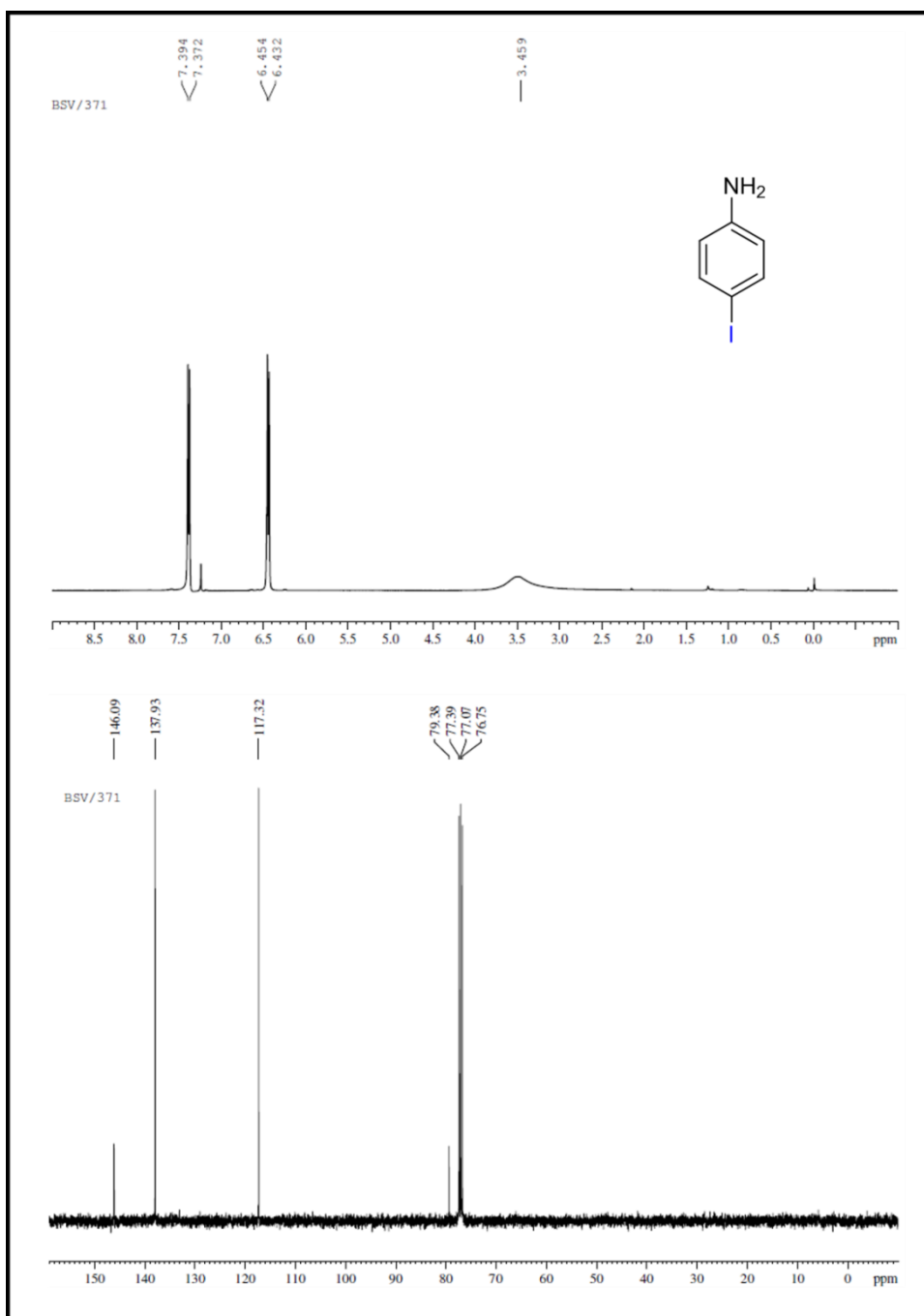


Figure S4. ¹H and ¹³C NMR spectra of 4-iodoaniline

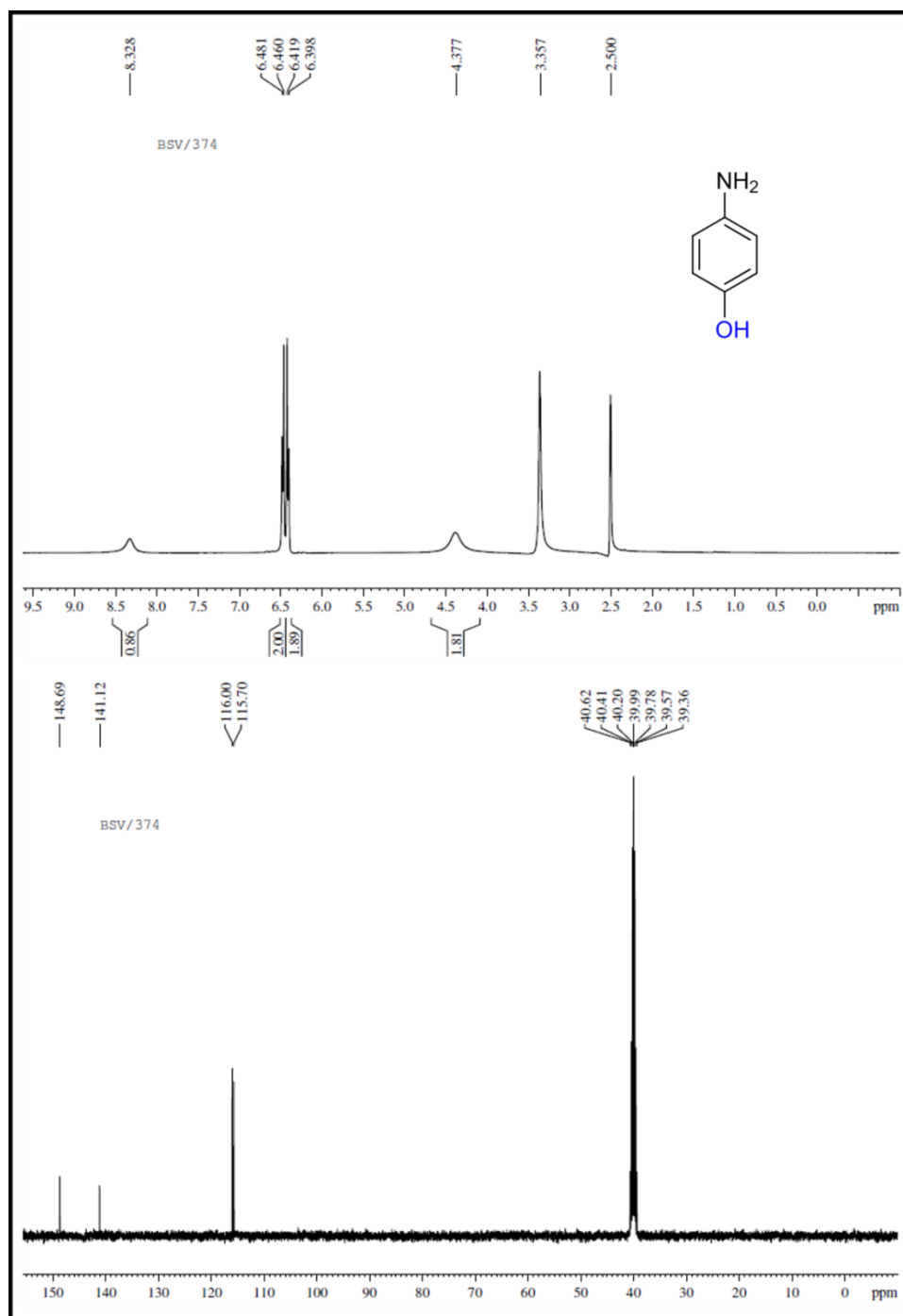


Figure S5. ^1H and ^{13}C NMR spectra of 4-aminophenol

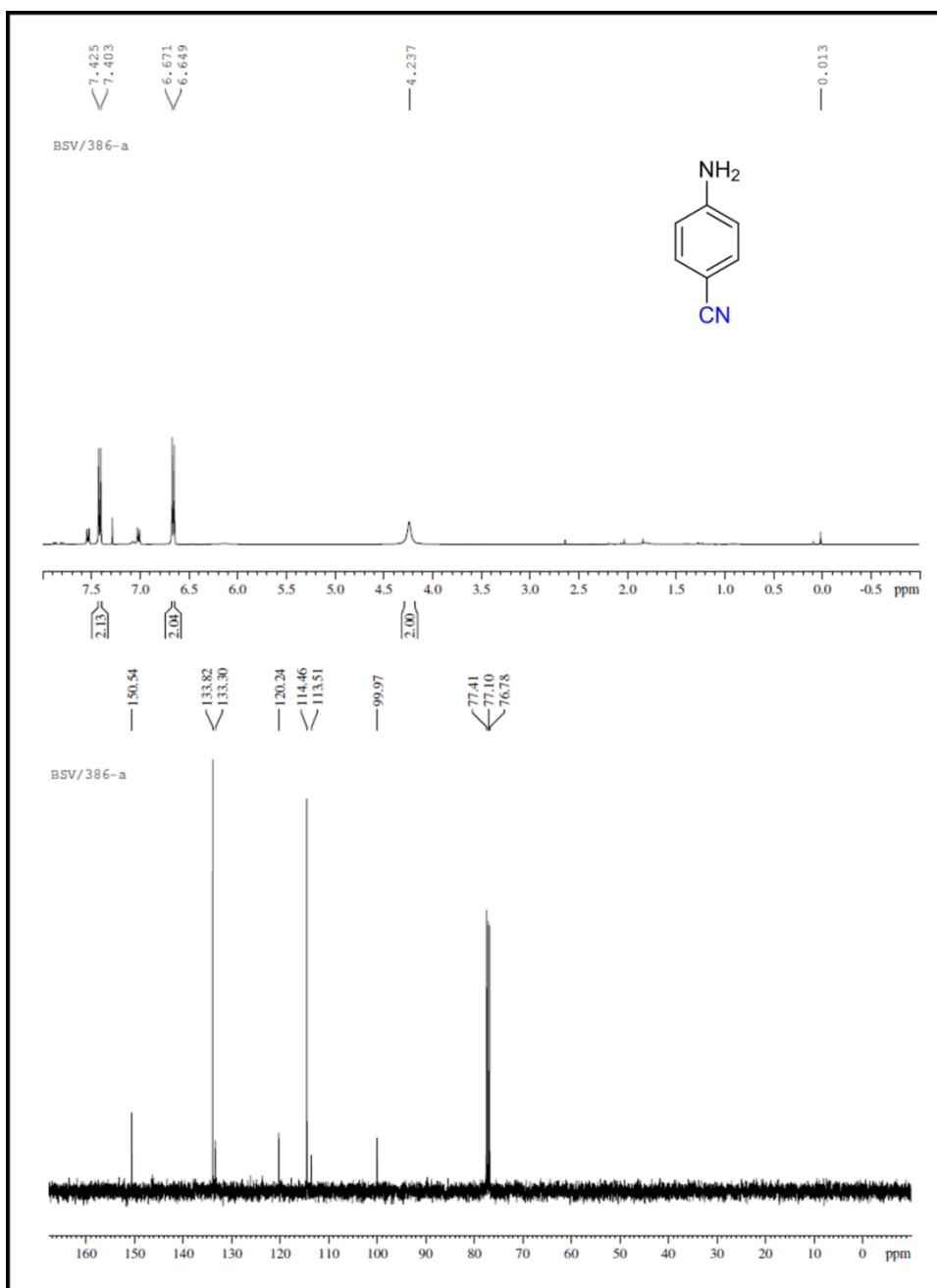


Figure S6. ¹H and ¹³C NMR spectra of 4-aminobenzonitrile

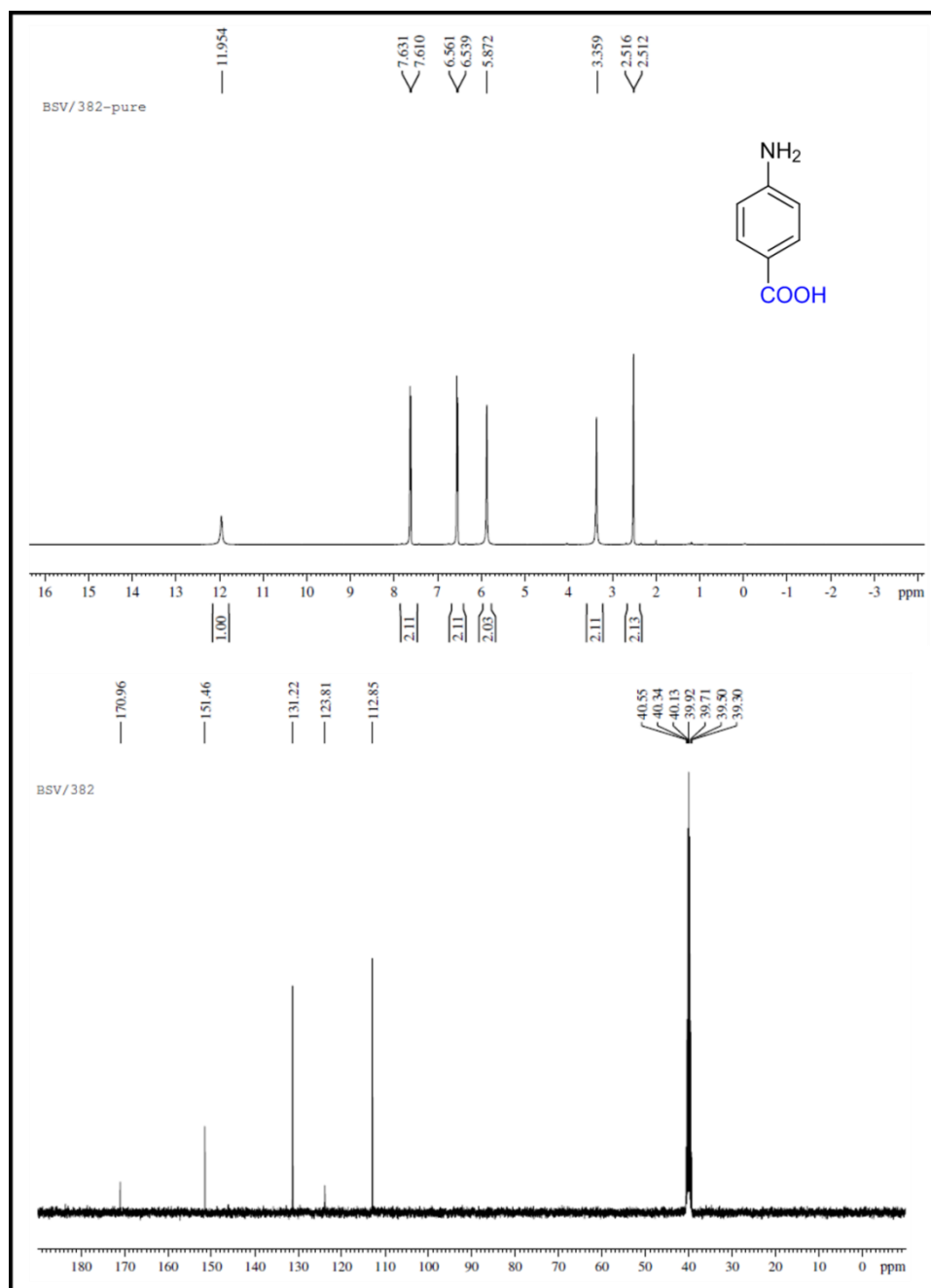


Figure S7. ¹H and ¹³C NMR spectra of 4-aminobenzoic acid

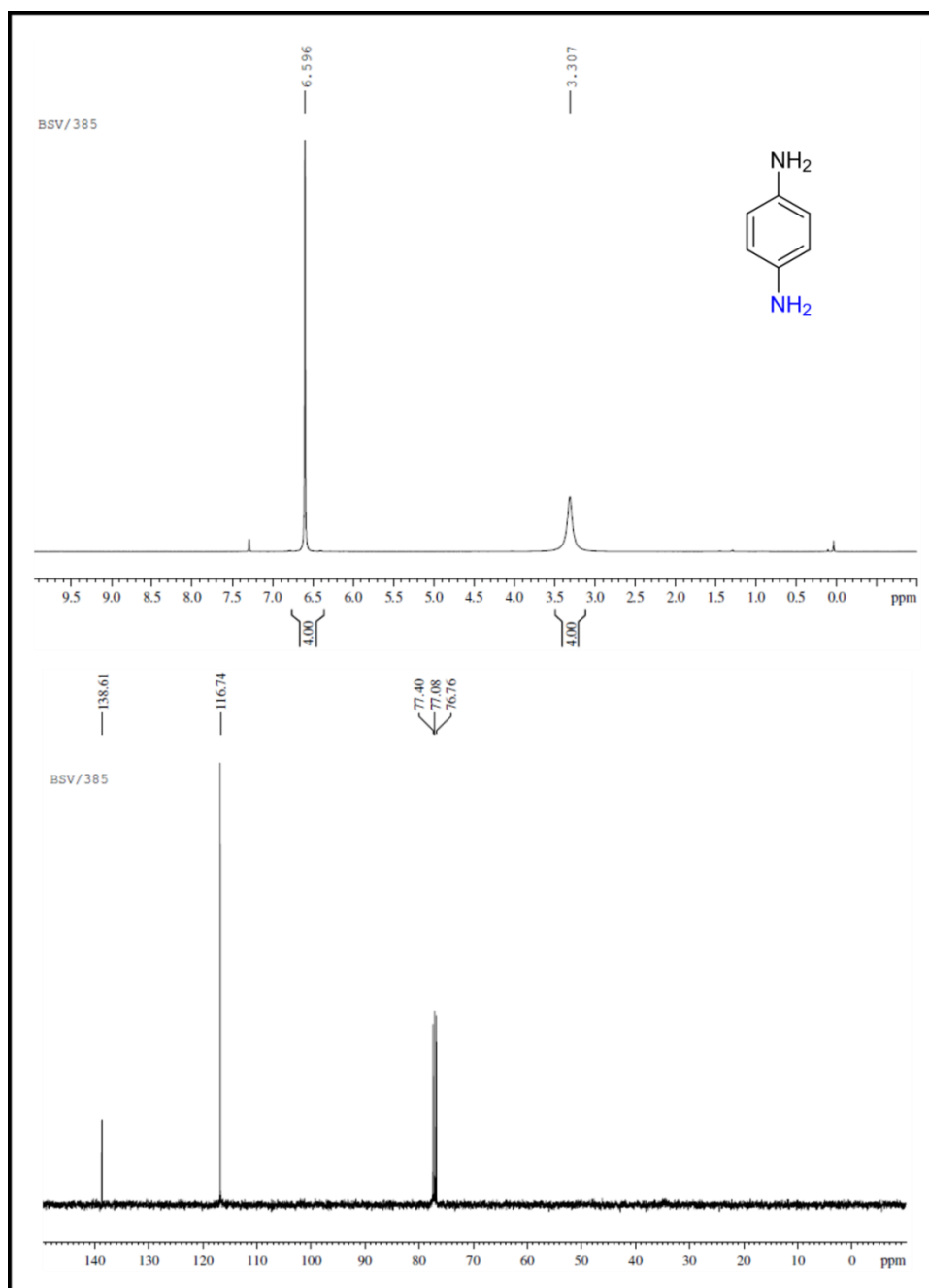


Figure S8. ^1H and ^{13}C NMR spectra of benzene-1,4-diamine

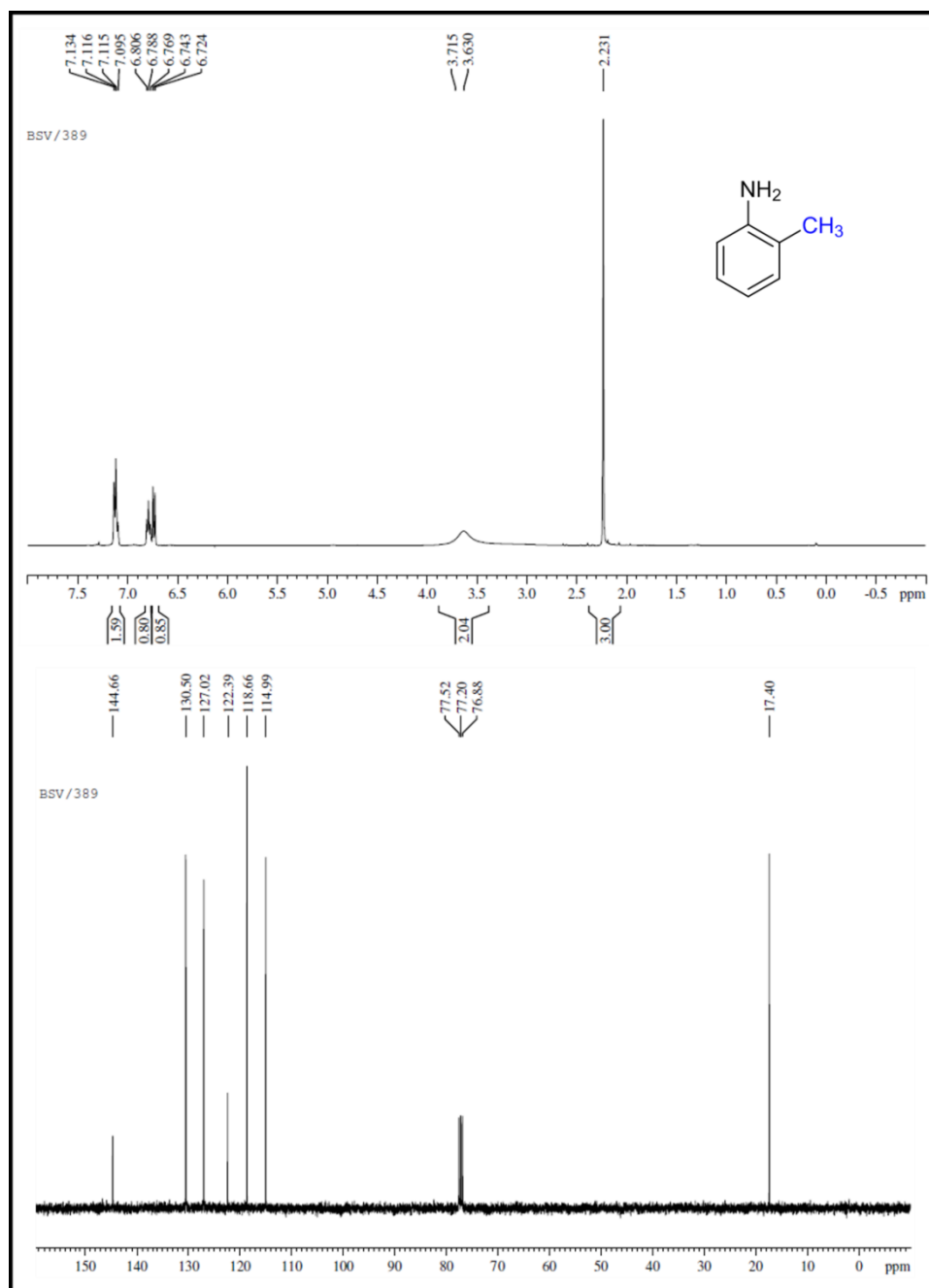


Figure S9. ^1H and ^{13}C NMR spectra of 1-methyl-2-nitrobenzene

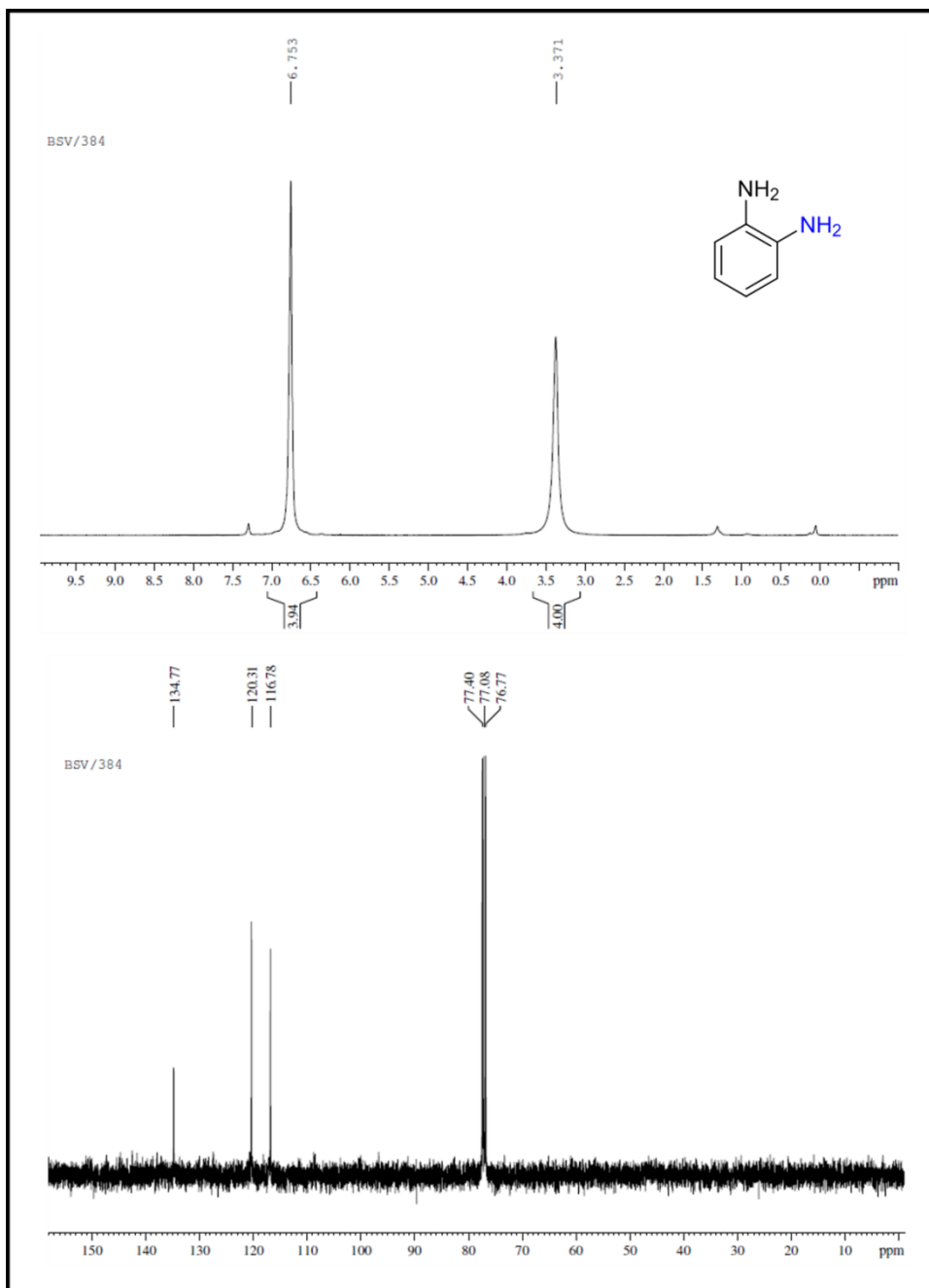


Figure S10. ¹H and ¹³C NMR spectra of benzene-1,2-diamine

List of Publications

Publications from thesis

1. **Billakanti Srinivas**, Baskaran Ganesh Kumar and Krishnamurthi Muralidharan, *Journal of Molecular Catalysis A: Chemical*, 2015, **410**, 8–18.
2. **Billakanti Srinivas** and Krishnamurthi Muralidharan, “Effect of surfactant or support material free CdS nanoparticles on Cr(VI) removal” *ChemistrySelect*, (In press).
3. **Billakanti Srinivas**, Baskaran Ganesh Kumar and Krishnamurthi Muralidharan, *ChemistrySelect*, 2017, **2**, 4753 – 4758.
4. Baskaran Ganesh Kumar, **Billakanti Srinivas** and Krishnamurthi Muralidharan, *Materials Research Bulletin*, 2017, **89**, 108–115.
5. Baskaran Ganesh Kumar, **Billakanti Srinivas**, Muvva Durga Prasad and Krishnamurthi Muralidharan, *J Nanopart Res.*, 2015, **17**, 325.
6. **Billakanti Srinivas** and Krishnamurthi Muralidharan, “Facile Synthesis of Cu_2SnS_3 and Cu_3SnS_4 Nanoparticles and Their Application in Photodetectors” (Manuscript under preparation).
7. **Billakanti Srinivas**, K. O. Anjana, Velpuri Venkateswara rao, Manzoor Ahmad Pandit and Krishnamurthi Muralidharan, “Ternary metal chalcogenides: Synthesis, characterization and solar cell fabrication of $\text{CuIn}(\text{S/Se})_2$ and $\text{CuInGa}(\text{S/Se})_2$ nanoparticles” (Manuscript under preparation).

Other publications

8. Heeralal Vignesh Babu, **Billakanti Srinivas**, Khevath Praveen Kumar Naik and Krishnamurthi Muralidharan, *J. Chem. Sci.* Vol. 127, No. **4**, 2015, 635–641.
9. Heeralal Vignesh Babu, **Billakanti Srinivas** and Krishnamurthi Muralidharan, *Polymer*, 2015, **75**, 10-16.

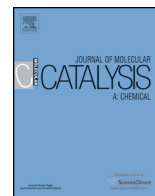
10. **Billakanti Srinivas**, Heeralal Vignesh Babu, K. O. Anjana and Krishnamurthi Muralidharan, “Phosphorus containing polymers syntheses, characterization and their lithium-ion conductivities” (Manuscript under preparation).

Poster and Oral Presentations

1. [Billakanti Srinivas](#) Participated in the workshop “National Workshop on Advances in X-ray Powder Diffractometry & Scanning Electron Microscopy” during **15-17 July. 2013** conducted by the Department of Metallurgical and Materials Engineering, Rajiv Gandhi University of Knowledge Technologies (RGUKT), Hyderabad, India.
2. [Billakanti Srinivas](#), Bhaskaran Ganesh Kumar and Krishnamurthi Muralidharan, presented a **poster** at Modern Trends in Inorganic Chemistry (MTIC- XV) held at department of chemistry **IIT- Roorkee**, India on **13-16 Dec. 2013**.
3. [Billakanti Srinivas](#), Heralala Vignesh Babu and Krishnamurthi Muralidharan, presented a **poster** in In-house symposium, School of Chemistry, University of Hyderabad on **12-13 Feb. 2013**. (**Chemfest-2013**)
4. [Billakanti Srinivas](#) and Krishnamurthi Muralidharan, presented a **poster** in In-house symposium, School of Chemistry, University of Hyderabad on **15-16 Feb. 2014**. (**Chemfest-2014**)
5. [Billakanti Srinivas](#) and Krishnamurthi Muralidharan, presented a **poster** at **1st Indo-Taiwan** Symposium on Recent Trends in Chemical Sciences on **17-18 Nov. 2014** organized by University of Hyderabad, Hyderabad, India.
6. [Billakanti Srinivas](#) Participated in the **Royal Society Of Chemistry** Indian Roadshow Workshop on **7 Nov 2014** organized by University of Hyderabad, Hyderabad, India.
7. [Billakanti Srinivas](#) and Krishnamurthi Muralidharan, presented a **poster** at International Symposium on Polymer Science and Technology (**MACRO-2015**), **23-26 Jan. 2015** at Indian Association for the Cultivation of Science, **Kolkata**, India.
8. [Billakanti Srinivas](#) Presented **Oral Presentation** on **Feb. 2016** “Stabilizer free copper sulphide nanostructures for rapid photocatalytic decomposition of rhodamine B” presented at **Chemfest-2016**, 13th Annual In-House

Symposium in School of Chemistry, University of Hyderabad, Hyderabad, India.

9. [Billakanti Srinivas](#) Presented **Oral Presentation** on **19th March, 2016** “Nanomaterials Synthesis and Their Applications” at **Dr. K.V. Rao Scientific Society**, Hyderabad, India.
10. [Billakanti Srinivas](#) participated in the **Block course** entitled “**Advanced Transmission Electron Microscopy and Spectroscopy**” conducted at the University of Hyderabad, Hyderabad. During the period **15th March- 15th April 2017**.
11. [Billakanti Srinivas](#) and Krishnamurthi Muralidharan, presented a **poster** at **CRSI NSC-21** conducted at the **CSIR-Indian Institute of Chemical Technology (IICT)**, Hyderabad. During the period **13-16 July, 2017**.



Stabilizer free copper sulphide nanostructures for rapid photocatalytic decomposition of rhodamine B



Billakanti Srinivas¹, Baskaran Ganesh Kumar¹, Krishnamurthi Muralidharan^{*}

School of Chemistry, University of Hyderabad, Hyderabad, India

ARTICLE INFO

Article history:

Received 6 April 2015

Received in revised form 14 August 2015

Accepted 31 August 2015

Available online 2 September 2015

Keywords:

Photocatalysis

Functional nanoparticles

CuS flowers

Inorganic materials

ABSTRACT

The capping agents present on the surfaces of nanoparticles unfavourably modify the properties of the nanostructures. Particularly in the catalysis, most of the potential catalytic centres are screened by the capping agents. Therefore, we have developed a novel method of synthesizing stabilizer-free CuS and Cu₂S nanostructures for photocatalytic applications. These nanostructures were synthesized by modified HMDS assisted synthetic method at 130 °C. The CuS microflowers were constructed by self-assembly of nanoflakes which was grown through anisotropic growth of (1 0 3) planes. We have demonstrated an efficient photocatalytic activity of CuS nanostructures through photocatalytic decomposition of Rhodamine B dye. The CuS flowers rapidly decomposed Rhodamine B in solution (12 min). The efficient catalytic activity is explained by invoking clean surfaces of nanoparticles. We have also demonstrated the influence of illumination intensity on the efficiency of catalyst and the recyclability.

© 2015 Published by Elsevier B.V.

1. Introduction

Colloidal syntheses of nanoparticles have opened enormous opportunities for the uses of nanoparticles by offering liquid state metals and semiconductors [1–10]. Furthermore, the colloidal syntheses provided accesses to the complex nanostructures like flowers [11,12], dandelions [13], wafers [14], heterodimers [15], core-shell particles [16], fibrous materials [17], porous materials [18] and other hierarchical nanostructures. Generally, the physical methods of production of nanoparticles do not have control on the complex hierarchical structural formation. However, the reaction conditions and reagents used in the chemical syntheses decide the dimensions and properties of the complex structures.

Microflowers are 3D-superstructures of intermediate size with remarkable properties [19–25]. Microflowers have a unique morphology; being in microscale but constructed by nanoscale flakes and therefore ensemble the properties of individual nanoflakes too. Thus, the structure helps in harnessing entire size dependent properties all at the same time. Photocatalysis was one among many fields benefitted from the flower morphology [26–30]. Other than contribution of the nano size, flower morphology provides porous cavities for photocatalytic activity [31]. Among

various photocatalytic materials, copper sulphide gained attention because of the low cost, abundance and tunability. Recently, copper sulphide nanostructures showed improved photocatalytic performance [32–40].

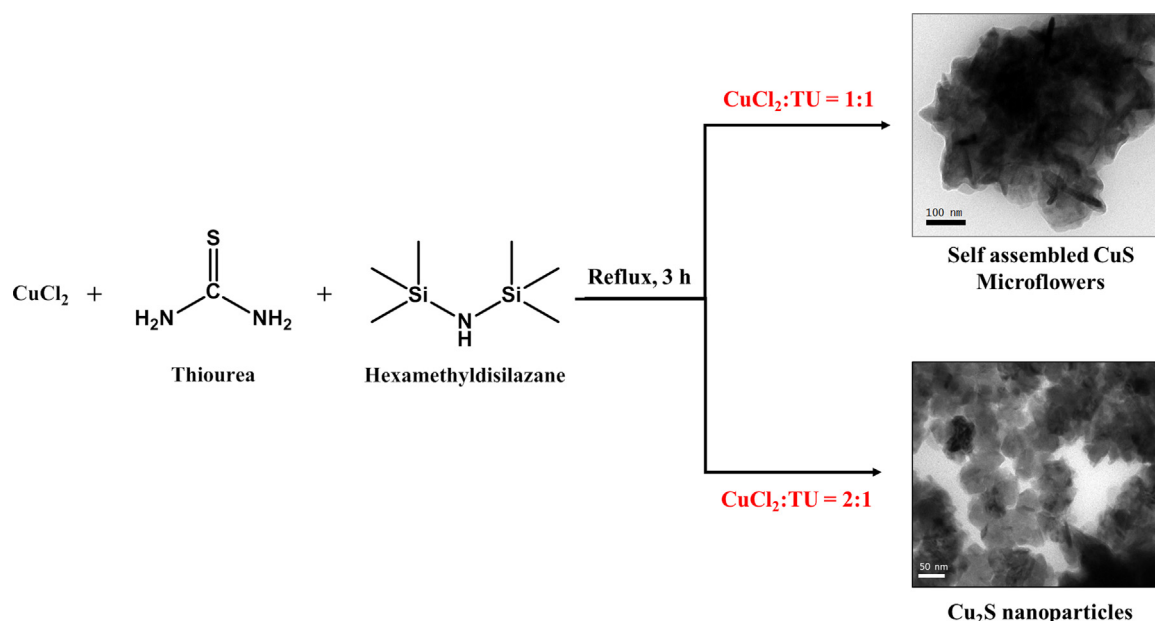
The surfactants/capping agents that present around/on the surfaces of nanoparticles unfavourably modify the properties of the nanostructures. Case in point, most of the potential catalytic centres in the nanoparticles are screened by the capping agents. However, synthesizing nanoparticles for catalysis, without organic surfactants but utilizing less energy, simple starting materials and simple purification procedures is a challenging task [41,42]. Herein, we have developed a direct synthesis of CuS microflowers assisted by hexamethyldisilazane (HMDS) and their photocatalytic activity. We have found that the nanoflakes constructed these microflowers. Using the same procedure, but by tailoring the stoichiometry of reaction, Cu₂S nanoparticles were also synthesised. HMDS used in these syntheses is a multifunctional reagent with capping and reducing abilities [43–45].

We have also demonstrated an efficient photocatalytic activity of CuS microflowers by photocatalytic degradation (within 12 min) of the Rhodamine B solution. We have investigated the influences of illumination intensity, amount of catalyst and flower morphology on the photocatalytic activity and quantified through rate constant measurements. We have also analysed the reason for the enhanced photocatalytic activity of CuS microflowers compared to the similar studies reported in literature [32–40].

^{*} Corresponding author.

E-mail address: kmsc@uohyd.ac.in (K. Muralidharan).

¹ Authors contributed equally to this work.



Scheme 1. Schematic Illustration of synthesis of CuS and Cu₂S nanoparticles.

2. Experimental Section

All chemicals were purchased from Aldrich, and used without purification.

2.1. Synthesis of CuS Microflowers

In a typical synthesis (Scheme 1, Fig. S1), a reaction flask containing copper (II) chloride (0.18 g, 1.4 mmol) and thiourea (0.10 g, 1.4 mmol) was degassed and flushed with dry nitrogen gas and then 1,1,1,3,3,3-bis(trimethylsilyl) amine (HMDS) (5 mL, 23.8 mmol) was injected into the flask. The reaction mixture was stirred at around reflux temperature ($\sim 130^\circ\text{C}$) under inert condition. Although the formation of copper sulphide was instantaneous, the reaction mixture was refluxed for 3 h to achieve uniform flower distribution. At the end of reaction hour, a black precipitate of CuS was isolated. The side products and unreacted HMDS were removed by vacuum. Then the black precipitate was washed with methanol (20 mL \times 3) followed by acetone (20 mL \times 3) at ambient temperature to remove unreacted copper (II) chloride and thiourea respectively. The final product was dried at 120°C for 3 h before analysis. Using synthetic procedure discussed here, we have synthesized copper sulphide nanoparticles up to 2.5 g, which showed the potential ease of method to scale up for commercial production.

2.2. Synthesis of Cu₂S Nanoparticles

Synthetic procedure of Cu₂S nanoparticles was same as the CuS flowers except for the reaction stoichiometric ratio (Scheme 1). Stoichiometry was set as 1:0.5 excess for CuCl₂ (0.2 g, 1.4 mmol), thiourea (0.053 g, 0.7 mmol) and HMDS (capping agent, 5 mL, 23.8 mmol) respectively. Since an excess of HMDS was present in the reaction, the mole ratio of HMDS was maintained constant for all reactions. The reaction mixture was stirred for 3 h at room temperature to avoid local concentration differences in the reaction mixture. A black precipitate of Cu₂S nanoparticles was obtained after 3 h of reflux. Modification of reaction time or temperature did not have any noticeable change in the product.

2.3. Photocatalysis

Decomposition of Rhodamine B in aqueous solution was studied in the presence of CuS microflowers as photocatalyst. All photocatalytic decomposition experiments were conducted in a cylindrical pyrex cell which was kept ~ 10 cm away from the light source to avoid thermal effect. In a standardized procedure, 60 mg of photocatalyst was added into the pyrex cell containing 60 mL aqueous solution of Rhodamine B of $3\ \mu\text{M}$ (1 g/L) concentration. Since it was a heterogeneous catalysis, CuS was added according to the weight-ratio (60 mg of CuS per 60 mL of $3\ \mu\text{M}$ of RhB). The solution was stirred before illumination under dark to create adsorption and desorption equilibrium (15 min). Blue LED controlled by Zahner Zennium electrochemical workstation (Zahner, Germany) illuminated the reaction mixture ($454\ \text{nm}$, $200\ \text{W m}^{-2}$). The reaction mixture was bubbled by constant flow of atmospheric oxygen. Analysing environments were maintained cool to avoid thermal assistance in photocatalysis.

The Rhodamine B concentration was monitored by colorimetry. During the photocatalysis, samples (5 mL) were withdrawn periodically (1 min) using syringes. Then the samples were centrifuged to remove residual catalyst particulates. This centrifugation process also avoided the scattering of UV light by CuS particles in analysis. Absorption spectra were collected until no changes observed in the absorption maximum. Rhodamine B concentrations in each sample were calculated by Beer Lambert law [$c = A/(\epsilon \times l)$]. Where, A = absorbance of dye at $553\ \text{nm}$, ϵ = molar absorption coefficient [46] of Rh B ($\epsilon = 87,000\ \text{M}^{-1}\ \text{cm}^{-1}$), l = path length of cuvette (1 cm). All absorption profiles were normalised for visual comparison. Rate constants were calculated from the slopes of plot $-\ln(C/C_0)$ versus irradiation time (t). Rate constants were expressed in inverse minutes. To ensure consistency, all analyses were repeated three times and standard errors were calculated.

To confirm recyclability, the catalyst was recovered by centrifugation after every cycle. The recovered catalyst was purified by washing with methanol (10 mL \times 5) and acetone (10 mL \times 2) and dried under vacuum for 2 h to obtain in powder form, which was used for recycling experiments and SEM analyses. Recycling experiments were also conducted under the standardized conditions mentioned above.

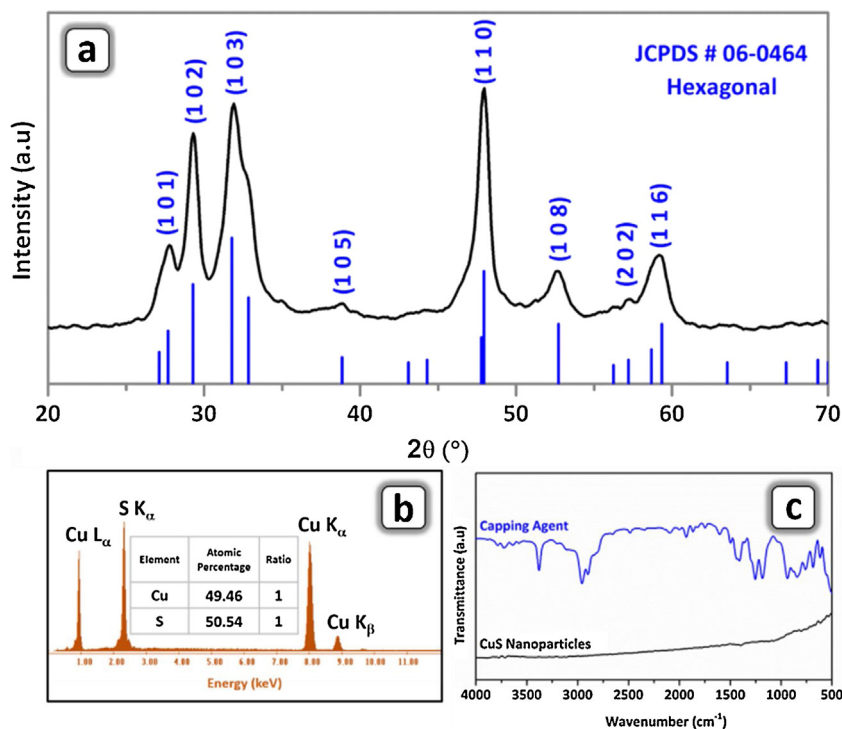


Fig. 1. (a) Powder X-ray diffraction pattern of copper sulphide microflowers. The vertical lines represent standard diffraction pattern from JCPDS library. CuS flowers had bulk hexagonal crystal structure. (b) EDAX spectrum of CuS microflowers. Peaks are labelled according to the energy values. Atomic ratio was 1:1. Peaks correspond to starting materials, capping agent and carbonaceous materials were not observed. (c) FTIR spectrum of copper sulphide microflowers. FTIR spectrum of HMDS is presented for visual comparison. Absence of capping agent in CuS microflowers was confirmed.

2.4. Instrumentation

Powder X-ray diffraction analyses of materials were carried out in Bruker D8 X-ray diffractometer with scan rate of 1° min^{-1} ($\text{Cu K}\alpha = 1.54 \text{ \AA}$; operating voltage = 40 kV; operating current = 30 mA). For scanning electron microscopic (SEM) studies, nanoparticles were dispersed in isopropyl alcohol and dry-casted onto ITO plates. Samples of EDAX measurements were mounted on a stub using a conductive carbon tape. FESEM and EDAX analyses were taken in Ultra 55 Carl Zeiss instrument with an operating voltage of 20 kV. For TEM measurements, nanoparticles were suspended in isopropyl alcohol and dry-casted on copper grids (200 mesh). TEM micrographs were obtained using FEI Technai G² 20 STEM with 200 kV acceleration voltage. Solid-state UV–vis absorption spectra were acquired using Shimadzu UV–3600 UV–vis spectrometer. Barium sulphate was used as filler. Liquid state UV measurements (for photocatalysis) were carried out from Cary 100 UV–vis spectrophotometer.

3. Results and discussion

3.1. Modified HMDS-assisted synthetic method

It is known that the solubility of reactants plays an important role in any reaction and decides the product(s) formed from the reaction [44,45]. We have developed a modified HMDS-assisted method [41–43] to synthesize CuS microflowers wherein easily soluble thiourea was used as the source of sulphur rather than elemental sulphur. Elemental sulphur was soluble in HMDS only at high reaction-temperature. In this reaction, copper(II) chloride was reacted with thiourea (1:1) in HMDS to obtain CuS microflowers (Scheme 1). Since thiourea was a soluble form of sulphur source at room temperature and its removal after the synthesis was easy.

Solubility of thiourea provided control in the present reaction and improved the quality of the materials obtained and further provided favourable condition to perform many reactions by adjusting the stoichiometry. While varying the stoichiometry of the reaction, Cu_2S nanoparticles were obtained when copper(II) chloride to thiourea ratio in the reaction was 2:1. Thus, the “modified HMDS-assisted synthesis” afforded a methodology for the production of both CuS microflowers and Cu_2S nanoparticles.

To explain the role of the HMDS in these reactions, a controlled reaction ($\text{CuCl}_2 + \text{thiourea}$) was performed. In this reaction, no copper sulphide was formed in the absence of HMDS explaining the necessity of HMDS to activate thiourea in the reaction. Dual role of HMDS as solvent and its involvement in arresting the growth of particles during syntheses in the HMDS-assisted methodology was explained clearly in the previous reports [43–45]. HMDS is presumed to play similar roles in this modified HMDS-assisted synthetic methodology for the production of metal sulphide nanomaterials.

3.2. Characterization of CuS nanomaterial

PXRD analysis confirmed the formation of CuS nanostructures and its crystal structure (Fig. 1a). In PXRD pattern obtained, the peak positions were resolved and broadened. Two dominant planes (103) and (110) were observed. Similar to the products obtained in other synthetic procedures, (110)_{CuS} plane grew higher than standard pattern [23,44]. Comparing with the standard diffraction pattern, it was concluded that CuS flowers had covellite crystal structure (JCPDS# 06-0464; hexagonal) and no other stoichiometric copper sulphide phases were identified in the PXRD pattern.

To confirm the composition of copper sulphide, EDAX (Fig. 1b) spectrum was obtained, which showed the atomic ratio of flowers as Cu:S = 1:1. The absence of chlorine (CuCl_2) and carbon signals

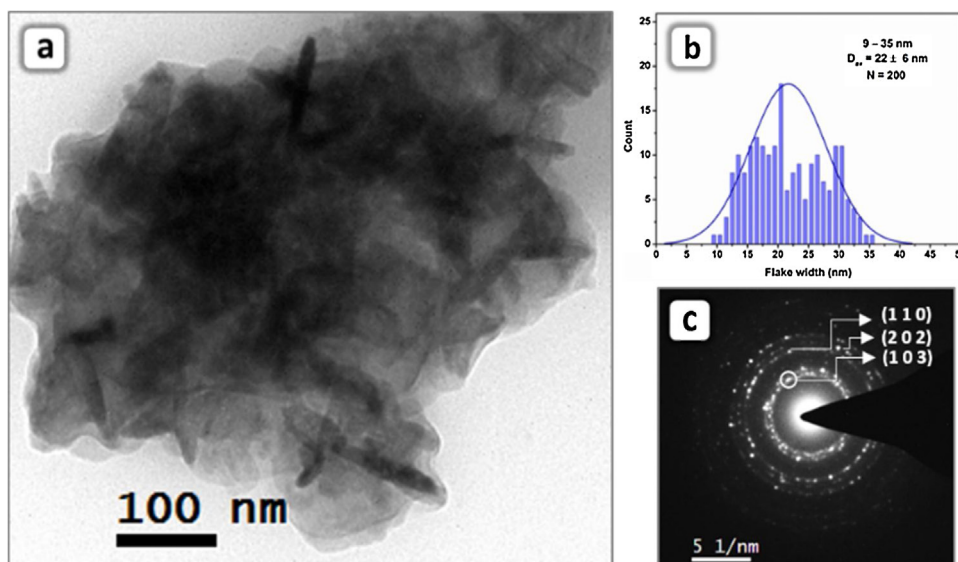


Fig. 2. (a) TEM micrograph of a copper sulphide microflower. The flower was constructed by flake shaped nanoparticles. (b) Distribution diagram of CuS flowers. Flake widths were 9–35 nm ($D_w = 22 \pm 6$ nm) and length of flakes varied with the size of the flowers. (c) Selected area diffraction pattern of flowers. Dotted pattern indicated the crystalline nature of flowers. Dominant (1 0 3)_{CuS} plane is highlighted by a circle.

in the spectrum confirmed complete removal of starting materials in the product and its purity. The absence of signal of silicon and carbonaceous species in EDAX spectrum and no absorbance in IR region (Fig. 1c) relating any organic moieties confirmed the clean surfaces of CuS flakes. Moreover, HRTEM micrographs did not show any signature of capping agent (amorphous layer) on the surface of nanoflakes (Fig. 3a). Since there was no capping agent on the surfaces of particles, the peak broadening in PXRD pattern was only due to the tiny sizes of particles. Although no capping agent (HMDS) was on the surfaces of nanoparticles, there was no agglomeration of nanoparticles and they were stable against oxidation. HMDS arrested the growth of nucleus formed during reaction but was removed in post synthetic process.

3.3. Dimensions and flower morphology of CuS particles

Dimensions and morphology of CuS particles formed in the present synthesis were analysed by transmission electron microscope. TEM micrographs showed a flower like architecture of CuS particles (Fig. 2a, Fig. S2). Low magnification images showed abundance and distribution of flowers. High magnification images showed that the flowers were constructed by nanoscale flake-shaped particles (Fig. 2a). Numerous flakes associated to construct three-dimensional architectures of flowers while the number of nanoflakes constructing flowers was not constant. Flower like structures were stable and not dissociated by sonication or concentration variation. Flower architecture was obtained in all reactions independent of variation in solvents and substrates.

The width of the flakes that constructing the flower like architecture was between 9 and 35 nm with the average of 22 ± 6 nm (Fig. 2b). The flakes had a constant width along the entire length of flakes. Flake widths were monodisperse and length varied according to the flower size. Polydispersity in length of flakes created polydispersity in the sizes of the flowers. Selected area diffraction (SAED) analysis of flowers showed a bright dotted pattern (Fig. 2c). The bright dots were indexed as (1 0 3), (2 0 2) and (1 1 0) planes of the bulk covellite structure. The dotted SAED pattern attributed to the crystalline nature of flakes. The obtained selected area diffraction pattern was consistent with powder diffraction pattern.

3.4. Anisotropic growth of (1 0 3)_{CuS} planes: self-assembly of nanoscale flakes

To understand the flake formation and their construction, inter-planar distances of a flake present in the periphery of a flower were measured by HRTEM (Fig. 3a). Lattice measurements of the flake showed lattice fringe of 2.8 Å (Fig. 3b), which corresponds to (1 0 3) planes of covellite structure. All the flakes possessed homogenous (1 0 3) planes irrespective to the size of the flowers. The (1 0 3) planes have grown parallel to the flakes. Hence, an anisotropic growth of (1 0 3) planes was responsible for flake like shape. This observation was in consistent with PXRD pattern. HRTEM images showed that flakes were crystalline without visual defects. Further, the flakes were magnified to the atomic level (Fig. 3c) and corresponding two-dimensional fast Fourier transformation (FFT) were obtained (Fig. 3d). FFT patterns were matching with patterns of PXRD and SAED.

All flakes seen in the TEM micrographs were uniform and without side arms. This observation eliminated the possibility of flower formation from the branching of single flake. There were no appreciable defective interfaces or twins were detected in high magnification TEM images of the flakes (Fig. 3c). Thus, the flower formation did not originate from oriented attachment of smaller nanoparticles [47]. In all micrographs, no flakes were interfaced with other flakes in flowers. All flakes existed individually in flowers. Hence, the flakes were the basic building blocks of flowers. Moreover, HRTEM image of flakes did not have amorphous layer on the surfaces (Fig. 3a). Hence, the capping agent was absent on the surface of nanoflakes. To minimize the surface energy, nanoflakes were self-assembled and constructed the flowers [20,44].

3.5. Stoichiometric modification—Cu₂S nanoparticles formation

Since copper sulphides exist in different stable stoichiometries, the reaction stoichiometric ratio was modified to understand the change in the product formation. When the stoichiometric ratio of CuCl₂:TU in the reaction is 2:1, Cu₂S nanoparticles were formed (Fig. S3). Other stoichiometric variations yielded the same Cu₂S nanoparticles. PXRD and EDAX analyses (Fig. 4a and b) confirmed successful synthesis of Cu₂S nanoparticles. PXRD pattern showed reflections of phase pure cubic Cu₂S (JCPDS # 65-2980). No traces

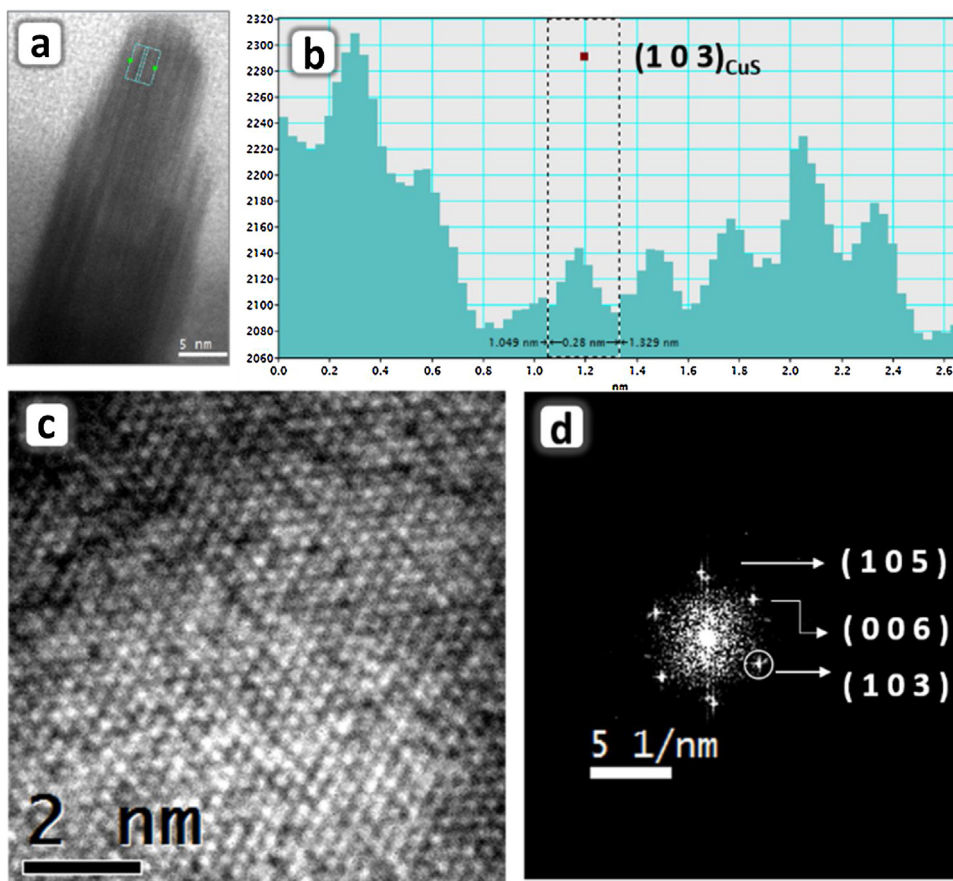


Fig. 3. (a) TEM image of a flake with width size of 16 nm. (b) Lattice profile of the flake. The flake grew parallel to $(1\ 0\ 3)_{\text{CuS}}$ plane. (c) HRTEM image of a flake. Lattices indicated the crystalline nature of the nanoflake. Lattices were free from defects. (d) Two dimensional fast Fourier transformation of image (c). Dominant $(1\ 0\ 3)$ plane is highlighted by a circle.

of other stoichiometric compounds were found. Peaks position and relative intensities were matching with standard pattern. EDAX spectrum showed Cu to S stoichiometric ratio in the product as 2:1. The absence of silicon signal in the EDAX spectrum and the absence of signature of HMDS in FTIR spectrum (Fig. 4c) confirmed the complete removal of capping agent on the surfaces of Cu_2S nanoparticles.

Morphology of Cu_2S nanoparticles was investigated by TEM analysis (Fig. 5a, Fig. S4). Cu_2S particles had a spherical shape with the diameter of 29–75 nm ($D_{\text{av}} = 52 \pm 10$ nm) (Fig. 5b). SAED pattern of Cu_2S nanoparticles showed a clear dotted pattern (Fig. 5c) confirming the crystalline nature of nanoparticles. HRTEM micrographs (Fig. 6a, c) showed one of the dominant planes (200). The information obtained from PXRD, SAED and HRTEM regarding crystallinity and interplanar distances were consistent with each other. Further, two-dimensional fast Fourier transformation acquired Cu_2S nanoparticles at higher magnification (Fig. 6c and d) was matching with the standard diffraction pattern. Defect-free particles confirmed single crystalline nature of the Cu_2S nanoparticles (Fig. 6d). In summary, Cu_2S nanoparticles were synthesised by stoichiometric modification in the CuS synthesis and characterised completely.

4. Optical properties

Optical properties of CuS and Cu_2S nanoparticles were examined by UV–vis spectroscopy. Solid-state spectra were recorded to understand the optical properties since complete removal of capping agent on the surface of nanoparticles reduced the solubility of

these materials. Solid-state UV spectrum of the CuS flowers showed a broad reflectance, but the shape of the spectrum was similar to the spectra reported earlier [23]. The spectrum of Cu_2S nanoparticles had a broad reflectance peak centred on 586 nm (Fig. 7).

4.1. CuS flowers as photocatalyst

Photocatalytic activities of CuS and Cu_2S nanoparticles were examined by following the photocatalytic degradation of Rhodamine B (Rh B) dye in solution. CuS flowers exhibited photocatalytic activity under illumination by visible light (blue, 454 nm, 200 W m^{-2}) while Cu_2S nanoparticles did not show photocatalytic activity. During analyses, colour of the solution was changing gradually from bright pink to colourless (12 min, Fig. 8a inset) in the presence of CuS. The decolouration explained that the structure of Rh B was destroyed during photocatalysis [48,49]. This observation can be attributed to the oxidative degradation of the Rh B in analytical solution [50].

Degradation of Rh B in aqueous solution (60 mL of 3 μM) in the presence of CuS microflowers (60 mg) was monitored by observing the change in Rh B concentration through absorption spectra (Fig. 8a and Fig. S5). The Fig. 8a illustrates, the absorbance maxima of Rh B ($\lambda_{\text{max}} = 553$ nm) was decreasing rapidly without any shift and no new absorption peak was appearing. Hence, the concentration changes and relative concentration (C/C_0) of Rh B were calculated from the absorbance maxima. Fig. 8b shows temporal progression of degradation of Rh B under various conditions. Photocatalytic degradation (decolouration) was practically instantaneous. Within 3 min, CuS flowers decomposed ~64% of Rh B

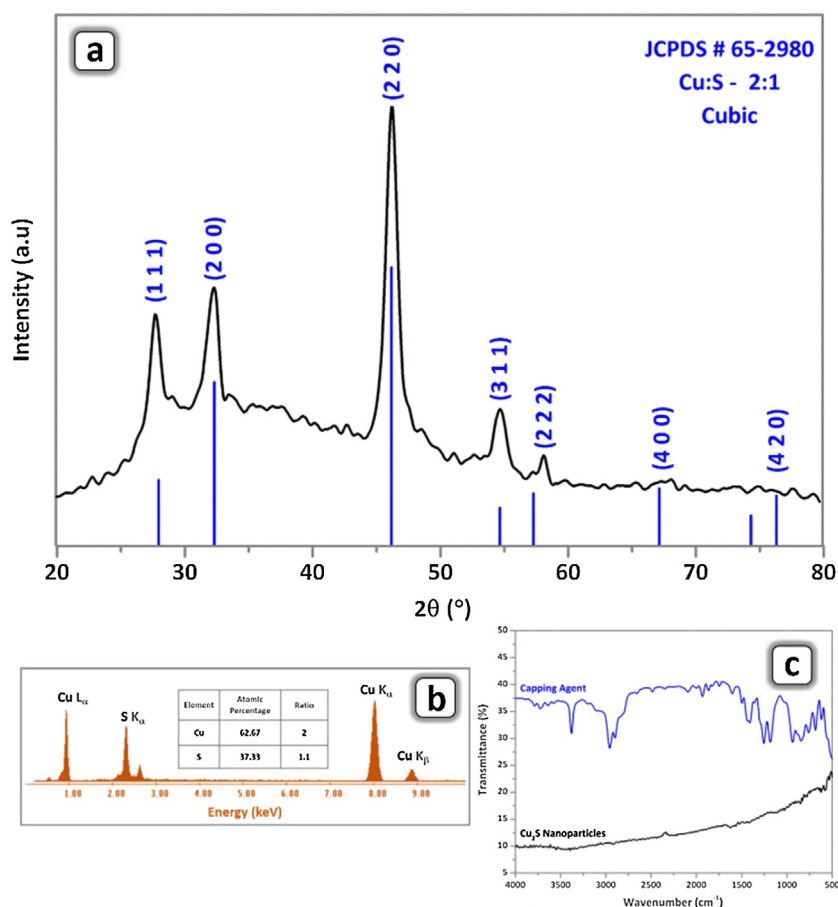


Fig. 4. (a) Powder X-ray diffraction pattern of Cu_2S nanoparticles. The vertical blue lines are the peak positions from JCPDS library. Cu_2S nanoparticles had bulk cubic-crystal structure. (b) EDAX spectrum of Cu_2S nanoparticles. Atomic ratio was calculated as Cu:S = 2:1.1. (c) FTIR spectrum of Cu_2S nanoparticles. Absence of capping agent on the surfaces of nanoparticles was confirmed.

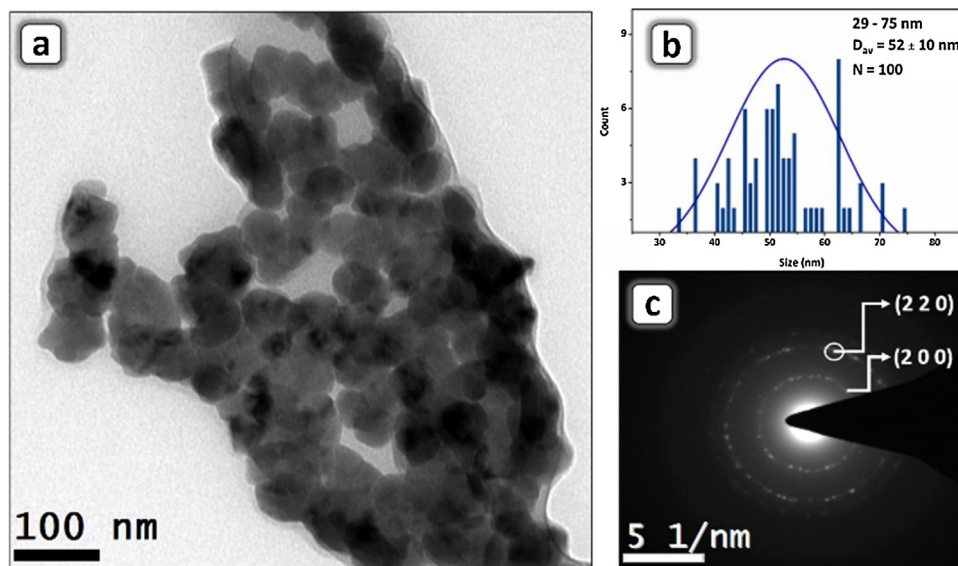


Fig. 5. (a) TEM image of Cu_2S nanoparticles. Particles had nearly spherical shape. (b) Particle size distribution diagram. Cu_2S particles had a size of 29–75 nm with $D_{50} = 52 \pm 10$ nm. (c) SAED pattern of Cu_2S nanoparticles. Dominant plane is highlighted by a circle.

solution. Complete photodegradation ($\sim 99\%$) of Rh B occurred within 12 min. Subsequent absorption visualized in the UV spectrum originated from the residual fragments in analytical solution [51]. Initial phase degradation was faster compared to the final

phase of degradation. We attribute this observation to the lack of availability of catalyst in the final phase of reaction. This rapid photocatalytic degradation of Rh B solution showed the effectiveness of CuS flowers as a photocatalyst.

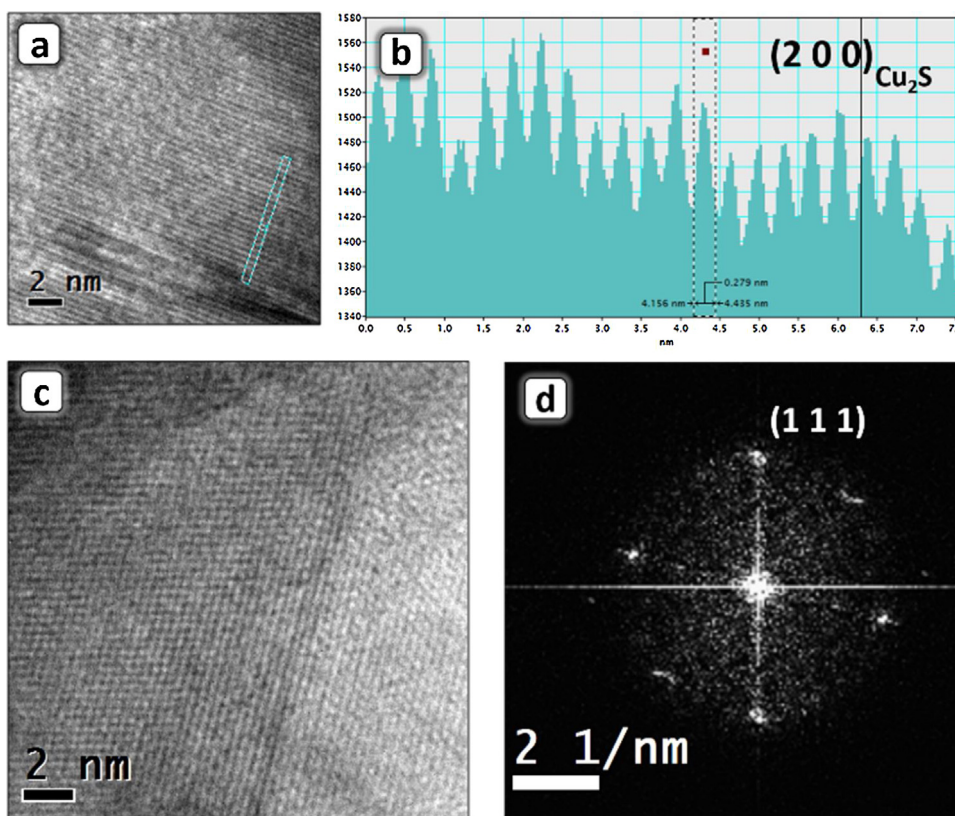


Fig. 6. (a) HRTEM micrograph of a Cu_2S nanoparticle. (b) Lattice profile of selected region of image. (a) Plane (200) of Cu_2S was observed. (c) HRTEM image showing continuous lattice points. Clear lattice points denoted the crystalline nature of nanoparticles. The lattices were free from defects. (d) Two dimensional fast Fourier transformation of image (c).

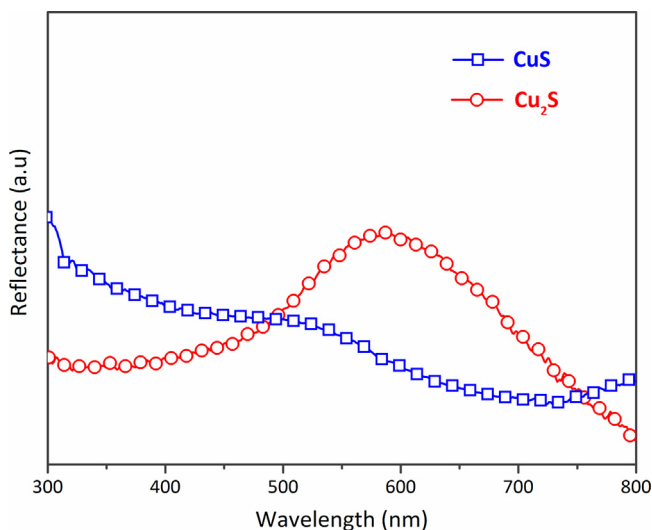


Fig. 7. (a) Solid UV–visible reflectance spectrum of CuS microflowers and Cu_2S nanoparticles.

To confirm photocatalytic activity as only the reason for degradation of Rh B, separate catalysis and photolysis were performed (Fig. 8b). Observation from the UV spectrum showed that changes in Rh B concentration were negligible in both photolysis and catalysis (Fig. 8b). There was no appreciable decrease in maxima of Rh B in both the process even after extended reaction time (120 min, Fig. S6). Hence, it was clear that the visible light irradiation alone

did not decompose Rh B (Fig. 8b, circles and Fig. S6a) and thus the failure of direct photolysis (without CuS) excluded the possibility of Rh B degradation by self-sensitisation. There was a slight decrease in the dye concentration when CuS (without UV irradiation) was added to the reaction mixture (Fig. 8b, squares and Fig. S6b). This may be due the decomposition of dye or adsorption dye on the surfaces of catalyst particles. Both results confirmed that independent photolysis (with photons and without catalyst) and catalysis (with catalyst and without photons), did not influence the decomposition of Rh B. Decomposition of Rh B was accelerated only when both catalyst and photons presented (Fig. 8b, triangles). Hence, both catalysis and photolysis synergistically influenced the decomposition of Rh B. CuS nanostructures effectively couple photons and catalytic activity to decompose the Rh B solution. In brief, controlled reactions clarified that CuS flowers degraded the Rh B solution through photocatalysis.

To quantify the photocatalytic activity, the rate constant of the photocatalytic degradation was calculated. Initial phase of the degradation (within first three minutes) fitted well in pseudo first order kinetics $[-\ln(C/C_0) = k \cdot t]$ [52,53]; where C and C_0 are reaction and the initial concentrations of Rh B, respectively, t is the irradiation time, k is the apparent reaction rate constant. Since major degradation occurred within three minutes, the rate constant (k_{obs}) observed at initial stage was used for all performance analyses [54]. The calculated rate constant was $0.50 \pm 0.02 \text{ min}^{-1}$. Larger rate constant value revealed the effectiveness of catalyst.

4.2. Effect of amount of catalyst and intensity of photons

When the amount (between 0.5 and 1.75 g L^{-1}) of CuS was varied there was increment in photocatalytic performance. The rate con-

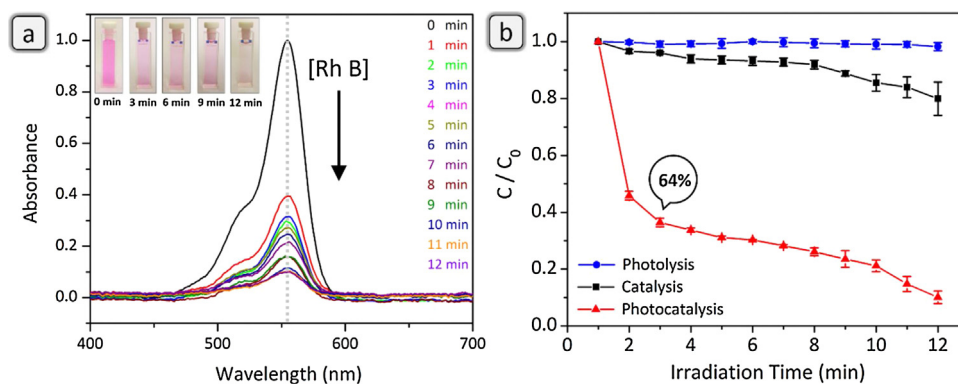


Fig. 8. Photocatalytic activity of the CuS Flowers. (a) Optical absorption profile of decomposition of Rh B aqueous solution. Changes in the concentration can be seen at 553 nm. Inset shows digital images of colour change during the decomposition. (b) Controlled reactions were described using the relative concentration of the Rh B (C/C_0). Photons alone (photolysis) did not decompose the Rh B (circles) and catalyst alone (catalysis) did not decompose Rh B (squares). Both photons and catalyst was synergistically decomposed Rh B (triangles). Error bars were calculated from three independent measurements. Plots of absorbance versus time has given in the supplementary information (Fig. S6).

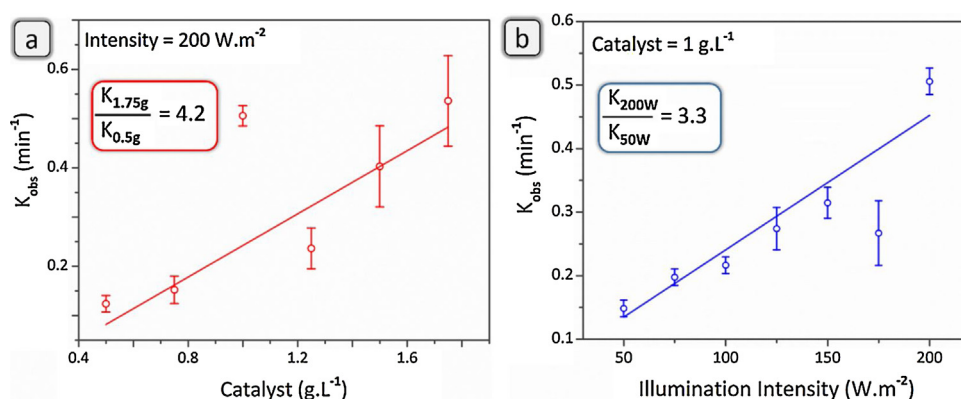


Fig. 9. Influence of photons (a) and catalyst (b) in the photocatalysis. Both influences had a linear relationship with the rate constant. Lines represent linear fit of the data. Error bars were calculated from three independent measurements.

stants showed, the amount of catalyst had a linear relationship with the rate constant (Fig. 9a). At initial variation, there may not be enough photocatalyst to enhance the degradation. The increasing amount of catalyst will provide more catalytic centres and hence more absorption of photons. At 1.75 g.L⁻¹, rate constant was 4.2 times higher than the initial value. At the higher concentrations, larger errors observed in measurements. This observation was due to scattering of light and opaqueness of the solution. Results suggested that the photocatalytic activity of CuS flowers could be enhanced by increasing the amount of catalyst.

We observed that photocatalytic performance of microflowers increased with increasing intensity of light. Hence, we conducted the intensity dependent studies on CuS photocatalyst by varying the intensity of the light at constant intervals (25 W.m⁻²). Other experimental conditions were unchanged. Photocatalyst amount was maintained as 1 g.L⁻¹. Rapid decolouration of Rh B degradation observed along with the increasing intensity of photons. The degradation was duly monitored by rate constant measurements. The rate constant had a direct relationship with intensity of light (Fig. 9b). Variation in rate constant along with light intensity confirmed that decomposition of Rh B had photon-assistance. At 200 W.m⁻², rate constant was 3.3 times higher than the initial value. This observation attributed to the fact that higher degree of illumination would generate more carriers in photocatalyst. Hence, the contribution of light in photocatalysis was more. In summary, photocatalytic performance of CuS flowers can be improved by increasing the amount of intensity of light.

4.3. Recyclability

To highlight CuS microflowers as a reusable photocatalyst, we have conducted recyclability studies. Under identical conditions, three catalytic cycles were consecutively performed (Fig. 10a). We fixed the concentrations of photocatalyst (1 g.L⁻¹) and Rh B (3 μM) in the analysis. Once Rh B degraded completely, microflowers were recovered and then used for another fresh catalytic reaction. Since the photocatalyst was denser than the analytical solution, it was recovered by centrifugation without impurities. The heterogeneous nature of CuS catalyst was the key to the photocatalysis and it simplified the recycling process. After every cycle, photocatalyst was reused without activation. Recyclability was monitored using absorption spectra through C/C_0 plots (Fig. 10a). Compared with the first cycle (12 min), both second (17 min) and third cycles of decomposition taken longer time (31 min) for completion. This observation indicated the deterioration of photocatalytic activity.

To compare cycles, recyclability was followed by rate constant calculations (Fig. 10b, Fig. S7). Results showed that rate constants decreased after each cycle of photocatalysis. The third cycle rate was 3.6 times smaller than first cycle. The smaller rate constant value indicated the slower degradation rate of Rh B. Hence, CuS photocatalyst was stable up to two cycles. It should be noted that stability of photocatalyst was moderate for recyclability. Reason for the decreased photocatalytic activity is explained in following section. Recyclability studies showed that the photocatalytic performance of the CuS microflowers reduced after every cycle.

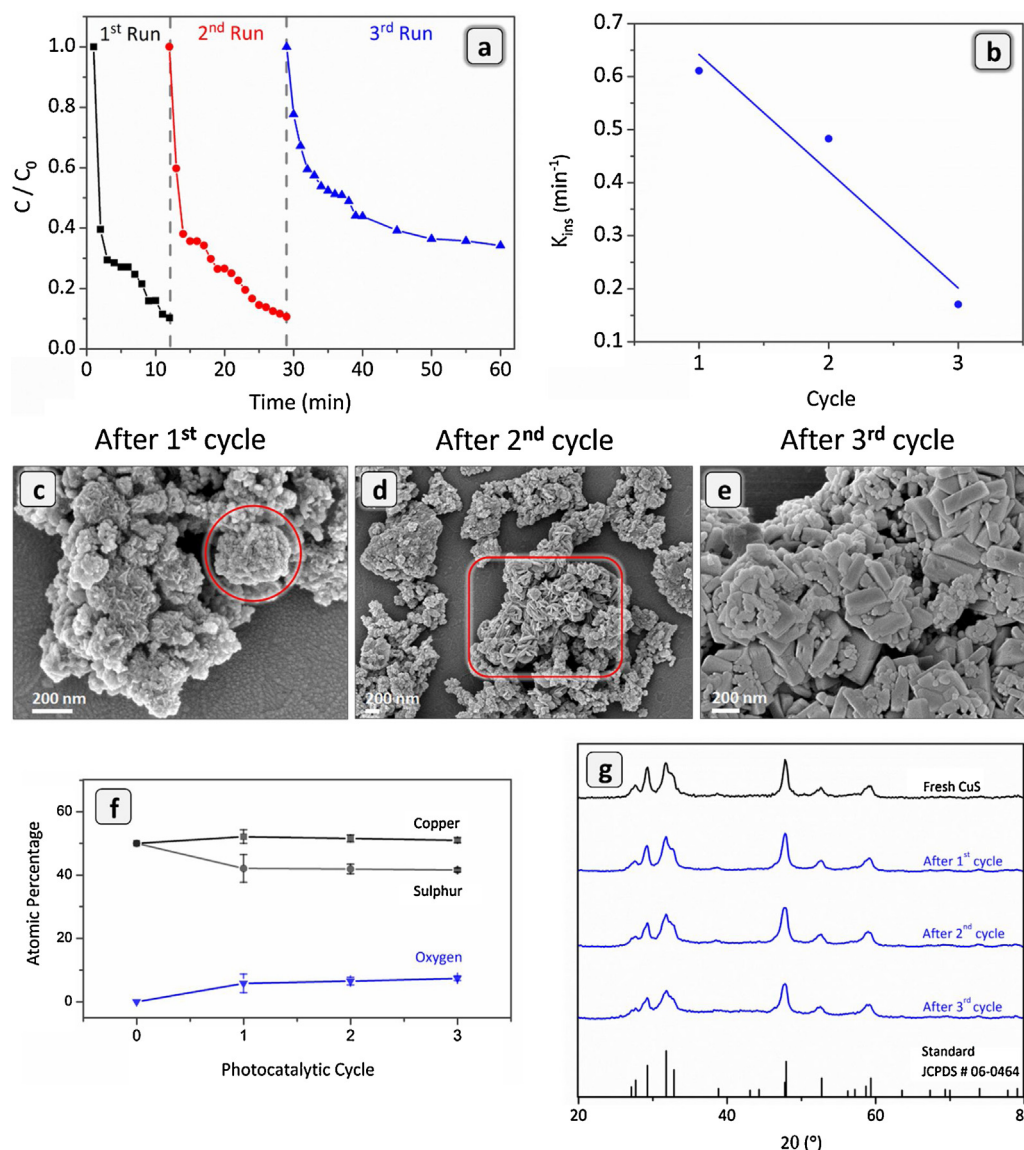


Fig. 10. Recyclability of CuS photocatalyst. (a) Recyclability is explained by C/C_0 measurements ($1 \text{ g}_{\text{cat}} \cdot \text{L}^{-1}$). (b) Trend of rate constants during recyclability of photocatalyst. After every cycle, rate constant decreased. (c) SEM micrographs after every cycle. (d) Flower structure disrupted after each cycle. Highlighted area shows major changes in the morphology. (e) After third cycle, nanoflakes transformed to bulk rods. (f) Atomic ratios measurements from EDAX analysis. Atomic Ratios were compared at each cycle. Oxide formation was observed after first cycle. (g) PXRD pattern after each cycle. The CuS phase was retained after three consecutive cycles. Copper oxide signature was absent and it might be due to the uneven oxidation or detection limit of PXRD measurements.

To explore the issues of recyclability, we investigated structural stability of the photocatalysts. After every cycle, photocatalyst was purified and subjected to SEM analysis (Fig. 10c–e). SEM studies indicated that photocatalytic activity was sensitive to the structural change of the flowers. The stability of flower architectures was weak and disrupted over cycles. Density of nanoflakes gradually decreased after the first cycle (Fig. 10a and b). After the second cycle, nanoflakes were separated and started growing as bulk particles. After third cycle, the nanoflakes transformed to the bulk rods (Fig. 10e). Rods were with a length of $266 \pm 62 \text{ nm}$ and width of $105 \pm 26 \text{ nm}$. Clearly, nano regime was lost during the photocatalysis. Hence, structural degradation was a reason for moderate recyclability.

Along with structural stability, we have duly followed the stability of the copper sulfide phase during the photocatalysis. After every cycle, copper sulfide was subjected to the EDAX and PXRD analyses (Fig. 10f and 10g). EDAX analysis showed that oxide formation ($\sim 8\%$) occurred during the photocatalysis. Every sulphur released

from CuS was quantitatively replaced by oxygen. However, PXRD patterns did not show any oxide formation. This observation may be attributed to uneven regional oxidation on the surfaces of nanoparticles and the detection limit of PXRD measurements. Hence, the chemical instability of CuS also deteriorated the activity of the catalyst. In summary, we identified that copper sulfide and its flower architectures were collectively contributed to photocatalytic activity.

4.4. Clean surfaces and enhancement of photocatalytic activity

The following factors explained the origin of structure dependence of photocatalytic activity. Porous cavities (Fig. 2a) among the nanoflakes in flowers behaved as additional catalytic centres [31]. Those nano cavities could have accommodated more Rh B than individual flakes. Thus, increment in the photodegradation. Moreover, these porous nature influences the absorbed light by the multiple reflections [31,55]. These reflections enhance the

photon harvesting capability of photocatalyst. Therefore, higher number of photo-generated electrons and holes would be generated. This process enhanced the photocatalytic efficiency of CuS flowers. The effective photocatalysis also owed to self-assembly of nano flakes forming flowers. These flowers could efficiently harvest photo-generated charges from all constituted nanoflakes [56]. These arguments were in accordance with recyclability studies; once the flower architectures lost, catalytic activity of copper sulfide decreased (Fig. 10b). Based on these observations, we propose that the efficient photocatalytic was due to the large surface area, porous structures and self-assembly.

EDAX and TEM analyses confirmed that capping agent was absent on the surfaces of nanoparticles (Figs. Fig. 11b and Fig. 33a). Since photocatalytic reactions occur on the surfaces of photocatalyst, clean surfaces could facilitate the photocatalytic activity of CuS nanostructures. Nanoparticles that obtained using modified HMDS-assisted synthetic method were free from capping agents and hence all potential catalytic surfaces would be readily available for photocatalysis [57]. Moreover, capping agent-free surfaces would create dangling bonds and trap states on the surfaces and thus could induce charges on photoexcitation of the catalyst [58–61]. These charges promoted more Rh B molecules approaching the surfaces of the photocatalyst. This was leading to the increased degradation of Rh B solution. The whole process collectively enhanced the photocatalytic activity of the CuS flowers. Based on observations, we concluded that photocatalytic enhancement was due to clean surfactant free surfaces of CuS flowers.

5. Conclusion

The described methodology enables synthesis of both CuS microflowers and Cu₂S nanoparticles from same starting materials. Cu₂S nanoparticles were synthesized by tuning the stoichiometry of the reaction. The nanoparticles were free from capping agent on the surfaces. Cu₂S nanoparticles had spherical shape and CuS nanoparticles had flower architecture. The flower nanostructures were synthesized without any linkers or post-modification process. Nanoflakes were a basic building block of flower architectures. Anisotropic growth of (1 0 3) planes was responsible for flake shape. Nanoflakes self-assembled and constructed flower architectures.

We demonstrated that CuS microflowers could serve as a photocatalyst and rapidly degraded Rh B solution (12 min). Recyclability studies showed that photocatalyst could be recycled up to three times. SEM analysis confirmed that flower architectures responsible for photocatalytic activity. Our results also suggested that a more amount of catalyst and higher illumination intensity enhanced the photocatalytic activity of flowers. An enhanced photocatalytic activity was due to unique flower morphology and clean surfaces. Facile synthesis, ease removal of capping agent and photocatalytic activity may influence possible applications of copper sulphide nanoparticles.

Acknowledgements

We thank Centre for Nanotechnology at University of Hyderabad for TEM facility. B.S. gratefully acknowledges University Grants Commission of India for fellowship. The authors thank Prof. Muga Vithal and Naveen Kumar Veldurthi, Department of Chemistry, Osmania University, Hyderabad, India for help in initial exploration of photocatalysis. Authors thank DST-SERB (project No.: SB/S1/IC-47/2013) for funding.

Appendix A. Supplementary data

Supplementary data associated with this article can be found, in the online version, at <http://dx.doi.org/10.1016/j.molcata.2015.08.028>.

References

- [1] A.P. Alivisatos, *Science* 271 (1996) 933.
- [2] B.L. Cushing, V.L. Kolesnichenko, C.J. O'Connor, *Chem. Rev.* 104 (2004) 3893.
- [3] B.O. Dabbousi, V.J. Rodriguez, F.V. Mikulec, J.R. Heine, H. Mattoussi, R. Ober, K.F. Jensen, M.G. Bawendi, *J. Phys. Chem. B* 101 (1997) 9463.
- [4] C.M. Hessel, V.P. Pattani, M. Rasch, M.G. Panthani, B. Koo, J.W. Tunnell, B.A. Korgel, *Nano Lett.* 11 (2011) 2560.
- [5] T.H. Larsen, M. Sigman, A. Ghezelbash, R.C. Doty, B.A. Korgel, *J. Am. Chem. Soc.* 125 (2003) 5638.
- [6] M.A. Malik, P. O'Brien, N. Revaprasadu, *Chem. Mater.* 14 (2002) 2004.
- [7] C.B. Murray, D.J. Noms, M.G. Bawendi, *J. Am. Chem. Soc.* 115 (1993) 8706.
- [8] J.B. Rivest, L.K. Fong, P.K. Jain, M.F. Toney, A.P. Alivisatos, *J. Phys. Chem. Lett.* 2 (2011) 2402.
- [9] Y. Xie, A. Riedinger, M. Prato, A. Casu, A. Genovese, P. Guardia, S. Sottini, C. Sangregorio, K. Misztal, S. Ghosh, T. Pellegrino, L. Manna, *J. Am. Chem. Soc.* 135 (2013) 17630.
- [10] S.R. Ghanta, K. Muralidharan, *J. Nanopart. Res.* 15 (2013) 1715.
- [11] Z. Yang, Z.H. Lin, C.Y. Tang, H.T. Chang, *Nanotechnology* 18 (2007) 255606.
- [12] B.I. Kharisov, *Recent Pat. Nanotechnol.* 2 (2008) 190.
- [13] T.K. Yong, L. Hyunjo, J.K. Hyoung, H.L. Tae, *Chem. Commun.* 46 (2010) 2085.
- [14] P. Jiang, M.J. McFarland, *J. Am. Chem. Soc.* 126 (2004) 13778.
- [15] G. Hongwei, Z. Rongkun, X.Z. Xi, X. Bing, *J. Am. Chem. Soc.* 126 (2004) 5664.
- [16] O. Hooisweng, R.L. Daniel, S. Mamta, A.B. Barbara, W.W. Watt, W. Ulrich, *Nano Lett.* 5 (2005) 113.
- [17] L. Mei, M. Stephen, *Langmuir* 16 (2000) 7088.
- [18] J. Peng, C. Joel, F.B. Jane, L.C. Vicki, *J. Am. Chem. Soc.* 121 (1999) 7957.
- [19] Q. Wang, X. Cui, W. Guan, W. Zheng, J. Chen, X. Zheng, X. Zhang, C. Liu, T. Xue, H. Wang, Z. Jin, H. Teng, *J. Phys. Chem. Solids* 74 (2013) 1470.
- [20] C. Zhiguo, W. Shaozhen, W. Qian, G. Baoyou, *Cryst. Eng. Comm.* 12 (2010) 144.
- [21] M.S. Akhtar, M.A. Khan, M.S. Jeon, O.B. Yang, *Electrochim. Acta* 53 (2008) 7869.
- [22] R. Wahab, S.G. Ansari, Y.S. Kim, H.K. Seo, G.S. Kim, G. Khang, H.S. Shin, *Mat. Res. Bull.* 42 (2007) 1640.
- [23] L. Benxia, X. Yi, X. Yi, *J. Phys. Chem. C* 111 (2007) 12181.
- [24] P. Kumar, M. Gusain, R. Nagarajan, *Inorg. Chem.* 50 (2011) 3065.
- [25] Z. Cheng, S. Wang, Q. Wang, B. Geng, *Cryst. Eng. Comm.* 12 (2010) 144.
- [26] L. Zhang, W. Wang, Z. Chen, L. Zhou, H. Xu, W. Zhu, *J. Mater. Chem.* 17 (2007) 2526.
- [27] B. Li, Y. Wang, *J. Phys. Chem. C* 114 (2010) 890.
- [28] Y. Guo, J. Wang, L. Yang, J. Zhang, K. Jiang, W. Li, L. Wang, L. Jiang, *Cryst. Eng. Comm.* 13 (2011) 5045.
- [29] Y. Zheng, K.L. Lv, X.F. Li, K.J. Deng, J. Sun, L.Q. Chen, L.Z. Cui, D.Y. Du, *Chem. Eng. Technol.* 34 (2011) 1630.
- [30] J. Zhang, Y. Wang, J. Zhang, Z. Lin, F. Huang, J. Yu, *ACS Appl. Mater. Interfaces* 5 (2013) 1031.
- [31] X. Meng, G. Tian, Y. Chen, R. Zhai, J. Zhou, Y. Shi, X. Cao, W. Zhou, H. Fu, *Cryst. Eng. Comm.* 15 (2013) 5144.
- [32] Z. Cheng, S. Wang, Q. Wang, B. Geng, *Cryst. Eng. Comm.* 12 (2010) 144.
- [33] M. Basu, A.K. Sinha, M. Pradhan, S. Sarkar, Y. Negishi, Govind, T. Pal, *Environ. Sci. Technol.* 44 (2010) 6313.
- [34] X. Meng, G. Tian, Y. Chen, R. Zhai, J. Zhou, Y. Shi, X. Cao, W. Zhou, H. Fu, *Cryst. Eng. Comm.* 15 (2013) 5144.
- [35] B. Li, Y. Xie, Y. Xue, *J. Phys. Chem. C* 111 (2007) 12181.
- [36] M. Tanveer, C. Cao, I. Aslam, Z. Ali, F. Idrees, M. Tahir, W.S. Khan, F.K. Butta, A. Mahmood, *RSC Adv.* 4 (2014) 63447.
- [37] Z.K. Yang, L.X. Song, Y. Teng, J. Xia, *J. Mater. Chem. A* 2 (2014) 20004.
- [38] M. Tanveer, C. Cao, Z. Ali, I. Aslam, F. Idrees, W.S. Khan, F.K. But, M. Tahir, N. Mahmood, *Cryst. Eng. Comm.* 16 (2014) 5290.
- [39] J. Kundu, D. Pradhan, *ACS Appl. Mater. Interfaces* 6 (2014) 1823.
- [40] Z. Li, L. Mi, W. Chen, H. Hou, C. Liu, H. Wang, Z. Zheng, C. Shen, *Cryst. Eng. Comm.* 14 (2012) 3965.
- [41] B.G. Kumar, K. Muralidharan, *J. Mater. Chem.* 21 (2011) 11271.
- [42] B.G. Kumar, K. Muralidharan, *Eur. J. Inorg. Chem.* (2013) 2102.
- [43] B.G. Kumar, K. Muralidharan, *RSC Adv.* 4 (2014) 28219.
- [44] M. Yuan, K.W. Kemp, S.M. Thon, J.Y. Kim, K.W. Chou, A. Amassian, E.H. Sargent, *Adv. Mater.* 26 (2014) 3513.
- [45] D.K. Harris, M.G. Bawendi, *J. Am. Chem. Soc.* 134 (2012) 20211.
- [46] O. Ma, M. Lavertu, J. Sun, S. Nguyen, M.D. Buschmann, F.M. Winnik, C.D. Hoemann, *Carbohydr. Polym.* 72 (2008) 616.
- [47] R.L. Penn, J.F. Banfield, *Science* 281 (1998) 969.
- [48] X. Li, N. Kikugawa, J. Ye, *Chem. Eur. J.* 15 (2009) 3538.
- [49] X. Li, N. Kikugawa, J. Ye, *Adv. Mater.* 20 (2008) 3816.
- [50] J. Zhao, T. Wu, K. Wu, K. Oikawa, H. Hidaka, N. Serpone, *Environ. Sci. Technol.* 32 (1998) 2394.
- [51] T.-J. Kuo, C.-N. Lin, C.-L. Kuo, M.H. Huang, *Chem. Mater.* 19 (2007) 5143.
- [52] H.U. Lee, S.C. Lee, Y.-C. Lee, B. Son, S.Y. Park, J.W. Lee, Y.-K. Oh, Y. Kim, S. Choi, Y.-S. Lee, *J. Lee, Sci. Rep.* 4 (2014) 6740.

- [53] H.U. Lee, S.C. Lee, S.H. Choi, B. Son, S.J. Lee, H.J. Kim, J. Lee, *Appl. Catal. B -Environ.* 129 (2013) 106.
- [54] F. Pincella, K. Isozaki, K. Miki, *Light Sci. Appl.* 3 (2014) e133.
- [55] L. Zhang, J.C. Yu, *Chem. Commun.* (2003) 2078.
- [56] A.G. Kanaras, C. Sonnichsen, H. Liu, A.P. Alivisatos, *Nano Lett.* 5 (2005) 2164.
- [57] H. Tong, S. Ouyang, Y. Bi, N. Umezawa, M. Oshikiri, J. Ye, *Adv. Mater.* 24 (2012) 229.
- [58] S. Li, L. Zhang, H. Wang, Z. Chen, J. Hu, K. Xu, J. Liu, *Sci. Rep.* 4 (2013) 3978.
- [59] W.-N. Wang, W.-J. An, B. Ramalingam, S. Mukherjee, D.M. Niedzwiedzki, S. Gangopadhyay, P. Biswas, *J. Am. Chem. Soc.* 134 (2012) 11276.
- [60] A.L. Linsebigler, G. Lu, J.T. Yates, *Chem. Rev.* 95 (1995) 735.
- [61] J.F. Hamilton, *Photogr. Sci. Eng.* 18 (1974) 493.

Materials Science inc. Nanomaterials & Polymers

Recyclable Ni_3S_4 Nanocatalyst for Hydrogenation of Nitroarenes

Srinivas Billakanti, Ganesh Kumar Baskaran, and Krishnamurthi Muralidharan*[a]

The synthesis of surface-clean nanoparticles of Ni_3S_4 , which is a rare phase of nickel sulphides, is described. Nanoparticles were synthesized in a single step via hexamethyldisilazane (HMDS) – assisted method using NiCl_2 and thiourea as starting materials. This synthetic method yielded phase pure, spherical Ni_3S_4 nanoparticles of mean size 17 ± 4 nm having clean surfaces. The nanoparticles were characterized thoroughly by data obtained from Powder X-ray diffraction (PXRD), Fourier-transform infrared spectra (FT-IR), Energy dispersive X-ray analysis (EDAX) and Transmission electron microscopy (TEM) analyses. Since newly produced Ni_3S_4 nanoparticles in our reaction had

exposed surfaces, the catalytic behaviour of these particles was assessed by using it as a catalyst in the reduction reaction of aromatic nitro groups. We have demonstrated Ni_3S_4 nanoparticle as a versatile catalyst for the nitro hydrogenation of both activated and deactivated nitrobenzenes using hydrazine as a hydrogen source to yield corresponding amines in high yield (~90%). The heterogeneous catalyst, Ni_3S_4 nanoparticles was recycled more than ten times without any change in its activity. We have ascribed the enhanced catalytic activity of these Ni_3S_4 nanoparticles to their clean surfaces without any surfactant molecules around them.

Introduction

Nanoparticles are the innovative class of catalytic materials having surface dependent catalytic properties.^[1–6] Compared with the bulk materials, the high surface to volume ratio of nanoparticles promotes the catalytic activity. However, stabilizing or surfactant molecules cover the surfaces of nanoparticles. The presence of these undesired capping agents hinders the chances of harnessing benefits of surface-dependent properties to their full potential.^[7–11] Hence, to enhance the catalytic activity, the capping agent might be removed from the surfaces of nanoparticles. On the other hand, many successful nanocatalysts used in organic synthesis were prepared by elegant and intricate designs.

Nickel sulphide exists in various stoichiometries such as NiS , NiS_2 , Ni_3S_2 , Ni_6S_5 , Ni_7S_6 , Ni_3S_4 , and Ni_9S_8 . There are several efforts to synthesize nickel chalcogenides nanoparticles,^[12–19] but many of them resulted in the formation mixture of sulphides. However, the challenge is to produce rare Ni_3S_4 phase in a simple bottom-up synthesis selectively. Since the formation of Ni_3S_4 is rare during the synthesis of nickel sulphides, and there is no commercial source available, many of its properties including the catalytic behaviour of Ni_3S_4 nanoparticles are unexplored.

Aromatic nitro hydrogenation is an important process in academia, industry, and nature^[20–22] because of the widespread

occurrence of the nitro group in the natural products and biologically active molecules. Therefore, many catalysts were utilized in the hydrogenation. Some of the catalysts are Pt/ carbon nanofibers, $\text{Fe}_2\text{O}_3/\text{Au}$, $\text{Fe}(\text{BF}_4)_2$, Fe_3O_4 , Rh_3Ni , Fe, Co, Rh, Ni, Pd, Pt, Cu, Ag, Au, and Zn.^[23–35] Though various catalysts are available for hydrogenation of nitroarenes, the performance of many of them still needs improvement. Also, some of the available reports did not mention TOF, which needed for complete understanding the catalytic performance.

Always there is a need for simplified method to produce catalyst, enhanced catalytic activity, recyclability of the heterogeneous catalyst, and versatility to use for various reactions. Many literatures indicated that the nanoparticle as catalysts can be easily separated and recycled with retention of catalytic activity compared to their bulk counterparts.^[36–39] In the past years, many hierarchical nanostructures have been used in catalysis. However, the dearth of simplicity in the production of nanocatalyst compared with conventional bulk catalyst is a major hurdle for their use in catalysis.

It was well acknowledged that a high specific surface area was constructive for increasing the active sites. However, if the surfactant molecules block the active sites, the catalyst would show less activity than its potential. Therefore, in pursuit of finding a simple procedure for the synthesis of nanoparticles, we have developed a novel HMDS-assisted method to produce nanoparticles having clean surfaces. In this work, we have demonstrated a selective synthesis of Ni_3S_4 phase of nickel sulphide as nanoparticles and their catalytic activity in hydrogenation reactions. To the best of our knowledge, there are no reports on the catalytic activity of surface clean Ni_3S_4 phase of nickel sulphide for hydrogenation of nitroarenes.

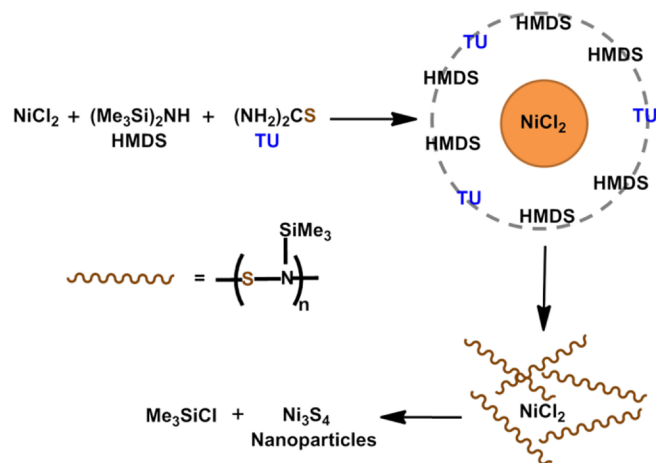
[a] S. Billakanti, G. K. Baskaran, Dr. K. Muralidharan
School of Chemistry, University of Hyderabad,
Gachibowli, Hyderabad - 500 046, Telangana, India
E-mail: murali@uohyd.ac.in
Homepage: <http://chemistry.uohyd.ac.in/~km/>

Supporting information for this article is available on the WWW under
<https://doi.org/10.1002/slct.201700320>

Results and Discussion

Synthesis of Ni_3S_4 Nanoparticles

We have demonstrated a novel HMDS-assisted method of synthesis of Ni_3S_4 nanocatalysts. The reaction shown in the Scheme 1 yielded phase pure Ni_3S_4 nanoparticles at the reflux



Scheme 1. Schematic representation of sequence of the reaction for nickel sulphide (Ni_3S_4) nanoparticles synthesis.

temperature (130°C) without mixing of any other stoichiometric products. As a replacement to the organometallic precursors, we used simple starting materials to prepare the Ni_3S_4 nanoparticles (nickel (II) chloride and thiourea). Synthesis at low temperature was possible because of the activation of metal by HMDS. Driving force of the reaction was the ability of HMDS to function as a capping agent, stabilizing surfactant molecule and solvent. During the reaction, two large trimethylsilyl groups of HMDS behaved as a surfactant and prevented the growth of Ni_3S_4 nanoparticles while the lone pair of electrons on nitrogen atom effectively passivated the surface of nanoparticles. Unreacted HMDS was removed from the surfaces of particles by high vacuum since it was a low boiling organic compound.

In many reactions involving sulphur and nitrogen, albeit yielding the pure products, there is an ambiguity on the nature of intermediate steps. However, we have established the activation of HMDS-assisted syntheses of metal chalcogenides through the formation of an S–N intermediate, which was formed by the reaction of HMDS with sulphur. In the present study, thiourea has been used as a sulphide source instead of elemental sulphur due to its solubility at room temperature. Many reactions in organic and inorganic syntheses, thiourea has been used as a source of sulphide (S^{2-}). Similarly, it might have interacted with the HMDS and formed a similar S–N intermediate. This intermediate subsequently reacted with nickel chloride forming nickel sulphide and in turn released trimethylsilyl chloride as a side product.^[40–44] The sequence of the reaction is shown in the Scheme 1.

To confirm the sequence of reactions, we performed a few control reactions, which are shown in the Table 1. In our

Table 1. Controlled reactions for Ni_3S_4 nanoparticles synthesis

NO.	Reactions	Product
1.	$\text{NiCl}_2 + \text{Thiourea} + \text{Toluene}$	No reaction
2.	$\text{Thiourea} + \text{HMDS}$	S–N Intermediate
3.	$\text{NiCl}_2 + \text{Thiourea} + \text{HMDS}$	Ni_3S_4 nanoparticles

optimized reaction condition, there was no reaction between nickel chloride and thiourea in toluene. However, thiourea reacted with HMDS (reaction 2, Table 1) yielding a compound, which is similar to the one obtained in the reaction of S and HMDS. This observation was confirmed from the time dependent ^{29}Si NMR spectra (Figure S1) of samples that are withdrawn from the reaction. The observed small multiplet peak around δ_{Si} 6.6 ppm corresponds to the probable S–N intermediate envisaged in the reaction S and HMDS (HMDS: δ_{Si} 2.3 ppm).

Characterization of Ni_3S_4 nanoparticles

The crystal structure and phase purity of just synthesized Ni_3S_4 nanoparticles were established by powder X-ray diffraction studies (Figure 1). The intensity and position of diffraction lines

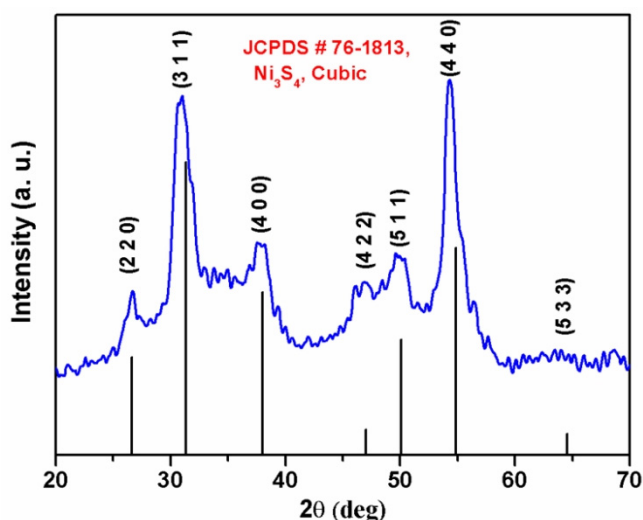


Figure 1. Primary characterization of Ni_3S_4 nanocatalyst. Powder X-ray diffraction pattern of Ni_3S_4 nanoparticles. Ni_3S_4 phase was confirmed as cubic using the data from JCPDS library.

of nanoparticles matched with the standard pattern of the cubical phase of Ni_3S_4 (JCPDS # 76–1813). There were no undesirable or additional peaks related to other phases of nickel sulphide. Clear PXRD pattern obtained signified the selectivity of the synthetic method. Further, any variation in the stoichiometry of reaction did not change the selectivity of nickel sulphide formation. Phase selectivity of the present method was further probed by a time-dependent PXRD study (Figure S2). During the synthesis, nanoparticles were isolated

periodically, purified and analysed by PXRD. In the PXRD patterns, there was no signature of any other stoichiometry at any stage of the reaction. Thus, the time-dependent PXRD study supports the selective formation of Ni_3S_4 in the reaction from the beginning. EDAX spectra (Figure 2d) of the product

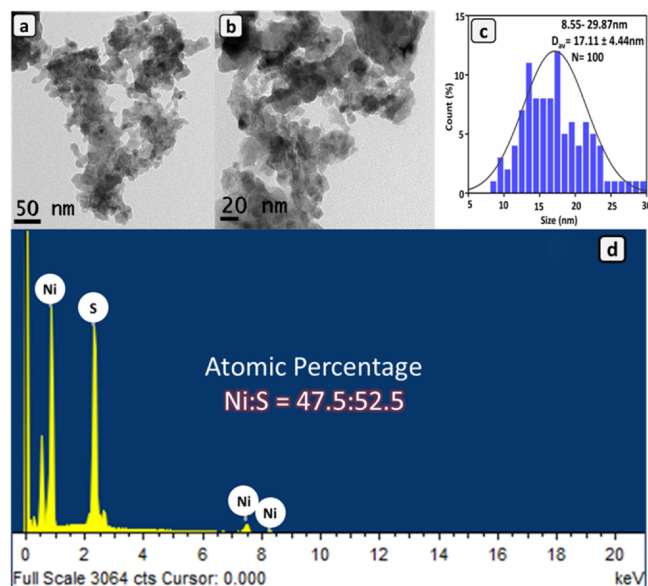


Figure 2. Microscopic investigation of Ni_3S_4 nanocatalyst. (a) and (b) are TEM micrographs of nanoparticles. (c) Particles distribution diagram obtained by measurements in the TEM micrographs. Particles were mono dispersed with the average size of 17 ± 4 nm. (d) Elemental analysis by the energy dispersive X-ray spectroscopy. Atomic ratios were matching with the theoretical values.

obtained in our reactions showed no signature of starting materials (absence of chloride and silicon), while the atomic ratio was matching with Ni_3S_4 ($\text{Ni}:\text{S} = 3:4$) only. Hence, the HMDS-assisted method was phase specific and yielded only Ni_3S_4 nanoparticles.

Microscopic investigation of Ni_3S_4 nanoparticles

TEM micrographs showed the aggregated spherical nanoparticles having (Figure 2a, b and S3) diameter of 8–29 nm and an average size of 17 ± 4 nm (Figure 2c). HRTEM micrographs showed the lattice spacing of 2.8 Å and 1.6 Å, which was corresponding to the inter-spacing of (3 1 1) and (4 0 0) planes of the standard pattern (Figure 3a). These planes were matching with the principal planes observed in the PXRD pattern of Ni_3S_4 nanoparticles. A thorough analysis using HRTEM (Figure S4) showed no amorphous boundaries (signature of HMDS) on the surface of nanoparticles indicating the complete removal of capping agents. Selected area diffraction showed a clear dotted pattern with (3 1 1) planes as dominating, which was indicative of the single-crystalline nature of Ni_3S_4 nanoparticles (Figure 3c). The SAED observations were consistent with the PXRD pattern of Ni_3S_4 nanoparticles. FTIR spectrum did not have any signal of amine or alkane (HMDS) confirming the

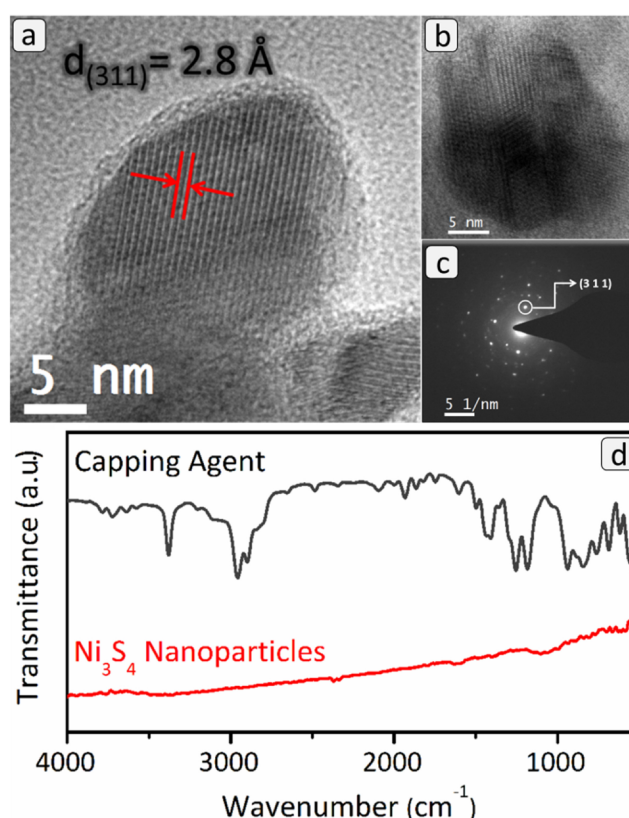


Figure 3. Surface characterization of the Ni_3S_4 nanocatalyst: (a) HRTEM micrograph of the nanoparticles. Particles were crystalline and dominant planes matched with PXRD pattern. (b) Individual nanoparticle (c) Selected area diffraction of the nanoparticles. Dominant plane is indicated by the circle which is complemented with the PXRD pattern. Dotted pattern represents the crystalline nature of the nanoparticles. (d) FTIR spectra of the nanoparticles. Since there was no signal of the amine (HMDS), capping agent was completely removed from the surfaces.

absence of capping agent on the surface (Figure 3d). Similarly, we did not observe the signal of silicon (HMDS) (Figure 2d) in the EDAX spectra. We obtained an ICP data and found no element other than Ni and S in our product. In summary, data from HRTEM, SAED, EDAX, ICP and FTIR analyses confirmed the capping agent free surfaces of nanoparticles (Figure 3 and S4).

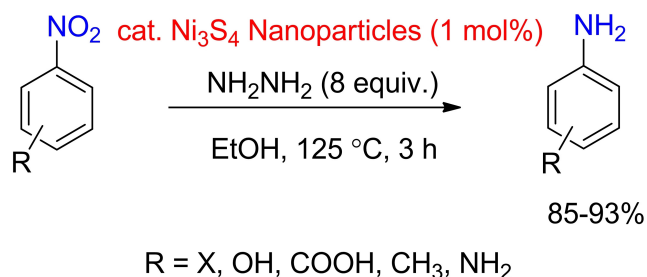
Ni_3S_4 nanoparticles as the catalyst

Since nickel sulphide obtained in our reaction had clean surfaces; we assessed the catalytic activity of Ni_3S_4 nanoparticles using it as a catalyst in the reaction of hydrogenation of nitrobenzene (Table 2). The reduction of aromatic amines was chosen because of its important in the total synthesis of many organic molecules.^[22] The Ni_3S_4 nanoparticles displayed a remarkable catalytic activity towards the hydrogenation of nitrobenzene to aminobenzene under optimal conditions (Table 2). Reduction reactions were performed efficiently using 1 mol% of Ni_3S_4 nanoparticles in ethanol using hydrazine as a hydrogen source. It was observed that under the optimized condition, 8 equivalents of hydrazine hydride was required to

Table 2. Results of nickel sulphide catalysed reduction of nitrobenzenes

Entry	Substrate	TOF(min ⁻¹)	Yield(%)
1		0.45	88
2		0.21	89
3		0.24	91
4		0.23	90
5		0.22	85
6		0.48	93
7		0.22	87
8		0.23	90
9		0.19	88
10		0.22	89

All the reactions were carried out under optimal conditions. Reactant = 6 mmol; hydrazine = 48 mmol; temperature = 125 °C, catalyst = 1 mol%. Size of nanoparticles = 17 nm; Time = 3 h; solvent = ethanol, 10 ml.

**Scheme 2.** Reduction of nitroarenes using Ni₃S₄ nanoparticles as catalyst.

reduction of nitrobenzenes.^[23–35] Few reports demonstrated the catalytic activity of different forms of nickel sulphides (except Ni₃S₄ phase) (Table 3). However, the present work is an

Table 3. Comparison table of numerous catalysts with various nitroaromatics.

Catalyst	Substrate	Time	Yield (%)	TOF (min ⁻¹)	Reference
Pt/CNF	CNB	5 h	99	610	23
Fe ₂ O ₃ /Au	NB	8 h	90	–	24
Fe(BF ₄) ₂	NB	2 h	89	–	25
Fe ₃ O ₄	PNP	8 min	99	–	26
Rh ₃ Ni	CNB	5 h	97	–	27
Fe	NB	2–3 h	95	–	28
Co	NB	15 h	99	–	29
Rh	NB	10 h	93	–	30
Ni	NB	4 h	93	–	31
Pd	NB	1 h	89	–	32
Pt	PNP	3 h	99	–	33
Cu, Ag, Au	PNP	< 10 min	–	–	34
Zn	NB	2.5 h	99	–	35
Ni ₇ S ₆	NB	24 h	–	–	37
(Ni ₃ S ₄)					
NiS	PNP	400 sec	–	–	38
(Ni ₃ S ₄)					
NiS _{2+x} /g-C ₃ N ₄	NB	1 h	–	–	39
Ni ₃ S ₄	NB	3 h	88	0.45	Present work

CNB = Chloro nitrobenzene; NB = Nitrobenzene; PNP = p-Nitrophenol;

complete the reaction.^[19] The maximum yield achieved under the optimized conditions was 88% with TOF of 0.45 min⁻¹.

In control reactions, the hydrogenation of nitrobenzene did not proceed either in the absence of Ni₃S₄ nanoparticles or hydrazine in the reaction (Figure S5). This observation confirmed the need for both these compounds to complete the reaction. The versatility of the catalyst was examined further in the reduction of substituted nitrobenzenes (O₂NC₂H₄R; R = X, CH₃, NH₂, COOH, OH) under optimized reaction condition, which is shown in the Scheme 2. The reactions successfully yielded corresponding aminobenzenes with high yields (85–93%). The products were confirmed by NMR spectral data (Figure S6–15). Various catalytic systems were used for the

elaborate study on catalytic activity of Ni₃S₄, which showed the excellent result with high TOF and yield.^[41–43] Thus, the study showed the effectiveness of Ni₃S₄ nanoparticles as a catalyst towards the hydrogenation of various substituted nitrobenzenes.

In the reactions involving heterogeneous catalysis, the reacting molecules adsorb on the catalytically active solid surface. Then the chemical bonds are broken and formed on the surface, and finally the products are released. However, the catalytic activity of nanoparticles depends on various factors such as particle size, surface area, structure-insensitivity/sensitivity, and the number of atoms/molecules in the surface that are available for catalytic activity.^[45] We determined the surface area of Ni₃S₄ nanoparticles by BET analysis as 6.49 m²/g

(Figure S16). In spite of less surface area, these Ni_3S_4 nanoparticles showed a significant catalytic activity. Interestingly, Radek Zboril and co-workers^[46] also observed high catalytic activity iron(III) oxide nanoparticles at relatively lesser surface area for the decomposition of hydrogen peroxide. They ascribed the reason to the absence of an amorphous phase. In the present study, the surprisingly high catalytic activity of Ni_3S_4 nanoparticles having less surface area can be attributed to the availability of more number of bare active sites at the surface since there was no other material surrounding the nanoparticles. These free surfaces were possible because of the inherent advantage HMDS-assisted synthesis.

Rioux et al.^[47] observed a difference in the particle sizes polymer coated Pt determined by a chemisorption method and from PXRD lines. This observation was explained based on the reduced exposed surface area due to the existence of unremoved polymer coated on the surface of Pt nanoparticles which hindered the adsorption of gas. This observation also supported that not only the surface area or size of the nanoparticles but also the availability of exposed active site at the surface are relevant to enhanced catalytic activity observed in this present study. However, any tangible evidence is needed for the prediction of a definite mechanism of the reaction.

Recyclability

For practical applications, recycling capability is desirable for any catalyst. Further, sulphur atoms often leach from sulphur-based compounds leading to the deactivation of their catalytic activity. Interestingly, the Ni_3S_4 nanoparticles prepared in our reactions showed an excellent stability and recyclability in the reduction of nitrobenzenes. When the reaction mixture was filtered at hot condition, a minute solubility of Ni_3S_4 was observed. However, at room temperature, the catalyst precipitated from the solution. Therefore, we recovered and reused the catalyst more than ten times without any activation procedures (Figure 4a). After the each reaction, the catalyst was separated by centrifugation from organic layer and, washed, dried and reused. Throughout ten cycles, the reaction yield was almost constant; then there was a slight reduction in the yield (from 88% to 85%).

Thermogravimetric analysis showed that nanoparticles were stable approximately up to 200 °C and the catalytic activity did not destroy them (Figure 4b). A clear weight loss at 500 °C seen in the TGA plot was presumable due to loss of trapped HMDS or intermediate during the reaction. However, in the reused catalyst these trapped compounds would have dissolved into the reaction solvent and hence there was no sharp loss in weight. Further, analysis of nanoparticles by TEM after cycles of catalysis did not show any significant change in shape and size of the particles even after ten cycles (Figure 4c). Presumably, retaining of size and shapes of nanoparticles ensured a constant catalytic activity for many cycles. In summary, the nanoparticles were recyclable for many catalytic reactions due to their chemical stability and the preservation of the Nano-regime.

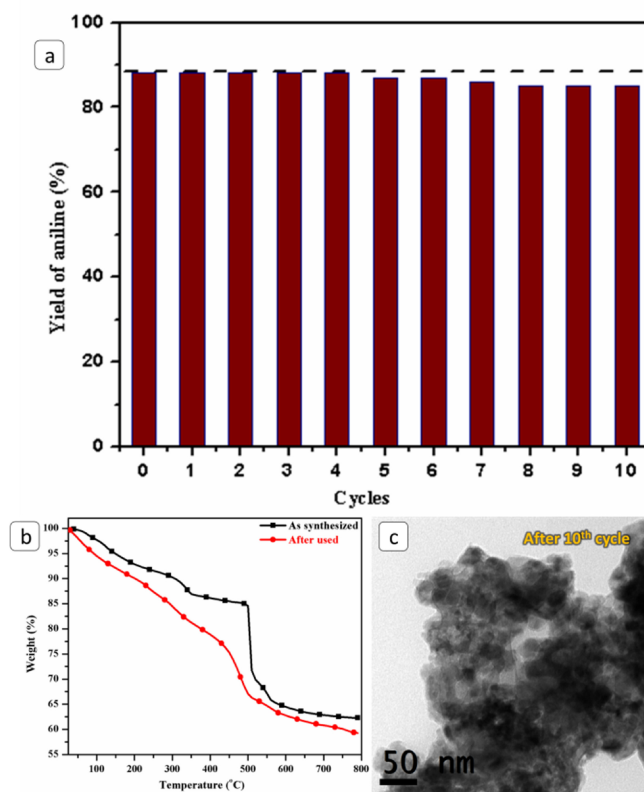


Figure 4. Stability of the catalyst. (a) Recyclability analysis of the nickel sulphide. The yield of the aniline was not significantly reduced even after 10 cycles. (b) TGA analysis of Ni_3S_4 nanoparticles. Potential use of catalyst at high temperature was explored. (c) TEM micrograph of the nanoparticles. Size of the particles were retained after catalysis.

Conclusions

We have developed a novel method for the production of a rare stoichiometric form of nickel sulphide (Ni_3S_4) nanoparticles. The newly developed procedure was simple, single step and scalable for bulk preparation. The method yielded nanoparticles with clean surfaces, which was characterized methodically by various techniques. We have demonstrated hitherto unexplored catalytic activity of Ni_3S_4 phase of nickel sulphide nanoparticles in the hydrogenation of nitroarenes. The broad scope of substrates, easy recovery and recyclability highlight the potential of Ni_3S_4 as a catalyst. The high catalytic activity of Ni_3S_4 having less surface area is ascribed to the clean, surfactant free surface of nanoparticles, which is an inherent advantage of HMDS-assisted synthesis.

Supporting Summary

Experimental details as well as ^{29}Si , ^1H , ^{13}C -NMR, PXRD, TEM, HRTEM and BET characterizations are provided in the supporting information.

Acknowledgements

DST-SERB of India funded the work through award No.: SB/S1/IC-47/2013. B. G. K acknowledges the DST-SERB Research Associate Fellowship. B. S. gratefully acknowledges the University Grant Commission (UGC), India for a senior research fellowship. The authors thank the Centre for Nanotechnology at the University of Hyderabad for the TEM facility and FE-SEM facility, School of Chemistry, University of Hyderabad, Hyderabad, India.

Conflict of Interest

The authors declare no conflict of interest.

Keywords: Chemical synthesis • heterogeneous catalysis • Ni_3S_4 nanoparticles • nitroaromatics • reduction

- [1] R. Narayanan, M.-A. El-Sayed, *Nano Lett.* **2004**, *4*, 1343–1348.
- [2] Z.-C. Zhang, B. Xu, X. Wang, *Chem. Soc. Rev.* **2014**, *43*, 7870–7886.
- [3] Y. Zhang, X. Cui, F. Shi, Y. Deng, *Chem. Rev.* **2012**, *112*, 2467–2505.
- [4] M. B. Gawande, A. Goswami, F.-X. Felpin, T. Asefa, X. Huang, R. Silva, X. Zou, R. Zboril, R. S. Varma, *Chem. Rev.* **2016**, *116*, 3722–3811.
- [5] R. Narayanan, M.-A. El-Sayed, *J. Phys. Chem. B* **2005**, *109*, 12663–12676.
- [6] E. Hariprasad, T. P. Radhakrishnan, *Chem. Eur. J.* **2010**, *16*, 14378–14384.
- [7] H. Li, G. Chen, H. Yang, X. Wang, J. Liang, P. Liu, M. Chen, N. Zheng, *Angew. Chem. Int. Ed.* **2013**, *52*, 8368–8372.
- [8] M. A. Boles, D. Ling, T. Hyeon, D. V. Talapin, *Nat. Mater.* **2016**, *15*, 141–153.
- [9] Z. Niu, Y. Li, *Chem. Mater.* **2014**, *26*, 72–83.
- [10] X. Chen, G. Wu, J. Chen, X. Chen, Z. Xie, X. Wang, *J. Am. Chem. Soc.* **2011**, *133*, 3693–3695.
- [11] J.-J. Feng, A.-Q. Li, Z. Lei, A.-J. Wang, *ACS Appl. Mater. Interfaces* **2012**, *4*, 2570–2576.
- [12] A. Ghezelbash, M. B. Sigman, Jr., B. A. Korgel, *Nano Lett.* **2004**, *4*, 537–542.
- [13] A. Ghezelbash, B. A. Korgel, *Langmuir* **2005**, *21*, 9451–9456.
- [14] R. D. Tilley, D. A. Jefferson, *J. Phys. Chem. B* **2002**, *106*, 10895–10901.
- [15] L. Zhang, J. C. Yu, M. Mo, L. Wu, Q. Li, K. W. Kwong, *J. Am. Chem. Soc.* **2004**, *126*, 8116–8117.
- [16] B. X. Jiang, Y. Xie, J. Lu, L. Zhu, W. He, Y. Qian, *Adv. Mater.* **2001**, *13*, 1278–1281.
- [17] A. Olivas, J. Cruz-Reyes, V. Petranovskii, M. Avalos, S. Fuentes, *J. Vac. Sci. Technol. A* **1998**, *16*, 3515–3520.
- [18] Y. Zhang, W. Sun, X. Rui, B. Li, H. T. Tan, G. Guo, S. Madhavi, Y. Zong, Q. Yan, *Small* **2015**, *11*, 3694–3702.
- [19] C. Jiang, Z. Shang, X. Liang, *ACS Catal.* **2015**, *5*, 4814–4818.
- [20] R. Parry, S. Nishino, J. Spain, *Nat. Prod. Rep.* **2011**, *28*, 152–167.
- [21] R. S. Downing, P. J. Kunkeler, H. V. Bekkum, *Catal. Today* **1997**, *37*, 121–136.
- [22] a) N. Ono, *The Nitro Group in Organic Synthesis*, Wiley-VCH, New York, **2001**. b) J. P. Adams, *J. Chem. Soc., Perkin Trans.* **2002**, *1*, 2586–2597.
- [23] M. Takasaki, Y. Motoyama, K. Higashi, S.-H. Yoon, I. Mochida, H. Nagashima, *Org. Lett.* **2008**, *10*, 1601–1604.
- [24] Q. Peng, Y. Zhang, F. Shi, Y. Deng, *Chem. Commun.* **2011**, *47*, 6476–6478.
- [25] G. Wienhöfer, I. Sorribes, A. Boddien, F. Westerhaus, K. Junge, H. Junge, R. Llusar, M. Beller, *J. Am. Chem. Soc.* **2011**, *133*, 12875–12879.
- [26] D. Cantillo, M. Baghbanzadeh, C. O. Kappe, *Angew. Chem. Int. Ed.* **2012**, *51*, 10190–10193.
- [27] S. Cai, H. Duan, H. Rong, D. Wang, L. Li, W. He, Y. Li, *ACS Catal.* **2013**, *3*, 608–612.
- [28] R. Dey, N. Mukherjee, S. Ahammed, B. C. Ranu, *Chem. Commun.* **2012**, *48*, 7982–7984.
- [29] a) T. Schwob, R. Kempe, *Angew. Chem. Int. Ed.* **2016**, *55*, 15175–15179. b) L. Liu, P. Concepción, A. Corma, *Journal of Catalysis* **2016**, *340*, 1–9.
- [30] a) R. G. D. Noronha, C. C. Romao and A. C. Farnandes, *J. Org. Chem.* **2009**, *74*, 6960–6964; b) A. B. Taleb and G. Jenner, *J. Mol. Catal.* **1994**, *91*, 149–153. c) H. Berthold, T. Schotten and H. Honig, *Synthesis* **2002**, 1607–1610.
- [31] S. K. Mahapatra, S. U. Sonavane, R. V. Jayaram and P. Selvam, *Org. Lett.* **2002**, *4*, 4297–4300.
- [32] a) Ronald J. Rahaim, Jr. and Robert E. Maleczka, Jr., *Org. Lett.* **2005**, *7*, 22 5087–5090. b) B. Sreedhar, P. Surendra Reddy and D. Keerthi Devi, *J. Org. Chem.* **2009**, *74*, 8806–8809.
- [33] Y. Motoyama, K. Kamo, H. Nagashima, *Org. Lett.* **2009**, *11*, 1345–1348.
- [34] N. Pradhan, A. Pal, T. Pal, *Langmuir* **2001**, *17*, 1800–1802.
- [35] C. Boix and M. Poliakov, *J. Chem. Soc., Perkin Trans.* **1999**, *1*, 1487–1490.
- [36] P. S. Rathore, R. Patidar, T. Shripathic, S. Thakore, *Catal. Sci. Technol.* **2015**, *5*, 286–295.
- [37] F. Cao, R. Liu, L. Zhou, S. Song, Y. Lei, W. Shi, F. Zhao, H. Zhang, *J. Mater. Chem.* **2010**, *20*, 1078–1085.
- [38] R. Karthikeyan, D. Thangaraju, N. Prakash, Y. Hayakawa, *CrystEngComm* **2015**, *17*, 5431–5439.
- [39] Y.-N. Zhang, X.-H. Li, Y.-Y. Cai, L.-H. Gong, K.-X. Wang, J.-S. Chen, *RSC Adv.* **2014**, *4*, 60873–60877.
- [40] B. G. Kumar, K. Muralidharan, *J. Mater. Chem.* **2011**, *21*, 11271–11275.
- [41] B. G. Kumar, K. Muralidharan, *Eur. J. Inorg. Chem.* **2013**, 2102–2108.
- [42] B. G. Kumar, K. Muralidharan, *RSC Adv.* **2014**, *4*, 28219–28224.
- [43] B. G. Kumar, B. Srinivas, M. D. Prasad, K. Muralidharan, *J. Nanopart. Res.* **2015**, *17*, 325–335.
- [44] B. Srinivas, B. G. Kumar, K. Muralidharan, *J. Mol. Catal. A: Chem.* **2015**, *410*, 8–18.
- [45] a) M. Boudart, *J. Mol. Catal.* **1985**, *30*, 27–38. b) S. Chaturvedi, P. N. Dave, N. K. Shah, *J. Saudi Chem. Soc.* **2012**, *16*, 307–325. c) F. Yang, D. Deng, X. Pan, Q. Fu, X. Bao, *Natl. Sci. Rev.* **2015**, *2*, 183–201.
- [46] C. Gregor, M. Hermanek, D. Jancik, J. Pechousek, J. Filip, J. Hrbac, Radek Zboril, *Eur. J. Inorg. Chem.* **2010**, 2343–2351.
- [47] R. M. Rioux, H. Song, J. D. Hoefelmeyer, P. Yang, G. A. Somorjai, *J. Phys. Chem. B* **2005**, *109*, 2192–2202.

Submitted: February 16, 2017

Revised: June 2, 2017

Accepted: June 6, 2017

Accepted Manuscript

Title: Photo-responsive Bi₂S₃ nanoflakes: Synthesis and device fabrication at ambient conditions

Authors: Baskaran Ganesh Kumar, Billakanti Srinivas, Krishnamurthi Muralidharan



PII: S0025-5408(17)30312-4
DOI: <http://dx.doi.org/doi:10.1016/j.materresbull.2017.01.029>
Reference: MRB 9122

To appear in: *MRB*

Received date: 9-5-2016
Revised date: 19-10-2016
Accepted date: 20-1-2017

Please cite this article as: Baskaran Ganesh Kumar, Billakanti Srinivas, Krishnamurthi Muralidharan, Photo-responsive Bi₂S₃ nanoflakes: Synthesis and device fabrication at ambient conditions, Materials Research Bulletin <http://dx.doi.org/10.1016/j.materresbull.2017.01.029>

This is a PDF file of an unedited manuscript that has been accepted for publication. As a service to our customers we are providing this early version of the manuscript. The manuscript will undergo copyediting, typesetting, and review of the resulting proof before it is published in its final form. Please note that during the production process errors may be discovered which could affect the content, and all legal disclaimers that apply to the journal pertain.

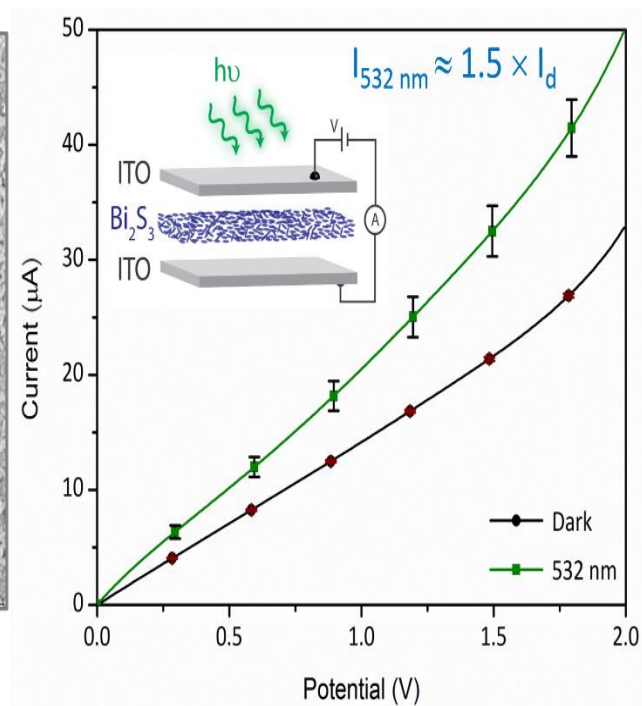
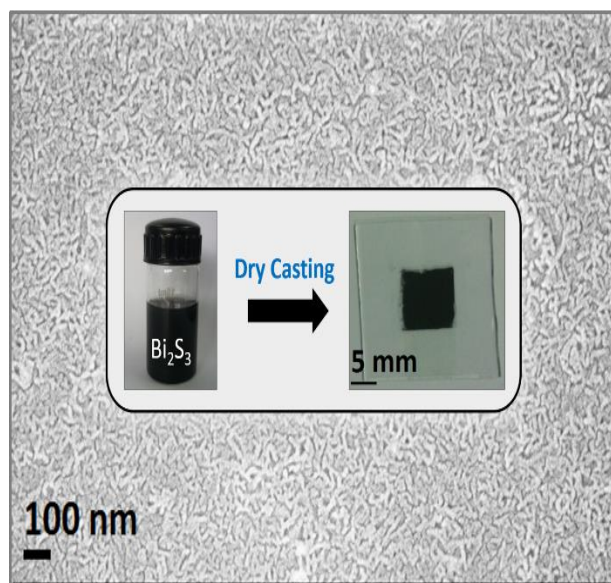
Photo-responsive Bi_2S_3 Nanoflakes: Synthesis and Device Fabrication at Ambient Conditions

Baskaran Ganesh Kumar, Billakanti Srinivas and Krishnamurthi Muralidharan*

School of Chemistry, University of Hyderabad, Hyderabad, India.

E-mail: murali@uohyd.ac.in

Graphical abstract



Highlights:

- New organic free Bi₂S₃ nanoflakes were synthesized using the HMDS-assisted wet chemical method
- Gram scale synthesis (2 g) with 98% morphological yield of flakes was demonstrated
- Prototype photodetector was fabricated, and its photo-response was analysed
- Synthesis, processing and device making were performed in ambient conditions

Abstract

Since the optoelectronic devices consist multicomponent interfaces, the synthesis of nanoparticles and fabrication of devices play a significant role in quality, cost, and fast fabrication of devices. The wet chemical synthesis holds the great promise of controlling of these factors. Herein, we have developed a wet chemical method for the synthesis of one-dimensional Bi₂S₃ nanoflakes and demonstrated its photo-responsivity by fabricating prototype device by dry-casting of Bi₂S₃ suspensions on the electrodes. A key advantage of the present approach is the synthesis and fabrication were carried out in the ambient conditions.

Keywords: chemical synthesis, optical properties, chalcogenides, optical materials, electronic materials

1. Introduction

Material processing technology is a key industrial component for the mass production of optoelectronic devices.¹⁻¹² The solution processing technology offers the advantage of making

the devices at ambient conditions because of the possibility of making devices from solution using any of the following techniques; spray coating,^{1, 2} mist coating,³ spin coating,^{4, 5} dry casting,^{6, 7} dip coating,^{8, 9} roll-to-roll printing¹⁰ and inkjet printing.^{11, 12} Furthermore, these processing methods allow the fabrication of flexible modern electronics by integrating nanomaterials with any substrates. Thus, the nanomaterials prepared by wet chemical methods offer the way for cheap and fast processing technology.

Photodetectors have received much attention as an important class of optoelectronic devices owing to their extensive use in electronic eyes,¹³⁻¹⁵ night vision devices,¹⁶ tumour detection,¹⁷ imaging^{18, 19} and quality control of industrial products.²⁰ Photodetectors made out of inorganic materials will have tuneable absorption, stability, and high quantum yield. Bi₂S₃ is a useful photo-responsive material with a direct band gap of 1.3 eV²¹ and a large absorption coefficient.²² The high availability of sulphide and bismuth in the earth crust is also an important factor for the use of Bi₂S₃ for optoelectronic applications. While a significant work on the Bi₂S₃ based photodetector is known,²³⁻³² there are still need for the search for the best synthetic methods³³⁻⁴⁸ and simplicity in processing methods.

We have explored the use of hexamethyldisilazane (HMDS) - assisted method for the synthesis of In₂S₃, CuS, and Ag₂S nanoparticles.^{49, 50, 51} In this work we have demonstrated a novel synthesis of Bi₂S₃ (bismuth sulphide) nanoparticles using the HMDS-assisted method. Interestingly, the Bi₂S₃ nanoflakes have been synthesized in a short duration (3 h) using readily available bismuth chloride and thiourea as starting materials. The Bi₂S₃ nanoflakes had width 15-82 nm with the average 48 ± 15 nm and the length up to few microns and obtained in a high morphological yield (~98%). The reaction produced one-dimensional nanoflakes without any seeds or shape selection procedures. Markedly, the synthesized nanoparticles were free from the capping agent on the surfaces.

In this work, we have fabricated a prototype of photodetectors, with a configuration of ITO/Bi₂S₃/ITO, by dry-casting the Bi₂S₃ suspensions. The devices showed a green light-induced conductivity that had a linear response to the intensity of the light. Further, the transient measurements established a reversible "on" and "off" switching phenomena with the rise-and-decay time as 1.11 ± 0.10 ns and 2.06 ± 0.21 ns. Herein, we present the synthesis and photo responsive study of organic surfactant free Bi₂S₃ nanoflakes.

2. Results and Discussion

2.1. Synthesis

We have successfully synthesized organic-free Bi_2S_3 nanoflakes by the HMDS-assisted method with the yield of $62 \pm 4\%$. We have used soluble thiourea in the present procedure as a sulphur source due to the prospect of easy handling in pre and post-synthetic manipulations. In these reactions, HMDS performed dual role as a capping agent as well as a solvent. Bulk trimethylsilyl group of HMDS acted as capping group and avoided the agglomeration of nanoparticles (Scheme 1) during their formation. Hence, HMDS stabilized the nanoparticles and yielded quantum confined one-dimensional Bi_2S_3 nanoflakes. The key advantage of the method was that the capping agent (HMDS) could be removed from the nanoparticles efficiently by high vacuum. Thus, nanoparticles were free from insulating organic layer. Because of mild reaction conditions and simple purification procedure, the present synthetic design is worthy for scale up. Thus, we have produced 2 g of nanoflakes and used it for device fabrication. Therefore, the current synthetic procedure is robust for large scale synthesis also offers quantum confined Bi_2S_3 nanoflakes.

2.2 Structure and composition of Bi_2S_3 nanoflakes

Primarily, the acquired powder X-ray diffraction patterns (Figure 1a) confirmed the formation Bi_2S_3 in our reaction. Intensities and position of observed lines were matching with the standard pattern of orthorhombic structure bulk Bi_2S_3 (JCPDS Library; Card # 84-0279); but with a preferred orientation of (1 1 1) and (1 2 1) planes. Supported by HRTEM images (Figure 2d), we have identified (1 2 1) planes as responsible for the flake shape. The absence of signature of secondary amines or any other signals related to organic compounds in the FTIR spectrum (Figure 1b) ruled out the possibility of broadening of lines by organic impurities. Therefore, broadening of lines in diffraction patterns was attributed only to the nano regime of the Bi_2S_3 flakes. Thus, the absence of the capping agent (HMDS) on the surface of the Bi_2S_3 nanoflakes was self-evident.

Scanning electron microscopy images of Bi_2S_3 (Figure 1c) showed a uniform distribution of particles of size ranging up to 2 μm , but with a high morphological yield of nanoflakes

(~98%). Any change in reaction parameters like temperature, stoichiometry, and solvents did not alter the morphology and dimensions of nanoparticles obtained. EDAX measurements showed the stoichiometric ratio of Bi:S as 1.7: 3 which clearly showed 3% bismuth deficiency in nanoparticles obtained from our reactions (figure 1d). Bismuth ratio was not improving even after the addition of excess BiCl_3 . However, the bismuth deficiency did not influence the properties of Bi_2S_3 nanoflakes or fabricated devices. EDAX did not have the signature of Si and Cl, which showed the purity of nanoparticles and the absence of the capping agent. This observation explained that nanoflakes were free from the insulating organic layer on the surface of the nanoparticles. Surprisingly, even in the absence of the capping agent, nanoflakes were well separated, and we did not observe agglomeration. Thus, the growth or stoichiometry of the nanoparticles and morphological yield was insensitive to the experimental parameters.

TEM micrographs confirmed the flake shape of the nanoparticles obtained from the present procedure. (Figure 2a). TEM micrographs also showed the high abundance of nanoparticles (Figure S1). The nanoflakes had the width of the 15-82 nm with the average of 48 ± 15 nm (Figure 2b). Also, the nanoflakes had the length up to few micrometers. Since the width of the few flakes was less than Bohr radius of Bi_2S_3 (~ 30 nm)⁵², weak confinement along the width was observed (spectrally determined bandgap = 1.40 eV; Figure S2b). The width of the flakes was constant along the length and but the edges were sharp. The observed modification at the edges might be to tolerate the strain in the growth.⁵⁰ Selected area diffraction (SAED) showed a clear dotted pattern which was indicative of the single-crystalline nature of nanoparticles (Figure 2c) and we did not observe rings which is characteristic of amorphous organic capping agents indicating their absence.

Parallel to the observation in the PXRD pattern, the HRTEM micrographs (Figure 2d) showed (1 2 1) as dominating planes. Two-dimensional FFT (Figure 2e) also confirmed construction of nanoflakes by the principal (1 2 1) and (1 3 0) planes. Moreover, we have not observed any dislocation, distortion, and twins in lattices of nanoflakes. Hence, the oriented growth mechanism did not influence the flake shape of the nanoparticles.⁵³ Since there was no capping agent on the surfaces, to minimize the surface energy of the particles, the planes might be grown to flake shape. Nanoflakes were crystalline along the whole length of the axis as confirmed by HRTEM studies. An interesting observation is that high crystallinity was achieved using a moderate reaction temperature. Altogether, the HRTEM observations suggested that the

nanoflakes were single crystals and structurally constructed to flakes by (1 2 1) and (1 3 0) planes.

2.3 optical properties

The solid state optical spectrum showed the broad characteristic absorption of the Bi_2S_3 nanoparticles with the maxima positioned at ~ 602 nm (Figure S2a). Due to the poor solubility of the Bi_2S_3 nanoparticles solid phase spectrum was recorded. The bandgap of Bi_2S_3 was calculated from the absorption spectra (Figure S2b) using the Kubelka-Munk method by assuming Bi_2S_3 as a direct bandgap material.⁵⁴ We determined band gap as 1.40 eV which was slightly higher than that reported for bulk band gap (1.3 eV).²¹ Since the width size of fewer flakes is lower than the Bohr radius (~ 30 nm), we attributed the minor blue shift to weak confinement of carriers in the width of the nanoflakes.

2.4 Electronic properties

2.4.1 Device Construction

The capping agent free nanoparticles are critical for efficient optoelectronic applications,^{55, 56} and these capping agents will create an insulating barrier on every nanoparticle and decrease the efficiency of the devices. Hence, we have synthesized organic-free Bi_2S_3 nanoflakes and built a prototype device of the photodetector (Figure. 3a). Among the various processing techniques, dry-casting is an attractive laboratory-friendly technique to fabricate the devices with small substrates (~ 1 cm). Moreover, the dry-casting technique does not require any costly equipment and the thickness of the active layer in the device can be controlled by the concentration of the nanoparticles. We fabricated the devices by binding the dry-casted Bi_2S_3 active layer between two ITO electrodes with the instrument configuration of ITO/ Bi_2S_3 /ITO, and the active area was $1 \text{ cm} \times 1 \text{ cm}$.

Figure 3a illustrates the fabrication process of the device at ambient conditions. At first, the active layer was made by the dry-casting of the suspension of Bi_2S_3 nanoflakes (40 mg in 1.5 mL) on the etched ITO substrate. The non-active area of ITO plates was etched to avoid shorting of the circuit while binding. We observed the dewetting of the Bi_2S_3 layer from the ITO substrates at higher concentrations. Slow evaporation of the Bi_2S_3 suspension of the nanoparticles helped in achieving a high-quality active layer. Then, another ITO plate was

sandwiched with binder clips to make the final device. An identical parallel ITO electrode structure was used to support the charge collection (Figure 3b). Figure 3c explains the working principle of the device. Illumination by green light generated a photocurrent at Bi_2S_3 layer and charge separation occurred in ITO junctions. Three devices were analysed to check the reproducibility of performance. The performance of the device was stable in air, and no degradation was observed after two months.

2.4.2 I-V Studies

We evaluated I-V characteristics of the devices made from Bi_2S_3 nanoflakes. Figure 3d shows the representative I-V curves of devices under dark and illuminated conditions. Illumination of device by green light (532 nm, 122 W.m^{-2}) showed the enhanced photoconductivity compared to dark condition ($I_{532 \text{ nm}} \approx 1.5 \times I_d$). Both dark and illuminated conditions exhibited a linear response. The linear behaviour indicated that Ohmic contact was established between the nanoflakes and the ITO.⁵⁷ The change in the slope of the curves between dark and illuminated conditions specified increase in current with the illumination which indicates high sensitivity. We have observed photoexcited current of $50 \mu\text{A}$ at the bias voltage of 2 V. Compared to the photocurrent ($46 \mu\text{A}$) generated by the device of similar Bi_2S_3 architecture reported earlier²³ we have achieved slightly higher photocurrent of $50 \mu\text{A}$ at the increased voltage (2 V). Thus, the capping agent free nature of the nanoparticles enhanced the photocurrent. The observed photocurrent generation even below 1 V can be attributed to the low resistance of the devices. Above 1 V, the difference between the dark current and photocurrent increased because the higher voltages enhanced the separation of photogenerated electrons and holes. The error bar in the I-V curves exemplified the stability of the device and the reproducibility of data. Even though ITO plates were bound physically, there was no breakdown of the device during measurements. All these findings indicated that the capping agent free Bi_2S_3 nanoflakes exhibit considerable photoresponse under the green light illumination.

It is to be mentioned that considerable dark current was observed in the devices which can be attributed the trap-assisted current⁵⁸⁻⁶² and minimal resistance (Section 2.4.5). Since the nanoparticles did not have the capping agent on the surfaces, there were more surface traps and less resistance.⁵⁷⁻⁶¹ The charges might be trapped in the devices and contribute to the current in

dark conditions. It seems the capping agent free surfaces generated more surface traps leading to moderate device performance. However, we have accomplished the workable photoconductor with a simple device design. Hence, the synthetic method or fabrication procedure requires modification to achieve a balance between surface traps and better conductivity.

2.4.3 Intensity dependent studies

We examined the effect of illumination on the photocurrent (Figure 4a) by exposing the device to green light of varying intensity. Interestingly, the photocurrent increased linearly with the intensity of illuminated light according to the power law $I \propto P^{0.070}$. It was observed the photocurrent rose from 37 μA (at dark) and reached a maximum of 44 μA at the 50 W.m^{-2} . The linear increase in the current with the green light indicates the more carrier generation in the device. Compared with a standard Bi_2S_3 based photodetectors ($I \propto P^{0.77}$),²⁷ we have observed little power dependence in the present system. The low responsiveness may be attributed to the reflective ITO glass substrates⁶³ and surface trap based recombination centers.⁶⁴ We have tested the device up to 50 W.m^{-2} without damaging the device performance. These findings indicated the stability of device without any break-down and the robust nature of the Bi_2S_3 nanoflakes at an incident light of high intensity. In summary, the high-intensity illumination can improve the photoresponse of the Bi_2S_3 nanoflakes.

2.4.4 Transient studies

We next evaluated the use of Bi_2S_3 as a photodetector by transient state measurements (Figure 4b). Square wave pulse of 50 W.m^{-2} with the interval of 40 s was given as an input optical signal to the device and output current was measured. While the pulse is turned on, the photocurrent increased from 4.5 nA to 5.6 nA. The photo current reached the steady state and sustained until it is switched off. The photocurrent curves replicated the pattern of input optical signals. The rise time of the device was calculated as 1.11 ± 0.10 s and decay time was 2.06 ± 0.21 s (Figure 4c and Table S1). Rise time was calculated from the interval of 10-90% of its peak value while the decay time was calculated from the range of 90-10% of its peak value. Since the rise and fall curves are symmetric, the device can produce reliable photodetection. The photocurrent was almost constant during all the cycles. The photocurrent On: Off switching current ratio was 1:1.3. Every cycle was identical and reproducible without any detectable degradation in the

device performance. Photocurrent was switchable to the on-off ratio even after the 700 s. Reversibility and stability of photocurrent in the transient studies exemplified the performance of the devices. It is to be mentioned that we have achieved the rise and decay time without any device structure optimization. All these observations indicated that response and decay time were in seconds, and the device can detect the fast varying optical signals.

2.4.5 Impedance analysis

With the intention of making electronic grade nanomaterials, we designed the HMDS-assisted method for making capping agent free nanoparticles.^{49, 50, 51} Organic impurity-free nanoparticles expected to have better carrier mobility and hence good conductivity.⁵⁵ Hence, impedance analysis was carried out to analyse the effect of the absence of the capping agent on the surfaces. Impedance measurements were performed using the two probe method. Fully expressed semicircles were observed in the analyses (Figure 4d). The resistance was directly measured by extrapolating the semicircle at the lower frequencies in the Nyquist plot and was found to be $3.15 \pm 0.02 \text{ k}\Omega$. It was in the optimal range of the device operation. There were no other types of resistances (semicircles) observed in the measurements. The small resistance was also responsible for good ohmic contact and linear response in I-V studies. Thus, the present synthetic procedure yielded low-resistance nanoparticles for a better optoelectronic application.

3. Conclusions

We have developed a solution phase synthetic method for the synthesis of Bi_2S_3 nanoparticles with the capping agent free surfaces to enhance the photoresponse. Using the HMDS-assisted method, 2 g of the Bi_2S_3 nanoflakes was produced. The method was a straightforward and scalable method for the synthesis of Bi_2S_3 flakes. A prototype device photodetector was fabricated from Bi_2S_3 nanoflakes using dry casting method. The device exhibited a linear response to the intensity of light under illumination and had the repose time of 1.1 s. We found that the higher light illumination can enhance photoresponse of the present system. Further, Bi_2S_3 nanoflakes had the resistance of $3.15 \pm 0.02 \text{ k}\Omega$ which was in the optimal range photodetector operation. Altogether, we have demonstrated simplicity in the synthesis, processing and device making. We have also shown that synthesis and device making can be achieved using a minimum energy at ambient conditions.

4. Experimental Section

4.1 Synthesis of Bi₂S₃ nanoflakes

We have used the HMDS-assisted method to synthesize Bi₂S₃ nanoflakes.^{49, 50, 51} All the chemicals were purchased from Aldrich and used without further purification. Reactions were carried out in a dry N₂ atmosphere with glove box and schlenk line techniques. In a typical method, bismuth(III) chloride (0.20 g, 0.63 mmol) and thiourea (0.072 g, 0.94 mmol) were added to the reaction flask. Then, HMDS (5.0 mL, 23.8 mmol) was injected into the flask and stirred for the homogeneity. Then the reaction mixture was heated to reflux and maintained for 3 h. The black precipitate was obtained at the end of the reaction. The reaction mixture was smelly, and the precipitate was separated out by the filtration. (Caution: intermediate is smelly and will widely diffuse in the air). Then the precipitate was washed with methanol (20 mL × 3) and acetone (20 mL × 2) by centrifugation (3500 rpm, 5 min). Purification procedures were carried out under ambient conditions. The product was dried under high vacuum (120 °C, 1 h) and the fine black powder was obtained. The reaction procedure was reproducible, and yield was 62 ± 4%.

4.2 Instrumentation

PXRD measurements were made in Bruker D8 X-ray diffractometer with the scan rate of 1° min⁻¹ (Cu K α = 1.54 Å). And the operating voltage was turned to 40 kV and operating current to 30 mA. The PXRD spectrum was obtained between 5 - 80°. FTIR measurements were recorded in the Alpha FTIR spectrometer. Samples were mixed with KBr and made as a pellet. The obtained spectrum was subtracted from the substrate. FESEM micrographs were recorded using Ultra 55 Carl Zeiss. The samples were dispersed in isopropyl alcohol and coated on the ITO plates. The samples were sputter coated with Au/Pd mixture before the imaging. For the EDAX analysis, powder samples were dusted on the carbon tape. The stoichiometric ratios were repeatedly measured, and the average was reported. TEM analysis was performed in Technai G² 20 STEM with 200 mesh carbon grids. The isopropyl dispersion of the Bi₂S₃ nanoflakes was prepared and coated on the grids. Solid state absorptions were conducted due to the poor solubility of the Bi₂S₃ nanoflakes. The spectrum was obtained using Shimadzu UV-3600 UV-Vis spectrometer. The

samples were mixed with barium sulphate and spectrum was obtained. The bandgap of Bi_2S_3 nanoflakes was calculated using the Kubelka-Munk method. In this approach, the energy derived from the UV spectrum ($\text{Energy (E)} = 1239.84 / \lambda_{\text{nm}}$) was plotted against $F(R).E^2$, and $F(R) = (1 - R)^2 / 2R$. Where R is the absolute reflectance ($R/100$) and band gap was obtained from the x-axis intercept.

4.3 Electronic measurements

Device configuration was ITO/ Bi_2S_3 /ITO. The prototype photodetectors devices are made from dry casting the samples on the surface of the ITO plates. Conductive indium tin oxide glass plates were used (resistance = $60 \Omega.\text{sq}^{-1}$). The active area of the device was $1 \text{ cm} \times 1 \text{ cm}$. Before the coating, ITO plates were washed with a detergent solution followed by the ultrasonication in acetone. Electrode area of the device was directed by masking with Teflon tape. Then etching of the device performed on the other ITO plate (10% of HCl solution; 3 h). Then the plates washed with IPA solution. Then the sample was coated with isopropyl alcohol suspension of Bi_2S_3 nanoflakes (40 mg in 1.5 mL). The coated samples were air-dried for a uniform active layer. Finally, devices were made by binding the coated plate with other ITO by binder clips. Two-probe method was used to study the optoelectronic properties. The photoconductivity of the device was analysed by I-V measurements. Green LED (532 nm, 122 W.m^{-2} , bandwidth = 22 nm) was utilized for the illumination of the device. Green LED was controlled by Zahner Zennium electrochemical workstation (Zahner, Germany). In transient studies, the light intensity of 90 W.m^{-2} was used. Reproducibility of the devices was confirmed by three different batches of the synthesis and device making. All the analytical data were plotted with standard error. Device measurements were conducted in the ambient conditions. For the energy level diagram, energy values were adopted from the literature.⁶⁵

Impedance measurements were carried out in Zahner Zennium electrochemical workstation and procedures are mentioned below. The two-probe analytical method was utilized for the impedance measurements. The Bi_2S_3 was made as a pellet under pressure (3 ton). The pellet dimensions were with radius = 0.8 cm and thickness = 0.062 cm. The resistance was calculated from the impedance spectroscopy. We utilised frequency range from 100 Hz to 4 MHz with AC amplitude of 20 mV. The temperature was stabilized for 30 min before the measurements. Measurements were repeated three times and standard error was reported in the

manuscript. Bulk resistance was calculated from the real axis intercept of the semicircle in the Nyquist plot.

Acknowledgements

The work was funded by DST-SERB of India. Award No.: SB/S1/IC-47/2013). B. G. K. acknowledges DST-SERB for the postdoctoral fellowship. B. S. gratefully acknowledges University Grants Commission of India for the senior research fellowship. We also thank Centre for Nanotechnology at the University of Hyderabad for TEM facility

References

- [1] K. -J. Chen, H. -C. Chen, K. -A. Tsai, C. -C. Lin, H. -H. Tsai, S. -H. Chien, B. -S. Cheng, Y. -J. Hsu, M. -H. Shih, C. -H. Tsai, H. -H. Shih, H.-C. Kuo, *Adv. Funct. Mater.* **2012**, 22, 5138–5143.
- [2] I. J. Kramer, J. C. Minor, G. M. -Bautista, L. Rollny, P. Kanjanaboos, D. Kopilovic, S. M. Thon, G. H. Carey, K. W. Chou, D. Zhitomirsky, A. Amassian, E. H. Sargent, *Adv. Mater.* **2015**, 27, 116–121.
- [3] T. Zhu, K. Shanmugasundaram, S. C. Price, J. Ruzyllo, F. Zhang, J. Xu, S. E. Mohny, Q. Zhang, A. Y. Wang, *Appl. Phys. Lett.* **2008**, 92, 023111.
- [4] J. Zhao, J. A. Bardecker, A. M. Munro, M. S. Liu, Y. Niu, I. -K. Ding, J. Luo, B. Chen, A. K. -Y. Jen, D. S. Ginger, *Nano Lett.* **2006**, 6, 463-467.
- [5] G. Konstantatos, I. Howard, A. Fischer, S. Hoogland, J. Clifford, E. Klem, L. Levina, E. H. Sargent, *Nature* **2006**, 442, 180-183.
- [6] Q. Guo, H. W. Hillhouse, R. Agrawal, *J. Am. Chem. Soc.* **2009**, 131, 11672.

- [7] M. G. Panthani, V. Akhavan, B. Goodfellow, J. P. Schmidtke, L. Dunn, A. Dodabalapur, P. F. Barbara, B. A. Korgel, *J. Am. Chem. Soc.* **2008**, *130*, 16770-16777.
- [8] M. Law, L. E. Greene, J. C. Johnson, R. Saykally, P. Yang, *Nat. Mater.* **2005**, *4*, 455 – 459.
- [9] X. Wang, L. Zhi, K. Müllen, *Nano Lett.* **2008**, *8*, 323-327.
- [10] J. Leppäniemi, T. Mattila, T. Kololuoma, M. Suhonen, A. Alastalo, *Nanotechnology* **2012**, *23*, 305204.
- [11] V. Wood, M. J. Panzer, J. Chen, M. S. Bradley, J. E. Halpert, M. G. Bawendi, V. Bulović, *Adv. Mater.* **2009**, *21*, 2151–2155.
- [12] H. M. Haverinen, R. A. Myllylä, G. E. Jabbour, *Appl. Phys. Lett.* **2009**, *94*, 073108.
- [13] D. Floreano, R. P. -Camara, S. Viollet, F. Ruffier, A. Brückner, R. Leitel, W. Buss, M. Menouni, F. Expert, R. Juston, M. K. Dobrzynski, G. L'Eplattenier, F. Recktenwald, H. A. Mallot, N. Franceschini, *Proc. Natl. Acad. Sci.* **2013**, *23*, 9267-9272.
- [14] I. Jung, J. Xiao, V. Malyarchuk, C. Lu, M. Li, Z. Liu, J. Yoon, Y. Huang, J. A. Rogers, *Proc. Natl. Acad. Sci.* **2011**, *108*, 1788.
- [15] H. C. Ko, M. P. Stoykovich, J. Song, V. Malyarchuk, W. M. Choi, C. -J. Yu, J. B. Geddes III, J. Xiao, S. Wang, Y. Huang, J. A. Rogers, *Nature* **2008**, *454*, 748-753.
- [16] M. Ettenberg, *Adv. Imag.* **2005**, *20*, 29–32.
- [17] X. Gao, Y. Cui, R. M. Levenson, L. W. K. Chung, S. Nie, *Nature Biotechnol.* **2004**, *22*, 969–976.
- [18] M. Caria, L. Barberini, S. Cadeddu, A. Giannattasio, A. Rusani, A. Sesselego, A. Lai, S. D'Auria, F. Dubecky, *Appl. Phys. Lett.* **2002**, *81*, 1506-1508.
- [19] J. Wang, M. S. Gudiksen, X. Duan, Y. Cui, C. M. Lieber, *Science* **2001**, *293*, 1455-1457.
- [20] A. Abuazza, D. Brabazon, M. A. El-Baradie, *J. Mater. Process. Tech.* **2003**, *143–144*, 875–879.
- [21] H. Bao, X. Cui, C. M. Li, Y. Gan, J. Zhang, J. Guo, *J. Phys. Chem. C* **2007**, *111*, 12279-12283.
- [22] M. Nair, P. Nair, *Semicond. Sci. Technol.* **1990**, *5*, 1225–1230.
- [23] G. Xiao, Q. Dong, Y. Wang, Y. Sui, J. Ning, Z. Liu, W. Tian, B. Liu, G. Zou, B. Zou, *RSC Adv.* **2012**, *2*, 234-240.
- [24] M. T. S. Nair, P. K. Nair, *Semicond. Sci. Technol.* **1990**, *5*, 1225.

- [25] T. W. Case, *Phys. Rev.* **1917**, 9, 305.
- [26] R. Suarez, P. K. Nair, P. V. Kamat, *Langmuir* **1998**, 14, 3236–3241
- [27] G. Konstantatos, L. Levina, J. Tang, E. H. Sargent, *Nano Lett.* **2008**, 8, 4002–4006.
- [28] G. Chen, Y. Yu, K. Zheng, T. Ding, W. Wang, Y. Jiang, Q. Yang, *Small* **2015**, 11, 2848–2855.
- [29] H. Li, J. Yang, J. Zhang, M. Zhou, *RSC Adv.* **2012**, 2, 6258–6261.
- [30] R. Li, J. Yang, N. Huo, C. Fan, F. Lu, T. Yan, Z. Wei, J. Li, *Chem. Phys. Chem.* **2014**, 15, 2510–2516.
- [31] Yi. Xi, C. Hu, X. Zhang, Y. Zhang, Z. L. Wang, *Solid State Commun.* **2009**, 149, 1894–1896.
- [32] G. Manna, R. Bose, N. Pradhan, *Angew. Chem. Int. Ed.* 2014, 53, 6743–6746
- [33] L. Cademartiri, R. Malakooti, P. G. O’Brien, A. Migliori, S. Petrov, N. P. Kherani, G. A. Ozin, *Angew. Chem., Int. Ed.* **2008**, 47, 3814–3817.
- [34] L. Tian, T. H. Yao, J. Vittal, *J. Cryst. Growth Des.* **2008**, 8, 734–738.
- [35] Q. F. Han, J. Chen, X. J. Yang, L. Lu, X. Wang, *J. Phys. Chem. C* **2007**, 111, 14072–14077.
- [36] W. Lou, M. Chen, X. Wang, W. Liu, *Chem. Mater.* **2007**, 19, 872–878.
- [37] X. -P. Shen, G. Yin, W. -L. Zhang, Z. Xu, *Solid State Commun.* **2006**, 140, 116–119.
- [38] A. K. Jain, V. Sharma, R. Bohra, A. A. Sukumar, V. S. Raju, J. E. Drake, M. B. Hursthouse, M. E. Light, *J. Organomet. Chem.* **2006**, 691, 4128–4134.
- [39] G. Xie, Z. P. Qiao, M. H. Zeng, X. M. Chen, S. L. Gao, *Cryst. Growth Des.* **2004**, 4, 513–516.
- [40] P. Boudjouk, M. P. Remington, D. G. Grier, B. R. Jarabek, G. McCarthy, *J. Inorg. Chem.* **1998**, 37, 3538–3541.
- [41] L. S. Li, N. J. Sun, Y. Y. Huang, Y. Qin, N. Zhao, J. N. Gao, M. X. Li, H. H. Zhou, L. M. Qi, *Adv. Funct. Mater.* **2008**, 18, 1194–1201.
- [42] A. Alemi, M. Dolatyari, *Rad. Eff. Def. Sol.* **2008**, 163, 123–130.
- [43] W. H. Li, *Mater. Lett.* **2008**, 62, 243–245.
- [44] J. Ota, S. K. Srivastava, *J. Phys. Chem. C* **2007**, 111, 12260–12264.
- [45] J. Xu, N. Petkov, X. Wu, D. Iacopino, A. J. Quinn, G. Redmond, T. Bein, M. A. Morris, J. D. Holmes, *Chem. Phys. Chem.* **2007**, 8, 235–240.

- [47] A. K. Jain, R. Bohra, *Appl. Organomet. Chem.* **2006**, *20*, 411–415.
- [48] J. Tang, A. P. Alivisatos, *Nano Lett.* **2006**, *6*, 2701–2706.
- [49] B. G. Kumar, K. Muralidharan, *J. Mater. Chem.* **2011**, *21*, 11271.
- [50] B. G. Kumar, K. Muralidharan, *Eur. J. Inorg. Chem.* **2013**, 2102.
- [51] B. G. Kumar, K. Muralidharan, *RSC Adv.* **2014**, *4*, 28219.
- [52] B. Pejova, I. Grozdanov, *Mater. Chem. Phys.* **2006**, *99*, 39–49.
- [53] R. L. Penn, *J. Phys. Chem. B* **2004**, *108*, 12707–12712.
- [54] J. B. M. Goodall, S. Kellici, D. Illsley, R. Lines, J. C. Knowles, J. A. Darr, *RSC Adv.* **2014**, *4*, 31799–31809.
- [55] M. V. Kovalenko, M. Scheele, D. V. Talapin, *Science* **2009**, *324*, 1417.
- [56] D. V. Talapin, J. –S. Lee, M. V. Kovalenko, E. V. Shevchenko, *Chem. Rev.* **2010**, *110*, 389–458.
- [57] L. Li, Y. Yu, G. J. Ye, Q. Ge, X. Ou, H. Wu, D. Feng, X. H. Chen, Y. Zhang, *Nat. Nanotechnol.* **2014**, *9*, 372–377.
- [58] T. Zhai, X. Fang, M. Liao, X. Xu, L. Li, B. Liu, Y. Koide, Y. Ma, J. Yao, Y. Bando, D. Golberg, *ACS Nano* **2010**, *4*, 1596–1602.
- [59] M. B. Jarosz, V. J. Porter, B. R. Fisher, M. A. Kastner, M. G. Bawendi, *Phys. Rev. B* **2004**, *70*, 195327.
- [60] D. S. Ginger, N. C. Greenham, *J. Appl. Phys.* **2000**, *87*, 1361.
- [61] O. L. -Sanchez, D. Lembke, M. Kayci, A. Radenovic, A. Kis, *Nat. Nanotechnol.* **2013**, *8*, 497.
- [62] J. P. Clifford, K. W. Johnston, L. Levina, E. H. Sargent, *Appl. Phys. Lett.* **2007**, *91*, 253117.
- [63] A. W. Blakers, A. Wang, A. M. Milne, J. Zhao, M. A. Green, *Appl. Phys. Lett.* **1989**, *55*, 1363.
- [64] Y. Jin, J. Wang, B. Sun, J. C. Blakesley, N. C. Greenham, *Nano Lett.* **2008**, *8*, 1649–1653.
- [65] H. -C. Liao, M. -C. Wu, M. -H. Jao, C. -M. Chuang, Y. -F. Chend, W. -F. Su, *Cryst. Eng. Comm.* **2012**, *14*, 3645–3652.

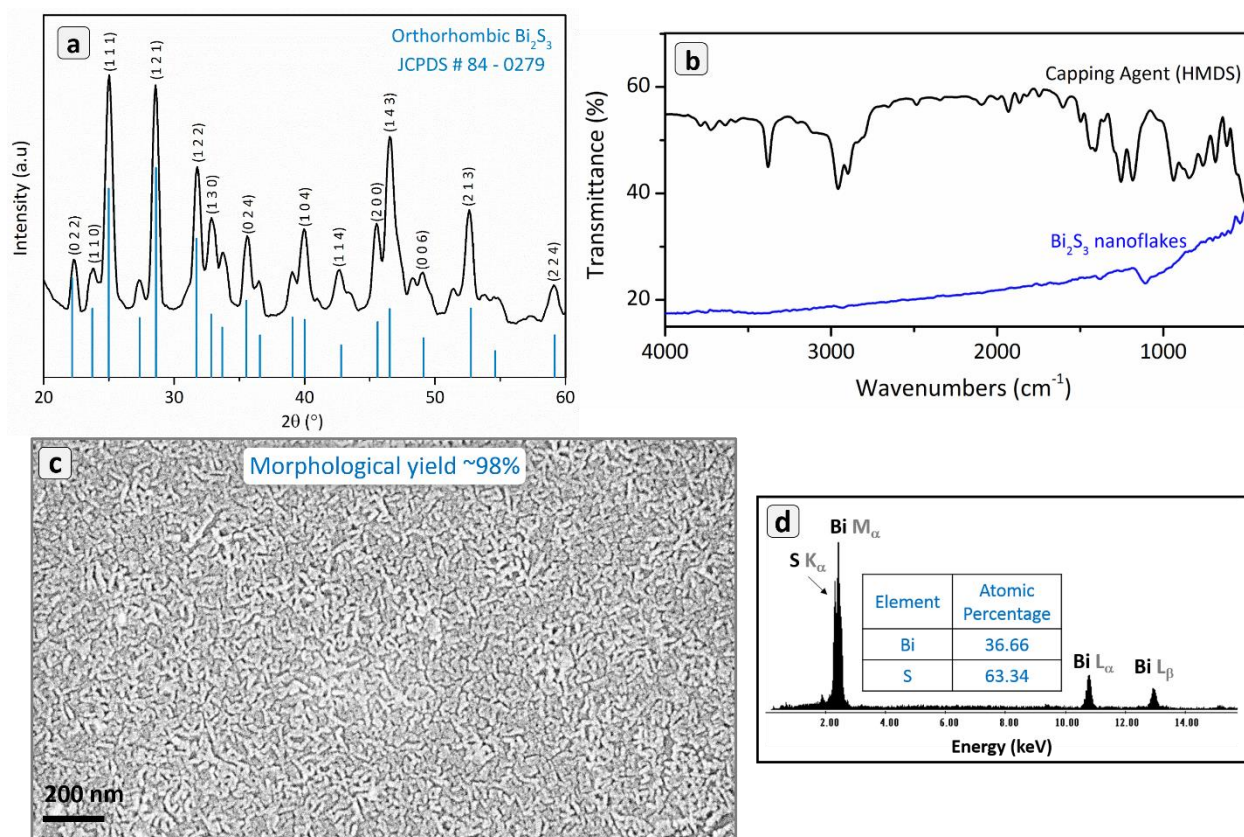


Figure 1. Primary characterization of Bi_2S_3 nanoparticles. (a) PXRD pattern of the nanoflakes. We observed that the obtained pattern matched with orthorhombic bulk Bi_2S_3 (JCPDS # 84-0279). (b) FTIR spectrum of the nanoflakes. HMDS spectrum was plotted for the visual comparison. (c) FESEM micrographs of the nanoparticles. (d) EDAX spectrum of the nanoflakes. Atomic ratio showed that obtained product was slightly bismuth deficient (3%).

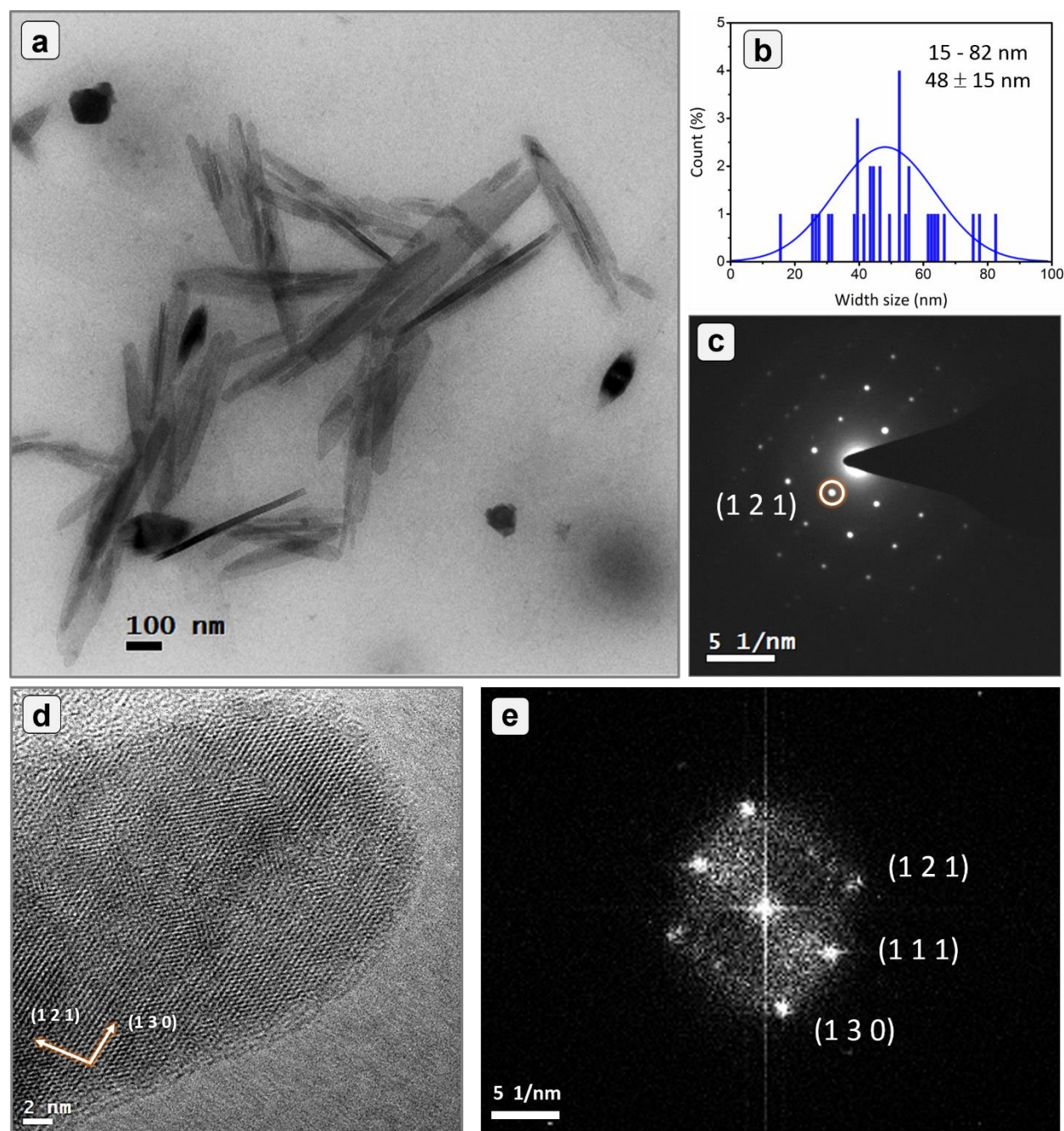


Figure 2. TEM micrographs of the Bi_2S_3 nanoparticles. (b) Particle distribution diagram. (c) SAED pattern of the flake. The circle indicates dominant (1 2 1) planes. (d) HRTEM analysis of a flake. (e) FFT analysis of whole flake in the image (d).

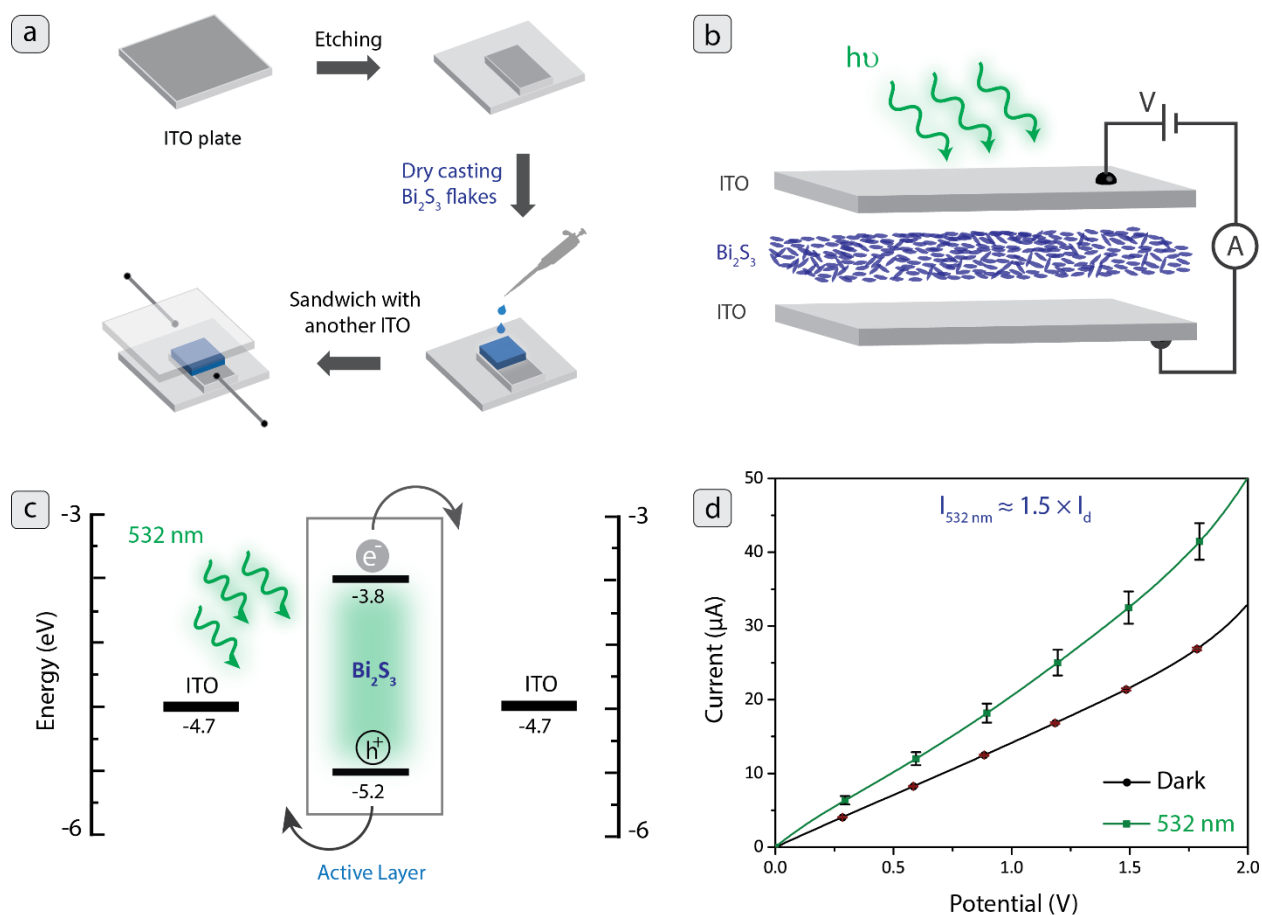


Figure 3. (a) Device making from the dry casting. Devices were made by binding the active layer between ITO electrodes. Active area of the device was $1 \text{ cm} \times 1 \text{ cm}$ (b) Cross sectional view of the device with circuits. (c) Energy level diagram of the device components (d) Two probe I-V measurements (532 nm, 122 W.m^{-2}).

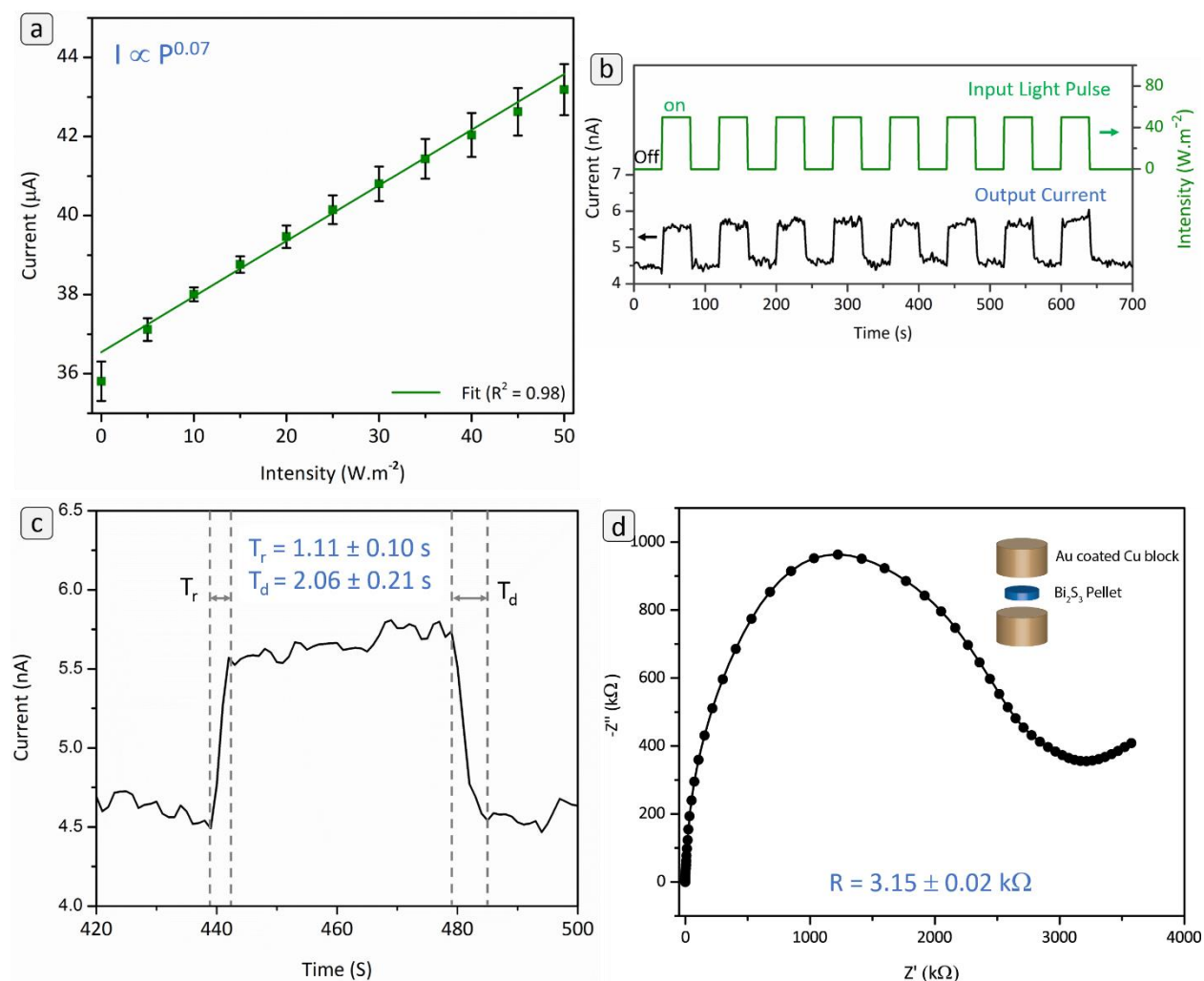
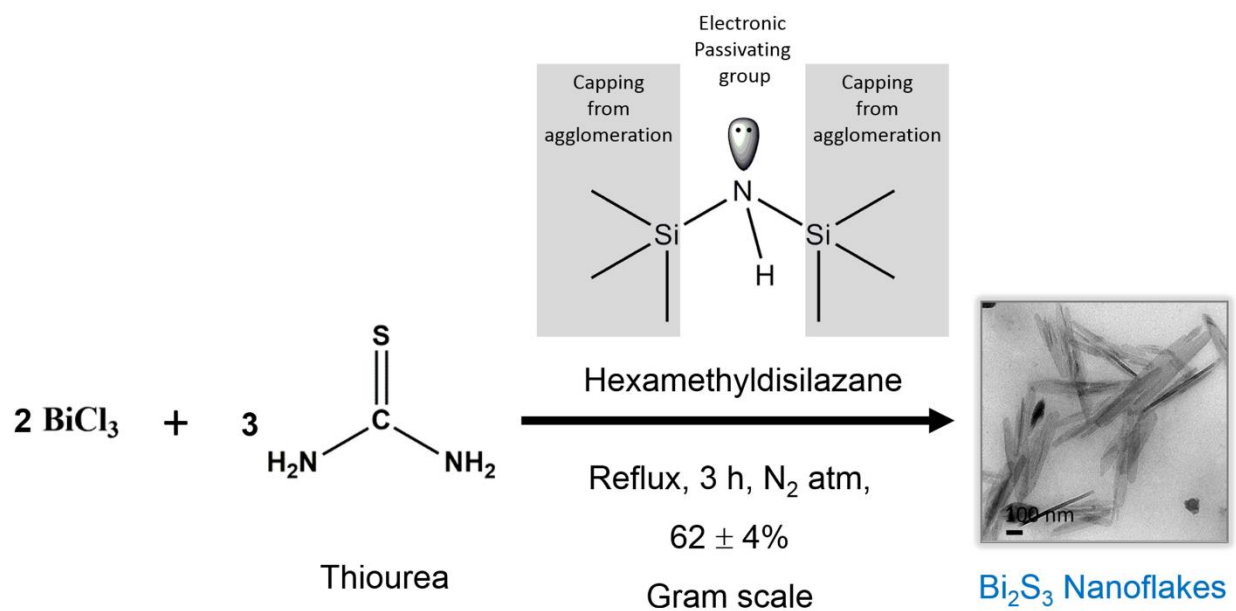


Figure 4. Optoelectronic properties of the devices. (a) Intensity-dependent measurement of the device. (b) Transient measurements of the device. For the comparison, Input square pulse is also shown. (c) A magnified cycle of the transient studies. (d) Nyquist plot of Bi_2S_3 nanoflakes. Dots are experimental data, and the solid lines are trend line. Inset showing the measurement design (exploded view) of the impedance analysis.



Scheme 1. The modified HMDS-assisted synthesis of Bi₂S₃ nanoflakes

Ag/Ag₂S heterodimers: tailoring the metal–semiconductor interface in a single nanoparticle

Baskaran Ganesh Kumar · Billakanti Srinivas ·
Muvva D. Prasad ·
Krishnamurthi Muralidharan

Received: 19 April 2015 / Accepted: 19 July 2015
© Springer Science+Business Media Dordrecht 2015

Abstract Heterodimers are conjoined particles of two inorganic materials, and they are generally synthesised in multiple steps. But, the multi-step syntheses are less effective because of the low yield, long reaction time, labour intensive process and complexity in the synthesis and thus not ideal for scale up. Herein, we have demonstrated single-step, one-pot syntheses for two different types of Ag/Ag₂S heterodimers. Two types of heterodimers were obtained while varying stoichiometry in the reaction of AgNO₃ with sulphur in the presence of hexamethyldisilazane (HMDS) at 140 °C. To the best of our knowledge, this was the first demonstration of single-step process to synthesise Ag/Ag₂S heterodimers. Heterodimers had dumbbell shape with both metal and semiconductor domains in single particle which were constructed by spherical Ag and Ag₂S nanoparticles. Ag (2 0 0) and Ag₂S (0 2 2) planes associated to form heterodimers. The presence of metal–semiconductor interfaces was confirmed by HRTEM and UV analysis. Thus, we have demonstrated the HMDS-assisted

synthesis as a promising method for direct synthesis of Ag/Ag₂S heterodimers.

Keywords Heterodimers · Ag₂S nanoparticles · Ag nanoparticles · Hexamethyldisilazane and HMDS-assisted methodology · Composite nanoparticles

Introduction

Heterodimers (HDs) are hybrid nanomaterials formed by the attachment of two different inorganic materials as a single unit. (Talpin et al. 2003; Gu et al. 2004; Mokari et al. 2004; Kudera et al. 2005; Mokari et al. 2005; Yu et al. 2005; Cozzoli et al. 2006; Yang et al. 2006; Casavola et al. 2008; Jiang et al. 2008; Yang and Ying 2009; Jiang et al. 2011; Pang et al. 2010; Zhu and Xu 2011; Xiong et al. 2013; Gu et al. 2004; Tang et al. 2006). HDs integrate different functional materials of desired interest and are multifunctional due to their hybrid properties of constituting materials (Mokari et al. 2005; Casavola et al. 2008; Xiong et al. 2013; Lee et al. 2010). Hence, the properties of both materials can be harnessed at the same time. Resulting properties can be tuned by the size and dimensions of constituent nanoparticles in HDs. Among various HDs, Ag/Ag₂S is unique because of the combination of metal and semiconductor. Because of the interface, Ag/Ag₂S HD exhibited excellent photocatalytic efficiency, (Jiang et al. 2011) photosensitivity, (Xiong

Electronic supplementary material The online version of this article (doi:10.1007/s11051-015-3126-y) contains supplementary material, which is available to authorized users.

B. G. Kumar · B. Srinivas · M. D. Prasad ·
K. Muralidharan (✉)
School of Chemistry, University of Hyderabad,
Hyderabad, India
e-mail: kmsc@uohyd.ernet.in; murali@uohyd.ac.in

et al. 2013) and antibacterial activity (Pang et al. 2010).

In most of the synthetic procedures, HDs were prepared by sequential synthesis, i.e. post modification on one of the domains. To mention few, Mokari et al. synthesised Au/CdSe HD by post attachment of gold nanoparticles with CdSe rods (Mokari et al. 2004). Yu et al. obtained Au/Fe₃O₄ HD by decomposition of Fe(CO)₅ on the surface of Au nanoparticles followed by oxidation (Yu et al. 2005). Manna et al. reported the CoPt₃/Au HD production by nucleation of Au on CoPt₃ nanoparticles (Cuzzoli et al. 2006). Lee et al. synthesised PbS/Au HD by mixing of Au nanoparticles with PbS nanoparticles (Yang et al. 2006). Ying et al. synthesised the Fe₂O₃/Ag HD using Fe₂O₃ nanoparticles as seeds (Jiang et al. 2008). Talapin et al. synthesised FePt/PbS HD using FePt nanoparticles as seeds (Lee et al. 2010). Zeng et al. made Ag₂S/Ag HD through ion exchange and photo-assisted reduction (Pang et al. 2010). Thus, most of the methods required multiple steps and unique reaction procedures to synthesise HDs. However, the multi-step syntheses are less effective because of the low yield, long reaction time, labour intensive process and complexity in the synthesis and thus not ideal for scale up.

Herein, we report single-step synthesis of two different types (HD-I and HD-II) of Ag/Ag₂S HDs. We have synthesised these HDs without linkers or pre/post synthetic modifications but using hexamethyldisilazane-assisted method (HMDS-assisted methodology) (Kumar and Muralidharan 2011, 2013). HD formation was achieved by designing reaction condition suitable for the simultaneous formation of Ag and Ag₂S nanoparticles in one pot. To the best of our knowledge, this is the first report on the direct wet chemical synthesis of Ag/Ag₂S HDs. HD-I had a dumbbell shape with equal amount of metallic Ag nanoparticles and semiconducting Ag₂S nanoparticles. Silver domain in the HDs was tuned by varying the amount of sulphur in the reaction ((AgNO₃:S = 2:0.9)). The structure and mechanism of formation of HDs were investigated by analysing the interfaces by HRTEM and UV spectra.

Experimental section

All the materials of analytical grade were purchased from commercial suppliers and used without further

purification. The reaction was performed in air-free conditions using schlenk line. Glove-box was used to handle and store air-sensitive chemicals.

Synthesis of Ag/Ag₂S heterodimer-I

Ag/Ag₂S heterodimer-I (HD-I) was synthesised using a stoichiometric ratio of AgNO₃:S in the reaction as 2:0.3 (Scheme 1). In typical synthesis, AgNO₃ (0.400 g, 2.40 mmol) and sulphur (0.011 g, 0.31 mmol) was added into 50 mL round bottom flask. The flask was purged with nitrogen gas (10 min), and then an excess amount hexamethyldisilazane (HMDS) (10 mL, 47.7 mmol) was injected. The reaction mixture was heated to reflux (140 °C) for 1 h to ensure the completion of the reaction. A shiny black precipitate was formed at the end of reaction. Volatile side-products and unreacted capping agent were removed by vacuum. The residue was washed with methanol (20 mL × 3) and toluene (20 mL × 3) to remove unreacted AgNO₃ and sulphur, respectively, under ambient condition. It was dried at 120 °C for 4 h. HD was stable in dark and was stored in a desiccator.

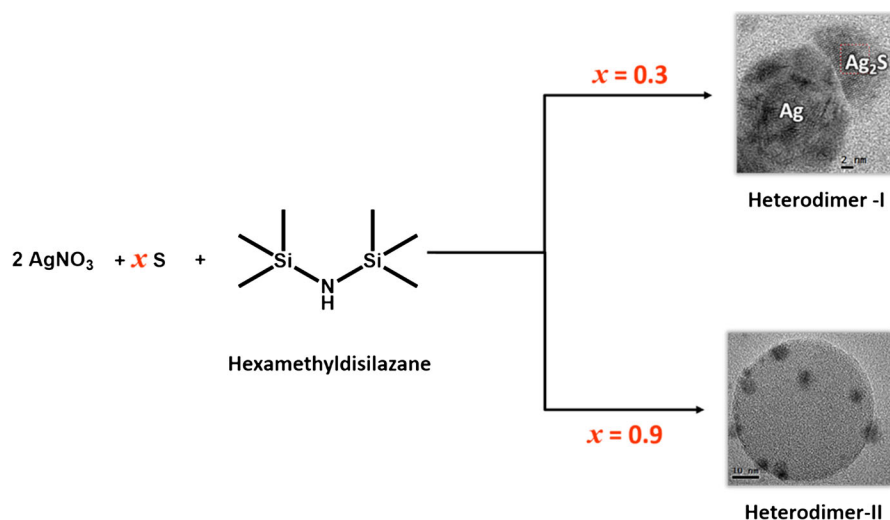
Synthesis of Ag/Ag₂S heterodimer-II

Ag/Ag₂S heterodimer-II (HD-II) was synthesised using the reaction stoichiometric ratio of AgNO₃:S as 2:0.9 (Scheme 1). The procedure was similar to the HD-I synthesis. In typical synthesis, AgNO₃ (0.400 g, 2.40 mmol) and sulphur (0.034 g, 1.08 mmol) were used. The amount of HMDS in the reaction was kept constant. The reaction was carried out at reflux temperature for 1 h, and black precipitate of HD-II was obtained. The precipitate was purified similar to HD-I and stored in dark conditions.

Instrumentation

Powder X-ray diffraction patterns of HDs were collected from Bruker D8 X-ray diffractometer [$\lambda_{\text{Cu-K}\alpha} = 1.54 \text{ \AA}$] with the scan rate of 1° min^{-1} . Powder samples were supported by PMMA holder, and the studies were carried out at room temperature. Solid-state UV/Vis absorption spectra of HDs were recorded in Shimadzu UV-3600 UV/Vis spectrophotometer. The samples were mixed with UV-grade barium sulphate, and the reflectance was recorded.

Scheme 1 Reaction explaining the synthesis of two forms of Ag/Ag₂S HDs



The absorbance was derived from the reflectance by Kubelka–Munk conversion. IR spectra were acquired using Alpha FTIR spectrometer. The FTIR spectra of HDs were subtracted from the spectrum of pure substrate. TEM, DFTEM and SAED analyses of HDs were carried out on FEI Technai G² 20 STEM instrument. To prevent light-induced modifications, light exposure was avoided while handling HDs for microscopic analysis. Samples were dispersed in isopropyl alcohol (2 mL) and sonicated for 8 min prior to TEM analysis. The dispersions of HDs were coated on carbon-coated Nickel grids (200 mesh). Since copper grids were reacting with ionic silver particles in HDs, the nickel grids were used for TEM measurements. For the particle distribution analysis, diameter of 300 particles was measured and plotted. TEM-EDAX measurements were recorded in several places for complete analysis.

Results and discussion

Designing of heterodimer synthesis

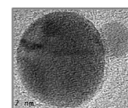
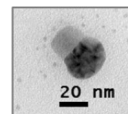
The HMDS-assisted synthesis of nanoparticles is emerging as an interesting method for the production of various organic surfactant-free nanoparticles (Kumar and Muralidharan 2011, 2013, 2014). Earlier, we have reported the sulphur ratio controlled formation of Ag nanoparticles and Ag₂S nanoparticles assisted by HMDS (Kumar and Muralidharan 2014). Ag₂S

nanoparticles were obtained when the reaction stoichiometry of AgNO₃:S was 2:1, while Ag nanoparticles were obtained with the absence of sulphur. Since the amount of sulphur in the reaction directed the preferential formation of products, we varied the reaction stoichiometry between AgNO₃ and S (2:0.2–0.9) with the intention of synthesising HDs. Interestingly, two types of HDs were formed when the ratio of AgNO₃:S = 2:0.3 and 2:0.9 while other reactions yielded simple mixtures of Ag and Ag₂S nanoparticles. HDs were categorised based on the amount of the Ag particles in the HDs. Silver-rich heterodimers (HD-I) were formed at Ag:S = 2:0.3 ratio. The second HD (HD-II) was obtained at the stoichiometric ratio of AgNO₃:S = 2:0.9.

To explore the HDs formation, we have performed few controlled reactions (Table 1). The role of HMDS and formation of S–N intermediate in the HMDS-assisted synthesis were well established earlier (Kumar and Muralidharan 2014). Similar to earlier observations, without HMDS, there was no progress in the present reaction. To avoid the influence of concentration of HMDS on the HD formation, a large excess of it was added (~41 times of mole ratio) in all reactions. Thus, we have demonstrated stoichiometry controlled synthesis of HDs assisted by HMDS. Every reaction was duly followed by TEM analysis. In the absence of sulphur in the reaction, Ag nanoparticles formed (Table 1, Reaction 1; Fig. S1). (Kumar and Muralidharan 2014). At the stoichiometric ratio of AgNO₃:S = 2:1 in HMDS, formation of Ag₂S

Table 1 Controlled reactions. HDs were synthesised by one-pot synthesis of Ag and Ag₂S nanoparticles

S. No	Reactions	Products
1.	AgNO ₃ + HMDS	Ag nanoparticles (Kumar and Muralidharan 2014)
2.	2 AgNO ₃ + S + HMDS	Ag ₂ S nanoparticles (Kumar and Muralidharan 2014)
3.	2 AgNO ₃ + 0.3 S + HMDS	Ag/Ag ₂ S heterodimers-I
4.	2 AgNO ₃ + 0.9 S + HMDS	Ag/Ag ₂ S heterodimers-II
5.	2 AgNO ₃ + <i>x</i> S + HMDS	Mixture of Ag and Ag ₂ S nanoparticles (<i>x</i> = 0.2–0.8 except 0.3)



nanoparticles was observed (Reaction 2, Table 1, Fig. S1) (Kumar and Muralidharan 2014). The intermediate stoichiometric condition (AgNO₃:S = 2:0.2–0.9) yielded binary mixtures of both Ag and Ag₂S nanoparticles except for the following observations. At the stoichiometric amount of AgNO₃:S = 2:0.3, HD-I was formed (Reaction 3, Table 1), and HD-II was formed when the sulphur quantity in the reaction was high (AgNO₃:S = 2:0.9) (Reaction 4, Table 1).

Tailoring metal–semiconductor domains

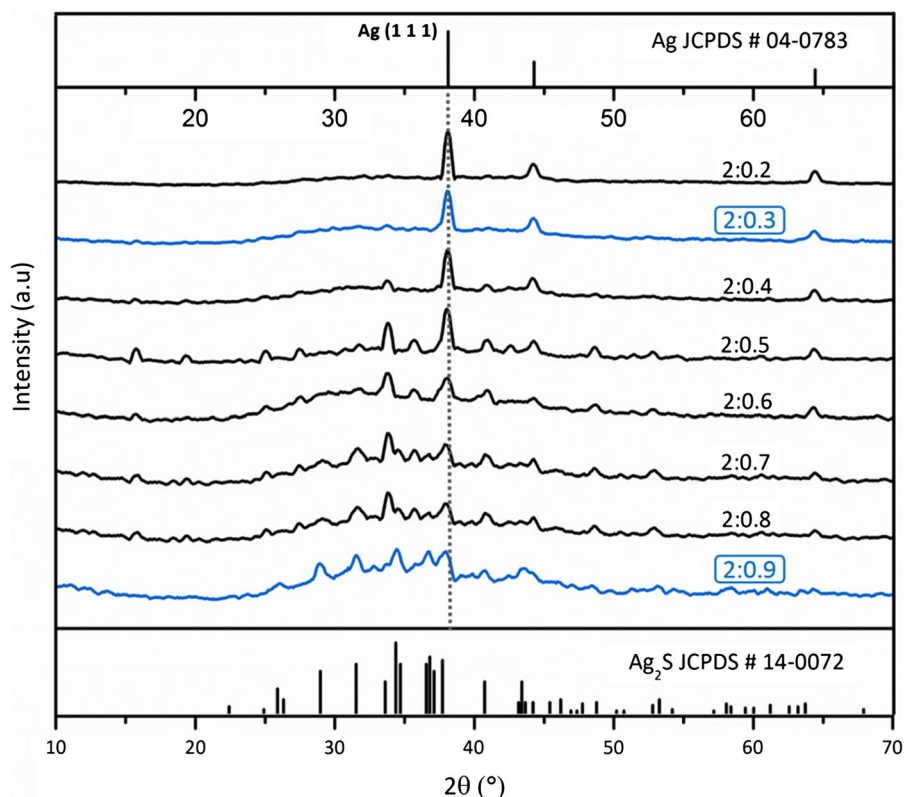
Figure 1 shows PXRD patterns of materials obtained from the reactions of varying stoichiometry. Even though all the non-stoichiometric ratios had mixed Ag and Ag₂S pattern, TEM analysis showed that only Ag:S = 2:0.3 and 2:0.9 ratio yielded HDs (Figs. 2, 4). For all materials, a combined pattern of bulk phase Ag and Ag₂S crystal structures was observed. Ag₂S phase had monoclinic crystal system (JCPDS # 14-0072) while Ag phase had a cubic crystal system (JCPDS # 04-0783). The diffraction peaks were broad and merged with adjacent peaks. Yet, the relative intensities of the peaks and position of Ag and Ag₂S reflections were consistent with standard individual patterns. All peaks were accounted and identified as either Ag or Ag₂S reflections. Since there were no peaks due to carbonaceous species or HMDS in FTIR spectra of HD-I and II (Fig. S3), line broadening due to the contribution of organic moieties was excluded. Although excess of silver ions was presented in the

reaction, diffraction patterns were phase pure and no other Ag-rich stoichiometric phases were identified. No lattice stress or no reflections were compromised for the HD formation (Fig. S2). The individual PXRD patterns explained that individual characteristics were retained during the formation of HDs. We infer Ag and Ag₂S nanoparticles existed with an own identity in HDs, and lattices were not compromised for the formation of HDs. To analyse the nature of individual Ag and Ag₂S domains and HD formation, the particles was analysed using HRTEM and DFTEM. FFT and lattice profiling were also obtained.

Metal-rich Ag/Ag₂S heterodimer-I

The TEM micrographs confirmed that HDs were formed at the reaction ratio of Ag and S that was 2:0.3 (Figs. 2, S4). TEM micrographs showed that HD-I had dumbbell shape and formed by an attachment of Ag and Ag₂S spherical nanoparticles. We observe a sharp contrast difference between Ag and Ag₂S domains in HD-I nanoparticles and they were visible even under low magnifications. The size distribution of Ag nanoparticles was within 9–38 nm with average diameter of 19 ± 6 nm while that of Ag₂S nanoparticles was 9–34 nm with an average diameter of 17 ± 5 nm (Fig. 2 inset). Both distributions of Ag and Ag₂S nanoparticles were nearly monodisperse and reproducible. The reaction mixture was required to be stirred rigorously to avoid local concentration of reactants; otherwise, HD particles of random size distribution were obtained as seen in TEM. As

Fig. 1 Powder X-ray diffraction patterns of materials obtained from various reactions of different stoichiometric ratios. Heterodimers were obtained at the stoichiometric ratio of $\text{AgNO}_3:\text{S} = 2:0.3$ and $2:0.9$. Standard diffraction patterns of Ag (cubic) and Ag_2S (monoclinic) are also shown for comparison



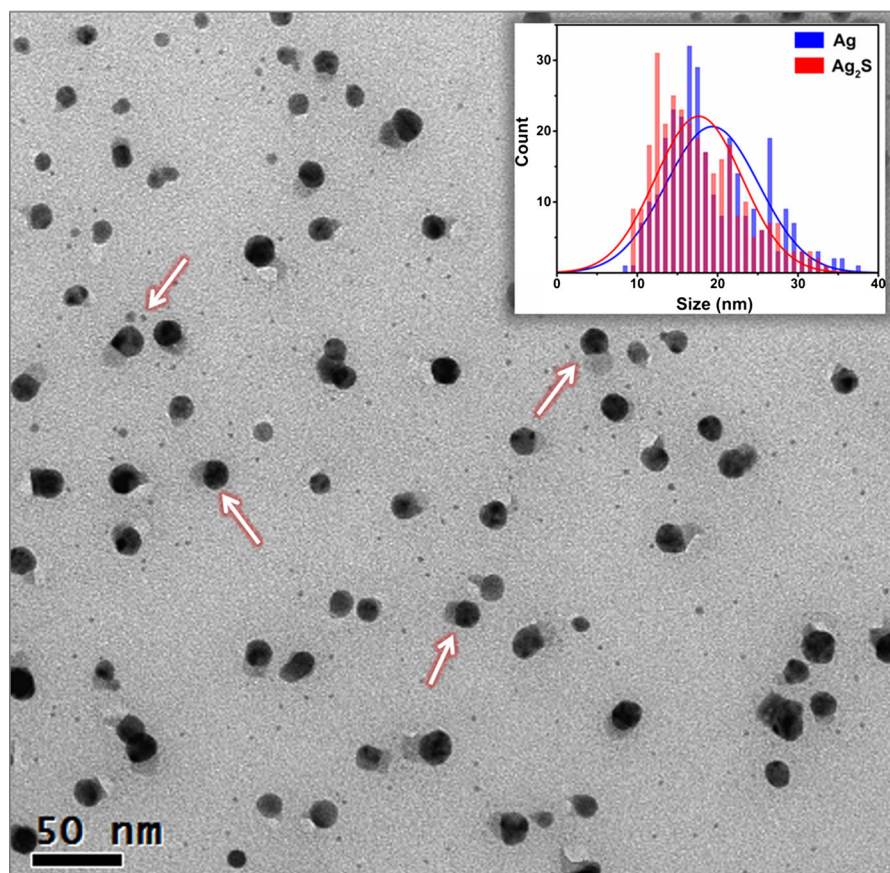
determined by TEM-EDAX, the Ag and S atomic ratios in HD-I were not constant in all HD-I particles but distributed over a range. For every S atom, the atomic ratio of Ag was ranging from 2.3 to 2.9 (Fig. S5). This may be due to the various volume proportions of Ag and Ag_2S nanoparticles. The absence of silicon signal in the EDAX spectrum confirmed the absence of HMDS (capping agent) on the particle surfaces. Elemental profiling measurements of individual HDs were not successful because of the small size of particles (Fig. S6).

HRTEM and DFTEM images duly confirmed the single crystalline nature of both Ag and Ag_2S parts in HD were not compromised while forming HDs. Since the contrast difference between Ag and Ag_2S domain in a single frame was interfering, the individual domains were differentiated by lattice fringe measurements. High quality individual HRTEM images were achieved by sacrificing either Ag or Ag_2S lattice (Fig. 3a). Since Ag and Ag_2S have similar diffraction pattern, Ag_2S was differentiated from Ag by higher distant planes $[(1\ 1\ 1)]$. Dark field TEM (DFTEM)

images combined with SAED pattern utilised as a guiding tool for identifying the difference between Ag and Ag_2S nanoparticles (Fig. 3c–f).

HRTEM micrographs (Figs. 3, 5) showed specific interaction between Ag and Ag_2S particles. The studies confirmed that HD-I was formed by the interaction of Ag (2 0 0) planes and Ag_2S (0 2 2) planes (Fig. 5). Lattice mismatch at the junction of the Ag (2 0 0) and Ag_2S (0 2 2) planes was calculated as ($\sim 21\%$). This lattice mismatch was the reason for HD formation rather than core–shell nanostructures since core–shell nanostructures required $<5\%$ of lattice mismatching (Palmstrom 1995; Ray et al. 2014; Zhang et al. 2010). The large lattice mismatch explained that the structure of HD not an epitaxial type of growth on each other. In the epitaxial growth, the crystal will grow on lattice matched crystal on the surface to minimise the surface energy. Clearly, the lattice mismatch and selective interaction were responsible for the formation of HDs. The association of Ag and Ag_2S nanoparticles was strong and not reversed/disrupted by the sonication. Compared with other synthetic procedures of HDs, we

Fig. 2 TEM image of the heterodimer. Arrows indicate representative HD. Silver nanoparticles had strong imaging contrast than Ag_2S nanoparticles. Inset Particles distribution diagram



achieved higher volume proportion of Ag in Ag/ Ag_2S HDs (Jiang et al. 2011; Pang et al. 2010; Xiong et al. 2013; Zhu and Xu 2011).

Ag/ Ag_2S Heterodimer-II having more semiconductor domain

PXRD pattern and TEM micrographs confirmed the formation of Ag_2S -rich heterodimer (HD-II) when the reaction stoichiometric ratio of AgNO_3 :S was 2:0.9. In PXRD pattern, Ag_2S peaks were dominated and screened the peaks of Ag (Fig. 1). Reflections of the Ag nanoparticles in HD were weak due to the small volume fraction, but Ag (1 1 1) peak was distinguishable from Ag_2S pattern. The large area TEM images (Fig. 4a) showed that Ag and Ag_2S nanoparticles associated to form HD-II among which most of the particles further self-assembled to form chain like morphology. The high magnification images showed that the smaller spherical Ag nanoparticles were

embedded on bigger Ag_2S nanoparticles like cactus-opuntia plant to form HD-II nanoparticles (Fig. 4b). The sizes of Ag domain were between 3 and 28 nm with an average diameter of 9 ± 4 nm while that of Ag_2S was between 18 and 71 nm with an average diameter of 38 ± 8 nm (Fig. 4c). For the dark field TEM measurements, entire diffraction pattern was collected without any special selection of diffraction pattern of Ag or Ag_2S nanoparticles. In the dark field TEM images of HD-II, Ag and Ag_2S were distinguished since Ag domain was brighter than Ag_2S domain (Fig. 4d–g). HRTEM studies showed that Ag nanoparticles had the random orientation on the Ag_2S nanoparticles (Fig. 6a–c). HRTEM showed clear lattice fringes of Ag and Ag_2S domains (Fig. 6a). Patterns of two-dimensional Fast Fourier Transformations were in agreement with PXRD pattern. Besides HD, the higher order association was also observed (trimers, tetramer, etc.; Figs. 4b, 6f). But morphological yield of the dimers was relatively higher than trimer, tetramer, etc.

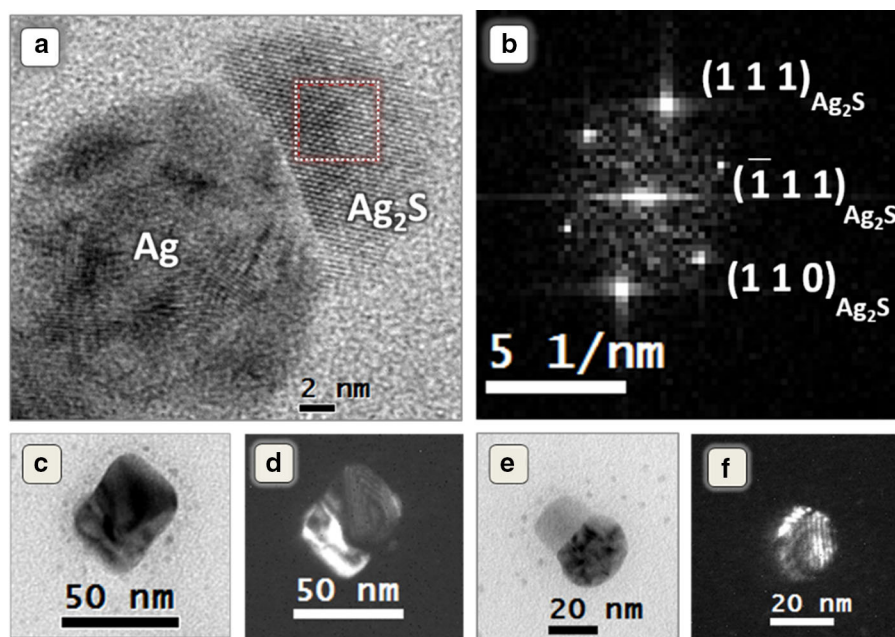
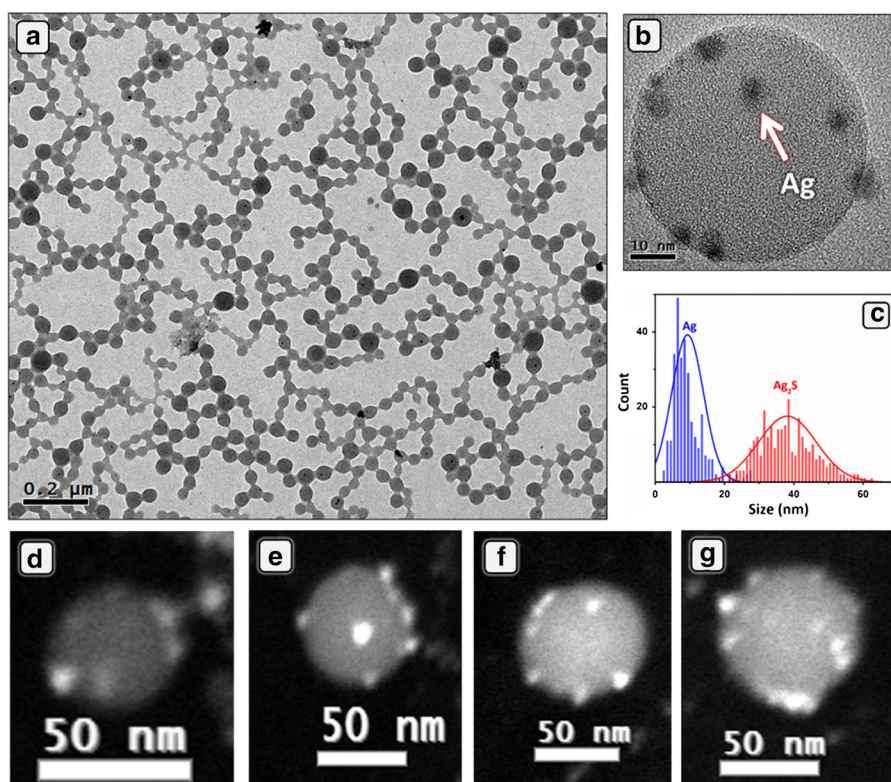


Fig. 3 **a** HRTEM images of an HD-I. Dotted square indicates the selected area for FFT. **b** Corresponding fast Fourier transformed micrograph of Ag_2S region. **c**, **e** TEM image of

the HD-I. **d**, **f** corresponding Dark Field images. Ag nanoparticles were brighter than Ag_2S nanoparticles

Fig. 4 **a** Low-magnification TEM image. **b** Magnified view of HD-II. Ag nanoparticles embedded on the Ag_2S nanoparticles. Arrow indicates Ag nanoparticles. **c** Particle distribution diagram. **d–g** Dark field images of HDs. Silver nanoparticles were brighter than Ag_2S nanoparticles



Why heterodimers formed?

The HMDS-assisted synthesis is known to proceed via the formation of S–N polymeric intermediate (Kumar and Muralidharan 2014). The formation of S–N intermediate and the absence of surfactants around the particles played a key role in the formation of the HDs. The intermediate was formed using available sulphur which in turn reacted with AgNO_3 yielding Ag_2S nanoparticles. Remaining AgNO_3 in the same reaction was reduced by HMDS to form Ag nanoparticles. Consequently, when the amount of S in the reaction was low, less amount intermediate was formed leaving more AgNO_3 to be reduced to Ag nanoparticles. This situation yielded Ag-rich HD-I. Similarly, when S was more in the reaction, more amount of intermediate was formed leading to the formation of higher quantity of Ag_2S leaving less amount AgNO_3 to be reduced to form Ag nanoparticles. This situation led to HD-II. Interestingly, since the HD formation was rapid, no other individual Ag or Ag_2S nanoparticles were observed. Thus, the co-formation of the Ag and Ag_2S nanoparticles in a single-pot favoured HDs formation.

Since the nanoparticles in HDs were not stabilised by capping agents, the surface energies of both nanoparticles were high. Therefore, surfaces of the Ag_2S nanoparticles would readily accessible to Ag nanoparticles. To minimise the surface energy, both Ag and Ag_2S nanoparticles associated and formed the HDs. If the interaction was specific, HD-I particles were formed (Fig. 5). Ag (2 0 0) and Ag_2S (0 2 2) constructed the HD-I (Fig. 5c, f). At the same time, if the interaction was non-specific, HD-II particles were formed (Fig. 6). Moreover, in the non-specific interaction, association of Ag and Ag_2S nanoparticles might be continued until the surface energy was low. Hence, the higher order associations (trimers, tetramer, etc.) were found (Fig. 6d–g). DFTEM also confirmed the multiple associations of Ag nanoparticles on the surfaces of the Ag_2S nanoparticles (Fig. 4d–g). The number of Ag particles on the surfaces of Ag_2S particles was not constant.

We have observed that the purified metal sulphide nanoparticles did not agglomerate even in the absence of capping agents, whereas it is a common phenomenon for metal nanoparticles. The agglomeration of metal nanoparticles is generally promoted by the

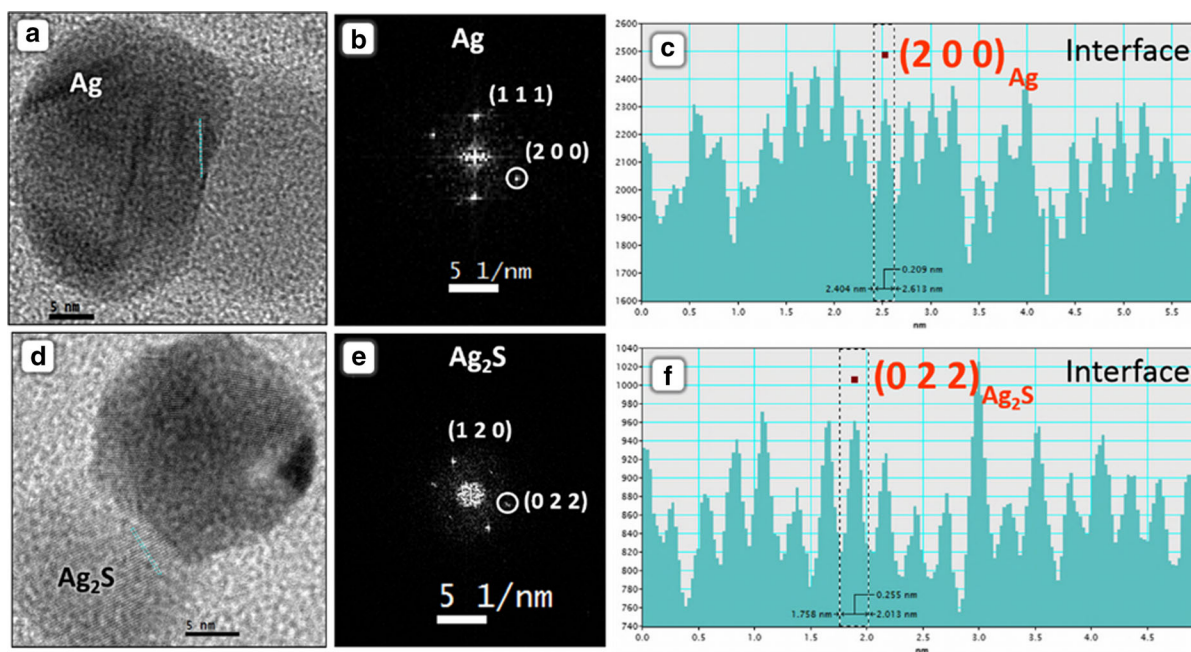
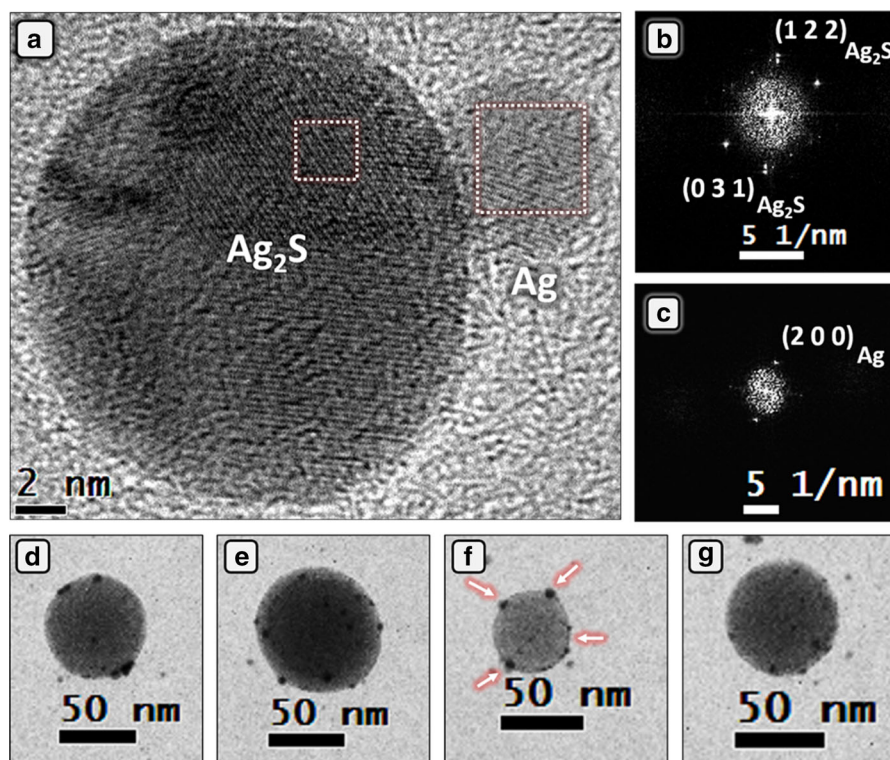


Fig. 5 a, d HRTEM image lattice planes of Ag and Ag_2S . b, e Corresponding two-dimensional FFT patterns of Ag and Ag_2S , respectively. c, f are lattice profiles at the interface

Fig. 6 **a** Representative HRTEM image of HD-II showing the embedded silver nanoparticles on the Ag_2S surface. Reversible imaging contrast was observed since HD particles were tilted while acquiring image. **b, c** Corresponding two-dimensional FFT of Ag_2S and Ag region. **d–g** TEM images showing higher order association of Ag and Ag_2S nanoparticles. Arrows indicate multiple associations



possibility of metallic bonds while Ostwald-ripening process is helping the growth of nucleus on the expenses of smaller particles for various metal sulphides and sulphates. In our intermediate-controlled reaction, Ag_2S was formed first but the particles growth continued with Ag particles available in excess. In this process, either HD-I (Ag rich) or HD-II (Ag less) particles were formed based on the availability of Ag during syntheses. Based on all observations, we proposed that HDs were formed by Ostwald-ripening directed association of Ag and Ag_2S particles (Mokari et al. 2005). These HD nanoparticles are rare examples of the particles having both metal and semiconductor domains which were obtained in a single-step synthesis. The preferential formation of HDs only at specific reaction stoichiometry and reason for association of nanoparticles to form HDs under particular reaction condition are not clear. However, it seems that the collective effect of reaction condition, reaction stoichiometry, and the surface energy of particles operate at various stages of the synthesis and finally superimpose to encourage the formation of HDs at particular magic ratios.

Optical properties: mixed electronic states of Ag and Ag_2S

The UV spectra of HDs were obtained to identify the electronic nature of interactions of planes which were responsible for HDs formation (Fig. 7). Since complete removal of capping agent resulted in poor solubility of nanoparticles, solid state UV spectra were preferred to comprehend the optical properties. Broad absorption of Ag_2S nanoparticles dominated the whole spectrum of both the HDs (Kryukov et al. 2004). Broad spectrum of Ag_2S nanoparticles also suggested that individual properties of nanoparticles were not compromised for the formation of HDs. Compared with HD-II, HD-I had an additional new peak at 321 nm. This peak is attributed to the combination of electronic states of metallic Ag and semiconductor Ag_2S nanoparticles (Casavola et al. 2008; Yang et al. 2006). Interfacial mixing of Ag (2 0 0) and Ag_2S (0 2 2) planes to the different degrees might modify the density of electronic states causing a broad peak. This observation evidenced interaction of metallic Ag and semiconducting Ag_2S nanoparticles

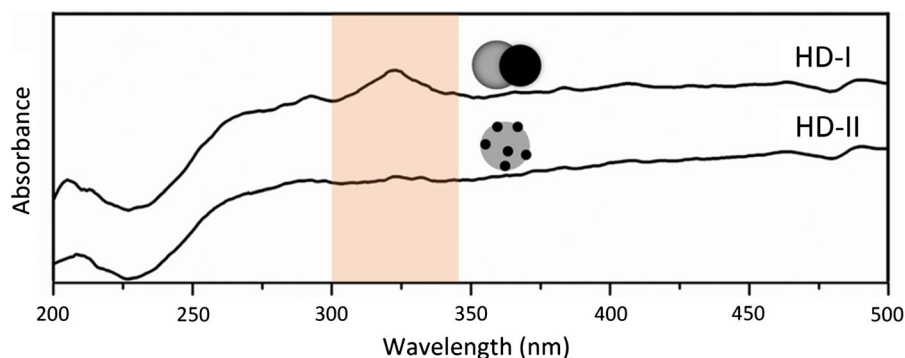


Fig. 7 Absorption spectra of HDs showing a characteristic peak at 321 nm for HD-I caused by the selective interaction of Ag (2 0 0) and Ag₂S (0 2 2) planes. The peak at 321 nm was absent in the spectrum of HD-II

in HD-I. At the same time, HDs had distinct electronic properties than constituent Ag and Ag₂S nanoparticles. In HD-II, Ag adsorption on Ag₂S was non-selective, and hence, the 321 nm peak was not observed. It is to be mentioned that we did not observe the surface Plasmon band corresponding to Ag nanoparticles. This observation may be attributed to the thin dampening Ag₂S layer on the surface of Ag nanoparticles (Link and El-Sayed 1999; Mulvaney 1996). Electronic spectra suggested selective interaction planes in HD-I and simple association Ag and Ag₂S nanoparticles in the HD-II by non-selective interaction between the Ag and Ag₂S planes. The non-selective interaction was responsible for the formation of higher order particles like trimers, tetramers, etc. along with HD-II.

Conclusion

We have demonstrated direct synthesis of HDs by HMDS-assisted method. The Ag/Ag₂S HDs were synthesised without any pre/post modifications. The reaction conditions were identified to produce HDs by conducting controlled experiments, and both HDs were quantitatively reproduced in those conditions. We have scaled-up HDs synthesis up to 2 g. The method resulted in near monodispersity and crystallinity of nanoparticles. It was clear from the controlled reactions that one-pot formation of Ag and Ag₂S nanoparticles induced the direct synthesis of HDs. Versatility of synthetic design is exemplified by the synthesis of two types of HDs. Noticeably, with one variable (stoichiometry of sulphur) in the reaction, we reliably controlled the HD compositions and tuned

the metal and semiconductor domains in HD particles. It was observed that the interface of HD-I was composed of Ag (2 0 0) and Ag₂S (0 2 2) planes which caused absorption at 321 nm. HD-II did not have any selective interaction at the interface but higher order associations occurred. The combination of heterostructure, organic-free surfaces and mixed electronic states is expected to make HDs functional and could be used as building blocks for future single molecular electronic devices.

Acknowledgments The work was supported by DST-SERB of India (Project No.: SB/S1/IC-47/2013). B. G. K. acknowledges DST-SERB for the postdoctoral fellowship. B. S. gratefully acknowledges University Grants Commission of India for fellowship. We thank Centre for Nanotechnology at University of Hyderabad for TEM facility.

References

- Casavola M, Buonsanti R, Caputo G, Cozzoli PD (2008) Colloidal strategies for preparing oxide-based hybrid nanocrystals. *Eur J Inorg Chem* 6:837
- Cozzoli PD, Pellegrino T, Manna L (2006) Synthesis, properties and perspectives of hybrid nanocrystal structures. *Chem Soc Rev* 35:1195
- Gu H, Zheng R, Zhang X, Xu B (2004) Facile one-pot synthesis of bifunctional heterodimers of nanoparticles: a conjugate of quantum dot and magnetic nanoparticles. *J Am Chem Soc* 126:5664
- Jiang BJ, Gu H, Shao H, Devlin E, Papaefthymiou GC, Ying JY (2008) Bifunctional Fe₃O₄-Ag heterodimer nanoparticles for two-photon fluorescence imaging and magnetic manipulation. *Adv Mater* 20:4403
- Jiang F, Tian Q, Tang M, Chen Z, Yang J, Hu J (2011) One-pot synthesis of large-scaled Janus Ag-Ag₂S nanoparticles and their photocatalytic properties. *Cryst Eng Commun* 13:7189

- Kryukov AI, Stroyuk AL, Zinchuk NN, Korzhak AV, Kuchmii SY (2004) Optical and catalytic properties of Ag_2S nanoparticles. *J Mol Catal A* 221:209
- Kudera S, Carbone L, Casula MF, Cingolani R, Falqui A, Snoeck E, Parak WJ, Manna L (2005) Selective growth of PbSe on one or both tips of colloidal semiconductor nanorods. *Nano Lett* 5:445
- Kumar BG, Muralidharan K (2011) Hexamethyldisilazane-assisted synthesis of indium sulphide nanoparticles. *J Mater Chem* 21:11271
- Kumar BG, Muralidharan K (2013) Organic-free self-assembled copper sulphide microflowers. *Eur J, Inorg Chem* **2102**
- Kumar BG, Muralidharan K (2014) S_4N_4 as an intermediate in Ag_2S nanoparticle synthesis. *RSC Adv* 4:28219
- Lee JS, Bodnarchuk MI, Shevchenko EV, Talapin DV (2010) “Magnet-in-the-Semiconductor” FePt-PbS and FePt-PbSe nanostructures: magnetic properties, charge transport, and magnetoresistance. *J Am Chem Soc* 132:6382
- Link S, El-Sayed MA (1999) Spectral properties and relaxation dynamics of surface plasmon electronic oscillations in gold and silver nanodots and nanorods. *J Phys Chem B* 103:8410
- Mokari T, Rothenberg E, Popov I, Costi R, Banin U (2004) Selective growth of metal tips onto semiconductor quantum rods and tetrapods. *Science* 304:1787
- Mokari T, Sztrum CG, Salant A, Rabani E, Banin U (2005) Formation of asymmetric one-sided metal-tipped semiconductor nanocrystal dots and rods. *Nat Mater* 4:855
- Mulvaney P (1996) Surface plasmon spectroscopy of nanosized metal particles. *Langmuir* 12:788
- Palmstrom CJ (1995) Epitaxy of dissimilar materials. *Annu Rev Mater Sci* 25:389–415
- Pang M, Hu J, Zeng HC (2010) Synthesis, morphological control, and antibacterial properties of hollow/solid $\text{Ag}_2\text{S}/\text{Ag}$ heterodimers. *J Am Chem Soc* 132:10771
- Ray M, Basu TS, Bandyopadhyay NR, Klie RF, Ghosh S, Raja SO, Dasgupta AK (2014) Highly lattice-mismatched semiconductor-metal hybrid nanostructures: gold nanoparticle encapsulated luminescent silicon quantum dots. *Nanoscale* 6:2201
- Talapin DV, Koeppe R, Gotzinger S, Kornowski A, Lupton JM, Rogach AL, Benson O, Feldmann J, Weller H (2003) Highly emissive colloidal CdSe/CdS heterostructures of mixed dimensionality. *Nano Lett* 3:1677
- Tang Q, Yoon SM, Yang HJ, Lee Y, Song HJ, Byon HR, Choi HC (2006) Selective degradation of chemical bonds: from single-source molecular precursors to metallic Ag and semiconducting Ag_2S nanocrystals via instant thermal activation. *Langmuir* 22:2802
- Xiong S, Xi B, Zhang K, Chen Y, Jiang J, Hu J, Zeng HC (2013) Ag nanoprisms with Ag_2S attachment. *Sci Rep* 3:2177
- Yang J, Ying JY (2009) Room-temperature synthesis of nanocrystalline Ag_2S and its nanocomposites with gold. *Chem Commun* 1:3187
- Yang J, Elim HI, Zhang Q, Lee JY, Ji W (2006) Rational Synthesis, Self-Assembly, and Optical Properties of $\text{PbS} - \text{Au}$ Heterogeneous Nanostructures Via Preferential Deposition. *J Am Chem Soc* 128:11921
- Yu H, Chen M, Rice PM, Wang SX, White RL, Sun S (2005) Dumbbell-like bifunctional $\text{Au-Fe}_3\text{O}_4$ nanoparticles. *Nano Lett* 5:379
- Zhang J, Tang Y, Lee K, Ouyang M (2010) Nonepitaxial growth of hybrid core-shell nanostructures with large lattice mismatches. *Science* 327:1634
- Zhu G, Xu Z (2011) Controllable growth of semiconductor heterostructures mediated by bifunctional Ag_2S nanocrystals as catalyst or source-host. *J Am Chem Soc* 133:148

Polymerization behaviour of butyl bis(hydroxymethyl)phosphine oxide: Phosphorus containing polyethers for Li-ion conductivity

HEERALAL VIGNESH BABU, BILLAKANTI SRINIVAS,
KHEVATH PRAVEEN KUMAR NAIK and KRISHNAMURTHI MURALIDHARAN*
School of Chemistry, University of Hyderabad, Gachibowli, Hyderabad 500 046, India
e-mail: kmsc@uohyd.ernet.in

MS received 30 October 2013; accepted 24 July 2014

Abstract. Synthesis of phosphorus containing polyethers and their lithium-ion conductivities for the potential use as solid polymer electrolyte (SPE) in high-energy density lithium-ion batteries have been described. Co-polymerization of butyl bis(hydroxymethyl)phosphine oxide with three different dibromo monomers were carried out to produce three novel phosphorous containing polyethers (**P1–P3**). These polymers were obtained via nucleophilic substitution reactions and were characterized by ^1H , ^{31}P NMR spectral data and gel permeation chromatography. SPEs were prepared using polyethers (**P1** and **P2**) with various amounts of lithium bis(trifluoromethanesulfonyl)imide (LiTFSI). The lithium-ion conductivity of **SPE2** containing 40 wt% of LiTFSI was $2.1 \times 10^{-5} \text{ S cm}^{-1}$ at room temperature and $3.7 \times 10^{-4} \text{ S cm}^{-1}$ at 80°C .

Keywords. Phosphorus; polyether; solid polymer electrolyte; lithium-ion conductivity.

1. Introduction

Demand for efficient energy storage devices has increased due to the requirements of higher energy storage capacity and portability.¹ Rechargeable lithium-ion batteries are the major power sources for portable electronics. At present, the performance of lithium-ion battery for miniature portable electronic devices is satisfactory. However, the current technology cannot be promoted to automobile batteries due to the potential fire hazard of organic liquid electrolyte present in batteries.² Moreover, organic liquid electrolytes suffer from volatility, pressure build-up or even explosion hazard, limited operating temperature range and harmful leakage. The fundamental solution to this problem is substitution of the flammable organic liquid electrolyte with non-flammable solid polymer electrolyte (SPE). Besides the safety considerations, other interesting properties such as flexibility, easy manipulation, wide operating temperature range, high electrochemical stability and light weight fabrication allows possibilities for advanced lithium-ion polymer secondary batteries. In addition, both ion conduction and mechanical separation can be attained in a single solid electrolyte membrane. Furthermore, a battery can be fabricated in any desired shape and size due to the flexibility of polymer membranes.³ Therefore, a better SPE with flame

retardant property for high-energy density lithium-ion batteries is always in demand to replace the organic liquid electrolyte.

Wright and co-workers revealed the ability of poly(ethylene oxide) (PEO) to dissolve inorganic salts and exhibiting ion conduction at room temperature.⁴ But, the room temperature ionic conductivity of PEO based polymer electrolyte is too low ($10^{-7} \text{ S cm}^{-1}$) for practicable applications. Our interest is to prepare SPEs having good ionic conductivity with flame retardant property. So, it is necessary to understand the conduction mechanism in order to improve the ionic conductivity of SPEs. The ionic conductivity in amorphous polymers depends on local segmental motions of polymer chains and such a favourable situation was obtained only at temperatures above T_g .⁵ Hence, an amorphous, solid polymer with low glass transition temperature is preferred for ionic conductivity.

Our aim is to induce conformational flexibilities by incorporating phosphorus in the form of C-P-C bonds in the chain. Integration of heteroatoms into the carbon-carbon polymer chain can be an intriguing strategy to tailor the properties to expand the applications of materials. However, incorporation of heavier main-group element in the polymer backbone is synthetically challenging. We have used bis(hydroxymethyl)phosphine oxides as monomer in a co-polymerization reaction to lead to polyethers. Herein, we report the polymerization behaviour of butyl bis(hydroxymethyl)phosphine oxide

*For correspondence

and the influence of phosphorus containing polyethers on ionic conductivity.

2. Experimental

2.1 Materials and instruments

All manipulations involving air and moisture sensitive compounds were carried out using standard Schlenk techniques under the atmosphere of dry nitrogen. All solvents to be used under inert atmosphere were thoroughly deoxygenated using freeze-pump-thaw method before use. They were dried and purified by refluxing over a suitable drying agent followed by distillation under nitrogen atmosphere. The compounds, tris(hydroxymethyl)phosphine (**S1**),⁶ 1,4-bis(bromomethyl)-2,3,5,6-tetramethylbenzene⁷ (**M3**), 1,4-bis(bromomethyl)-2,3,5,6-tetramethoxybenzene⁸ (**M4**) were synthesized according to the literature procedures. The compounds, tetrakis(hydroxymethyl)phosphonium chloride (Acros); 1,5-dibromo-pentane (**M5**), 1-iodobutane and lithium bis(trifluoromethanesulfonyl)imide $\text{LiN}(\text{SO}_2\text{CF}_3)_2$ (LiTFSI) were purchased from Aldrich and were used as received without purification. K_2CO_3 (Merck) was dried at 100°C for 6 h under vacuum prior to use.

Structures of all the products were confirmed by ^1H , ^{31}P and ^{13}C NMR spectra. All the NMR spectra were recorded on a Bruker Avance 400 MHz FT NMR spectrometer at room temperature using either CDCl_3 or CD_3OD as solvent. The chemical shifts are reported in parts per million (δ) relative to tetramethylsilane as reference for ^1H and $^{13}\text{C}\{^1\text{H}\}$ NMR (100 MHz). The $^{31}\text{P}\{^1\text{H}\}$ NMR (162 MHz) spectra referenced to 85% H_3PO_4 . The Netzsch STA 409 PC model was used for thermogravimetric and differential thermal analysis (TG-DTA) to examine the thermal stability. The decomposition behaviour of polymers was studied from 30 to 900°C under the nitrogen flow with a heating rate of 10°C/min. The temperature of 5% weight loss was chosen as onset point of decomposition (T_d). The glass transition temperatures (T_g) of polyethers were measured on a Differential Scanning Calorimeter (DSC) from PerkinElmer (Pyris Diamond DSC 8000). The measurements were performed at a heating rate of 10°C/min under the nitrogen. T_g was assigned as the inflection point in the thermogram. The molecular weights of the polymers were determined by Gel Permeation Chromatography (GPC) of Shimadzu 10AVP model equipped with refractive index (RI) detector. The separation was achieved using a Phenogel mixed bed column (300 × 7.80 mm) operated at 30°C with a flow rate of 0.5 mL/min. using tetrahydrofuran (THF) as

the eluent. The molecular weight and molecular weight distributions were calculated using polystyrene as a standard.

The impedance measurements of polymer electrolytes were performed in Zahner zennium electrochemical work station with built-in Thales software for data acquisition. The measurements were done in the frequency range of 1 Hz to 4 MHz. The specimens in the form of pellets were sandwiched between two gold plated electrodes housed in a homemade cell. For variable temperature measurements, cell was equilibrated at each temperature for 30 min. before measuring. The conductivity was calculated using the equation $\sigma = d/(\text{AR}_b)$, where d is the thickness of the polymer electrolyte disc, A is the surface area of the pellet and R_b is the bulk resistance value which can be obtained from the Nyquist plot.⁹

2.2 Experimental procedure

2.2a Synthesis of butyl bis(hydroxymethyl)phosphine oxide (M1): The synthesis of **M1** was achieved in three steps as follows: A solution of tris(hydroxymethyl)phosphine (**S1**) (12.60 g, 0.1 mol) in methanol (20 mL) was taken into a 500 mL two-necked flask under nitrogen. To this, deoxygenated mixture of 1-iodobutane (37.43 g, 0.2 mol) and methanol (140 mL) was added dropwise at 0°C for 30 min. The reaction mixture was refluxed for 4 h and the solvent was evaporated under high vacuum to get a viscous oily product. Purification of this product was unsuccessful because it was non-volatile oily liquid.

To the above mixture (25.38 g), dry triethylamine (190 mL) was added in one portion under nitrogen with stirring. The resulting mixture was then heated to 60°C for 1 h and then allowed to cool to room temperature. The solid $[\text{NHEt}_3]\text{Cl}$ byproduct was filtered off and triethylamine solvent was distilled out at atmospheric pressure to give a crude product which was then heated to 90°C for 5 h under reduced pressure. A viscous oily product was obtained.

To the above oily product (10.88 g) in methanol (25 mL), 30% hydrogen peroxide solution (8.3 mL, 72 mmol) was added dropwise at 15°C and stirred for 2 h. The solution was concentrated under vacuum which was purified by column chromatography on silica gel eluting with $\text{CH}_2\text{Cl}_2/\text{MeOH}$ (6:1) to give a clear colourless liquid butyl bis(hydroxy methyl)phosphine oxide (**M1**). (TLC was analyzed by immersing the plate in 5% sulfuric acid in methanol followed by heating using hot-air drier for 2 min. and spots were visualized by naked eye) Yield: 5.40 g, 45%. ^1H NMR (CD_3OD): δ 4.86 (s, 2H, $-\text{OH}$), 3.97 (dd, $J = 26.5, 14.1$ Hz, 4H,

–OCH₂P), 1.91–1.79 (m, 2H, –PCH₂CH₂), 1.71–1.56 (m, 2H, –CH₂CH₂CH₃), 1.53–1.41 (m, 2H, –CH₂CH₃), 0.96 (t, $J = 7.3$ Hz, 3H, –CH₃). ¹³C NMR (CD₃OD): δ 58.45 (d, $J = 79$ Hz, –PCH₂O), 26.39 (d, $J = 13$ Hz, –CH₂), 24.98 (d, $J = 4$ Hz, –CH₂), 24.13 (d, $J = 62$ Hz, –CH₂), 15.07 (s, –CH₃). ³¹P NMR (CD₃OD): δ 51.54. EI-MS: m/z 333 (2M⁺+1, base peak). Anal. calcd for C₆H₁₅O₃P: C, 43.37; H, 9.10. Found: C, 43.28; H, 9.25. Further continuation of elution yielded tris(hydroxymethyl)phosphine oxide (**M2**). Yield: 1.50 g, 12%. ¹H NMR (CD₃OD): δ 4.11 (s, 6H, –CH₂), 2.55 (s, –OH). ¹³C NMR (CD₃OD): δ 57.14 (d, $J = 76$ Hz, –CH₂). ³¹P NMR (CD₃OD): δ 46.00.

2.2b General procedure for the copolymerization of M1 with M3–M5: A typical polymerization procedure is as follows. The mixture of BuP(O)(CH₂OH)₂ (**M1**) (3 mmol), corresponding co-monomer (**M3**, **M4** or **M5**) (3.3 mmol) and K₂CO₃ (7.2 mmol) in N, N-dimethylacetamide (2.5 mL) was taken in a 100 mL round-bottom flask equipped with a Dean-Stark trap. To this, toluene (20 mL) was added as an azeotrope. The reaction mixture was heated to 130°C for 5 h in order to remove water that formed during the reaction. Then, the reaction mixture was heated to 160°C and maintained for 30 h. The viscous reaction mixture was poured into ethanol and filtered off. The product was purified by dissolving in THF and reprecipitating in hexane. This process was repeated for three more times to obtain pure polymers.

Polymer 1 (P1) (Copolymer of M1 and M3): After purification, **P1** was obtained as a white colour powder. Yield: 83%. ¹H NMR (CDCl₃): δ 4.81–4.62 (m, 4H, OCH₂Ph), 3.98–3.82 (m, 4H, PCH₂O), 2.45–2.18 (m, 12H, –CH₃), 1.79–1.65 (m, 2H, –PCH₂), 1.63–1.50 (m, 2H, –CH₂), 1.48–1.31 (m, 2H, –CH₂CH₃), 0.88 (t, 3H, –CH₃). ³¹P NMR (CDCl₃): δ 44.15.

Polymer 2 (P2) (Copolymer of M1 and M4): After purification, **P2** was obtained as a white color powder. Yield: 80%. ¹H NMR (CDCl₃): δ 4.77–4.56 (m, 4H, OCH₂Ph), 4.32–3.91 (m, 4H, PCH₂O), 3.90–3.68 (m, 12H, –OCH₃), 1.93–1.78 (m, 2H, –PCH₂), 1.66–1.51 (m, 2H, –CH₂), 1.48–1.35 (m, 2H, –CH₂CH₃), 0.88 (t, 3H, –CH₃). ³¹P NMR (CDCl₃): δ 45.75.

Polymer 3 (P3) (Copolymer of M1 and M5): After purification, **P3** was obtained as a colorless liquid. Yield: 82%. ¹H NMR (CDCl₃): δ 3.95–3.68 (m, 4H, OCH₂P), 3.57–3.38 (m, 4H, –CH₂O), 1.86–1.69 (m,

2H, –PCH₂), 1.67–1.50 (m, 6H, –CH₂), 1.48–1.24 (m, 4H, –CH₂), 0.87 (t, 3H, –CH₃). ³¹P NMR (CDCl₃): δ 44.92.

2.2c General preparation of solid polymer electrolytes SPE1 and SPE2: The polymers **P1** and **P2** were dried at 60°C and 40°C under vacuum for 8 h. LiN(SO₂CF₃)₂ was dried at 150°C under vacuum for 10 h before use. All manipulations were carried out in an MBraun glove box filled with ultrapure nitrogen gas. Electrolytes with different ratio were prepared as follows: the polymer was dissolved in THF with lithium salt and stir for 12 h at 25°C. After this, THF was evaporated under vacuum and dried the residue at 60°C for 12 h. The residue was loaded in to a die and then pressed to make a pellet. Specimens of 0.07–0.08 cm thickness and 0.9 cm diameter were obtained for conductivity studies. These pellets were sandwiched between two gold plated electrodes housed in a home-made cell for conductivity studies. The consistency of results was checked by repeating the experiment three times.

3. Results and Discussion

The following methods are generally used to achieve flame retardant property for polymers: (a) blending polymers with phosphorus containing molecules; (b) covalently attaching phosphorus containing molecules as pendant group to the polymer chains; (c) phosphorus containing polymers in which phosphorus present in main chain of polymer.¹⁰ We are interested to synthesize polyethers having phosphorus in main chain of polymer. It is known that the hydroxymethyl groups of alkyl bis(hydroxymethyl)phosphine RP(CH₂OH)₂ behaved like masked –PH₂ group. But it behaves as a normal diol when the phosphine was converted to phosphine oxide RP(O)(CH₂OH)₂.¹¹ A variety of natural and synthetic polymers where phosphorus is in main chain with O-P-O linkages are known. However, polymers with C-P-C linkages are challenging for synthesis. Therefore, use of alkyl substituted bis(hydroxymethyl) phosphine oxide as monomer to produce polyether is attractive methodology to obtain polymers with C-P-C links.

3.1 Synthesis of monomer (M1)

While tris(hydroxymethyl)phosphine (**S1**) was treated with 1-iodobutane in methanol, followed by the addition of triethylamine and hydrogen peroxide yielded **M1** as a major product and **M2** as a minor product

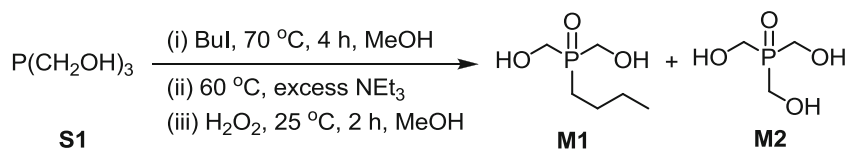
(scheme 1). These compounds were separated by column chromatography. The compound $P(CH_2OH)_3$ **S1** was known to release formaldehyde (HCHO) when heated. The HCHO thus formed in turn reacted with unreacted $P(CH_2OH)_3$ similar to well-known Wittig reaction forming **M2**. This is also a reason for low yield of **M1**. The structures of **M1** and **M2** were confirmed by 1H , ^{13}C and ^{31}P NMR spectral data.

3.2 Synthesis of polyethers (**P1–P3**)

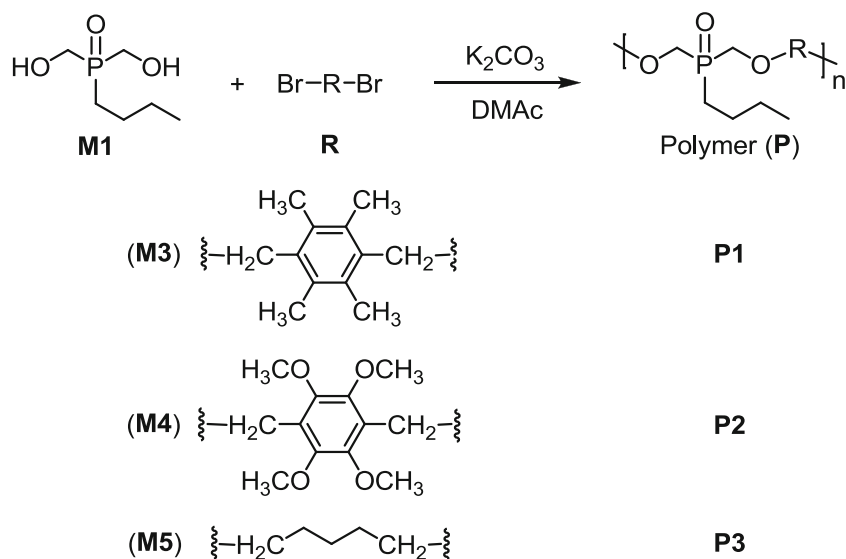
1,4-bis(bromomethyl)-2,3,5,6-tetramethylbenzene (**M3**) and 1,4-bis(bromomethyl)-2,3,5,6-tetramethoxybenzene (**M4**) were synthesized from durene and 2,5-dihydroxy-1,4-benzoquinone respectively according to the literature procedures.^{7,8} The butyl bis(hydroxy methyl)phosphine oxide **M1** was copolymerized with different dibromo monomers such as **M3**, **M4** and 1,5-dibromopentane **M5** to obtain polyethers **P1–P3** respectively via

nucleophilic substitution reactions (scheme 2). The condensation polymers were synthesized in the presence of K_2CO_3 as base in N, N-dimethylacetamide (DMAc). The polymerization procedure was carried out in two stages. First, toluene was added to the reaction mixture and azeotropic distillation was continued until water that formed during the reaction was removed from the reaction mixture.¹² In the later stage, temperature was increased to 160°C and polymerization was progressed for required time. All the crude polymers were purified by reprecipitation from THF in hexane.

The polyethers **P1** and **P2** are solids while **P3** is liquid and they are readily soluble in chloroform, THF and dimethyl sulfoxide. The polyethers **P1–P3** were characterized by 1H and ^{31}P NMR spectral data which showed that the data were consistent with the expected molecular structure. The $^{31}P\{^1H\}$ NMR spectra of polymers **P1–P3** showed a single peak and appeared at δ 44.15, 45.75 and 44.92 ppm respectively. The decomposition



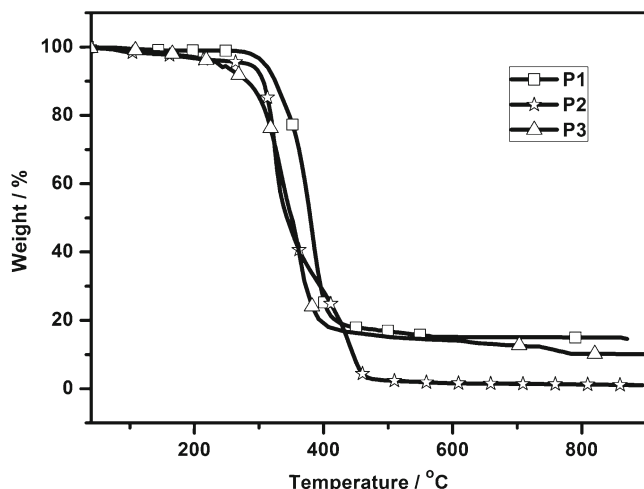
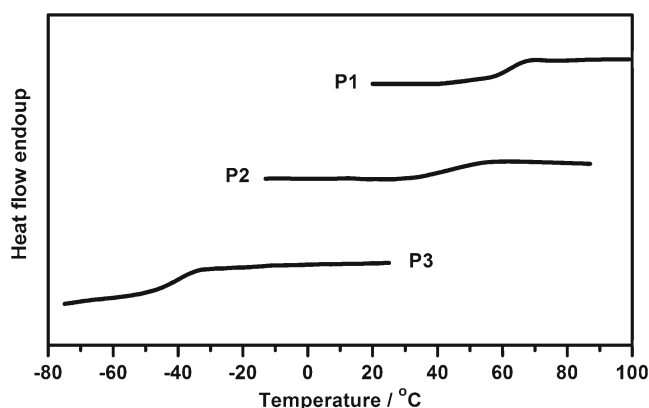
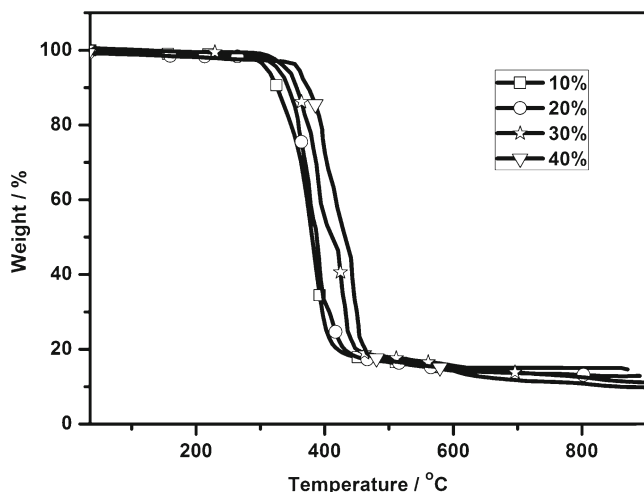
Scheme 1. Synthesis of butyl bis(hydroxymethyl)phosphine oxide (**M1**).



Scheme 2. Synthesis of phosphorus containing polyethers **P1–P3**.

Table 1. Properties of polyethers **P1–P3**.

Entry	Co-monomer	Polymer (P)	T_d (°C)	T_g (°C)	M_n (g mol ⁻¹)	M_w (g mol ⁻¹)	PDI
1	M3	P1	308.2	65.1	9414	15156	1.61
2	M4	P2	279.9	43.4	8420	14230	1.69
3	M5	P3	240.7	-40.5	10077	16425	1.63

Figure 1. TGA plots of polyethers **P1–P3**.Figure 2. DSC plots of polyethers **P1–P3**.Figure 3. TGA plots of **SPE1 (10–40%)**.

temperature (T_d), glass-transition temperature (T_g), molecular weight (M_n and M_w) and PDI of polyethers **P1–P3** are listed in table 1. The copolymers **P1–P3** have molecular weight (M_w) in the range of 14.2–16.4 kg mol⁻¹. Thermogravimetric analyses (figure 1) revealed the thermal stability of polymers **P1–P3** lies in the range of 240–308°C. The polymers **P1–P3** are completely amorphous and they did not show any peak corresponds to melting temperature (T_m) on DSC analyses (figure 2).

3.3 Solid polymer electrolyte (SPE)

P1 and **P2** were utilized to prepare **SPE1** and **SPE2** using various amounts of lithium bis(trifluoromethanesulfonyl)imide (LiTFSI) (10, 20, 30 and 40 wt%). The liquid polymer **P3** was not used to make an electrolyte. The polymers and lithium salt was dissolved in THF at 25°C and maintained for 12 h. THF was evaporated and dried under vacuum to obtain SPEs. Compared to **P1** and **P2**, thermal stability of **SPE1** and **SPE2** was increased with increasing lithium salt content from 10 wt% of LiTFSI (**10%**) to 40 wt% of LiTFSI (**40%**) (figure 3 and S1; table 1 and 2). Likewise, T_g of **SPE1** and **SPE2** increased continuously with the addition of lithium salt from 10% to 40% (figure 4 and S2; table 1 and 2). The rise in T_d and T_g compared to their corresponding polymer might be due to the effective coordination of polymer chains with lithium-ion. Based on the following observations from DSC analyses: (a) absence of peaks matching the melting temperature (T_m) of lithium salt; (b) a single T_g ; (c) increase in T_g with the addition of lithium salt; it was concluded, LiTFSI is completely miscible in **P1** and **P2** that affords a homogeneous amorphous phase and did not exist as aggregates. The absence of melting point of salts is attributable to the solvation of lithium-ions by coordination of polymer.

The conductivities of **SPE1** with 10–40 wt% of LiTFSI [**SPE1(10–40%)**] and **SPE2** with 10–40 wt% LiTFSI [**SPE2(10–40%)**] were calculated from the bulk resistance determined from complex impedance spectra.¹³ The ionic conductivities at 30°C and 80°C of **SPE1(10–40%)** and **SPE2(10–40%)** are listed in table 2. Figure 5 shows the temperature dependent

Table 2. Properties of **SPE1 (10–40%)** and **SPE2 (10–40%)**.

SPEs (wt% of LiTFSI)	SPE1		T _d (°C)	T _g (°C)	SPE2		T _d (°C)	T _g (°C)
	Conductivity σ (S cm ⁻¹)				Conductivity σ (S cm ⁻¹)			
	30°C	80°C			30°C	80°C		
SPE (10%)	5.1×10^{-7}	5.6×10^{-6}	324.1	78.9	3.2×10^{-6}	2.3×10^{-5}	290.2	52.4
SPE (20%)	6.5×10^{-7}	8.3×10^{-6}	332.5	86.7	6.5×10^{-6}	8.8×10^{-5}	298.1	65.3
SPE (30%)	9.5×10^{-7}	4.4×10^{-5}	341.6	102.4	1.2×10^{-5}	1.4×10^{-4}	310.5	70.6
SPE (40%)	2.6×10^{-6}	7.3×10^{-5}	355.8	116.2	2.1×10^{-5}	3.7×10^{-4}	321.7	78.1

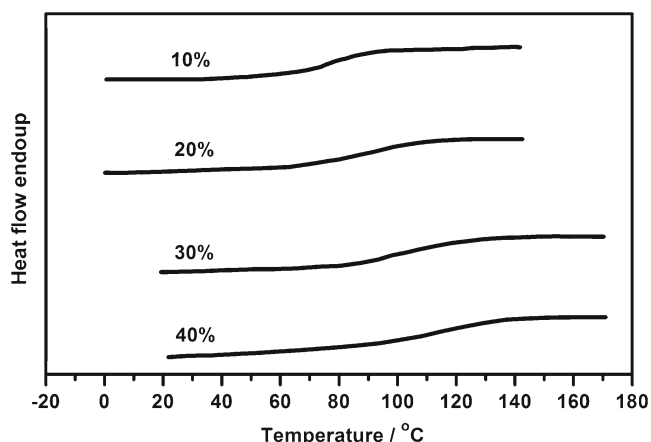


Figure 4. DSC plots of SPE1 (10–40%).

nyquist plots of SPE1 (10–40%) and Arrhenius plots of SPE1 (10–40%) and SPE2 (10–40%). While increasing the lithium salt content progressively from 10% to 40%, the ionic conductivity of SPE1 and SPE2 increased. Further, ionic conductivity of SPE1 (10–40%) and SPE2 (10–40%) were increasing with temperature. The room temperature ionic conductivity of SPE1 (10–40%) and SPE2 (10–40%) lies in the range of $5.1 \times 10^{-7} - 2.1 \times 10^{-5} \text{ S cm}^{-1}$. The maximum conductivity of $3.7 \times 10^{-4} \text{ S cm}^{-1}$ was attained for SPE2 (40%) at 80°C. Among SPE1 and SPE2, SPE2 exhibited better ionic conductivity with various amounts of lithium salt and with temperature. The presence of more

coordinating group (-OMe) in P2 as well as low T_g of P2 compared to P1 makes a better host polymer for lithium-ion conductivity.

4. Conclusions

In conclusion, we have described the synthesis of phosphorus containing polyethers wherein phosphorus exists in the main chain of polymer with C-P-C links. The utilization of alkyl substituted bis(hydroxyl-methyl)phosphine oxide as monomer for polymer synthesis was studied. The completely amorphous, highly stable and flame retardant polymers (P1–P3) were obtained by condensation polymerization. The solid polymer electrolytes SPE1 and SPE2 were prepared and their ionic conductivity behaviour was examined. The SPE2 (40%), prepared from P2, showed the highest conductivity of $3.7 \times 10^{-4} \text{ S cm}^{-1}$ at 80°C. SPE2 may be a promising SPE having good ionic conductivity with possible flame retardant property that would find potential application in larger batteries.

Supplementary Information

TGA, DSC and nyquist plots of SPE2, ^1H , ^{13}C and ^{31}P NMR of M1 and M2, ^1H and ^{31}P NMR of P1–P3 are available at www.ias.ac.in/chemsci.

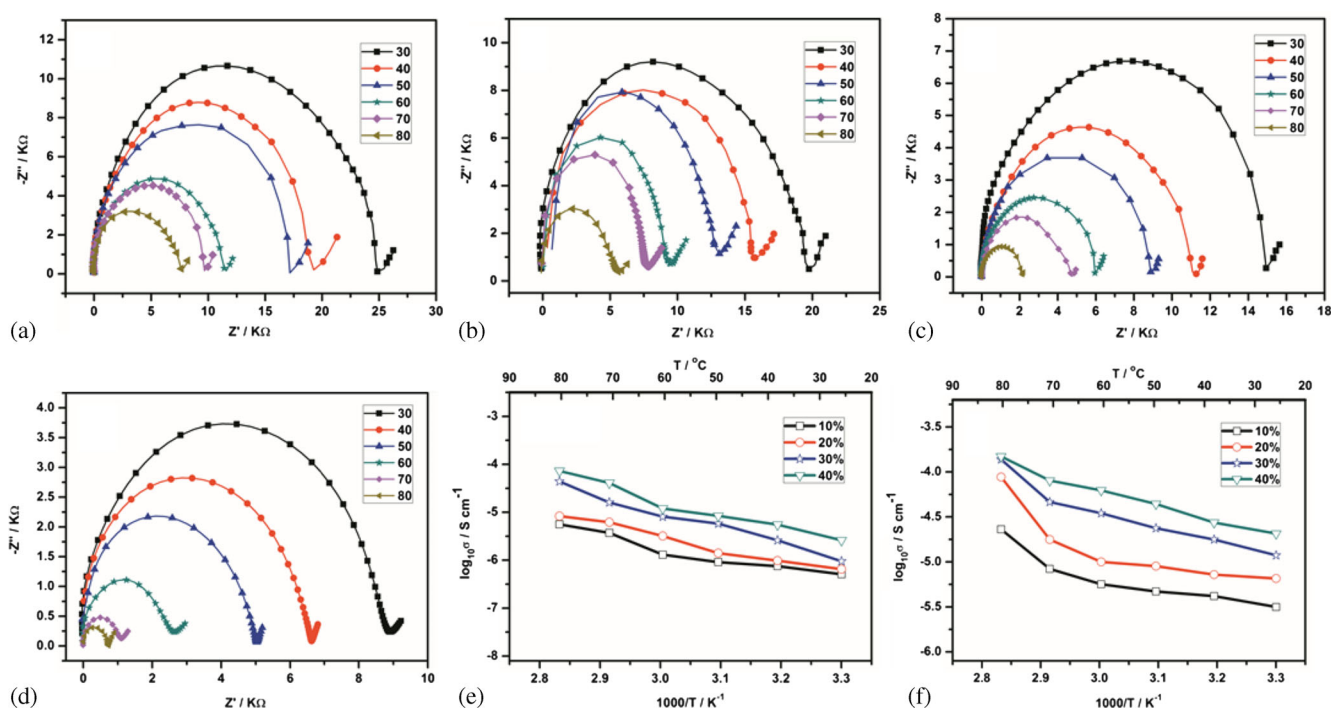


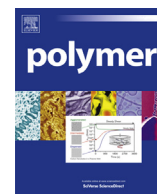
Figure 5. Temperature dependent nyquist plots of SPE1 (a) 10% (b) 20% (c) 30% (d) 40%. Arrhenius plots of temperature dependent conductivities of e) SPE1 (10–40%) f) SPE2 (10–40%).

Acknowledgements

HVB is thankful to CSIR India for a fellowship. The authors acknowledge the DST, India for financial support of the DST fast track project No. SR/FTP/CS-60/2007.

References

1. Bruce P G, Freunberger S A, Hardwick L J and Tarascon J-M 2012 *Nature Mater.* **11** 19
2. (a) Thielen J, Meyer W H and Landfester K 2011 *Chem. Mater.* **23** 2120; (b) Bruce P G, Scrosati B and Tarascon J-M 2008 *Angew. Chem. Int. Ed.* **47** 2930; (c) Arico A S, Bruce P G, Scrosati B, Tarascon J-M and Schalkwijk W V 2005 *Nature Mater.* **4** 366
3. Chandrasekhar V, Krishnan V, Athimoolam A and Nagendran S 2000 *Curr. Sci.* **78** 464
4. (a) Fenton D E, Parker J M and Wright P V 1973 *Polymer* **14** 589; (b) Wright P V 1975 *Br. Polym. J.* **7** 319; (c) Wright P V 1976 *J. Polym. Sci. Polym. Phys. Ed.* **14** 955
5. (a) Stoeva Z, Litas I M, Staunton E, Andeev Y G and Bruce P G 2003 *J. Am. Chem. Soc.* **125** 4619; (b) Bruce P G, Campbell S A, Lightfoot P and Mehta M A 1995 *Solid State Ionics* **78** 191
6. Ellis J W, Harrison K N, Hoyer P A T, Orpen A G, Pringle P G and Smith M B 1992 *Inorg. Chem.* **31** 3026
7. Behera G and Ramakrishnan S 2004 *J. Polym. Sci. Part A: Polym. Chem.* **42** 102
8. (a) Wessig P and Mollnitz K 2008 *J. Org. Chem.* **73** 4452; (b) Mlochowski L S J and Klock 1983 *Tetrahedron* **39** 781
9. (a) Kumar J, Rodrigues S J and Kumar B 2010 *J. Power Sources* **195** 327; (b) Lee K-H, Park J-K and Kim W-J 2000 *Electrochim. Acta* **45** 1301; (c) Morales E and Acosta J L 1999 *Electrochim. Acta* **45** 1049
10. (a) Peckham T J, Massey J A, Honeyman C H and Manners I 1999 *Macromolecules* **32** 2830; (b) Allcock H R 2003 In *Chemistry and applications of polyphosphazenes* (Hoboken: Wiley Interscience); (c) Chandrasekhar V 2005 In *Inorganic and Organometallic Polymers* (Heidelberg: Springer); (d) Sato M, Tada Y and Yokoyama M 1980 *Eur. Polym. J.* **16** 671; (e) Vlad-Bubulac T and Hamciuc C 2009 *Polymer* **50** 2220; (f) Bourbigot S and Duquesne S 2007 *J. Mater. Chem.* **17** 2283; (g) Lu S Y and Hamerton I 2002 *Prog. Polym. Sci.* **27** 1661
11. (a) Muralidharan K, Reddy N D and Elias A J 2000 *Inorg. Chem.* **39** 3988; (b) Ramakrishna T V V and Elias A J 2001 *J. Organomet. Chem.* **637** 382; (c) Reddy N D, Elias A J and Vij A 2000 *Inorg. Chem. Commun.* **3** 29
12. Chen X-T, Sun H, Tang X-D and Wang C-Y 2008 *J. Appl. Polym. Sci.* **110** 1304
13. (a) Abraham K M, Jiang Z and Carroll B 1997 *Chem. Mater.* **9** 1978; (b) Yoshida K, Nakamura M, Kazue Y, Tachikawa N, Tsuzuki S, Seki S, Dokko K and Watanabe M 2011 *J. Am. Chem. Soc.* **133** 13121; (c) Britz J, Meyer W H and Wegner G 2007 *Macromolecules* **40** 7558



Design of polymers with an intrinsic disordered framework for Li-ion conducting solid polymer electrolytes



Heeralal Vignesh Babu, Billakanti Srinivas, Krishnamurthi Muralidharan*

School of Chemistry, University of Hyderabad, Hyderabad 500 046, India

ARTICLE INFO

Article history:

Received 9 May 2015

Received in revised form

28 July 2015

Accepted 3 August 2015

Available online 6 August 2015

Keywords:

For Li-ion conducting

Solid polymer electrolytes

ABSTRACT

Polymers with phosphorus in the main chain with intrinsic disordered framework for lithium-ion conductivity were synthesized. Conductivity of one of the solid polymer electrolytes prepared from those polymers with 40 wt% of LiTFSI was $8.9 \times 10^{-4} \text{ S cm}^{-1}$ at 30°C and $5.3 \times 10^{-3} \text{ S cm}^{-1}$ at 80°C . The impressive conductivity is explained by the availability of high conduction pathways provided by frozen chain disorder.

© 2015 Published by Elsevier Ltd.

1. Introduction

Advanced materials and molecules for energy harvesting and storage devices are in demand to improve their performance and efficiency. Case in point, the Li-ion batteries are fast developing as replacement to lead-acid batteries to run automobiles [1]. However, some of its disadvantages – such as high cost and more weight of the Li-ion batteries – and the imperatives to increase its energy density and working temperature necessitate further evolution of new electrode materials and polymer electrolyte systems [2]. Further, there is a need for a thorough understanding of the conduction mechanism to focus on improving ionic conductivities of solid polymer electrolytes [3].

According to the conventional theory, amorphous polymers exhibit ionic conductivity whereas crystalline polymers most likely behave as insulator. The ionic conductivity in amorphous polymer is due to the movement of ions, ensued by the local segmental motion of the polymer chain particularly above its glass transition temperature (T_g). Above T_g , the superstructure of polymers has disordered and flexible environment. Since the polymer chains are in constant motion above its T_g , a vacant space would continually create and disappear, through which an ion move by coordination. It means an ion has to wait to find a new coordination site and a free volume for hopping. This clearly describes that the rate of ion transport depends on local chain dynamics of polymer [4]. Our interest is creating a

fixed perpetual free space through which the ion can move without delay. It would improve the mobility of ion leading to higher ionic conductivity. For that, we have chosen to synthesize materials with a needed structural framework for better lithium ion transport [5].

Many efforts are directed toward synthesizing polymers for lithium ion transport without sacrificing their properties. One such approach is constructing a perfect polymer framework through a crystalline arrangement of polymer chains by either metal organic framework (MOFs) or covalent organic framework (COFs). MOFs and COFs are well known for applications in gas storage, catalysis and molecular separation [6]; but synthesizing the material by MOF and COF approach for lithium ion transport without sacrificing their desired properties is challenging. Alternatively, an amorphous covalent organic framework can be achieved in hyper-cross linked polymers or intrinsic porous polymers. Herein, we report the synthesis of soluble polymers with intrinsic disordered framework supportive of Li-ion conductivity.

2. Experimental section

2.1. Materials and instrumentation

All manipulations involving air and moisture sensitive compounds were carried out using standard Schlenk techniques under dry nitrogen. All solvents to be used under inert atmosphere were thoroughly deoxygenated using freeze–pump–thaw method before use. They were dried and purified by refluxing over a suitable drying agent followed by distillation under nitrogen. The following drying agents were used: sodium benzophenoneketyl

* Corresponding author.

E-mail address: kmsc@uohyd.ernet.in (K. Muralidharan).

(hexane, toluene, tetrahydrofuran), P_2O_5 (triethylamine), $Mg(OMe)_2$ (methanol). The compounds, ferrocenylmethyl bis(hydroxymethyl)phosphine sulfide [7] (**M1**), benzyl bis(hydroxymethyl)phosphine sulfide [8] (**M2**) and 1,4-bis(bromomethyl)-2,3,5,6-tetramethylbenzene [9] (**M3**) were synthesized according to the literature procedures. The compound lithium bis(trifluoromethanesulfonyl)imide, $LiN(SO_2CF_3)_2$ purchased from Acros was used as received without purification.

Structures of all monomers and polymers were confirmed by 1H and ^{31}P NMR spectroscopy. All the NMR spectra were recorded on a Bruker Avance 400 MHz FT NMR spectrometer at room temperature. Chemical shifts were reported in parts per million (δ) relative to tetramethylsilane as reference for 1H and ^{13}C NMR. The ^{31}P (162 MHz) spectra were referred to 85% H_3PO_4 . The Netzsch STA 409 PC model was used for thermogravimetric and differential thermal analysis (TG–DTA) to examine the thermal stability. The decomposition behaviour of polymers was studied from 30 °C to 900 °C under the nitrogen flow with a heating rate of 10 °C/min. The temperature of 5% weight loss was chosen as onset point of decomposition (T_d). A Differential Scanning Calorimeter (DSC) from PerkinElmer (Pyris Diamond DSC 8000) was used to find the glass transition temperature (T_g). Measurements were performed at a heating rate of 10 °C/min from 25 °C to 240 °C in case of polymers and 25 °C–280 °C in case of solid polymer electrolytes (**SPEs**). Mass spectra was obtained using Shimadzu–LCMS–2010 instrument operating at an ionizing voltage of 70 eV using EI technique. Molecular weights of the polymers were determined by using Gel Permeation Chromatography (GPC) of Shimadzu 10AVP model equipped with refractive index (RI) detector. The separation was achieved using a Phenogel mixed bed column (300 × 7.80 mm) operated at 30 °C with a flow rate of 0.5 mL/min using tetrahydrofuran (THF) as the eluent and polystyrene as the standard.

2.2. General procedure for the synthesis of polymers P1–P4

To a solution of RP(S) (CH_2OH)₂ (7.7 mmol) and 1,4-bis(bromomethyl)-2,3,5,6-tetramethylbenzene (2.46 g, 7.7 mmol) in N,N-dimethylacetamide (DMAc) (30 mL), 60% sodium hydride (0.77 g, 19.3 mmol) was added at 0 °C under nitrogen. The mixture was then allowed to warm to 25 °C within 1 h. After 40 h stirring at required temperature, the reaction mixture was poured into hydrochloric acid (3% v/v, 500 mL) to precipitate the polymer as powder. The product was purified by washing with methanol for 24 h using soxhlet apparatus to yield pure polymer.

Polymer 1 (**P1**): Yield 81%. 1H NMR (400 MHz, $CDCl_3$): δ 4.82–4.61 (m, 4H, OCH_2Ph), 4.30–4.03 (m, 9H, Fc), 3.96–3.77 (m, 4H, PCH_2O), 3.28–2.94 (m, 2H, $FcCH_2$), 2.47–2.07 (bs, 12H, CH_3). ^{31}P { 1H } NMR (162 MHz, $CDCl_3$): δ 45.44.

Polymer 2 (**P2**): Yield 72%. 1H NMR (400 MHz, $CDCl_3$): δ 7.67–7.27 (m, 5H, C_6H_5), 4.67–4.36 (m, 4H, OCH_2Ph), 4.18–3.68 (m, 4H, PCH_2O), 3.56–3.32 (m, 2H, $PhCH_2$), 2.47–1.96 (bs, 12H, CH_3). ^{31}P { 1H } NMR (162 MHz, $CDCl_3$): δ 47.94.

Polymer 3 (**P3**): Yield 78%. 1H NMR (400 MHz, $CDCl_3$): δ 4.83–4.56 (m, 4H, OCH_2Ph), 4.34–4.00 (m, 9H, Fc), 3.97–3.69 (m, 4H, PCH_2O), 3.23–2.86 (m, 2H, $FcCH_2$), 2.46–2.05 (bs, 12H, CH_3). ^{31}P { 1H } NMR (162 MHz, $CDCl_3$): δ 44.98 (m), 41.03 (m).

Polymer 4 (**P4**): Yield 75%. 1H NMR (400 MHz, $CDCl_3$): δ 7.76–7.35 (m, 5H, C_6H_5), 4.92–4.49 (m, 4H, OCH_2Ph), 4.03–3.53 (m, 4H, PCH_2O), 3.41–3.00 (m, 2H, $PhCH_2$), 2.42–1.99 (bs, 12H, CH_3). ^{31}P { 1H } NMR (162 MHz, $CDCl_3$): δ 46.19 (m), 42.84 (m).

2.3. Model reaction

To a solution of **M2** (0.20 g, 1 mmol) and benzyl bromide (0.34 g, 2 mmol) in DMAc (2.4 mL) was added sodium hydride (0.05 g,

2 mmol) at 0 °C under nitrogen. The mixture was then allowed to warm to 25 °C within 1 h. After 3 h stirring, methanol (1 mL) was added and the reaction mixture was poured in to water (25 mL). The reaction mixture was extracted with chloroform (20 mL × 3). The organic layer was washed with water (20 mL × 2). Solvent was evaporated to give the crude product, which was purified by column chromatography on silica gel eluting with hexane/ethyl acetate (9: 1). Yield 79%. 1H NMR (400 MHz, $CDCl_3$): δ 7.42–7.32 (m, 10H, C_6H_5), 7.30–7.26 (m, 5H, C_6H_5), 4.65 (dd, J = 21.4 Hz, J = 11.8 Hz, 4H, OCH_2Ph), 3.95–3.84 (m, 4H, OCH_2P), 3.38 (d, J = 13.8 Hz, 2H, PCH_2Ph). ^{13}C { 1H } NMR (100 MHz, $CDCl_3$): δ 136.7, 130.2, 130.1, 128.9, 128.5, 128.4, 128.3, 128.2, 128.1, 127.3, 75.5 (d, J = 10.3 Hz), 67.3 (d, J = 63.9 Hz), 33.5 (d, J = 44.2 Hz). ^{31}P { 1H } NMR (162 MHz, $CDCl_3$): δ 43.50. EI–MS: m/z 397 (M^+ + 1).

2.4. Preparation of solid polymer electrolytes SPE1–SPE4

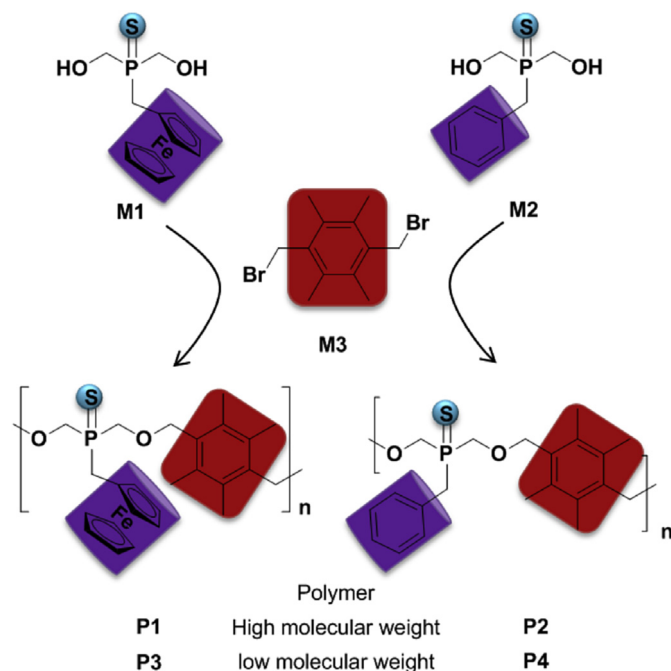
All manipulations were carried out in MBraun glove box filled with ultrapure nitrogen gas. The polymers (**P1–P4**) were dried at 90 °C under vacuum for 8 h. $LiN(SO_2CF_3)_2$ was dried at 150 °C under vacuum for 10 h before making **SPEs**. Initially, the films were made by dissolving the polymers and $LiN(SO_2CF_3)_2$ in a mixture of solvents THF/ $CHCl_3$ at room temperature. However, films of **SPEs** were brittle. Therefore, it was difficult to cut into a proper shape for conductivity studies. Hence, the **SPEs** in the form of pellets were prepared for impedance measurements.

The solid electrolytes with different ratio were prepared as follows. The polymer and lithium salt was ground together inside the glove box and then sealed. Then the flask containing the mixture was tied with a mechanical stirrer rotating at a constant speed (blending) for 24 h. The process was repeated for three times (Total 72 h). The homogeneities of the blended **SPEs** were confirmed as follows: After blending the polymer with lithium salt, samples were taken from the four different regions and their glass transition temperature (T_g) was examined. The T_g of all the samples were matching well with each other. In both cases, the solids were loaded in to a die and then pressed (5 ton) to make pellets of 0.07–0.08 cm thickness and 0.9 cm diameter were obtained for conductivity studies. The **SPE** pellets were sandwiched between two gold plated electrodes housed in a homemade cell.

2.5. Impedance measurements of polymer electrolytes

The impedance measurements and electrochemical stability studies of polymers and **SPEs** were performed in Zahner–Zennium electrochemical workstation with built-in Thales software for data acquisition. The measurements were done in the frequency range of 1 Hz–4 MHz. The measurement cell was constructed in such a way that it can hold specimen (pellet) tightly in order to achieve good interfacial contacts between the electrodes and electrolyte. The measurement cell was sealed completely to avoid contaminations. It was further upheld from the measurements using with different pellets of **SPE1**, which showed the same pattern of results and bulk resistance (R_b).

The conductivities were calculated [10] according to the equation $\sigma = d/(AR_b)$, where d is the thickness of the polymer electrolyte disc, 'A' is the surface area of the pellet and R_b is the bulk resistance value which can be calculated from the intercept of the curve with real axis. Further, an equivalent circuit model was obtained from the computerised least square parameters fitting. Then, the experimental bulk resistance (R_b) was compared with the bulk resistance (R_b) obtained from equivalent circuit model. The consistency of results was checked by repeating three times. The conductivity of blended **SPEs** and **SPEs** derived from evaporation method were in good agreement. For variable temperature



Scheme 1. Synthesis of polymers **P1–P4**. Reaction condition: NaH, DMAc, 60 °C (**P1** and **P2**), 25 °C (**P3** and **P4**).

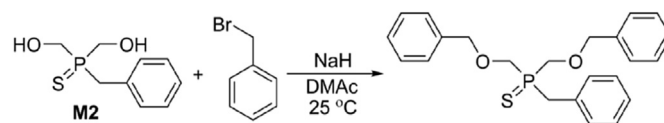
measurements, cell was equilibrated at each temperature for 30 min before the measurements.

The electrochemical stability of **SPEs** at room temperature was determined using SS|electrolyte|SS cell configuration (SS: gold plated stainless steel electrode) over a wide voltage range (–1 to 8 V) at a scan rate of 5 mV s^{–1}. The samples were sandwiched between gold plated stainless steel electrodes. The third cycle data were used for analysis.

3. Results and discussion

3.1. Synthesis of polyether having phosphorus in main chain

Polyphosphazenes [11a] and polysiloxanes [11b], were good hosts for lithium ion conductivity, accordingly they were reported to have maximum conductivity of 5 × 10^{–5} S cm^{–1} and 4.5 × 10^{–4} S cm^{–1}, respectively. However, their jelly nature hindered the practical use. Polycarbonates [12] were another interesting lithium ion conducting solid polymer host. But they showed a conductivity of 1.5 × 10^{–6} S cm^{–1} which were very low for practicable applications. Alternatively, introduction of phosphorus–carbon bonds, in lieu of carbon–carbon bonds in a polymer chain, could provide disordered arrangement due to an inefficient packing of polymer chains [13,14]. This may lead to interesting physical and chemical properties such as amorphous nature, flame retardant and stability at high temperatures to the polymers [15]. In order to synthesize phosphorus containing polymers; various phosphorus containing monomers are employed. Perhaps, use of



Scheme 2. Synthetic scheme for the model reaction confirming the nucleophilic substitution in the presence of NaH.

substituted bis(hydroxymethyl) phosphine sulfides [16] (Scheme 1) could be an interesting choice to introduce phosphorus–carbon bonds in the main chain of a polymer.

Based on the functional groups present in the monomers (**M1–2** and **M3**), condensation polymerization method was preferred to synthesize the copolymers (Scheme 1). Further, in view of understanding the influence of molecular weight on the ionic conductivities of polymers, we desired to synthesize same polymers of varying molecular weights. The monomers **M1** or **M2** was copolymerized with **M3** (1:1 ratio) in the presence of NaH as a base in dimethylacetamide (DMAc) to yield polymers **P1–P4** (Table 1). The condensation polymers **P1** and **P2** were prepared successfully via nucleophilic substitution reaction at 60 °C whereas the low molecular weight polymers **P3** and **P4** were synthesized at 25 °C. Further increase in reaction temperature led to the formation of insoluble polymers. The crude polymers were purified by washing with methanol in a Soxhlet extractor for 24 h. These reactions yielded novel polyethers wherein the phosphorus atoms are in main chain of the polymers. To confirm the possibility of such nucleophilic substitution reactions, we have carried out a model reaction wherein the monomer **M2** was reacted with benzyl bromide and corresponding product was isolated and characterized (Scheme 2).

All these polymers were solids and readily soluble in chloroform and dimethyl sulfoxide. The ³¹P{¹H} NMR spectra of polymers (**P1**: 45.4 and **P2**: 47.9 ppm) showed a single peak whereas polymers **P3** and **P4** showed two peaks appearing at 41.03, 44.96 ppm (Fig. S10) and at 42.84, 46.18 (Fig. S11) respectively. The difference in ³¹P NMR spectra of high and low molecular weight polymers was due to the chain length. When the length of the polymer chain was small, then the terminal groups were distinguishable from inner groups. Comparing with the chemical shifts of monomers (**M1**: 47.2 ppm and **M2**: 49.2 ppm), the first set of peaks were assigned to the core internal phosphorus atoms of the polymers while the second set of peaks for the terminal group phosphorus atoms of the polymers [17]. The copolymers **P1** and **P2** possess relatively higher molecular weight (*M_w*) than **P3** and **P4** (Table 1).

Thermogravimetric analyses on polymers revealed the thermal stability up to 250 °C (Table 1, Fig. S1). Comparison of **P1** vs. **P3** and **P2** vs. **P4** showed that both *T_d* and *T_g* increased with increasing in chain length (Table 1). The absence of melting temperature (*T_m*) in DSC curves confirmed that the polymers (**P1–P4**) were completely amorphous even with low molecular weight polymers **P3** and **P4** (Fig. S2). The amorphous nature of these polymers further revealed the presence of highly disordered and thereby inefficient packing of polymer chains.

3.2. Solid polymer electrolytes and Li-ion conductivities

Solid polymer electrolytes (**SPE1–SPE4**) were prepared by blending the polymers (**P1–P4**) with lithium bis(trifluoromethanesulfonyl)imide (LiTFSI) in suitable ratios and lithium ion conductivities were determined. The polymers (**P1–P4**) were dried at 90 °C under vacuum for 8 h. LiN(SO₂CF₃)₂ was dried at 150 °C under vacuum for 10 h before making **SPEs**. Absence of reaction solvent and moisture in the dried polymer was confirmed from ¹H-NMR

Table 1
Properties of polymers **P1–P4**.

M	T (°C) ^a	P	T _d (°C)	T _g (°C)	M _n (kg mol ^{–1})	M _w (kg mol ^{–1})	PDI
M1	60	P1	288.1	137.0	6.8	11.9	1.74
M2	60	P2	354.4	143.4	9.6	14.6	1.52
M1	25	P3	276.2	130.1	1.8	2.8	1.56
M2	25	P4	250.3	112.3	2.1	4.3	2.03

^a Temperature at which the polymerization was carried out.

Table 2Properties of **SPE1–SPE4 (10%–40%)** and their room temperature conductivity.

Conductivity of polymer at room temperature σ (S cm ⁻¹)	P1			P2			P3			P4		
	6.3×10^{-12}			8.1×10^{-12}			3.7×10^{-11}			2.2×10^{-11}		
SPEs (wt% of LiTFSI)	SPE1			SPE2			SPE3			SPE4		
	O:Li	Conductivity σ (S cm ⁻¹)	T_g (°C)	O:Li	Conductivity σ (S cm ⁻¹)	T_g (°C)	Conductivity σ (S cm ⁻¹)	T_g (°C)	Conductivity σ (S cm ⁻¹)	T_g (°C)	Conductivity σ (S cm ⁻¹)	T_g (°C)
SPE (10%)	5.4:1	2.1×10^{-6}	148.7	6.9:1	8.7×10^{-7}	156.4	2.0×10^{-5}	184.3	7.7×10^{-7}	148.9		
SPE (20%)	2.4:1	4.2×10^{-6}	179.3	3.1:1	1.1×10^{-6}	166.5	2.9×10^{-5}	207.8	1.1×10^{-6}	154.5		
SPE (30%)	1.4:1	1.6×10^{-5}	189.1	1.8:1	1.8×10^{-6}	171.0	7.4×10^{-5}	226.4	2.8×10^{-5}	206.6		
SPE (40%)	1.0:1	4.5×10^{-4}	204.8	1.2:1	8.9×10^{-4}	192.8	1.4×10^{-4}	236.1	7.7×10^{-5}	209.6		

spectra of polymers. Electrolytes of varying weight ratio were prepared by the efficient grinding of polymer with lithium salt followed by blending. **SPE1–SPE4** were characterized by using IR, TGA and DSC. The stacked IR spectra of **P1** and **SPE1** with 10–40 wt % of LiTFSI [**SPE1 (10%–40%)**] is shown in Fig. S3. IR absorption peak for C–O–C group of **P1** appeared at 1088 cm⁻¹, but the absorption peak for C–O–C group of **SPE1** was shifted to lower frequency (1053 cm⁻¹). The intensity of peak at 1053 cm⁻¹ increased with the increasing wt% of lithium salt. The shift in frequency supported the interaction of C–O–C group with lithium ion [18]. Further, there was no absorption in the spectra matching water confirming the absence of trapped moisture in the **SPEs**.

The TGA analyses (Fig. S4) revealed that thermal stabilities of **SPE1** and **SPE2** remained the same compared with their respective

polymers (**P1** and **P2**); while that of **SPE3** and **SPE4** were increased to 300 °C and 370 °C respectively compared to **P3** and **P4**. The glass transition temperatures (T_g) of **SPEs (10%–40%)** obtained from DSC are shown in Table 2. The absence of melting temperature (T_m) peak of **SPEs** in DSC clearly indicated, after blending with polymers, the LiTFSI did not exist in the form of aggregates (Fig. S5). **SPEs** with 40 wt% of LiTFSI [**SPEs (40%)**] also did not show the peak for T_m , which implied the effective solvation by polymers even with higher wt% of lithium salt. For higher concentration of lithium salts, T_g of **SPEs** was not obvious from DSC graphs even after varying the scanning rates and with more amounts of samples (Fig. S5). The increase in T_g of **SPEs** comparing with respective polymers and difficulty in measuring T_g of **SPEs** with higher salt concentration can be attributed to the effective coordination of oxygen atoms in

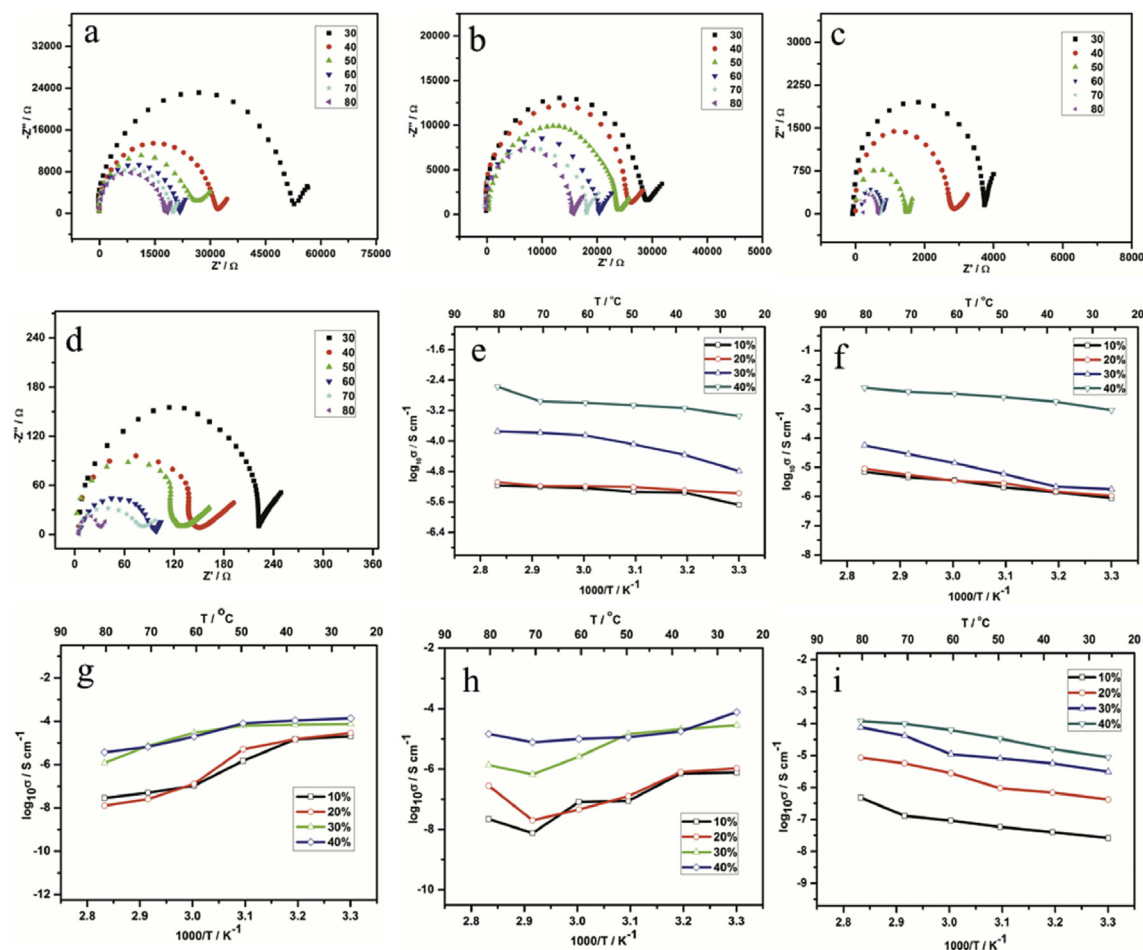


Fig. 1. Temperature dependent Nyquist plots of **SPE1** a) 10% b) 20% c) 30% d) 40%. Arrhenius plots of temperature dependent conductivities of e) **SPE1** f) **SPE2** g) **SPE3** h) **SPE4** i) **SPE4** 2nd heating.

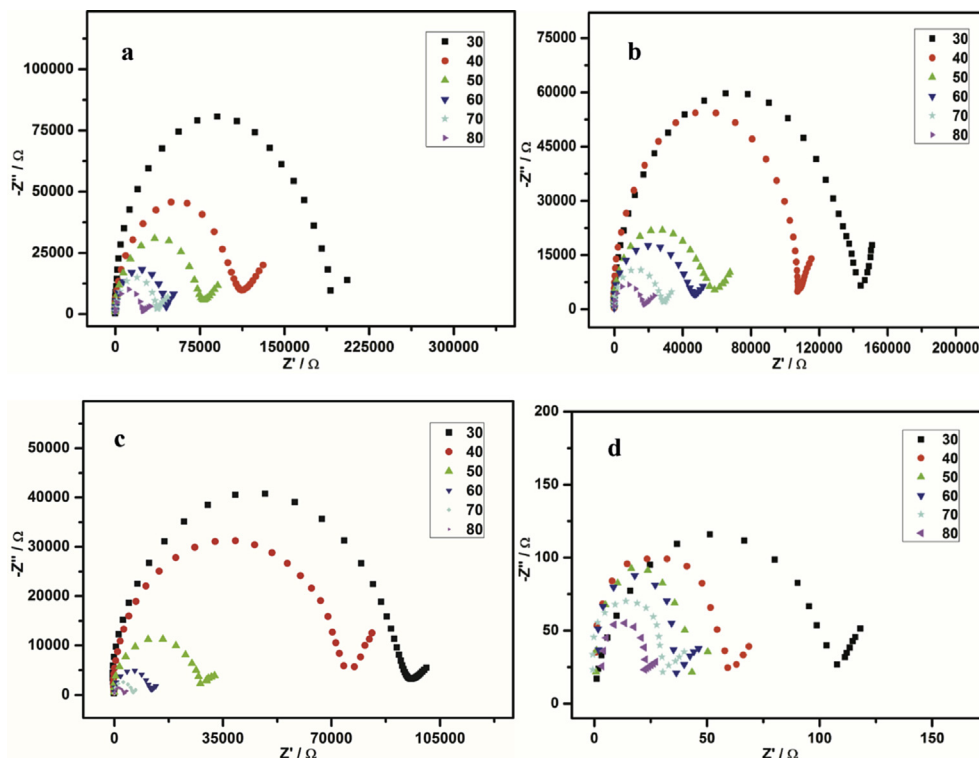


Fig. 2. Temperature dependent Nyquist plots of SPE2 a) 10% b) 20% c) 30% d) 40%.

Table 3
Conductivities of SPE1 (40%)–SPE4 (40%) at increasing temperature.

T (°C)	Conductivity σ (S cm ⁻¹) with 40 wt% of LiTFSI			
	SPE1	SPE2	SPE3	SPE4
30	4.5×10^{-4}	8.9×10^{-4}	1.4×10^{-4}	7.7×10^{-5}
40	7.3×10^{-4}	1.8×10^{-3}	1.1×10^{-4}	1.8×10^{-5}
50	8.7×10^{-4}	2.5×10^{-3}	7.9×10^{-5}	1.1×10^{-5}
60	1.0×10^{-3}	3.3×10^{-3}	2.0×10^{-5}	1.0×10^{-5}
70	1.1×10^{-3}	3.9×10^{-3}	6.6×10^{-6}	7.7×10^{-6}
80	2.7×10^{-3}	5.3×10^{-3}	3.7×10^{-6}	1.5×10^{-5}

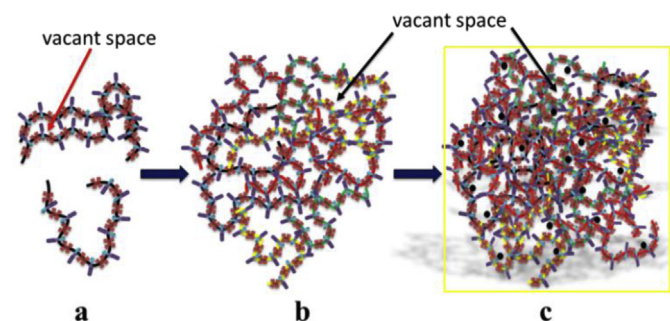


Fig. 3. Schematic representation of a) a fragment of building block polymer chain P1 or P2 b) If the building block grows in 2D c) If the building block grows in 3D (SPE) (Black dots represent lithium-ion).

the polymer chains with lithium ions. With higher salt contents, coordination of polymer with lithium ions could have restricted the stretching and segmental motion of polymer chains. The electrochemical stabilities of SPEs were evaluated (Fig. S7) using SS|electrolyte|SS cell configuration, which showed the anodic limiting potential of SPE1 and SPE2 as 4.8 V and 5.3 V respectively [19].

The conductivities of pure polymers alone were in the region of 10^{-11} S cm⁻¹– 10^{-12} S cm⁻¹ indicating that there was no protonic or electronic conductance. Table 2 depicts the conductivities of SPEs at 30 °C. Among all combinations studied, around room temperature, the SPE2 (40%) exhibited the highest conductivity of 8.9×10^{-4} S cm⁻¹. The Nyquist and Arrhenius plots of temperature dependent conductivities of various SPEs are shown in Figs. 1 and 2. In addition, the conductivities of SPE1 (40%) – SPE4 (40%) at increasing temperature are listed in Table 3. It is evident from Arrhenius plots that when the temperature was increased the conductivities of SPE1 (10%–40%) and SPE2 (10%–40%) were also increasing. The maximum conductivity of 5.3×10^{-3} S cm⁻¹ was attained for SPE2 (40%) at 80 °C. The conductivity of SPE2 (40%) reached the value of 10^{-3} S cm⁻¹ within 40 °C. Conductivities of SPEs were very high compared with their individual polymers. Clear semicircle Nyquist plots suggested that the total conductivity was mainly due to Li⁺ ions only; if some other impurities contributed to the measured conductivity, the plots could have been complicated. The conductivities of SPEs stored in inert conditions for more than six months showed no considerable change. To the best of our knowledge, this is the highest conductivity achieved so far in all solid-state polymer electrolytes reported in literature [13,14,18,20,21]. It is worth mentioning here is that the highest conductivity was achieved in its pure form without any extra additives added to it.

3.3. Reason for high Li-ion conductivity

Generally, amorphous polymers support ion conductivity at a temperature above their T_g. In a normal solid polymer electrolyte (SPE), there were no conductivity observed below T_g. However, our polymers showed good conductivities even at temperatures less than their T_g, nevertheless the properties were much more resembling glassy electrolyte having brittle nature with high T_g.

This observation demanded an alternative explanation [22] to the one based on T_g alone. Angell and coworkers [23] proposed polymer-in-salt electrolytes systems and explained the enhanced conductivity in various Li-polymer electrolytes [24]. Polymer-in-salt systems were characterized by a high salt concentration with much less polymer concentration. This condition lead to a softening of highly associated amorphous salt domains of LiTFSI and similar salts which was the source of enhanced ionic conductivity. However, the polymer concentration was more in our solid electrolytes than the Li-ion concentration. Therefore, the observed high conductivities is explained proposing an inherent disorder in the system as follows.

The polymers **P1–P4** were produced using flexible monomers (**M1** and **M2**) having bulky rigid pendant groups and a steric rigid co-monomer (**M3**). Repetitive combination of flexible monomers and steric rigid co-monomers could yield unsymmetrical shape to polymer chains. Further, the steric control of bulky rigid pendant groups *i.e.* ferrocenylmethyl (**P1** and **P3**) or benzyl (**P2** and **P4**), as well as a rigid tetramethylbenzene unit (**M3**) could restrict the polymer chains coming closer and prevent tight folding of polymer chains within or between them. Additionally, the rigid bulky groups could also restrict the rotational freedom of polymer backbone. All these circumstances collectively resulting disordered arrangement and inefficient packing of polymer chains. Fig. 3 schematically explains the formation of free space by polymer chains. When polymer chains with restricted segmental motion are packing, a space would create (Fig. 3a). As several polymer chains are arranged, it can form perpetual interconnected vacant space (Fig. 3b and c). The interconnected perpetual free volume would introduce intrinsic fixed conduction pathway inside the polymer matrix (Fig. 3c). However, at the highest salt concentrations, the ratio Li:O is near 1:1 and thus a classical solution by formation of lithium complexes with 3–4 donor atoms is uncertain. Therefore, though the intrinsic fixed conduction pathway inside the polymer matrix seems helping the seamless mobility of Li ions, in order to confirm the mechanism of high conductivity, one needs more evidence [13].

To understand the ion conductivity further, we have measured temperature dependent conductivities of all SPEs (Table 3). Normally, local segmental motion of polymer chains increases with increasing temperature leading to increase in conductivity. As expected, conductivities of **SPE1** (10%–40%) and **SPE2** (10%–40%) increased with increasing temperature. Similar results were obtained in second and third cycle heating of **SPE1** and **SPE2**. Though these temperature dependent conductivities of SPEs did not strictly follow either Arrhenius or VTF behaviours [25], the order of magnitude of the measured conductivities at 30 °C is attracting.

In contrast, the conductivity of **SPE3** (10%–40%) and **SPE4** (10%–40%) decreased with increase in temperature (Table 3 and Fig. 1g and h). It suggested a secondary influence on ionic conduction due to a non-stable polymeric network. It can be explained as follows; since the polymer chain lengths of **P3** and **P4** were smaller, it was possible that the polymer chains can stretch and unfold easily with increasing temperature and begin to rearrange in such a way destroying the framework. Since the intrinsic fixed free space were disconnected, which was the responsible for effortless mobility, resulting chaotic conductivities at higher temperatures. Nevertheless, the polymers **P1** and **P2** presumably retain their framework even at higher temperatures because of longer chain lengths. With **SPE4** (40%), the conductivity started increasing after 70 °C and attained the value of $1.5 \times 10^{-5} \text{ S cm}^{-1}$ at 80 °C (Fig. 1h). After the measurements at 80 °C, the **SPE4** (10%–40%) sample was allowed to cool to room temperature and the measurements were repeated from 30 to 80 °C. It was found that the conductivities of **SPE4** (10%–40%) increased with increasing temperature (Fig. 1i) probably because of the mechanism described elsewhere [25].

4. Conclusions

In conclusion, other than poly(ethylene oxide), only few polymers like polycarbonates [12] were shown as a potential candidate for lithium-ion polymer electrolytes; however, their ionic conductivities were too low at room temperature. The synthesized phosphorus containing polymers **P1–P4** were highly stable polymers, solids at room temperature and completely amorphous in nature. The **SPE2** (40%) showed the highest conductivity of $8.9 \times 10^{-4} \text{ S cm}^{-1}$ at 30 °C, which demonstrated the significance of structural arrangement of polymer framework. The impressive conductivities may be explained by the intrinsic fixed free space could be generated by the inefficient packing of polymer chains while assemblage. The working voltage range of SPEs was in the range from 0 V to 5.3 V, which was substantially high for the Li-ion batteries concern. Apart from these, presence of phosphorus in these polymers would bring flame-retardant property to SPEs [26].

Acknowledgement

The authors acknowledge the DST, India for financial support of the DST fast track project No. SR/FTP/CS-60/2007. HVB is thankful to CSIR India for fellowship. The authors also thank Centre for Nanotechnology (TEM), Central Instruments Laboratory (SEM) and School of Physics (FE-SEM) at University of Hyderabad.

Appendix A. Supplementary data

Supplementary data related to this article can be found at <http://dx.doi.org/10.1016/j.polymer.2015.08.004>.

References

- [1] J. Thielen, W.H. Meyer, K. Landfester, *Chem. Mater.* 23 (2011) 2120–2129.
- [2] (a) P.G. Bruce, B. Scrosati, J.M. Tarascon, *Angew. Chem. Int. Ed.* 47 (2008) 2930–2946;
(b) A.S. Arico, P.G. Bruce, B. Scrosati, J.M. Tarascon, W.V. Schalkwijk, *Nat. Mater.* 4 (2005) 366–377.
- [3] (a) P.V. Wright, Y. Zheng, D. Bhatt, T. Richardson, G. Ungar, *Polym. Int.* 47 (1998) 34–42;
(b) P.V. Wright, *Electrochim. Acta* 43 (1998) 1137–1143;
(c) F.B. Dias, S.V. Batty, J.P. Voss, G. Ungar, P.V. Wright, *Solid State Ion.* 85 (1996) 43–49.
- [4] (a) Z. Stoeva, I.M. Litas, E. Staunton, Y.G. Andeev, P.G. Bruce, *J. Am. Chem. Soc.* 125 (2003) 4619–4626;
(b) P.G. Bruce, S.A. Campbell, P. Lightfoot, M.A. Mehta, *Solid State Ion.* 78 (1995) 191–198.
- [5] (a) W. Li, D. Zhao, *Chem. Commun.* 49 (2013) 943–946;
(b) M.E. Davis, *Nature* 417 (2002) 813–821;
(c) A. Corma, *Chem. Rev.* 97 (1997) 2373–2419.
- [6] (a) T. Tozawa, J.T.A. Jones, S.I. Swamy, S. Jiang, D.J. Adams, S. Shakespeare, R. Clowes, D. Bradshaw, T. Hasell, S.Y. Chong, C. Tang, S. Thompson, J. Parker, A. Trewin, J. Bacsa, A.M.Z. Slawin, A. Steiner, A.I. Cooper, *Nat. Mater.* 8 (2009) 973–978;
(b) L.J. Barbour, *Chem. Commun.* (2006) 1163–1168;
(c) A. Thomas, *Angew. Chem. Int. Ed.* 49 (2010) 8328–8344.
- [7] N.J. Goodwin, W. Henderson, B.K. Nicholson, J.K. Sarfo, J. Fawcett, D.R. Russell, *J. Chem. Soc. Dalton Trans.* (1997) 4377–4384.
- [8] (a) K. Muralidharan, N.D. Reddy, A.J. Elias, *Inorg. Chem.* 39 (2000) 3988–3994;
(b) *Chem. Abstr.* 88 (1978) 23147j.
- [9] G. Behera, S. Ramakrishnan, *J. Polym. Sci. A Polym. Chem.* 42 (2004) 102–111.
- [10] (a) K.H. Lee, J.K. Park, W.J. Kim, *Electrochim. Acta* 45 (2000) 1301–1306;
(b) E. Morales, J.L. Acosta, *Electrochim. Acta* 45 (1999) 1049–1056;
(c) S.Y. An, I.C. Jeong, M.-S. Won, E.D. Jeong, Y.-B. Shim, *J. Appl. Electrochem.* 39 (2009) 1573–1578.
- [11] (a) H.R. Allcock, D.L. Olmeyer, S.J.M. O'Connor, *Macromolecules* 31 (1998) 753–759;
(b) R. Hooper, L.J. Lyons, M.K. Mapes, D. Schumacher, D.A. Moline, R. West, *Macromolecules* 34 (2001) 931–936.
- [12] (a) M. Matsumoto, T. Uno, M. Kubo, T. Itoh, *Ionics* 19 (2013) 615–622;
(b) B. Sun, J. Mindemark, K. Edström, D. Brandell, *Solid State Ion.* 262 (2014) 738–742;
(c) A.M. Elmer, P. Jannasch, *J. Polym. Sci. B Polym. Phys.* 45 (2007) 79–90.
- [13] (a) H.V. Babu, K. Muralidharan, *Polymer* 55 (2014) 83–94;
(b) H.V. Babu, B. Srinivas, K.P.K. Naik, K. Muralidharan, *J. Chem. Sci.* 127 (2015)

- 635–641.
- [14] (a) Z. Jin, B.L. Lucht, *J. Organomet. Chem.* 653 (2002) 167–176;
(b) T. Baumgartner, R. Reau, *Chem. Rev.* 106 (2006) 4681–4727.
- [15] (a) D.P. Gates, *Annu. Rep. Prog. Chem. Sect. A Inorg. Chem.* 100 (2004) 489–508;
(b) R.D. Archer, *Inorganic and Organometallic Polymers*, Wiley-VCH, New York, 2001;
(c) T. Vlad-Bubulac, C. Hamciuc, O. Petreus, *High. Perform. Polym.* 18 (2006) 255–264.
- [16] (a) N.J. Goodwin, W. Henderson, J.K. Sarfo, *Chem. Commun.* (1996) 1551–1552;
(b) N.J. Goodwin, W. Henderson, B.K. Nicholson, *Chem. Commun.* (1997) 31–32;
(c) N.J. Goodwin, W. Henderson, B.K. Nicholson, J.K. Sarfo, J. Fawcett, D.R. Russell, *J. Chem. Soc. Dalton Trans.* (1997) 4377–4384;
(d) K. Muralidharan, N.D. Reddy, A. Elias, *J. Inorg. Chem.* 39 (2000) 3988–3994;
(e) T.V.V. Ramakrishna, A.J. Elias, *J. Organomet. Chem.* 637 (2001) 382–389.
- [17] (a) Y. Morisaki, Y. Ouchi, K. Tsurui, Y. Chujo, *J. Polym. Sci. A Polym. Chem.* 45 (2007) 866–872;
(b) Y. Morisaki, Y. Ouchi, K. Naka, Y. Chujo, *Chem. Asian. J.* 2 (2007) 1166–1173.
- [18] (a) X. Zuo, X.-M. Liu, F. Cai, H. Yang, X.-D. Shen, G. Liu, *J. Mater. Chem.* 22 (2012) 22265–22271.
- [19] (a) D. Kumar, S.A. Hashmi, *Solid State Ion.* 181 (2010) 416–423;
(b) N. Vassal, E. Salmon, J.-F. Fauvarque, *Electrochim. Acta* 45 (2000) 1527–1532.
- [20] (a) P.R. Chinnam, S.L. Wunder, *J. Mater. Chem. A* 1 (2013) 1731–1739;
(b) Y. Lin, J. Li, Y. Lai, C. Yuan, Y. Cheng, J. Liu, *RSC Adv.* 3 (2013) 10722–10730.
- [21] (a) W. Xu, C.A. Angell, *Solid State Ion.* 147 (2002) 295–301;
(b) X.-G. Sun, C.A. Angell, *Solid State Ion.* 175 (2004) 257–260;
(c) X.-G. Sun, C.A. Angell, *Solid State Ion.* 175 (2004) 743–746.
- [22] (a) A.L. Agapov, A.P. Sokolov, *Macromolecules* 44 (2011) 4410–4414;
(b) Y. Wang, N.A. Lane, C.-N. Sun, F. Fan, T.A. Zawodzinski, A.P. Sokolov, *J. Phys. Chem. B* 117 (2013) 8003–8009;
(c) G. Polizos, E. Tuncer, A.L. Agapov, D. Stevens, A.P. Sokolov, M.K. Kidder, J.D. Jacobs, H. Koerner, R.A. Vaia, K.L. More, I. Sauers, *Polymer* 53 (2012) 595–603;
(d) A.L. Agapov, Y. Wang, K. Kunal, C.G. Robertson, A.P. Sokolov, *Macromolecules* 45 (2012) 8430–8437;
(e) F. Fan, Y. Wang, T. Hong, M.F. Heres, T. Saito, A.P. Sokolov, *Macromolecules* 48 (2015) 4461–4470.
- [23] (a) C.A. Angell, C. Liu, E. Sanchez, *Nature* 362 (1993) 137–139;
(b) J. Fan, C.A. Angell, *Electrochim. Acta* 40 (1995) 2397–2400.
- [24] (a) Z. Florjańczyk, E. Zygadło-Monikowska, W. Wiczorek, A. Ryszawy, A. Tomaszewska, K. Fredman, D. Golodnitsky, E. Peled, B. Scrosati, *J. Phys. Chem. B* 108 (2004) 14907–14914;
(b) Y. Karatas, R.D. Banhatti, N. Kaskhedikar, M. Burjanadze, K. Funke, H.-D. Wiemhöfer, *J. Phys. Chem. B* 113 (2009) 15473–15484.
- [25] (a) M.G. McLin, C.A. Angell, *Polymer* 37 (1996) 4713–4721;
(b) C.A. Angell, *Polymer* 38 (1997) 6261–6266.
- [26] (a) S. Bourbigot, S. Duquesne, *J. Mater. Chem.* 17 (2007) 2283–2300;
(b) S.Y. Lu, I. Hamerton, *Prog. Polym. Sci.* 27 (2002) 1661–1712.

Modified Hexamethyldisilazane (HMDS) - assisted synthesis of surfactant free metal chalcogenide nanoparticles and their applications as catalysts and photoresponsive materials

ORIGINALITY REPORT

% **7**

SIMILARITY INDEX

% **2**

INTERNET SOURCES

% **5**

PUBLICATIONS

% **2**

STUDENT PAPERS

PRIMARY SOURCES

1

Srinivas, Billakanti, Baskaran Ganesh Kumar, and Krishnamurthi Muralidharan. "Stabilizer free copper sulphide nanostructures for rapid photocatalytic decomposition of rhodamine B", Journal of Molecular Catalysis A Chemical, 2015.

Publication

% **3**

2

Submitted to University of Hyderabad, Hyderabad

Student Paper

% **1**

3

Jiang, Nan, Zhiliang Xiu, Zheng Xie, Hongyun Li, Gang Zhao, Wenpeng Wang, Yongzhong Wu, and Xiaopeng Hao. "Reduced graphene oxide–CdS nanocomposites with enhanced visible-light photoactivity synthesized using ionic-liquid precursors", New Journal of Chemistry, 2014.

Publication

<% **1**

4

Internet Source

<% 1

5

Submitted to National University of Singapore

Student Paper

<% 1

6

Peter D. Matthews, Paul D. McNaughter, David J. Lewis, Paul O'Brien. "Shining a light on transition metal chalcogenides for sustainable photovoltaics", Chem. Sci., 2017

Publication

<% 1

7

Xu, Hu, Wenjin Zhang, Wei Jin, Yiwen Ding, and Xinhua Zhong. "Facile synthesis of ZnS–CdIn₂S₄-alloyed nanocrystals with tunable band gap and its photocatalytic activity", Journal of Luminescence, 2013.

Publication

<% 1

8

conservancy.umn.edu

Internet Source

<% 1

9

www.elp.uji.es

Internet Source

<% 1

10

Kumar, Baskaran Ganesh, and Krishnamurthi Muralidharan. "Hexamethyldisilazane-assisted synthesis of indium sulfide nanoparticles", Journal of Materials Chemistry, 2011.

Publication

<% 1

11

www.nature.com

Internet Source

<% 1